Universität der Bundeswehr München
Fakultät für Luft- und Raumfahrttechnik
Institut für Mechanik

Predeformation and frequency dependence of filler-reinforced rubber under vibration

Experiments - Modelling - Finite Element Implementation

Dipl.-Ing. Daniel Wollscheid

Vollständiger Abdruck der von der
Fakultät für Luft- und Raumfahrttechnik
der Universität der Bundeswehr München
zur Erlangung des akademischen Grades eines

Doktor-Ingenieurs (Dr.-Ing.)

eingereichten Dissertation.

Vorsitzender:	Prof. Dr.-Ing. Hans-Joachim Wünsche
1. Berichterstatter:	Prof. Dr.-Ing. habil. Alexander Lion
2. Berichterstatter:	Prof. Dr. Sci. (Tech.) Leif Kari

Diese Dissertation wurde am 23. April 2014 bei der Universität der Bundeswehr München, 85577 Neubiberg eingereicht und durch die Fakultät für Luft- und Raumfahrttechnik am 11. August 2014 angenommen.

Tag der Prüfung: 31. Oktober 2014

Acknowledgements

The present work was developed during my employment as a scientific employee at the Institute of Mechanics at the Department of Aerospace Engineering of the Universität der Bundeswehr München. At this point, I would like to thank everyone for the support and assistance which was given to me during my employment and the development of this work.

My outstanding thanks first go to my doctoral thesis supervisor Prof. Dr.-Ing. habil. Alexander Lion who accompanied me during my work at the Institute. Moreover, I would like to thank Prof. Dr.-Ing. habil. Alexander Lion for the excellent academic education given to me, for his outstanding support, for his great interest in my work and the resulting discussions about various topics which were all essential to successfully develop this work.

My special thanks also go to the Deutsche Forschungsgemeinschaft for financing of this project.

Furthermore, I would like to thank Prof. Dr. Sci. (Tech.) Leif Kari for his special interest in my work as well as for his great support during the development of this thesis.

Apart from this, I would also like to thank all my colleagues at the Institute of Mechanics for the great time during my employment. My special thanks go to Dr.-Ing. Michael Johlitz and to Dipl.-Ing. Nico Diercks for the interesting and helpful discussions we had.

Finally, I would like to thank my family, especially my grandparents Mrs. Ruth Ladwein and Dr. med. Herbert Ladwein for the great support they provided me during the development of this work.

Daniel Wollscheid

Universität der Bundeswehr München

Abstract

Department of Aerospace Engineering
Institute of Mechanics

Dipl.-Ing. Daniel WOLLSCHEID

Predeformation and frequency dependence of filler-reinforced rubber under vibration

The dynamic mechanical properties of filler-reinforced rubber are characterised by a significant dependence on predeformation, dynamic amplitude and frequency if they are loaded with a large static predeformation superimposed by small harmonic vibrations. If the strain amplitudes are below 0.1 %, amplitude dependence does not occur. This is satisfied in the current thesis. In view of this, the main objective of this work is focused on the introduction of a three-dimensional constitutive model of finite viscoelasticity formulated in the frequency domain which is able to represent the vibroacoustic behaviour of the material with respect to predeformation and frequency dependence of the storage and the loss modulus in a broad frequency domain up to 10^5 Hz.
In order to derive a mathematical description of material behaviour, the predeformation and frequency dependent dynamic properties of four different carbon-black filled rubber vulcanisates are first examined through quasi-static and dynamic investigations. The quasi-static experiments are mainly focused on the predeformation dependent equilibrium stress response of the material, whereas the dynamic tests are performed via the dynamic mechanical analysis technique to characterise the predeformation and frequency dependence of the dynamic moduli in the frequency domain. Since this work does not account for stress-softening phenomena like the Mullins effect and the amplitude dependent Payne effect, preliminary quasi-static and dynamic tests are carried out to characterise the influence on these phenomena.
Based on these experimental facts, a suitable constitutive model is derived to represent the observed vibroacoustic behaviour with respect to the dependence of the storage and the loss modulus on predeformation and frequency. The formulation is based on the general approach by Haupt and Lion (2002) and starts with a decomposition of the deformation gradient into a volumetric and an isochoric part.

Thereafter, a second time-relative decomposition is applied to the isochoric part of the deformation gradient and the specific Helmholtz free energy is defined by the additive decomposition into an equilibrium part and a viscous overstress part. In order to account for the predeformation dependence, a deformation dependent relaxation function is introduced. On this basis, the constitutive equations are first derived in the time domain using the dissipation principle. In order to make the constitutive equations applicable for a transformation into the frequency domain, a geometrical linearisation in the neighbourhood of the predeformed state is applied. Finally, the solution for small harmonic oscillations in the neighbourhood of the static predeformation is evaluated and the dynamic modulus tensor of fourth order is derived.

In terms of computational efficiency, a second version of the constitutive approach is introduced by the extension of the classical formulation using the concept of fractional derivatives.

In order to identify the material parameters of both formulations, the specified identification equations are derived to simulate the experimental data. Thereafter, the material parameters are determined by the minimisation of errors between experimental data and numerically simulated data. The numerical simulations of both constitutive models are compared to each other to reveal the performance of the extended fractional approach.

After identification of the parameters, both constitutive approaches are implemented into the finite element code MSC Marc to perform efficient three-dimensional simulations of complex structures. Finally, the constitutive models are validated by the finite element simulation of dynamic tests with rubber-steel compounds up to 10^4 Hz.

Prior printed publications

During the development of this work, several prior printed publications which relate to parts of this work, have been published. These prior printed publications were approved by the Universität der Bundeswehr München and are listed below:

- D.Wollscheid and A. Lion (2012)
  Modelling of predeformation- and frequency-dependent material behaviour of filled rubber under large predeformations superimposed with harmonic deformations of small amplitudes, Proceedings in Applied Mathematics and Mechanics (PAMM), Vol. 12, Issue 1, 291–292, 2012.

- D.Wollscheid and A. Lion (2013)
  On the dynamic material behaviour of filled rubber with respect to preload and frequency
  Constitutive Models for Rubber VIII, CRC Press/Balkema, Taylor & Francis Group, London, 87–93, 2013.

- D.Wollscheid and A. Lion (2013)
  Predeformation- and frequency-dependent material behaviour of filler-reinforced rubber: Experiments, constitutive modelling and parameter identification
  International Journal of Solids and Structures, No. 50, 1217–1225, 2013.

- D.Wollscheid and A. Lion (2013)
  The benefit of fractional derivatives in modelling the dynamics of filler-reinforced rubber under large strains: a comparison with the Maxwell-element approach
  Computational Mechanics, Vol. 53, No. 5, 1015–1031, Springer-Verlag Berlin Heidelberg, ISSN: 0178-7675, 2014 (online 2013).

Contents

List of Figures

List of Tables

Abbreviations

CDI	**C**lausius **D**uhem **I**nequality
CPI	**C**lausius **P**lanck **I**nequality
DSC	**D**ifferential **S**canning **C**alorimetry
DMA	**D**ynamic **M**echanical **A**nalysis
EPDM	**E**thylene-**B**utadiene-**D**iene **R**ubber
EPDM20	**E**thylene-**B**utadiene-**D**iene **R**ubber with **20** phr of carbon-black
FEM	**F**inite **E**lement **M**ethod
NR	**N**atural **R**ubber
NR40	**N**atural **R**ubber with **40** phr of carbon-black
SBR	**S**tyrene-**B**utadiene **R**ubber
SBR20	**S**tyrene-**B**utadiene **R**ubber with **20** phr of carbon-black
SBR40	**S**tyrene-**B**utadiene **R**ubber with **40** phr of carbon-black
TPM	**T**ree-**P**arameter-**M**odel
WLF	**W**illiams-**L**andel-**F**erry equation

Symbols

Scalar values

a, b, c	material parameter
e	internal energy
c_1, c_2	material parameters of the WLF equation
m	mass
r	internal radiant heat
s	specific time at $t = s$
t	time
$\log a_\theta$	shifting function
A	surface
E	elastic spring stiffness
f	frequency
G^*	complex modulus
G'	storage modulus
G''	loss modulus
$G(t)$	relaxation function
N_a	shape function
T	absolute temperature in K
V	Volume
dv	material volume element of the current configuration
dV	material volume element of the reference configuration
α	material parameter of the fractional damper
$\varepsilon, \varepsilon_e, \varepsilon_{in}$	strain, elastic strain, inelastic strain
η	viscosity

η_k	viscosity of the k-th Maxwell element
$\hat{\eta}$	entropy production inside a material body
θ	temperature in °C
λ	stretch
μ	stiffness
μ_k	stiffness of the k-th Maxwell element
ξ	iso-parametric coordinate
ρ	mass density of the current configuration
ρ_0	mass density of the reference configuration
σ	engineering stress
σ_{eq}, σ_{ov}	equilibrium stress, overstress
$\sigma, \sigma_{eq}, \sigma_{ov}$	damaged stress
τ	relaxation time
τ_k	relaxation time of the k-th Maxwell element
Ψ	specific Helmholtz free energy
ω	angular frequency

Vectors

$\mathrm{d}\mathbf{a}$	material surface element of the current configuration
$\mathrm{d}\mathbf{A}$	material surface element of the reference configuration
$\mathbf{k}$	external forces
$\mathbf{q}$	heat flux of the current configuration
$\mathbf{q}_0$	heat flux of the reference configuration
$\mathbf{u}$	displacement vector
$\delta\mathbf{u}$	virtual displacement
$\Delta\mathbf{u}$	incremental displacement
$\mathbf{v}$	velocity
$\mathbf{x}$	position vector of the current configuration
$\mathbf{X}$	position vector of the reference configuration
$\mathrm{d}\mathbf{x}$	material line element of the current configuration
$\mathrm{d}\mathbf{X}$	material line element of the reference configuration

2nd order tensors

$\mathbf{0}$	zero tensor
$\mathbf{1}$	identity tensor
$\mathbf{a}$	Finger strain tensor
$\mathbf{A}$	Almansi strain tensor
$\mathbf{B}$	left Cauchy-Green tensor
$\mathbf{C}$	right Cauchy-Green tensor
$\mathbf{D}$	deformation rate tensor
$\mathbf{e}$	Piola strain tensor
$\mathbf{E}$	Green-Lagrange strain tensor
$\mathbf{F}$	deformation gradient
$\mathbf{L}$	velocity gradient
$\mathbf{I}$	linear momentum
$\mathbf{I}_R$	rotational momentum
$\mathbf{P}$	1st Piola-Kirchhoff stress tensor
$\mathbf{T}$	Cauchy stress tensor
$\tilde{\mathbf{T}}$	2nd Piola-Kirchhoff stress tensor
$\mathbf{U}$	right stretch tensor
$\mathbf{V}$	left stretch tensor
$\mathbf{W}$	spin tensor
$\boldsymbol{\Gamma}$	strain tensor of the elastic-inelastic configuration
$\boldsymbol{\varphi}_\eta$	entropy flux
$\boldsymbol{\sigma}_A$	surface stress
$\boldsymbol{\tau}$	weighted Cauchy stress tensor
$\boldsymbol{\tau}_{neq}$	stress tensor of the elastic-inelastic configuration
$\boldsymbol{\chi}$	bijective motion function

4th order tensors

$\overset{4}{\mathbf{1}}$	identity tensor
$\overset{4}{\mathbf{D}}$, $\mathbb{C}$	elasticity tensor
$\overset{4}{\mathbf{G}}$	dynamic modulus tensor
$\overset{4}{\mathbf{P}}$	projection tensor
$\overset{4}{\mathbf{R}}$	projection tensor

Configurations

$\mathcal{C}$	current configuration
$\mathcal{R}$	reference configuration
$\mathcal{I}$	intermediate configuration

Indexes & Operators

Indexes

$(\bullet)_{eq}$	equilibrium part of $\bullet$
$(\bullet)_{neq}$	non-equilibrium part of $\bullet$
$(\bullet)_{ov}$	overstress part of $\bullet$
$(\bullet)_{e}$	elastic part of $\bullet$
$(\bullet)_{in}$	inelastic part of $\bullet$
$(\bullet)_{t}$	time-relative part of $\bullet$
$(\bullet)_{0}$	constant static part of $\bullet$
$(\bullet)_{lin}$	linearised version of $\bullet$
$(\bullet)_{FE}$	finite element definition of a variable $\bullet$ in MSC Marc
$(\bullet)_{FE}$	variable $\bullet$ of classical model A
$(\bullet)_{FE}$	variable $\bullet$ of fractional model B
$(\hat{\bullet})$	volumetric part of a tensor $\bullet$
$(\bar{\bullet})$	isochoric part of a tensor $\bullet$
$\delta(\bullet)$	virtual value $\bullet$
$\Delta(\bullet)$	incremental value $\bullet$

Operators

$\mathrm{grad}(\bullet)$	spatial gradient of $\bullet$
$\mathrm{Grad}(\bullet)$	material gradient of $\bullet$
$\mathrm{div}(\bullet)$	divergence of $\bullet$
$\det(\bullet)$	determinant of $\bullet$
$\mathrm{tr}(\bullet)$	trace of $\bullet$
$(\bullet)^{-1}$	inverse of $\bullet$
$(\bullet)^{T}$	transposed of $\bullet$

$(\bullet)^{-T}$	inverse transposed of $\bullet$
$\dot{(\bullet)}$	time derivative of $\bullet$ with respect to time t
$(\bullet)'(s)$	time derivative of $\bullet$ with respect to time s
$(*)\,(*)$	simple scalar product of two vectors $*$
$(\bullet)\,(\bullet)$	simple scalar product of two tensors $\bullet$
$(\bullet)\,(*)$	simple scalar product of tensor $\bullet$ and vector $*$
$(\bullet)\cdot(\bullet)$	double scalar product of two tensors $\bullet$
$(\bullet)\otimes(\bullet)$	dyadic product of two tensors $\bullet$

Chapter 1

Introduction

1.1 Motivation

Rubber materials are characterised by fairly good dynamic mechanical properties. Thus, they are highly preferred in dynamic decoupling applications in the form of mounting systems and vibration isolators. In this context, they are used either to isolate the vibration of a dynamic system from the ambient structure or to prevent external vibrations from being transferred onto shock-sensitive systems. Thereby, the application area of rubber isolators and mounting systems stretches across a wide field reaching from washing machines, car engines and industrial systems up to bridges and buildings.

A very important application is found in the automotive industry where elastomer materials are commonly applied in the form of mounting systems for car engines. These engine mounts are typically loaded with a constant static predeformation which is caused by the engines' mass and is superimposed by small harmonic oscillations up to about 10^4 Hz once the engine is running. Since the automotive industry is focused on high driving comfort, the main task of an engine mount is to avoid the generated vibrations of the running engine from being transferred into the passenger cell, such that no vibration and noise is located inside the car. Due to the complex dynamic behaviour and the huge diversity of rubber vulcanisates, a great amount of preliminary tests have to be carried out in the design phase of an engine mount. In order to reduce time and costs at the design phase, effective finite element simulations have become very popular in modern industry. In fact, these simulations cannot completely replace experimental investigations, but they reduce the amount of experimental tests substantially and therefore save time and costs. Based on this, the purpose of this work is to provide an efficient finite element code for the simulation of engine mounts under various predeformations in a broad frequency range. With respect to the loading condition of engine mounts, the material behaviour of rubber has to be considered in terms of the dependence on the static predeformation and the frequency of the small harmonic vibration. Since finite element simulations are based on a mathematical description of material behaviour, the purpose of this work is to develop a three-dimensional constitutive approach that is capable of approximating the dynamic mechanical behaviour of

rubber with respect to the predeformation and frequency dependent dynamic material response. Due to computational efficiency, the constitutive model is transferred into the frequency domain and finally extended by the concept of fractional derivatives. After identification of the parameters, the classical and fractional extended formulations are implemented into the finite element code MSC Marc to allow for an efficient simulation of complex structures under various loading conditions.

1.2 Current state of research

The following section provides an overview of recent works dealing with investigations and constitutive modelling of the quasi-static and dynamic mechanical behaviour of rubber-like materials. As observed in recent studies, the mechanical material behaviour of polymers is characterised by numerous complex nonlinearities including the nonlinear stress-strain relation which occurs especially at finite strains, hysteresis effects, rate and frequency dependence, predeformation dependence, relaxation and retardation as well as softening effects such as the Mullins effect (Mullins 1948) or the amplitude dependent Payne effect (Payne 1961). For a comprehensive overview of the mechanical properties of rubber-like materials the reader is referred to specialised literature, e.g. the textbooks by Tobolsky (1967), Schwarzl (1990) or Sperling (2006).

Along with experimental investigation, the mathematical description of rubber-like materials has been grown to a huge theory in the past and is still enlarged today. To date, two powerful concepts in modelling the complex material behaviour of rubber have been established in literature. The first one is based on phenomenological constitutive formulations which do not account for the physical microstructure of the material. In this context, the material description of phenomenological constitutive models is usually based on unknown material parameters which are not related to physical background and have to be determined by experimental investigation and parameter identification. A comprehensive depiction of the phenomenological theory is provided, for instance, by Treloar (1975), Krawietz (1986) or Tschoegl (1989).
The second concept in modelling materials are micromechanical constitutive formulations. In contrast to phenomenological models, these approaches are based on the network theory and describe the material on the basis of its microstructure. Moreover, the material parameters of micromechanical formulations are related to physical background and thus enable for an interpretation of the material behaviour on the basis of the microstructure. A detailed overview of micromechanical concepts and the network theory is given by Heinrich et al. (1995).

The elastic properties of rubber-like materials are known to be only linear in a very small range of deformation. If the material is loaded at finite strains, its material response is usually characterised by a pronounced nonlinear relation between stress and strain. The mathematical description of this phenomenon is mostly managed via hyperelastic constitutive approaches which are based on isotropic strain energy functions. Phenemenological formulations of this type are proposed, for instance, by Mooney (1940), Rivlin (1948), Ogden (1972), James et al. (1975), James and Green (1975), Yeoh (1993), Gent (1996), Attard and Hunt (2004) or Dorfmann and Ogden

(2003) whereas micromechanically motivated strain energy functions are provided by Kilian and Viglis (1984), Heinrich et al. (1988), Arruda and Boyce (1993), Heinrich and Kaliske (1997), Kaliske and Heinrich (1999) or Heinrich et al. (2002). Hartmann (2001) provides a comprehensive overview of various hyperelastic strain energy functions and draws a comparison between them.

The viscoelastic material behaviour of rubber is a rate dependent phenomenon which occurs by means of hysteresis effects, frequency dependence, relaxation or creep. A comprehensive illustration of the physical structure of rubber and its linear viscoelastic material properties is provided in the textbook by Tobolsky (1967). The investigation and description of viscoelastic phenomena was first limited to linear viscoelasticity at small strains and has been gradually enlarged to complex nonlinear viscoelasticity at finite deformations. A detailed overview of the linear viscoelastic theory and the constitutive concepts in modelling linear viscoelasticity is given by Tschoegl (1989) or Lion (2007).
To date, the mathematical description of linear viscoelasticity is mostly based on rheological elements, such as elastic springs, viscous dampers and friction elements. These models are well established in literature and represent the material behaviour on the basis of linear differential equations of stress and strain. An individual element is only able to describe specific properties, such as pure elasticity, but they can be used in various combinations to represent complex material behaviour. A well-known element combination which enables for a representation of linear viscoelastic material properties is the so-called Maxwell element. This model is composed of an elastic spring and a viscous damper in series and thus appropriate to represent viscoelastic material properties, such as rate dependence or relaxation. An overview of this model and several other element combinations which are frequently applied to describe linear viscoelasticity is given by Lion (2007) or Ranz (2007). Regarding literature, the description of viscoelastic material behaviour on this basis is well established and applied in a multitude of works. In this context, the constitutive formulations by Holzapfel (1996), Kaliske and Rothert (1997a), Lion (1997a), Reese and Govindjee (1998), Drozdov (1998), Lion (2000b), Simo and Huges (2000), Middendorf (2001), Haupt and Lion (2002), Hartmann (2003) are mentioned among many others.
An essential approach for the mathematical description of linear viscoelastic behaviour under finite deformations was first provided by Coleman and Noll (1961). The authors introduced a three-dimensional formulation of finite linear viscoelasticity for isotropic materials which is based on linear convolution integrals and limited to strain states near the elastic equilibrium (Govindjee and Reese 1997). Other constitutive approaches which describe the mechanical behaviour of rubber on the basis of convolution integrals were proposed, for instance, by Simo (1987), Govindjee and Simo (1992a) or Kaliske and Rothert (1997a).
An effective tool to model nonlinear viscoelastic behaviour under finite strains is the concept of multiplicative viscoelasticity. This concept is based on a multiplicative decomposition of the deformation gradient into elastic and viscous parts and has been applied in several approaches, for instance, by Lubliner (1985), Lion (1997b) or Reese and Govindjee (1998). In Govindjee and Reese (1997), the authors compare the well-known viscoelastic damage model of Simo (1987) which is based on linear convolution integrals with the approach by Reese and Govindjee (1998) which applies the concept of

multiplicative viscoelasticity in combination with a nonlinear evolution law. In contrast to models using convolution integrals, the concept of multiplicative viscoelasticity is not restricted to strain states near the elastic equilibrium (Govindjee and Reese 1997). Apart from the description of nonlinear finite viscoelasticity, the multiplicative decomposition is also appropriate to describe other phenomena, such as thermoelasticity or elastoplasticity. For instance, Lee (1969) and Kaliske and Rothert (1998) decomposed the deformation gradient into elastic and plastic parts to model rate-independent elastoplasticity, whereas Haupt (2000) presented a formulation of finite thermoviscoelasticity which is based on a multiplicative decomposition of the deformation gradient into a thermal part and a mechanical part. An overview of the constitutive theory of multiplicative decomposition is provided by e.g. Meggyes (2001) and Lubarda (2004).
Eventually, modelling complex nonlinear viscoelasticity under finite deformations is mostly based on formulations applying convolution integrals or multiplicative viscoelasticity in combination with internal variables of stress or strain. Among a multitude of other works, well-known formulations of this type are proposed, for instance, by Simo (1987), Holzapfel (1996), Kaliske and Rothert (1997a), Lubliner (1985), Reese and Govindjee (1998), Hartmann and Haupt (1999), Huber and Tsakmakis (1999), or Lion (2000b).
Apart from constitutive modelling itself, computational and numerical aspects for the implementation of viscoelastic constitutive models into a finite element code are provided by Simo and Ju (1987), Hartmann and Haupt (1999) or Hartmann (2002).

Besides hyperelastic and viscoelastic properties of rubber, Mullins (1948) observed a strain-induced stress-softening during the first few loading cycles, which is known as the Mullins effect. This softening effect depends on the maximum amount of prestrain in the loading history and is irreversible at moderate temperatures (Mullins 1950; Bueche 1961; Mullins 1969). Since early investigations of Mullins (1950) revealed that the stress-softening is much more pronounced in filler loaded vulcanisates, the softening effect was first assumed to be only present in filler-reinforced rubbers and thus mainly related to a breakdown of the filler network. However, later investigations by Harwood et al. (1965) and Harwood and Payne (1966) disproved this theory and revealed a stress-softening in both, unfilled and filled vulcanisates. The authors even observed that the amount of stress-softening is similar for unfilled and filler-reinforced vulcanisates if the stress decrease is compared at the same level of stress instead of at the level of strain. Based on this observation, the softening of unfilled and filler-reinforced rubbers is mostly related to changes in the rubber matrix itself (Harwood et al. 1965). Thereby, the more pronounced occurrence of the Mullins effect for filler-reinforced rubbers is explained by the presence of the filler particles which cause an increase in local deformation of the rubber matrix (Harwood et al. 1965; Mullins and Tobin 1965; Harwood and Payne 1966). Referring to this assumption, Mullins and Tobin (1965) introduced the so-called strain-amplification factor to describe the increase of the local strain for filler-reinforced rubbers. Apart from the strain-induced softening itself, recent investigations by Ihlemann (2005) revealed an anisotropy of the Mullins effect. The author observed that the softening of the material depends on the loading direction and is pronounced differently in various directions.
The mathematical description of the stress-softening of rubber is mostly based on classical damage mechanics. Several phenomenological constitutive approaches on this

basis are the well-known damage formulation of Simo (1987) as well as other damage models proposed by, for instance, Miehe (1995), Lion (1996), Middendorf (2002), Chagnon et al. (2004) or Heimes (2005). As explained by Hoefer (2009), the basic idea of such damage models is related to a decrease of the load carrying area with increasing damage of the material. In order to describe this decrease mathematically, it is quite common to define the stored energy inside the material as a function of a scaling variable which can be interpreted as a measure of the damage inside the material. On this basis, increasing damage causes a reduction of the stored energy in the material and consequently results in a decrease of the stress response. A comprehensive constitutive formulation to describe more complex cyclic loading processes is introduced by Besdo and Ihlemann (2003). This phenomenological inelastic constitutive approach applies a material parameter which acts as a measure of the strain history. The model implies strong nonlinearities and is capable of describing hysteresis effects, the influence of the loading history as well as permanent deformations after unloading.
Among the phenomenological formulations, micromechanical damage models based on the theory of networks are introduced, too. In this context, Heinrich and Vilgis (1993), Klueppel and Schramm (2000) and Klueppel (2003) introduced micromecanical formulations which are based on the so-called "tube-model". Besides these, Govindjee and Simo (1991) and Govindjee and Simo (1992a) introduced a three-dimensional damage formulation to describe stress-softening of filler-reinforced rubber under finite strains. This approach is based on an additive decomposition of the deformation gradient and motivated by the assumption that the material consists of a hard phase which represents the filler particles and of a soft phase which specifies the rubber matrix (Mullins and Tobin 1957). On this basis, the authors decompose the free energy density into a part which is related to chains running between cross-links and a part that refers to chains running between particles. A micromechanical damage formulation which is motivated by a breakdown of bonds between filler particles is proposed by Miehe and Goektepe (2005). Further micromechanical damage models are given by Kaliske et al. (2001) or Qi and Boyce (2004).
Apart from the mentioned constitutive formulations, a very special concept is provided by Freund and Ihlemann (2010). The authors apply the concept of representative directions and introduce a three-dimensional generalisation which is independent of the type of the constitutive equations. The basic idea of this approach is to transfer a one-dimensional formulation into three dimensions by calculating the solution of the one-dimensional equations for various directions. Since the solution of the one-dimensional models is calculated with respect to various directions, another benefit of this approach is based on the fact that the anisotropy of the Mullins effect is automatically included without taking the anisotropy into account in the one-dimensional formulation itself.
Apart from the mathematical description, numerical aspects and formulations for the finite element implementation of constitutive models applying damage mechanisms are provided, for instance, by Simo and Ju (1987), Nacar et al. (1989), Govindjee and Simo (1992b), Miehe (1994), Heinrich and Kaliske (1997), Kaliske and Rothert (1997b), Miehe and Keck (2000), Kaliske et al. (2001), Besdo and Ihlemann (2003) or Matsuda et al. (2004).

The dynamic mechanical behaviour of elastomers is mostly studied using dynamic mechanical analysis (DMA). For a detailed description of this measuring technique, the reader is referred to the textbook by Menard (1999). In general, the material is loaded with a static predeformation which is superimposed by harmonic excitations. Via FFT-analysis, the dynamic material response is investigated in the frequency domain by means of the storage and loss modulus. On this basis, several dynamic mechanical properties, such as amplitude or frequency dependence, can be investigated via stepwise variation of e.g. strain amplitude or frequency during the harmonic loading.
In this context, first investigations of the dynamic mechanical behaviour of filler-reinforced rubber were made by Gehman et al. (1941) and Gehman (1942). These revealed a decrease of the dynamic stiffness with increasing dynamic amplitude of strain. This amplitude dependent softening is known as the Payne effect and was studied in more detail by Fletscher and Gent (1953), Payne (1961), Payne (1962a) and Payne (1962b). Apart from the decrease in the storage modulus with increasing strain amplitude, the authors observed a pronounced maximum in the loss modulus at middle amplitudes of strain. In contrast to the Mullins effect, the amplitude dependent softening is completely reversible and only present in filler-reinforced rubbers (Gehman 1942; Fletscher and Gent 1953; Hoefer 2009; Rendek and Lion 2010b).
Moreover, the manner in which the Payne effect occurs was found to be dependent on several parameters. Detailed investigations with respect to the amount and type of filler particles were done by Gehman (1942), Payne (1974), Dannenberg (1975), Dutta and Tripathy (1992) or Wang and Robertson (2005). These revealed that the Payne effect increases with an increasing amount of filler particles and is not pronounced in unfilled rubber vulcanisates. Additionally, it was observed that filler loaded systems with smaller particle size exhibit a more pronounced dependence on the dynamic strain amplitude (Dutta and Tripathy 1992; Rendek and Lion 2010b).
Moreover, Payne (1960) and Payne (1962a) observed that the appearance of the amplitude dependent softening is not present at arbitrary strains. The author found a yield point at very small dynamic amplitudes below which the dynamic stiffness remains constant and no amplitude dependence arises. This constance in the storage modulus was also established at very high strain amplitudes by Ulmer et al. (1974).
Among others, Payne (1962a), Dutta and Tripathy (1992), Rendek and Lion (2008) or Hoefer (2009) studied the influence of temperature on the dynamic moduli. These investigations revealed, that an increase of temperature results in a decrease of the dynamic moduli. Since Lion (1998), Rendek and Lion (2008) and Rendek and Lion (2010b) observed a heat build-up of the material under dynamic loading, which is increased with rising amplitude and frequency, temperature dependence should be considered if the material is loaded with great amplitudes and/or high frequencies.
Apart from the dependences already mentioned, the Payne effect is also affected by the static preload and frequency. In recent investigations, Rendek and Lion (2010b) found that the amplitude dependent softening is more pronounced at high frequencies whereas the static preload has a minor influence on the Payne effect.
The physical interpretation of the Payne effect is mostly related to a dynamic breakdown and recovery of the filler aggregates in the filled vulcanisate and is little affected by changes that take place in the rubber phase (Payne 1972; Klueppel and Heinrich 2002; Heinrich and Klueppel 2002; Heinrich and Klueppel 2004). Based on this assumption, Lion and Kardelky (2004) explain the amplitude dependent characteristics

of the storage and the loss modulus as follows: the monotonic decline of the storage modulus with increasing dynamic amplitudes is caused by a decrease in the number of intact filler bonds. Since the loss modulus is a measure of energy dissipation, it is proportional to the breakage rate of the filler bonds, which is proportional to the number of intact bonds and increases with increasing amplitudes. Thus, the loss modulus respectively the energy loss first increases with the amplitude because there are enough intact filler bonds, and decreases after a maximum with the amplitude because the number of intact bonds has considerably decreased.
Recent investigations in which the Payne effect was studied in more detail revealed complex dependencies on the loading process respectively on the loading history. Wang and Robertson (2005) and Robertson and Wang (2006) applied a special procedure of dynamic loadings and observed a complex dependence of the dynamic modulus on the loading history. Basically, the specimens were loaded with a constant dynamic amplitude for several hours and then allowed to rest for some time. After applying an amplitude sweep test, the authors observed jamming phenomena which they called the "hole burning effect". Dutta and Tripathy (1992), Chazeau et al. (2000) and Rendek and Lion (2010b) observed a dependence of the Payne effect on the loading process as well as recovery of the dynamic moduli. In order to study the amplitude dependence of the dynamic moduli with respect to complex dynamic loadings as they appear in real applications, Wrana et al. (2003), Wrana and Haertel (2008) and Rendek and Lion (2010b) applied bimodal loadings which consist of two superimposed harmonic oscillations of different frequencies.
Based on these experimental observations, numerous constitutive approaches to describe the amplitude dependence of the dynamic material properties are provided in literature. A well-known formulation in the frequency domain is the micromechanical Kraus model (Kraus 1984). As described in Lion (2006), this model is limited to the description of amplitude dependent effects and only valid in the frequency domain. The approach is motivated by a permanent breakdown and recovery of the filler bonds and the amplitude dependent effects are taken into account by a damage and a recovery rate of the physical bonds. In principle, the approach is also capable of representing temperature and frequency dependences if the parameters are defined as a function of temperature or frequency. Since the formulation of the storage modulus and of the loss modulus are independent of each other, there is no thermomechanical consistent formulation within the time domain (Lion 2000b; Lion 2005). Other micromechanical approaches based on the Kraus model are introduced by Vieweg et al. (1995) and Ulmer (1996). Further models which are motivated by the theory of networks are proposed, for instance, by Klueppel and Heinrich (1995), Huber et al. (1996), Boehm (2001) or Heinrich and Klueppel (2004). An overview of several micromechanical concepts and recent advances in the theory of filler networking is provided by Heinrich and Klueppel (2002).
Apart from the micromechanical formulations, the Payne effect is commonly described by rate independent phenomenological approaches. In this context, Rabkin et al. (2003) introduced a phenomenological concept to describe the amplitude dependent softening on the basis of friction elements. Other rate independent formulations of this type are proposed, for instance, by Besdo and Ihlemann (1996), Ahmadi and Muhr (1997) or Kaliske and Rothert (1998). Lion (2006) provides an overview of various concepts in modelling the Payne effect.

A phenomenological approach of thermoviscoelasticity which also includes temperature dependent effects is proposed by Lion (1998). The formulation is based on a multiplicative decomposition of the deformation gradient into a thermal and a mechanical part and uses a scaling function which depends on the temperature. Additionally, an internal variable is introduced and thixotropic effects are described by history dependent viscosities. Another model which includes the temperature dependence on the basis of a multiplicative decomposition of the deformation gradient into thermal and mechanical parts is proposed in a recent work by Hoefer (2009). There, the free energy function is additively decomposed into an elastic and inelastic mechanical parts and a thermal part. Furthermore, the formulation employs process dependent viscosities and an internal time scale to consider the complex deformation history.
A time domain formulation which describes transient effects arising due to changes in dynamic amplitude is proposed by Ahmadi et al. (2005) whereas frequency domain formulations are provided, for instance, by Joshi and Lenov (2001) or Richter et al. (2010). A three-dimensional formulation which is applicable for both, time and frequency domain, is proposed by Rendek and Lion (2010a). The authors linearise the constitutive equations in the neighbourhood of the predeformed state, introduce a dynamic modulus tensor of fourth order and provide an implementation of the model into finite element code.

The investigation and description of the vibroacoustic transfer behaviour of rubber at high frequency vibrations which are superimposed upon large static predeformation is mostly inspired by technical applications, such as mounting systems, vibration isolators or tyres. Due to the loading situation and the fact that the dynamic properties depend on predeformation and frequency, the influence of these values on dynamic stiffness and damping behaviour of rubber is of great importance. On the one hand, it is observed that the dynamic moduli increase with increasing frequency (Kari 2003; Hoefer and Lion 2009; Rendek and Lion 2010b), whereas, on the other hand, the dependence on static predeformation mostly appears in an increase in dynamic stiffness with increasing predeformation (Sjoeberg and Kari 2003; Lion et al. 2009; Rendek and Lion 2010a; Suwannachit and Nackenhorst 2010). Thereby, the predeformation dependent characteristics seem to be related to the hyperelastic behaviour of the material (Hoefer 2009). In compression tests of unfilled and filled NR vulcanisates, Kim and Youn (2001) observed an initial decline of dynamic stiffness at low precompression which was followed by a subsequent increase at higher precompression. The authors relate the initial decrease in dynamic stiffness to a breakage of the filler bonds whereas the subsequent increase is interpreted by the limited extensibility of the rubber chains.
In order to describe the vibroaccoustic of rubber under large predeformation superimposed by harmonic vibrations it is quite common to consider the effects of predeformation and harmonic vibration separately. This concept was provided by Lianis (1963) and is based on the assumption that the static predeformation is dated back in the past such that the material already reached its equilibrium state. Since the static predeformation represents an equilibrium state of the material, viscoelastic effects are only considered for the harmonic excitation. Moreover, the predeformed state is defined as a new reference configuration and the constitutive equations are usually linearised in the neighbourhood of the static predeformation.

Based on this concept, Morman and Nagtegaal (1983) propose a constitutive formulation for the finite element implementation of combined static predeformation with superimposed small harmonic oscillations into the finite element code MSC Marc. The constitutive approach inherits nine scalar-valued functions which depend on the first and second derivative of the specific Helmholtz free energy with respect to the first and second invariants and on the invariants themselves. From the separation of static predeformation and superimposed harmonic vibration, the analysis procedure is divided into two steps. First, the nonlinear material response due to the static predeformation is evaluated in the time domain without consideration of viscoelastic or inertia effects. In the second step, the nine scalar-valued material responses which result from the superimposed harmonic excitation are calculated in the frequency domain. In this part of the analysis, viscoelastic material behaviour and inertia effects are both considered. A recent constitutive approach to represent frequency dependence of filler-reinforced rubber and the corresponding finite element implementation on this basis is given by Retka (2011).
In order to describe the frequency dependent material behaviour in a broad range, it is very common to apply the concept of fractional derivatives (Lion and Kardelky 2004). In contrast to classical viscoelastic formulations, the benefit of viscoelastic models of fractional order is the small number of material parameters needed to represent the material properties sufficiently over a broad frequency domain (Kari 2001a; Kari 2001b). An overview about the mathematical theory of fractional derivatives is provided in the textbook by Oldham and Spanier (1974). In Kari (2001a) and Kari (2001b), the author presents a viscoelastic waveguide model based on fractional derivatives to describe the frequency dependent dynamic behaviour of the axial stiffness of cylindrical vibration isolators in the audible frequency range. This approach is validated by experimental investigations of a rubber cylinder with bonded steel plates in a broad frequency range from 10 Hz up to 5000 Hz and agrees very well within the hole frequency range. Sjoeberg and Kari (2002) and Sjoeberg and Kari (2003) introduce further fractional approachs to describe the experimentally observed frequency and amplitude dependence of rubber in the frequency domain. These models describe the frequency dependent behaviour on the basis of a Kelvin-Voigt element of fractional order and additionally account for amplitude dependent effects by a generalised friction element. Ramirez and Coimbra (2007) introduce a special type of fractional formulation by applying a fractional derivative which is a function of the independent time. The model is validated with experimental results and agrees very well in a wide frequency range over more than eight orders of magnitude. Fractional formulations based on the finite viscoelastic models of Simo (1987) and Reese and Govindjee (1998) as well as finite element implementation are introduced by Adolfsson and Enelund (2003) and Adolfsson (2004). A recent approach to describe the damping behaviour of VE dampers, which is based on a fractional Kelvin-Voigt model as well as on a fractional Maxwell model is presented by Lewandowski and Pawlak (2011). Other fractional approaches are proposed by Nonnenbacher (1991), Drozdov (1997) or Lion (2001).
With respect to finite element simulations, the numerical computation of fractional formulations in the time domain is very time-consuming which is due to the non-local character of the fractional derivative. In order to solve this problem, Schmidt (2003) delivers an efficient proposal for the finite element implementation of a model with fractional derivatives in the time domain. The basic assumption is related to a fading

memory of fractional derivatives such that it is possible to consider parts of the history with less temporal resolution without a loss of accurateness for the time integration. Other numerical concepts for finite element computation of fractional order in the time domain are given by Enelund and Josefson (1997), Enelund et al. (1999), Gaul and Schanz (1994) and Gaul and Schanz (1999).
Apart from formulations in the time-domain, frequency domain formulations to represent frequency and amplitude dependence of rubber bushings are proposed by Garcia (2006) and Garcia et al. (2007). The authors investigated the frequency and amplitude dependent dynamic behaviour of carbon-black filled rubber bushings in axial and radial directions. Based on their observations, they develop a model to describe the axial and radial dynamic stiffness of rubber bushings with respect to frequency and amplitude. The formulation is based on a separable elastic, viscoelastic and frictional material model and the amplitude dependence is included by means of equivalent shear moduli.

Apart from the description of just frequency dependent properties under harmonic vibrations, several works deal with the description of predeformation and frequency dependence under large static prestrain with superimposed oscillations. On the basis of the general formulation by Haupt and Lion (2002), Lion et al. (2009) introduce a frequency domain formulation to represent preload and frequency dependent phenomena. The authors derive a frequency dependent dynamic modulus tensor of fourth order to describe the dynamic viscoelastic behaviour in the frequency domain. The constitutive equations are first derived in the time-domain, then linearised in the neighbourhood of the predeformation and finally evaluated in the frequency domain. Kari (2003) investigates the dynamic stiffness of preloaded rubber isolators and presents a constitutive model which is capable of representing both, frequency and predeformation dependence, in the audible range up to 1000 Hz. In the same year, Sjoeberg and Kari (2003) investigated the quasi-static and dynamic force response of a rubber vibration isolator under large static predeformation superimposed by harmonic oscillations in the time and frequency domain and observed a strong dependence on static precompression, dynamic amplitude and frequency. The dynamic stiffness is found to increase with static precompression and frequency and to decrease with dynamic amplitude whereas the loss angle reveals a maximum at intermediate strains. Based on this, the authors present a nonlinear dynamic model to describe these dependencies on frequency, predeformation and amplitude simultaneously by splitting the total force into an elastic, a viscoelastic and a friction part. Thereby, the elastic force is represented by a nonlinear shape factor based approach, the viscoelastic force is modelled by a fractional derivative model, and the friction force is represented by a generalised friction element. Kim and Youn (2001) introduce another approach to describe the influence of frequency and predeformation. The formulation is derived by the linearisation of the nonlinear viscoelastic model of Simo (1987) in the neighbourhood of the static predeformation. On this basis, the authors define the predeformed state as the new reference configuration and separate the stress into static and dynamic parts. In order to describe the influence of prestrain, a correction factor for the static deformation is additionally introduced. Cho and Youn (2006) introduce an extension of the model proposed by Kim and Youn (2001) by applying another correction factor to describe the amplitude dependence of

the Payne effect as well. With respect to the loading condition of tyres, Suwannachit and Nackenhorst (2010) present a constitutive model to represent the inelastic behaviour of rubber under large cyclic preloading in combination with superimposed excitations of high frequency. The authors combine the nonlinear viscoelastic model of Simo (1987) with a pseudo-elastic approach to describe the related effects, such as nonlinear elasticity, hysteresis and damage at low frequencies. The deformation gradient is decomposed into a linear part which is associated with the behaviour at high frequencies and a nonlinear part which is related to the inelastic deformation at low frequency. Moreover, the authors present the linearisation of the constitutive approach and provide a finite element implementation on the basis of the proposal by Morman and Nagtegaal (1983).
Regarding computation aspects, a numerical approach for the finite element implementation of a tire model, the ALE-formulation, is introduced by Nackenhorst (2004). An implementation of the viscoelastic model provided by Kim and Youn (2001) into a finite element code is presented by Lee et al. (2003). Another numerical implementation of the fractional formulation given by Sjoeberg and Kari (2003) is provided by Gil-Negrete et al. (2009).

A very new area of investigation deals with so-called magneto sensitive rubbers. These are filled with iron particles such that their stiffness can be controlled by applying an external magnetic field. The sensitivity of the dynamic stiffness on the magnetic field appears in an increase of stiffness with the magnetic field (Blom and Kari 2011; Blom and Kari 2012). Based on experimental investigations, Blom and Kari (2011) made the following observations: The rubber reveals a strong amplitude dependence even for small strains and the magnetic sensitivity also strongly depends on the amplitude. Furthermore, the elastic component is found to be magneto-sensitive whereas the dependence of the viscoelastic component on the magnetic induction appears to be small. On the basis of these observations, the authors introduce a nonlinear constitutive model for the amplitude, frequency and magnetic field dependences of magneto-sensitive rubber in the audible frequency range which is in very good agreement with the experimental results.

1.3 Composition of this work

The comprehensive presentation of this work is separated into several chapters.
The first three chapters are meant to introduce the reader to the mathematical requirements needed for a better understanding. For this reason, the fundamentals of the continuum mechanical theory as well as the main concepts of material modelling this work refers to are first presented in chapters 2 and 3. Apart from the mathematical basis, the focus of chapter 4 is the introduction of the material class of elastomers and its complex material behaviour.
After the presentation of these basics, the experimental investigations to characterise the behaviour of the underlying elastomers are presented in chapter 5. In chapter 6, the classical and the fractional extended constitutive approaches to describe the dynamic mechanical material characteristics are presented. The identification of the material parameters and the implementation of the constitutive model into the finite element code MSC Marc are provided in chapter 7 and 8. Section 9 deals with the validation of the constitutive approach and provides a comparison between validation experiments and the finite element simulation. Moreover, the finite element computation of a real engine mount is performed in a frequency range up to 10 kHz. Finally, chapter 10 concludes with the outcome of this thesis and provides an outline of further improvements.

Appendix A provides a short overview about tensor algebra and is used to acquaint the reader with the mathematical notation which is used in this work.

Chapter 2

Basics of continuum mechanics

Introduction

The continuum mechanical theory is a powerful tool to describe physical phenomena of materials mathematically. Instead of considering the microstructure of materials, such as the molecular structure, the mathematical description of this theory is only focused on the macroscopic level. On this basis, the material body is considered as an uniformly distributed continuum which is composed of an infinite number of individual material points. Each of these materials points is providing the material properties and carrying all physical quantities, such as mass density or temperature. In general, the comprehensive theory of continuum mechanics can roughly be divided into three fields.
The first one is the kinematics which is focused on the mathematical description of motion, displacement and deformation of material bodies due to external forces.
The balance principles constitute the second field in continuum mechanics. These principles can be classified as natural laws arising from physical experience. They are introduced axiomatically and can not be proven.
The last field in continuum mechanics is related to the constitutive equations. They can be interpreted as mathematical material laws which deliver the connection between the external forces acting on a material body and the resulting deformation.

Outline

The focus of this chapter is to provide the basics of the continuum mechanical theory, which are relevant for this work. The first section gives an overview of the kinematics. The balance principles are introduced in the second section of this chapter, whilst the last section presents a special form of the second law of thermodynamics which is commonly used to formulate meaningful constitutive equations. Since the constitutive equations themselves define their own theory, these will be introduced in the next chapter separately. A comprehensive overview about the theory of continuum mechanics and materials is given in specialised literature, as for instance Haupt (2000), Holzapfel (2000) or Greeve (2003). Moreover, detailed discussions about the kinematics

and balance principles, the following presentation mostly refers to, are provided in the manuscripts by Lion (2008) and Johlitz (2009).

2.1 Kinematics

The kinematics delivers suitable kinematic variables and relations which are necessary for the description of motion, displacement and deformation of a material body. The following section briefly overviews the most important kinematic variables and relations, which are applied in this work. A detailed description of the kinematic variables and relations is provided by Haupt (2000), Holzapfel (2000) or Greeve (2003).

2.1.1 Motion and displacement

As explained by Johlitz (2009), the description of motion, displacement and deformation of material bodies is based on so-called configurations. As illustrated figure 2.1, two basic configurations are introduced in continuum mechanics. The first one is the reference configuration and the second one is the current configuration.

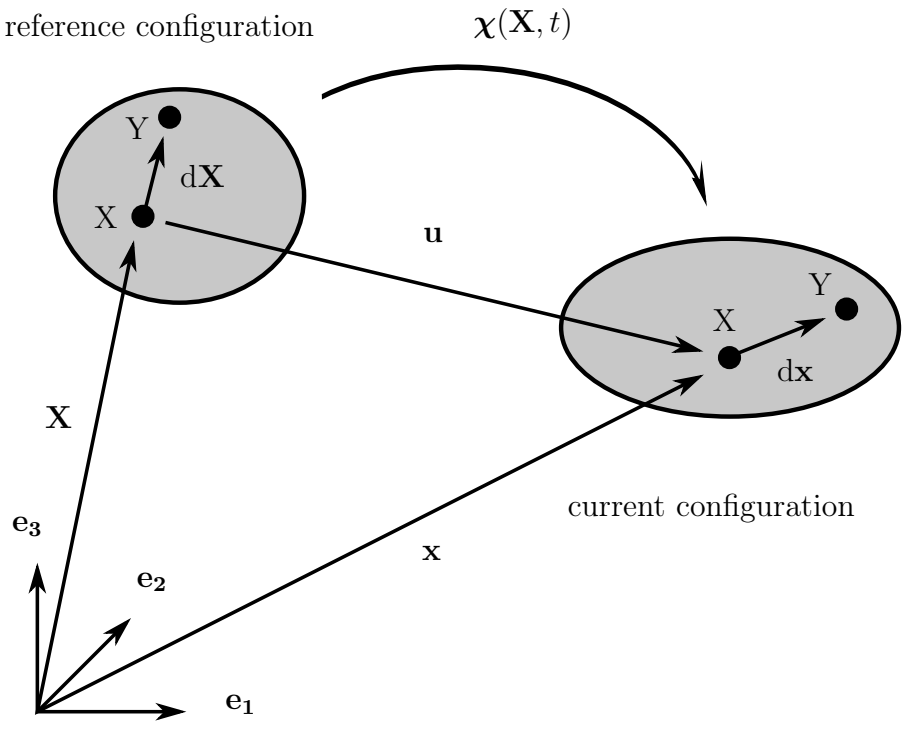

FIGURE 2.1: Reference and current configuration

The reference configuration usually refers to an undeformed state of the material body whereas the current configuration represents the current deformed state of the material. As given by figure 2.1, the positions of a material point X in the reference and current

configuration are specified by position vectors $\mathbf{X}$ and $\mathbf{x}$. The distances between two material points X and Y in the reference and current configuration are expressed by vectors $\mathrm{d}\mathbf{X}$ and $\mathrm{d}\mathbf{x}$.

In principle, the kinematic relations can be expressed with respect to each configuration such that a mathematical description of the material can be managed on the basis of the reference or the current configuration. If the material is described on the basis of the reference configuration, the variables are expressed by functions of the reference position vector $\mathbf{X}$. This type of consideration is usually called material or Lagrangian description. In contrast to that, a description on the basis of the current configuration implies that all variables are represented by functions of the current position vector $\mathbf{x}$. This type of consideration is commonly called spatial or Eulerian description.

Referring to the manuscript by Johlitz (2009), the relationship between both considerations is established by a bijective motion function which builds up the connection between the position vector $\mathbf{X}$ of a material point X in the reference configuration and its position vector $\mathbf{x}$ in the current configuration

$$\mathbf{x} = \boldsymbol{\chi}(\mathbf{X}, t) \quad \text{and} \quad \mathbf{X} = \boldsymbol{\chi}^{-1}(\mathbf{x}, t) \; . \tag{2.1}$$

Based on these relations, the velocity and acceleration fields with respect to the reference configuration are derived by differentiation of the motion with respect to time

$$\dot{\mathbf{x}}(\mathbf{X}, t) = \frac{\mathrm{d}\boldsymbol{\chi}(\mathbf{X}, t)}{\mathrm{d}t} = \mathbf{v}(\mathbf{X}, t) \quad \text{and} \quad \ddot{\mathbf{x}}(\mathbf{X}, t) = \frac{\mathrm{d}^2\boldsymbol{\chi}(\mathbf{X}, t)}{\mathrm{d}t^2} = \mathbf{a}(\mathbf{X}, t) \; . \tag{2.2}$$

In order to derive the velocity and acceleration fields in the current configuration, the position vector $\mathbf{X}$ in (2.2) is replaced by the inverse of the motion

$$\mathbf{v}(\mathbf{x}, t) = \dot{\mathbf{x}}(\boldsymbol{\chi}^{-1}(\mathbf{x}, t), t) \quad \text{and} \quad \mathbf{a}(\mathbf{x}, t) = \ddot{\mathbf{x}}(\boldsymbol{\chi}^{-1}(\mathbf{x}, t), t) \; . \tag{2.3}$$

By differentiation of the velocity field in (2.3), an alternative representation of the acceleration field in the current configuration is given by

$$\begin{aligned} \mathbf{a}(\mathbf{x}, t) &= \frac{\partial \mathbf{v}(\mathbf{x}, t)}{\partial t} + [\operatorname{grad} \mathbf{v}(\mathbf{x}, t)] \; \mathbf{v}(\mathbf{x}, t) \\ &= \frac{\partial \mathbf{v}(\mathbf{x}, t)}{\partial t} + \left[\frac{\partial \mathbf{v}(\mathbf{x}, t)}{\partial \mathbf{x}}\right] \mathbf{v}(\mathbf{x}, t) \; . \end{aligned} \tag{2.4}$$

Therein, the first term represents the local part of the acceleration whereas the second term denotes its convective part. The last quantity to be introduced is the displacement vector

$$\mathbf{u}(\mathbf{X}, t) = \mathbf{x}(\mathbf{X}, t) - \mathbf{X} \; . \tag{2.5}$$

It provides the connection between position vector $\mathbf{X}$ at the initial time t_0 and current position vector $\mathbf{x}$ at the time $t > t_0$ and thus represents the displacement of a material point X over time.

2.1.2 Deformation gradient

The deformation gradient $\mathbf{F}$ is a fundamental quantity to describe the deformation of a material body. It is a tensor of 2nd order

$$\mathbf{F} = F_{ij}\,[\mathbf{e}_i \otimes \mathbf{e}_j] \tag{2.6}$$

which is defined by differentiation of the motion with respect to the position vector $\mathbf{X}$

$$\mathbf{F} \;=\; \frac{\partial \boldsymbol{\chi}(\mathbf{X},t)}{\partial \mathbf{X}} \;=\; \frac{\partial \mathbf{x}}{\partial \mathbf{X}} \;=\; \mathrm{Grad}\,\mathbf{x} \;=\; \mathbf{1} \,+\, \mathrm{Grad}\,\mathbf{u} \;=\; \mathbf{1} \,+\, \mathbf{h}\;. \tag{2.7}$$

$\mathbf{1}$ is the identity tensor and $\mathbf{h}$ denotes the displacement gradient. As shown by Johlitz (2009), the deformation gradient maps material line elements $\mathrm{d}\mathbf{X}$ of the reference configuration onto material line elements $\mathrm{d}\mathbf{x}$ of the current configuration[1]

$$\mathrm{d}\mathbf{x} \;=\; \mathbf{F}\,\mathrm{d}\mathbf{X}\;. \tag{2.8}$$

The inverse of the deformation gradient is given by

$$\mathbf{F}^{-1} \;=\; \frac{\partial \boldsymbol{\chi}^{-1}(\mathbf{x},t)}{\partial \mathbf{x}} \;=\; \frac{\partial \mathbf{X}}{\partial \mathbf{x}} \;=\; \mathrm{grad}\,\mathbf{X} \tag{2.9}$$

and enables for the opposite transformation of material line elements

$$\mathrm{d}\mathbf{X} \;=\; \mathbf{F}^{-1}\,\mathrm{d}\mathbf{x}\;. \tag{2.10}$$

In addition, the deformation gradient and its determinant $J = \det\mathbf{F}$ offer the possibility to map material surface and volume elements between both configurations

$$\begin{aligned} \mathrm{d}\mathbf{a} \;&=\; (\det\mathbf{F})\,\mathbf{F}^{-T}\,\mathrm{d}\mathbf{A} \;&=\;& J\,\mathbf{F}^{-T}\,\mathrm{d}\mathbf{A}\;, \\ \mathrm{d}v \;&=\; \det\mathbf{F}\,\mathrm{d}V \;&=\;& J\,\mathrm{d}V\;. \end{aligned} \tag{2.11}$$

The deformation gradient $\mathbf{F}$ contains rotational and stretching parts of deformation. Regarding constitutive modelling, rotational parts of deformation are often not considered such that a separation into rotational and stretching parts of deformation is beneficial. In this context, the polar decomposition can be applied meaning that the deformation gradient is multiplicatively decomposed into a rotational tensor $\mathbf{R}$ and the stretching tensors $\mathbf{U}$ or $\mathbf{V}$

$$\mathbf{F} \;=\; \mathbf{R}\,\mathbf{U} \;=\; \mathbf{V}\,\mathbf{R}\;. \tag{2.12}$$

In this, the orthogonal tensor $\mathbf{R}$ specifies the rotational part of deformation whereas the left stretch tensor $\mathbf{V}$ respectively the right stretch tensor $\mathbf{U}$ characterise the stretching parts of deformation. Both stretching tensors are positively definite and symmetric and can be transformed into each other by applying the operations[2]

$$\mathbf{V} \;=\; \mathbf{R}\,\mathbf{U}\,\mathbf{R}^T \quad , \quad \mathbf{U} \;=\; \mathbf{R}^T\,\mathbf{V}\,\mathbf{R}\;. \tag{2.13}$$

[1] simple scalar product of tensor $\mathbf{A}$ and vector $\mathbf{b}$: $\mathbf{A}\,\mathbf{b} = A_{ij}\,b_j\,\mathbf{e}_i$ (cf. Appendix A)

[2] simple scalar product of 2nd order tensors $\mathbf{A}$ and $\mathbf{B}$: $\mathbf{A}\,\mathbf{B} = A_{ij}\,B_{ij}\,\mathbf{e}_i \otimes \mathbf{e}_j$ (cf. Appendix A)

Apart from the polar decomposition, it is straight forward to eliminate the rotational parts of deformation. In this context, the right Cauchy-Green tensor $\mathbf{C}$ on the reference configuration and the left Cauchy-Green tensor $\mathbf{B}$ on the current configuration are introduced as

$$\begin{aligned} \mathbf{C} &= \mathbf{F}^T\,\mathbf{F} = (\mathbf{R}\,\mathbf{U})^T\,(\mathbf{R}\,\mathbf{U}) = \mathbf{U}^T\,\mathbf{R}^T\,\mathbf{R}\,\mathbf{U} = \mathbf{U}^2 \;, \\ \mathbf{B} &= \mathbf{F}\,\mathbf{F}^T = (\mathbf{V}\,\mathbf{R})\,(\mathbf{V}\,\mathbf{R})^T = \mathbf{V}\,\mathbf{R}\,\mathbf{R}^T\,\mathbf{V}^T = \mathbf{V}^2 \;. \end{aligned} \tag{2.14}$$

In contrast to the deformation gradient $\mathbf{F}$, the tensors $\mathbf{C}$ and $\mathbf{B}$ are symmetric and link squares of material line elements. Thus, they only contain the stretching parts of deformation whereas its rotational part is eliminated.

2.1.3 Strain tensors

Apart from the deformation tensors, the theory of continuum mechanics introduces equivalent strain tensors with respect to each configuration. As presented in Johlitz (2009), these tensors can be derived by subtraction of squares of material line elements. In so doing, the Green-Lagrange strain tensor $\mathbf{E}$ acting on the reference configuration and the Almansi strain tensor $\mathbf{A}$ referring to the current configuration are defined by

$$\begin{aligned} \mathbf{E} &= \frac{1}{2}\,(\mathbf{C} - \mathbf{1}) \;, \\ \mathbf{A} &= \frac{1}{2}\,(\mathbf{1} - \mathbf{B}^{-1}) \;. \end{aligned} \tag{2.15}$$

Moreover, the strain tensors can be transformed into each other by applying the push-forward and the pull-back operation

$$\begin{aligned} \mathbf{A} &= \mathbf{F}^{-T}\,\mathbf{E}\,\mathbf{F}^{-1} \;, \\ \mathbf{E} &= \mathbf{F}^T\,\mathbf{A}\,\mathbf{F} \;. \end{aligned} \tag{2.16}$$

Regarding surface strains, the tensors $\mathbf{e}$ and $\mathbf{a}$ are obtained by subtraction of squares of material surfaces elements

$$\begin{aligned} \mathbf{e} &= \frac{1}{2}\,(\mathbf{C}^{-1} - \mathbf{1}) \;, \\ \mathbf{a} &= \frac{1}{2}\,(\mathbf{1} - \mathbf{B}) \;. \end{aligned} \tag{2.17}$$

The first one is the Piola strain tensor $\mathbf{e}$ which is related to the reference configuration whereas the second one is the Finger tensor $\mathbf{a}$ which operates on the current configuration. Similar to $\mathbf{E}$ and $\mathbf{A}$, both tensors can be transferred into each

$$\begin{aligned} \mathbf{a} &= \mathbf{F}\,\mathbf{e}\,\mathbf{F}^T \;, \\ \mathbf{e} &= \mathbf{F}^{-1}\,\mathbf{a}\,\mathbf{F}^{-T} \;. \end{aligned} \tag{2.18}$$

2.1.4 Deformation rate and strain rate

The velocity gradient and the strain rate are essential for the mathematical description of inelastic and viscous phenomena. The velocity gradient and the strain rate can be defined with respect to each of the configurations. Referring to the manuscript by Johlitz (2009), the material velocity gradient in the reference configuration is defined by the time derivative of the deformation gradient $\mathbf{F}$ respectively by the material gradient of the velocity field $\mathbf{v}(\mathbf{X}, t)$

$$\dot{\mathbf{F}} = \operatorname{Grad} \mathbf{v}(\mathbf{X}, t) = \frac{\partial \mathbf{v}}{\partial \mathbf{X}} . \tag{2.19}$$

Regarding the actual configuration, the spatial velocity gradient $\mathbf{L}$ arises from the spatial gradient of the velocity field $\mathbf{v}(\mathbf{x}, t)$

$$\mathbf{L} = \dot{\mathbf{F}}\,\mathbf{F}^{-1} = \operatorname{grad} \mathbf{v}(\mathbf{x}, t) = \frac{\partial \mathbf{v}}{\partial \mathbf{x}} . \tag{2.20}$$

The spatial velocity gradient $\mathbf{L}$ can be additively decomposed into a symmetric part $\mathbf{D}$ and a skew symmetric part $\mathbf{W}$

$$\mathbf{L} = \mathbf{D} + \mathbf{W} . \tag{2.21}$$

Therein, tensor $\mathbf{D}$ specifies the deformation rate tensor and tensor $\mathbf{W}$ is the spin tensor

$$\begin{aligned} \mathbf{D} &= \frac{1}{2}\left(\mathbf{L} + \mathbf{L}^T\right) = \mathbf{D}^T , \\ \mathbf{W} &= \frac{1}{2}\left(\mathbf{L} - \mathbf{L}^T\right) = -\mathbf{W}^T . \end{aligned} \tag{2.22}$$

Since both tensors arise from the spatial velocity gradient $\mathbf{L}$, they are part of the actual configuration as well. Moreover, the spatial velocity gradient $\mathbf{L}$ enables for a mathematical representation of the temporal changes of material line elements, surface elements and volume elements

$$\begin{aligned} (\mathrm{d}\mathbf{x})^{\bullet} &= \mathbf{L}\,\mathrm{d}\mathbf{x} , \\ (\mathrm{d}\mathbf{a})^{\bullet} &= \left((\operatorname{tr}\mathbf{L})\,\mathbf{1} - \mathbf{L}^T\right)\mathrm{d}\mathbf{a} , \\ (\mathrm{dv})^{\bullet} &= (\operatorname{tr}\mathbf{L})\,\mathrm{dv} . \end{aligned} \tag{2.23}$$

With respect to the reference configuration, the strain rate tensor $\dot{\mathbf{E}}$ is derived by differentiation of the Green-Lagrange strain tensor $\mathbf{E}$ with respect to time

$$\dot{\mathbf{E}} = \frac{1}{2}\left(\dot{\mathbf{F}}^T\mathbf{F} + \mathbf{F}^T\dot{\mathbf{F}}\right) . \tag{2.24}$$

The relation between both tensors $\mathbf{D}$ and $\dot{\mathbf{E}}$ is established by the push-forward and pull-back operation

$$\mathbf{D} = \mathbf{F}^{-T}\,\dot{\mathbf{E}}\,\mathbf{F}^{-1} \quad , \quad \dot{\mathbf{E}} = \mathbf{F}^T\,\mathbf{D}\,\mathbf{F} . \tag{2.25}$$

An alternative representation of the deformation rate tensor $\mathbf{D}$ is given by the upper Lie derivative of the Almansi strain tensor $\mathbf{A}$

$$\mathbf{D} = \overset{\triangle}{\mathbf{A}} = \dot{\mathbf{A}} + \mathbf{L}^T \mathbf{A} + \mathbf{A}\,\mathbf{L} \,. \tag{2.26}$$

For more details about the mentioned kinematics, the reader is referred to Haupt (2000) and Johlitz (2009).

2.1.5 Decomposition of the deformation gradient

As already shown by means of the polar decomposition, the multiplicative decomposition of the deformation gradient $\mathbf{F}$ is a common concept to split the deformation into several parts which can be considered separately. Thereby, the multiplicative decomposition usually goes along with the introduction of an intermediate configuration which exists between the reference and current configuration. Furthermore, the multiplicative decomposition usually leads to corresponding kinematic variables, as for instance values of deformation and stretch, which are acting on the intermediate configuration. Apart from the polar decomposition, several other types are provided in literature. One of these is the well-known decomposition of the deformation gradient into elastic and inelastic parts which is commonly applied in modelling nonlinear viscoelasticity under finite deformations. This concept is known as multiplicative viscoelasticity and was applied in numerous works in the past, e.g. Lubliner (1985) or Reese and Govindjee (1998). Another decomposition of the deformation gradient into thermal and mechanical parts is often used to describe thermoviscoelastic or thermoviscoplastic material properties. Formulations of this type which additionally take into account temperature effects, are proposed, for instance, by Lion (2000a) or Hoefer (2009). Lee (1969) originally introduced a plastic intermediate configuration and decomposed the deformation gradient into elastic and plastic parts to describe elastoplasticity. Among others, similar concepts were also applied by Simo (1988) or Kaliske and Rothert (1998). For an overview of the different types of decomposition, the reader is referred to the presentations given by Meggyes (2001) or Lubarda (2004).

The constitutive approach in this work is based on a proposal by Haupt and Lion (2002) and applies a relative decomposition in the time domain and a volumetric-isochoric decomposition of the deformation gradient. In order to facilitate understanding by the reader, the time-relative and the volumetric-isochoric decomposition are introduced in the following.

Volumetric-isochoric decomposition

The volumetric-isochoric decomposition is commonly applied to separate volume changes from changes in the shape. This type of decomposition is related to the assumption that the deformation of a material body consists of a volumetric part and an isochoric part which is caused by changes in the shape of the material body. In order to separate these two parts from each other, the deformation gradient $\mathbf{F}$ is multiplicatively

decomposed into a volumetric part $\bar{\mathbf{F}}$ and an isochoric part $\hat{\mathbf{F}}$

$$\mathbf{F} = \bar{\mathbf{F}}\,\hat{\mathbf{F}} \quad \text{with} \quad \bar{\mathbf{F}} = J^{\frac{1}{3}}\,\mathbf{1} \quad \text{and} \quad \hat{\mathbf{F}} = J^{-\frac{1}{3}}\,\mathbf{F}\ . \tag{2.27}$$

As illustrated in figure 2.2, the volumetric-isochoric decomposition goes along with the introduction of an intermediate isochoric configuration $\mathcal{I}_i$.

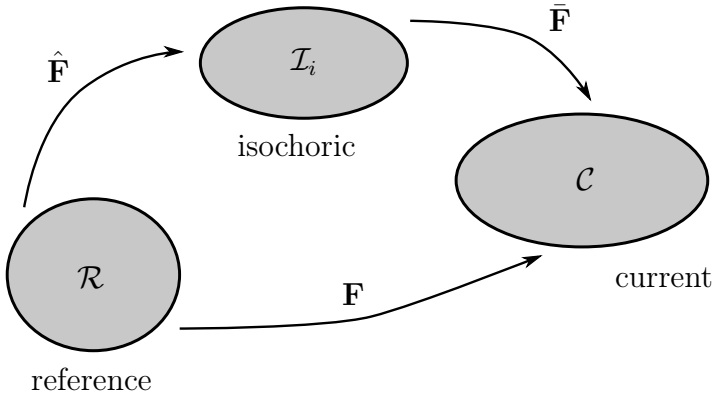

FIGURE 2.2: Volumetric-isochoric configuration

Considering this, the isochoric right Cauchy-Green tensor $\hat{\mathbf{C}}$ and the isochoric left Cauchy-Green tensor $\hat{\mathbf{B}}$ are defined by

$$\begin{aligned} \hat{\mathbf{C}} &= \hat{\mathbf{F}}^T\,\hat{\mathbf{F}}\ , \\ \hat{\mathbf{B}} &= \hat{\mathbf{F}}\,\hat{\mathbf{F}}^T\ . \end{aligned} \tag{2.28}$$

The isochoric Green-Lagrange strain tensor and the isochoric Piola strain tensor are given by

$$\begin{aligned} \hat{\mathbf{E}} &= \frac{1}{2}\left(\hat{\mathbf{C}} - \mathbf{1}\right)\ , \\ \hat{\mathbf{e}} &= \frac{1}{2}\left(\hat{\mathbf{C}}^{-1} - \mathbf{1}\right)\ . \end{aligned} \tag{2.29}$$

If the definition of the isochoric deformation gradient in (2.27) is taken into account, the isochoric right Cauchy-Green tensor can also be expressed in terms of the right Cauchy-Green tensor

$$\hat{\mathbf{C}} = \hat{\mathbf{F}}^T\hat{\mathbf{F}} = J^{-\frac{1}{3}}\,\mathbf{F}^T\,J^{-\frac{1}{3}}\,\mathbf{F} = J^{-\frac{2}{3}}\,\mathbf{F}^T\,\mathbf{F} = J^{-\frac{2}{3}}\,\mathbf{C}\ . \tag{2.30}$$

Relative decomposition

In contrast to the polar or volumetric-isochoric decomposition, the relative decomposition of the deformation gradient is a decomposition with respect to time. As illustrated in figure 2.3, a relative intermediate configuration $\mathcal{I}_t$ which is present at the time s, is first introduced. Since the intermediate configuration exists between the reference configuration $\mathcal{R}$ at time $t_0 = 0$ and the current configuration $\mathcal{C}$ at time t, it represents an arbitrary deformation state in the past history. The relative deformation gradient

$\mathbf{F}_t(s)$ is introduced as follows

$$\mathbf{F}_t(s) \;=\; \mathbf{F}(s)\,\mathbf{F}^{-1}(t)\;. \tag{2.31}$$

This tensor maps tangent vectors of the current configuration onto tangent vectors of a previous configuration $\mathcal{I}_t$ at time s, as for instance a predeformed state, and thus enables for a description of history dependence. Since the relative intermediate configuration does not possess its own kinematic variables, the deformation of the material body is described on the basis of the reference or the current configuration.

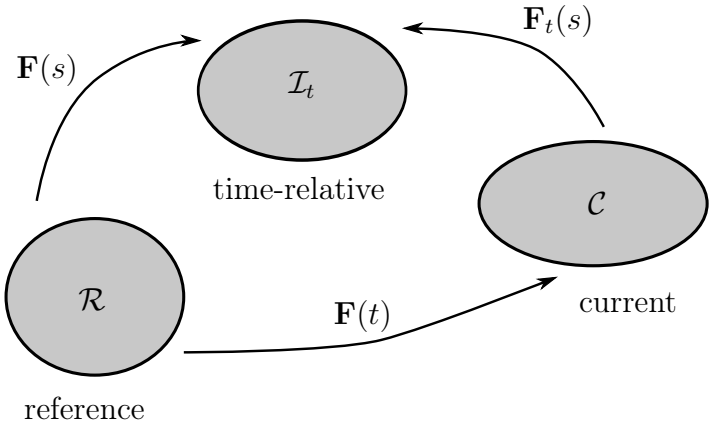

FIGURE 2.3: Relative decomposition

Based on the definition of the relative deformation gradient in (2.31), the corresponding relative kinematic tensors present at the time s can be introduced. The relative left and right Cauchy-Green tensors are defined by

$$\begin{aligned} \mathbf{B}_t(s) &= \mathbf{F}_t(s)\,\mathbf{F}_t^T(s)\;, \\ \mathbf{C}_t(s) &= \mathbf{F}_t^T(s)\,\mathbf{F}_t(s)\;, \end{aligned} \tag{2.32}$$

whereas the relative Green-Lagrange strain tensor and the relative Piola strain tensor at the time s are given by

$$\begin{aligned} \mathbf{E}_t(s) &= \frac{1}{2}\Big(\mathbf{C}_t(s) - \mathbf{1}\Big)\;, \\ \mathbf{e}_t(s) &= \frac{1}{2}\Big(\mathbf{C}_t^{-1}(s) - \mathbf{1}\Big)\;. \end{aligned} \tag{2.33}$$

In this work, the relative decomposition is only applied to the isochoric part of the deformation such that a relative isochoric deformation gradient arises

$$\hat{\mathbf{F}}_t(s) \;=\; \hat{\mathbf{F}}(s)\,\hat{\mathbf{F}}^{-1}(t)\;. \tag{2.34}$$

A detailed description of the relative decomposition is provided in the textbook by Truesdell and Noll (1965).

2.2 Balance equations

The balance equations are classified as natural laws which are mathematically introduced as axiomatic relations. A detailed description of the balance principles, the following presentation refers to, is given by Haupt and Lion (2002) and Johlitz (2009). The theory of continuum mechanics introduces the following five balance equations:

- the balance of mass,
- the balance of linear momentum,
- the balance of rotational momentum,
- the balance of internal energy,
- the balance of entropy.

These balance laws can generally be formulated in the local, strong form or in the global, weak form. Additionally, they can either be expressed with respect to the reference configuration or with regard to the current configuration. As presented by Johlitz (2009), each balance equation can be derived from a so-called master balance. In its global form, the master balance is defined by the following equation

$$\frac{\mathrm{d}}{\mathrm{d}t}\int_B \rho\,\Psi(\mathbf{x},t)\,\mathrm{d}v \;=\; \int_{\partial B} \boldsymbol{\varphi}(\mathbf{x},t)\,\mathrm{d}a \;+\; \int_B \sigma(\mathbf{x},t)\,\mathrm{d}v \;+\; \int_B \hat{\Psi}(\mathbf{x},t)\,\mathrm{d}v\;. \tag{2.35}$$

Based on this equation, the temporal change of a physical variable Ψ multiplied by the mass density ρ is equal to the sum of its flux $\boldsymbol{\varphi}$ over the boundary surface, a volume-distributed supply σ and a production term $\hat{\Psi}$. The corresponding local form of the master balance with regard to an arbitrary material point is given by

$$\rho\,\dot{\Psi} \;=\; \operatorname{div}\boldsymbol{\varphi} \;+\; \sigma \;+\; \hat{\Psi}\;. \tag{2.36}$$

Since this work only refers to the local form of the balance principles, they will only be introduced in their local formulation with respect to each configuration in the following.

2.2.1 Balance of mass

The balance of mass indicates that the mass m of a material body is constant and does not change over time

$$\frac{\mathrm{d}}{\mathrm{d}t}\,m \;=\; 0\;. \tag{2.37}$$

Following Johlitz (2009) and taking the local form of the master balance in (2.36) and the specification $\Psi = 1$, $\boldsymbol{\varphi} = \mathbf{0}$, $\sigma = 0$ and $\hat{\Psi} = 0$ into account, the local form of the balance of mass with respect to the current configuration is expressed by

$$\dot{\rho} \;+\; \rho\,\operatorname{div}\mathbf{v} \;=\; 0\;. \tag{2.38}$$

Therein, variable ρ denotes the mass density of the current configuration. The relation between ρ and the mass density ρ_0 in the reference configuration can be obtained by the relations $\rho_0 = dm/dV$, $\rho = dm/dv$ and (2.11)

$$\rho \;=\; \rho_0 \, J^{-1} \;. \tag{2.39}$$

The local form of the balance of mass with respect to the reference configuration is defined by

$$\rho_0 \;=\; \rho_0(\mathbf{X}) \;. \tag{2.40}$$

2.2.2 Balance of linear momentum

The balance of linear momentum quotes that the temporal change of the linear momentum $\mathbf{I}$ of a material body is equal to the external forces $\mathbf{k}$ which act on the body

$$\frac{\mathrm{d}}{\mathrm{d}t}\,\mathbf{I} \;=\; \mathbf{k} \;. \tag{2.41}$$

The local form of the balance of linear momentum in the current configuration is defined by

$$\operatorname{div}\mathbf{T} \;+\; \rho\,\mathbf{k} \;=\; \rho\,\frac{\mathrm{d}^2}{\mathrm{d}t^2}\,\mathbf{x} \;, \tag{2.42}$$

whereas the local form of the balance of linear momentum in the reference configuration is given by

$$\operatorname{Div}\mathbf{P} \;+\; \rho_0\,\mathbf{k} \;=\; \rho_0\,\frac{\mathrm{d}^2}{\mathrm{d}t^2}\,\mathbf{X} \;. \tag{2.43}$$

Therein, $\mathbf{T}$ is the Cauchy stress tensor and $\mathbf{P}$ is the 1st Piola-Kirchhoff stress tensor. The first one is a variable of the current configuration which relates the current force acting on a material body to its current cross section area. In contrast to that, the 1st Piola-Kirchhoff stress tensor relates the current force acting on a material body to its initial cross section area. The two remaining terms $\rho\,\mathbf{k}$ and $\rho_0\,\mathbf{k}$ are external forces per unit volume acting on the material body. As demonstrated in fundamental textbooks, the following relation between the 1st Piola-Kirchhoff stress tensor and the Cauchy stress tensor is obtained (Johlitz 2009)

$$\mathbf{P} \;=\; (\det\mathbf{F})\,\mathbf{T}\,\mathbf{F}^{-T} \;. \tag{2.44}$$

2.2.3 Balance of rotational momentum

The balance of rotational momentum states that the temporal change of the rotational momentum $\mathbf{I}_R$ is equal to the external moments $\mathbf{M}$ which act on a stationary material point of a material body

$$\frac{\mathrm{d}}{\mathrm{d}t}\,\mathbf{I}_R \;=\; \mathbf{M} \;. \tag{2.45}$$

The local form of the balance of rotational momentum with respect to the current configuration reads as

$$\mathbf{T} = \mathbf{T}^T \tag{2.46}$$

and implies the symmetry of the Cauchy stress tensor. Considering this outcome and (2.44), the balance of rotational momentum with regard to the reference configuration is given by

$$\mathbf{P}\,\mathbf{F}^T = \mathbf{F}\,\mathbf{P}^T \ . \tag{2.47}$$

2.2.4 Balance of internal energy

The balance of internal energy corresponds to the first law of thermodynamics and states that the internal energy per unit mass of a material body must be equal to the mechanical and thermal work which is performed on the body. As presented by Johlitz (2009), the local form of the balance of internal energy with respect to the current configuration is defined by[3]

$$\dot{e} = \frac{1}{\rho}\,\mathbf{T}\cdot\mathbf{D} - \frac{1}{\rho}\,\operatorname{div}\mathbf{q} + r \ . \tag{2.48}$$

From this equation, the temporal change of the internal energy per unit mass $\dot{e}$ is equal to the sum of the externally delivered stress power $\mathbf{T}\cdot\mathbf{D}$, heat flux $\mathbf{q}$ and volume-distributed heat supply r. Referring to Johlitz (2009), the local form of the balance of internal energy with respect to the reference configuration can be derived by applying the concept of dual variables (Haupt and Tsakmakis 1989)

$$\frac{1}{\rho_0}\,\tilde{\mathbf{T}}\cdot\dot{\mathbf{E}} = \frac{1}{\rho}\,\mathbf{T}\cdot\mathbf{D} \ . \tag{2.49}$$

In so doing, the balance of internal energy with respect to the reference configuration is written as

$$\dot{e} = \frac{1}{\rho_0}\,\tilde{\mathbf{T}}\cdot\dot{\mathbf{E}} - \frac{1}{\rho_0}\,\operatorname{Div}\mathbf{q}_0 + r \ . \tag{2.50}$$

Therein, $\tilde{\mathbf{T}}$ is the 2nd Piola-Kirchhoff stress tensor which is defined by

$$\tilde{\mathbf{T}} = (\det\mathbf{F})\,\mathbf{F}^{-1}\,\mathbf{T}\,\mathbf{F}^{-T} \ . \tag{2.51}$$

The variable $\mathbf{q}_0$ in (2.50) is the heat flux of the reference configuration and reads as

$$\mathbf{q}_0 = J\,\mathbf{F}^{-1}\,\mathbf{q} \ . \tag{2.52}$$

2.2.5 Balance of entropy

The balance of entropy considers the second law of thermodynamics. As described by Johlitz (2009), the second law of thermodynamics is defined by an inequality which

[3]The dot in (2.48) denotes the double scalar product of tensors $\mathbf{A}$ and $\mathbf{B}$: $\mathbf{A}\cdot\mathbf{B} = A_{ij}\,B_{ij}$ (cf. Appendix A)

indicates that the entropy production $\hat{\eta}$ inside a material body must be equal or greater than zero

$$\hat{\eta} \geq 0 \; . \tag{2.53}$$

With regard to the current configuration, the entropy inequality is given by

$$\rho \, \dot{\eta} + \operatorname{div}\left(\frac{\mathbf{q}}{\theta}\right) - \frac{\rho \, r}{\theta} = \hat{\eta} \geq 0 \; . \tag{2.54}$$

Therein, the first term denotes the change in entropy over time, the second term is the entropy flux, the third term represents the entropy supply and θ is the absolute temperature. With respect to the reference configuration, the entropy inequality reads as

$$\rho_0 \, \dot{\eta} + \operatorname{Div}\left(\frac{\mathbf{q}_0}{\theta}\right) - \frac{\rho_0 \, r}{\theta} = \hat{\eta} \geq 0 \; . \tag{2.55}$$

Regarding material modelling, physically consistent constitutive equations must be compatible with the second law of thermodynamics meaning that the internal entropy production is non-negative for arbitrary deformation and temperature processes. Constitutive equations which fulfil this requirement are called thermomechanically consistent.

2.2.6 Clausius-Duhem inequality

The Clausius-Duhem inequality (CDI) is an alternative representation of the second law of thermodynamics which is frequently applied in material modelling. In contrast to the second law of thermodynamics, the Clausius-Duhem inequality is not based on the entropy, but on the specific Helmholtz free energy

$$\Psi = e - \theta \, \eta \; , \tag{2.56}$$

with the specific entropy η, the specific internal energy e and the absolute temperature θ. In order to derive the Clausius-Duhem inequality, the specific Helmholtz free energy is first differentiated with respect to time and then inserted into the entropy inequality (2.54) respectively (2.55). As a result of these operations, the Clausius-Duhem inequality with respect to the current and the reference configurations is finally given by

$$\begin{aligned} -\rho \, \dot{\Psi} - \rho \, \eta \, \dot{\theta} - \frac{\mathbf{q}}{\theta} \operatorname{grad} \theta + \mathbf{T} \cdot \mathbf{D} &\geq 0 \; , \\ -\rho_0 \, \dot{\Psi} - \rho_0 \, \eta \, \dot{\theta} - \frac{\mathbf{q}_0}{\theta} \operatorname{Grad} \theta + \tilde{\mathbf{T}} \cdot \dot{\mathbf{E}} &\geq 0 \; . \end{aligned} \tag{2.57}$$

The benefit of the Clausius-Duhem inequality is based on the fact that this alternative expression applies the specific Helmholtz free energy as thermodynamic potential. On this basis, it is much easier to define thermomechanical consistent constitutive models. This work only deals with isothermal processes, which means that there are no temporal or spatial changes in the temperature θ. As a consequence of this fact, the Clausius-Duhem inequality reduces to the Clausius-Planck inequality (CPI) in the current and

reference configuration

$$\begin{aligned} -\rho\,\dot{\Psi} + \mathbf{T}\cdot\mathbf{D} &\geq 0\,, \\ -\rho_0\,\dot{\Psi} + \tilde{\mathbf{T}}\cdot\dot{\mathbf{E}} &\geq 0\,. \end{aligned} \tag{2.58}$$

From a physical point of view, the Clausius-Planck inequality postulates that the stress power supplied to a material body must be equal to or greater than the temporal change in the stored free energy inside the material body. Since this work is concerned with isothermal processes, the Clausius-Planck inequality forms the basis to derive thermomechanically consistent material laws.

Chapter 3

Theory of material modelling

Introduction

The mechanical properties of rubber-like materials are generally characterised by a number of nonlinearities. These include pronounced rate or frequency dependences, stress-softening phenomena, nonlinear stress-strain characteristics, amplitude dependences as well as numerous other effects. A comprehensive and detailed overview of the mechanical properties of polymers is provided in the specialised textbooks by Tobolsky (1967), Schwarzl (1990) or Sperling (2006).
The theory of material modelling focuses on the mathematical description of the complex material behaviour of elastomers by suitable material laws. These material laws are commonly called constitutive equations and deliver the relation between the deformation of a material body and the forces acting on it. As already stated in chapter 2, physically meaningful constitutive equations have to be formulated in a thermodynamically consistent manner such that they conform to the second law of thermodynamics or alternative representations, such as the Clausius-Duhem inequality.

Outline

The aim of this chapter is to introduce the basics of the theory of material modelling the present work is engaged with. For this reason, the following sections give a brief overview about

- hyperelasticity,
- linear viscoelasticity,
- fractional viscoelasticity,
- nonlinear finite viscoelasticity,
- and frequency-temperature shifting technique.

Thereby, the following presentation mostly refers to the writings by Lion (2007) and Johlitz (2009). Apart from these demonstrations, a detailed description of the constitutive theory including several other fields is provided, for instance, by Truesdell and Noll (1965), Treloar (1975), Krawietz (1986) or Tschoegl (1989). Since the constitutive approach of finite viscoelasticity by Haupt and Lion (2002) forms the basis of this work, the general approach will additionally be introduced.

3.1 Hyperelasticity

As illustrated in figure 3.1, rubber-like materials are mainly characterised by a nonlinear relation between stress σ and strain ε.

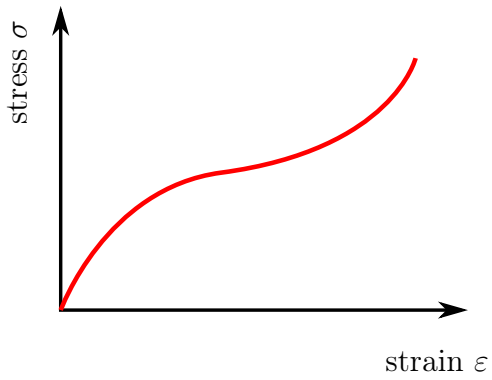

FIGURE 3.1: Nonlinear stress-strain relation

The mathematical description of this nonlinear material behaviour is commonly described via hyperelastic formulations meaning that the stress can be derived by differentiation of a strain energy function with respect to deformation. Among others, well-know hyperelastic approaches based on isotropic strain energy functions are proposed by Mooney (1940), Rivlin (1948) or Yeoh (1993). Moreover, a comprehensive overview and a comparison of several hyperelastic concepts of this type is given by Hartmann (2001).
As presented by (Johlitz 2009), the specific Helmholtz free energy Ψ is usually defined as a thermodynamic potential which depends on the left or the right Cauchy-Green tensor $\mathbf{B}$ or $\mathbf{C}$

$$\Psi = \Psi(\mathbf{B}) \quad \text{or} \quad \Psi = \Psi(\mathbf{C}) \, . \tag{3.1}$$

In order to derive a thermomechanical consistent formulation of the constitutive equation of the stress, it is necessary to calculate the time derivative of (3.1) and to evaluate the Clausius-Duhem inequality (2.57). In terms of isothermal processes at constant temperature, the nonlinear stress-strain relation can alternatively be deduced from the reduced Clausius-Planck inequality (2.58). Following this procedure and taking the reference configuration into account, the material time derivative of the specific Helmholtz free energy is first given by

$$\dot{\Psi}(\mathbf{C}) = \frac{\partial \Psi}{\partial \mathbf{C}} \cdot \dot{\mathbf{C}} \, . \tag{3.2}$$

Considering relation (2.15) between the right Cauchy-Green tensor $\mathbf{C}$ and the Green-Lagrange strain tensor $\mathbf{E}$, the time derivative $\dot{\mathbf{C}}$ in (3.2) can be replaced by

$$\dot{\mathbf{C}} \;=\; 2\,\dot{\mathbf{E}}\;, \tag{3.3}$$

such that (3.2) can be rewritten as

$$\dot{\Psi}(\mathbf{C}) \;=\; 2\,\frac{\partial \Psi}{\partial \mathbf{C}} \cdot \dot{\mathbf{E}}\;. \tag{3.4}$$

Inserting this expression into the Clausius-Planck inequality (2.58), the following inequality is obtained

$$\left[\tilde{\mathbf{T}} \;-\; 2\,\rho_0\,\frac{\partial \Psi}{\partial \mathbf{C}}\right] \cdot \dot{\mathbf{E}} \;\geq\; 0\;. \tag{3.5}$$

In terms of thermomechanical consistency, this inequality must hold for arbitrary deformation processes. In order to satisfy this requirement and subsequently derive a suitable mathematical description of the stress-strain relation, it is straight forward to follow the argumentation given by Coleman and Noll (1963). According to that, (3.5) must be satisfied for arbitrary rates of the Green-Lagrange strain tensor $\dot{\mathbf{E}}$. This requirement is automatically fulfilled if the term in brackets of (3.5) is equal to zero. Regarding this, the constitutive equation for the 2nd Piola-Kirchhoff stress tensor is given by

$$\tilde{\mathbf{T}} \;=\; 2\,\rho_0\,\frac{\partial \Psi}{\partial \mathbf{C}}\;. \tag{3.6}$$

With regard to the current configuration, the constitutive equation for the Cauchy stress can be derived in a similar manner and finally reads as

$$\mathbf{T} \;=\; 2\,\rho\,\mathbf{B}\,\frac{\partial \Psi}{\partial \mathbf{B}}\;. \tag{3.7}$$

Since this work is engaged with finite hyperelasticity and incompressible material behaviour, the concepts of finite hyperelasticity and incompressible hyperelasticity are introcuced in the following. A detailed description of these formulations, the following presentation refers to, is given by Johlitz (2009).

3.1.1 Finite hyperelasticity

Regarding finite deformations, the nonlinear stress-strain relation is usually described by means of a representation via invariants. In this context, the specific free Helmholtz energy is not defined as a function of $\mathbf{B}$ or $\mathbf{C}$ itself, but as a function of their main invariants $\mathrm{I}_{\mathbf{B}}, \mathrm{II}_{\mathbf{B}}, \mathrm{III}_{\mathbf{B}}$ or $\mathrm{I}_{\mathbf{C}}, \mathrm{II}_{\mathbf{C}}, \mathrm{III}_{\mathbf{C}}$

$$\Psi(\mathbf{B}) = \Psi(\mathrm{I}_{\mathbf{B}}, \mathrm{II}_{\mathbf{B}}, \mathrm{III}_{\mathbf{B}}) \quad \text{or} \quad \Psi(\mathbf{C}) = \Psi(\mathrm{I}_{\mathbf{C}}, \mathrm{II}_{\mathbf{C}}, \mathrm{III}_{\mathbf{C}})\;. \tag{3.8}$$

In this, the three main invariants are given by

$$\begin{aligned} \mathrm{I}_{\mathbf{C}} &= \mathrm{tr}\,\mathbf{C} = \mathbf{C}\cdot\mathbf{1}\,, \\ \mathrm{II}_{\mathbf{C}} &= \frac{1}{2}\left((\mathbf{C}\cdot\mathbf{1})^2 - \mathbf{C}^T\cdot\mathbf{C}\right)\,, \\ \mathrm{III}_{\mathbf{C}} &= \det\mathbf{C} = (\det\mathbf{F})^2\,. \end{aligned} \tag{3.9}$$

Following the same procedure as before and taking the reference configuration into account, the material time derivative of the specific Helmholtz free energy is first calculated

$$\dot{\Psi}(\mathbf{C}) = \frac{\partial\Psi}{\partial\mathbf{C}}\cdot\dot{\mathbf{C}} = \left[\frac{\partial\Psi}{\partial\mathrm{I}_{\mathbf{C}}}\frac{\partial\mathrm{I}_{\mathbf{C}}}{\partial\mathbf{C}} + \frac{\partial\Psi}{\partial\mathrm{II}_{\mathbf{C}}}\frac{\partial\mathrm{II}_{\mathbf{C}}}{\partial\mathbf{C}} + \frac{\partial\Psi}{\partial\mathrm{III}_{\mathbf{C}}}\frac{\partial\mathrm{III}_{\mathbf{C}}}{\partial\mathbf{C}}\right]\cdot\dot{\mathbf{C}}\,. \tag{3.10}$$

Therein, the derivatives of the invariants with respect to the right Cauchy-Green tensor $\mathbf{C}$ read as

$$\begin{aligned} \frac{\mathrm{dI}_{\mathbf{C}}}{\mathrm{d}\mathbf{C}} &= \mathbf{1}\,, \\ \frac{\mathrm{dII}_{\mathbf{C}}}{\mathrm{d}\mathbf{C}} &= \mathrm{I}_{\mathbf{C}}\,\mathbf{1} - \mathbf{C}\,, \\ \frac{\mathrm{dIII}_{\mathbf{C}}}{\mathrm{d}\mathbf{C}} &= (\det\mathbf{C})\,\mathbf{C}^{-T}\,. \end{aligned} \tag{3.11}$$

Inserting these relations into (3.12) and considering (3.3) as well as the symmetry of $\mathbf{C}$ ($\mathbf{C}^{-T} = \mathbf{C}^{-1}$), the material time derivative of the specific Helmholtz free energy is given by

$$\dot{\Psi}(\mathbf{C}) = 2\left[\frac{\partial\Psi}{\partial\mathrm{I}_{\mathbf{C}}}\mathbf{1} + \frac{\partial\Psi}{\partial\mathrm{II}_{\mathbf{C}}}(\mathrm{I}_{\mathbf{C}}\,\mathbf{1} - \mathbf{C}) + \frac{\partial\Psi}{\partial\mathrm{III}_{\mathbf{C}}}(\det\mathbf{C})\,\mathbf{C}^{-1}\right]\cdot\dot{\mathbf{E}}\,. \tag{3.12}$$

After evaluation of the Clausius-Planck inequality based on Coleman and Noll (1963), the constitutive equation for the 2nd Piola-Kirchhoff stress tensor reads as

$$\tilde{\mathbf{T}} = 2\,\rho_0\frac{\partial\Psi}{\partial\mathrm{I}_{\mathbf{C}}}\mathbf{1} + 2\,\rho_0\frac{\partial\Psi}{\partial\mathrm{II}_{\mathbf{C}}}(\mathrm{I}_{\mathbf{C}}\,\mathbf{1} - \mathbf{C}) + 2\,\rho_0\frac{\partial\Psi}{\partial\mathrm{III}_{\mathbf{C}}}(\det\mathbf{C})\,\mathbf{C}^{-1}\,. \tag{3.13}$$

Regarding the current configuration and taking the theorem of Cayley-Hamilton into account

$$\mathbf{B}^3 - \mathrm{I}_{\mathbf{B}}\,\mathbf{B}^2 + \mathrm{II}_{\mathbf{B}}\,\mathbf{B} - \mathrm{III}_{\mathbf{B}}\,\mathbf{1} = \mathbf{0}\,, \tag{3.14}$$

the constitutive equation for the Cauchy stress tensor finally reads as

$$\mathbf{T} = 2\,\rho\frac{\partial\Psi}{\partial\mathrm{III}_{\mathbf{B}}}\mathbf{1} + 2\,\rho\frac{\partial\Psi}{\partial\mathrm{I}_{\mathbf{B}}}\mathbf{B} - 2\,\rho\frac{\partial\Psi}{\partial\mathrm{II}_{\mathbf{B}}}\left(\mathrm{II}_{\mathbf{B}}\,\mathbf{1} - \mathrm{III}_{\mathbf{B}}\,\mathbf{B}^{-1}\right). \tag{3.15}$$

3.1.2 Finite incompressible hyperelasticity

In general, elastomer materials are characterised by nearly incompressible behaviour meaning that their volume remains constant over deformation. From a mathematical

point of view, incompressibility can be expressed by the conditions

$$\operatorname{div} \mathbf{v} = \mathbf{1} \cdot \mathbf{D} = 0 \quad , \quad \mathbf{C} \cdot \mathbf{C}^{-1} = 0 \quad \text{or} \quad J = \det \mathbf{F} = 1 \; . \tag{3.16}$$

Based on these conditions and relation (3.9), the third invariants of the left and right Cauchy-Green tensor are equal to 1 and thus vanish after differentiation with respect to deformation

$$\mathrm{I}_{\mathbf{B}} = \mathrm{I}_{\mathbf{C}} = (\det \mathbf{F})^2 = 1 \quad \Rightarrow \quad \dot{\mathrm{I}}_{\mathbf{B}} = \dot{\mathrm{I}}_{\mathbf{C}} = 0 \; . \tag{3.17}$$

On this basis, the specific Helmholtz free energy can be defined as a function of only the first and the second invariants of the left or right Cauchy-Green tensor

$$\Psi(\mathbf{B}) = \Psi(\mathrm{I}_{\mathbf{B}}, \mathrm{II}_{\mathbf{B}}) \quad \text{or} \quad \Psi(\mathbf{C}) = \Psi(\mathrm{I}_{\mathbf{C}}, \mathrm{II}_{\mathbf{C}}) \; . \tag{3.18}$$

In order to derive the stress-strain relation in terms of incompressible material behaviour, the relations $\mathbf{1} \cdot \mathbf{D} = 0$ and $\mathbf{C} \cdot \mathbf{C}^{-1} = 0$ are considered. Since the constitutively undetermined reaction stress does not contribute to the stress power, it is given by $-p\,\mathbf{1}$ in terms of the current configuration and by $-p\,\mathbf{C}^{-1}$ in terms of the reference configuration. If relations (3.11) and (3.3) are taken into account, the material time derivative of the specific Helmholtz free energy with respect to the reference configuration is defined by

$$\begin{aligned} \dot{\Psi}(\mathbf{C}) = \frac{\partial \Psi}{\partial \mathbf{C}} \cdot \dot{\mathbf{C}} &= \left[\frac{\partial \Psi}{\partial \mathrm{I}_{\mathbf{C}}} \frac{\partial \mathrm{I}_{\mathbf{C}}}{\partial \mathbf{C}} + \frac{\partial \Psi}{\partial \mathrm{II}_{\mathbf{C}}} \frac{\partial \mathrm{II}_{\mathbf{C}}}{\partial \mathbf{C}} \right] \cdot \dot{\mathbf{C}} \\ &= 2 \left[\frac{\partial \Psi}{\partial \mathrm{I}_{\mathbf{C}}} \mathbf{1} + \frac{\partial \Psi}{\partial \mathrm{II}_{\mathbf{C}}} (\mathrm{I}_{\mathbf{C}}\, \mathbf{1} - \mathbf{C}) \right] \cdot \dot{\mathbf{E}} \; . \end{aligned} \tag{3.19}$$

Inserting this expression into the Clausius-Planck inequality (2.58) and taking the reaction stress into account, the following inequality is obtained

$$\left[\tilde{\mathbf{T}} + p\,\mathbf{C}^{-1} - 2\,\rho_0 \frac{\partial \Psi}{\partial \mathrm{I}_{\mathbf{C}}} \mathbf{1} - 2\,\rho_0 \frac{\partial \Psi}{\partial \mathrm{II}_{\mathbf{C}}} (\mathrm{I}_{\mathbf{C}}\, \mathbf{1} - \mathbf{C}) \right] \cdot \dot{\mathbf{E}} \geq 0 \; . \tag{3.20}$$

Similar as before, this inequality is evaluated via the argumentation by Coleman and Noll (1963) which finally yields the constitutive equation for the 2nd Piola-Kirchhoff stress tensor

$$\tilde{\mathbf{T}} = -p\,\mathbf{C}^{-1} + 2\,\rho_0 \frac{\partial \Psi}{\partial \mathrm{I}_{\mathbf{C}}} \mathbf{1} + 2\,\rho_0 \frac{\partial \Psi}{\partial \mathrm{II}_{\mathbf{C}}} (\mathrm{I}_{\mathbf{C}}\, \mathbf{1} - \mathbf{C}) \; . \tag{3.21}$$

Applying the same procedure with respect to the current configuration and taking (3.14) into account, the constitutive equation for the Cauchy stress tensor is finally defined by

$$\mathbf{T} = -p\,\mathbf{1} + 2\,\rho \frac{\partial \Psi}{\partial \mathrm{I}_{\mathbf{B}}} \mathbf{B} + 2\,\rho \frac{\partial \Psi}{\partial \mathrm{II}_{\mathbf{B}}} \mathbf{B}^{-1} \; . \tag{3.22}$$

A more detailed description of the mentioned concepts in modelling finite and incompressible hyperelasticity are provided by Johlitz (2009).

3.2 Linear viscoelasticity

Apart from the nonlinear stress-strain relation, rubber-like materials are typically characterised by pronounced rate or frequency dependence. This behaviour is classified as viscoelasticity and occurs by means of hysteresis, stress relaxation, creep or damping effects. For an overview about mathematical concepts of linear viscoelasticity, the reader is referred to the manuscripts of Lion (2007) or Johlitz (2009). Moreover, a comprehensive and detailed depiction of the linear viscoelastic theory is provided in the textbook by Tschoegl (1989).
In general, viscoelasticity can be described by a dependence of the stress response σ of the material on strain ε and strain rate $\dot{\varepsilon}$. As illustrated in figure 3.2, the stress response of viscoelastic materials is typically increased for larger rates of strain ($\dot{\varepsilon}_1 > \dot{\varepsilon}_2$).

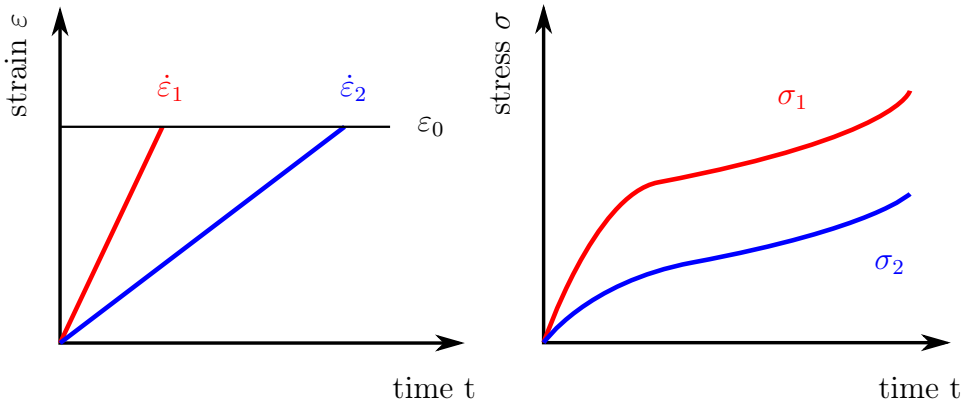

FIGURE 3.2: Viscoelastic material behaviour: dependence on the rate of strain

A common concept to mathematically describe viscoelasticity is based on time-dependent functionals of stress or strain history. In this context, the stress can be defined by

$$\sigma(t) = \mathcal{F}[\varepsilon(s)] \quad \text{with} \quad -\infty < s \leq t \,, \tag{3.23}$$

and the strain can be written as

$$\varepsilon(t) = \mathcal{F}^{-1}[\sigma(s)] \quad \text{with} \quad -\infty < s \leq t \,. \tag{3.24}$$

A linear approximation of these functionals which is frequently applied in modelling viscoelasticity is expressed by means of convolution integrals for stress and strain

$$\begin{aligned} \sigma(t) &= \int_{-\infty}^{t} G(t-s)\,\varepsilon'(s)\,\mathrm{d}s \,, \\ \varepsilon(t) &= \int_{-\infty}^{t} J(t-s)\,\sigma'(s)\,\mathrm{d}s \,. \end{aligned} \tag{3.25}$$

Therein, functions $G(t-s)$ and $J(t-s)$ are the relaxation and retardation functions. They describe the time-dependent connection between stress and strain in the time

domain. If one and the same material is described, $G(t)$ and $J(t)$ depend on each other.

A popular and easy interpretable concept to describe linear viscoelastic material behaviour is based on rheological elements, such as elastic springs and viscous dampers. These models represent the material behaviour on the basis of linear differential equations of stress or strain and are thus limited to the description of linear relationships. On their own, rheological elements are only able to represent specific material properties, such as pure elasticity (spring) or pure viscosity (damper). But used in combination, they offer the possibility to describe complex viscoelastic material behaviour.
The basic elements and popular element combinations to model linear viscoelastic material behaviour are introduced in the following sections. In general, the mathematical relations between stress and strain can be derived by solution of the differential equations with respect to specific functions of stress or strain. Since this work only deals with the stress-based formulation, the following presentation is limited to this type. For an overview of various element combinations and their properties, the interested reader is referred to the works by Lion (2007) and Ranz (2007). A detailed description of rheological elements, the following presentation mostly refers to, is given by Johlitz (2009).

3.2.1 Spring and damper

The elastic spring and the viscous damper are the two basic elements which are essential to describe linear viscoelastic material behaviour. The spring is capable of representing elastic properties whereas the damper is able to describe viscous phenomena. As illustrated in figure 3.3, the spring is determined by the modulus E and the linear damper is defined by its viscosity η.

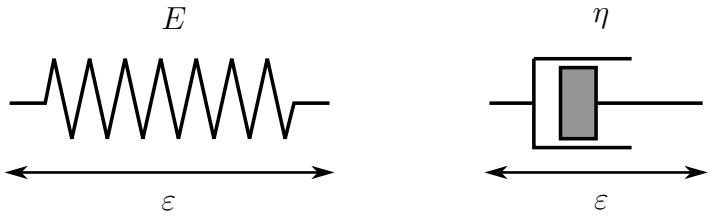

FIGURE 3.3: spring (left) and damper (right)

The stress response of the elastic spring is a linear function of strain and given by

$$\sigma = E\,\varepsilon \ . \tag{3.26}$$

In contrast to that, the stress response of the viscous damper is a linear function of strain rate and reads as

$$\sigma = \eta\,\dot{\varepsilon} \ . \tag{3.27}$$

Since the differential equations of both elements are linear in strain and strain rate, the spring and damper are limited to the description of linear elastic and linear viscous phenomena. The description of viscoelastic phenomena is usually managed by combinations of springs and dampers in series or in parallel.

3.2.2 Maxwell element

The Maxwell element is one of the simplest element combinations to represent linear viscoelastic material behaviour. As illustrated in figure 3.4, this element is composed of a spring with modulus E and a damper with viscosity η which are connected in series.

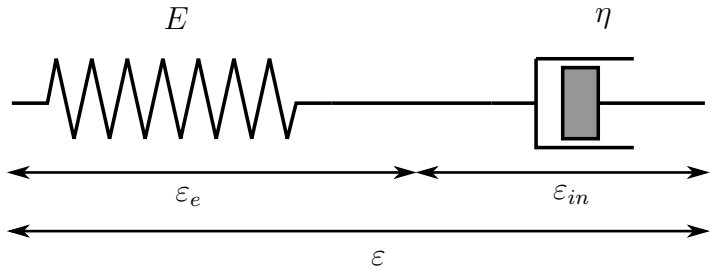

FIGURE 3.4: Maxwell element

It combines the elastic and viscous properties of spring and damper which enables for a representation of simple viscoelastic phenomena in a qualitative manner. Since both elements are connected in series, the total stress is equal for each element and reads as

$$\sigma = E\,\varepsilon_e = \eta\,\dot{\varepsilon}_{in} \; . \tag{3.28}$$

However, the total strain is distributed over both elements and separated into an elastic part ε_e which is associated with the spring and an inelastic part ε_{in} which is related to the damper. Regarding this, the total strain of the Maxwell element can be expressed by the sum of elastic and inelastic strains

$$\varepsilon = \varepsilon_e + \varepsilon_{in} \; . \tag{3.29}$$

The corresponding strain rate is obtained by differentiation with respect to time

$$\dot{\varepsilon} = \dot{\varepsilon}_e + \dot{\varepsilon}_{in} \; . \tag{3.30}$$

Taking into account the introduced relations (3.28), (3.29) and (3.30), the differential equation of the Maxwell element is given by

$$\dot{\sigma} + \frac{1}{\tau}\,\sigma = E\,\dot{\varepsilon} \tag{3.31}$$

with the relaxation time $\tau = \eta/E$. In order to obtain the general solution, the differential equation (3.31) must be integrated with respect to time. In so doing, the

constitutive equation of stress finally reads as

$$\sigma(t) \;=\; E \int_0^t \dot{\varepsilon}(s)\, \mathrm{e}^{-\frac{t-s}{\tau}}\, \mathrm{d}s \;=\; \int_0^t G(t-s)\, \dot{\varepsilon}(s)\, \mathrm{d}s \;. \tag{3.32}$$

Therein, the relaxation function $G(t-s)$ is defined by means of a decreasing exponential function

$$G(t-s) \;=\; E\, \mathrm{e}^{-\frac{t-s}{\tau}} \;. \tag{3.33}$$

More detailed calculations are presented by Johlitz (2009).

3.2.3 Three-parameter model (TPM)

The Three-parameter model (TPM) is an extension of the Maxwell element which is able to represent more complex viscoelastic properties. As presented in figure 3.5, the TPM is composed of an additional elastic spring which is connected with a Maxwell element in parallel.

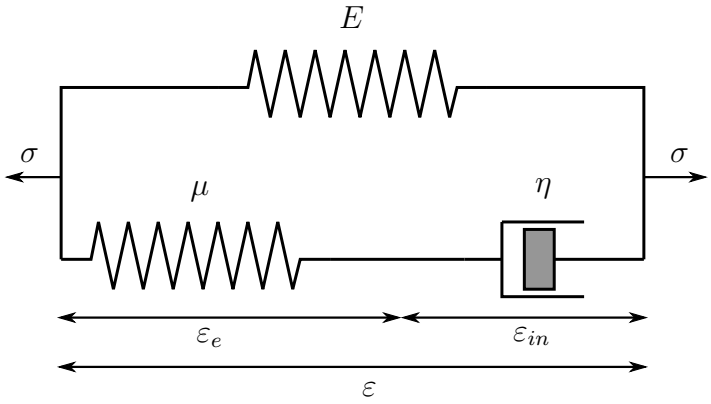

FIGURE 3.5: Three-parameter model

On this basis, the TPM is capable of describing viscoelastic material behaviour with consideration of quasi-static effects, such as creep at constant stress or relaxation at constant strain. The total stress of the TPM is distributed over the elastic spring and the Maxwell element. As a consequence, it is given by the sum of the equilibrium stress σ_{eq} of the elastic spring and the overstress σ_{ov} of the Maxwell element

$$\sigma \;=\; \sigma_{eq} \;+\; \sigma_{ov} \;. \tag{3.34}$$

Therein, the equilibrium stress and the overstress are defined by

$$\begin{aligned} \sigma_{eq} \;&=\; E\, \varepsilon \,, \\ \sigma_{ov} \;&=\; \mu\, \varepsilon_e \;=\; \eta\, \dot{\varepsilon}_{in} \;. \end{aligned} \tag{3.35}$$

The total strain of the TPM is of equal amount for the elastic spring and the Maxwell element whereby the strain of the Maxwell element is additively decomposed into elastic

and inelastic parts

$$\varepsilon = \varepsilon_e + \varepsilon_{in} \,. \tag{3.36}$$

From this, the strain rates follow by differentiation with respect to time

$$\dot{\varepsilon} = \dot{\varepsilon}_e + \dot{\varepsilon}_{in} = \frac{1}{\mu}\,\dot{\sigma}_{ov} + \frac{1}{\eta}\,\sigma_{ov} \,. \tag{3.37}$$

Based on these relations, the differential equation of the TPM can be calculated as follows (Johlitz 2009)

$$\begin{aligned}
& \dot{\sigma} - \dot{\sigma}_{eq} = \dot{\sigma}_{ov} \,, \\
\Leftrightarrow\ & \dot{\sigma} - E\,\dot{\varepsilon} = \mu\,\dot{\varepsilon}_e \,, \\
\Leftrightarrow\ & \dot{\sigma} - E\,\dot{\varepsilon} = \mu\left(\dot{\varepsilon} - \frac{1}{\eta}\,\sigma_{ov}\right) , \\
\Leftrightarrow\ & \dot{\sigma} - E\,\dot{\varepsilon} = \mu\left(\dot{\varepsilon} - \frac{1}{\eta}\,(\sigma - E\,\varepsilon)\right) , \\
\Leftrightarrow\ & \dot{\sigma} = (E+\mu)\,\dot{\varepsilon} - \frac{\mu}{\eta}\,\sigma + \frac{E\,\mu}{\eta}\,\varepsilon \,, \\
\Leftrightarrow\ & \dot{\sigma} + \frac{\mu}{\eta}\,\sigma = (E+\mu)\,\dot{\varepsilon} + \frac{E\,\mu}{\eta}\,\varepsilon \,.
\end{aligned} \tag{3.38}$$

If the relaxation time $\tau = \eta/\mu$ is introduced, (3.38) can be rewritten as

$$\dot{\sigma} + \frac{1}{\tau}\,\sigma = (E+\mu)\,\dot{\varepsilon} + \frac{E}{\tau}\,\varepsilon \,. \tag{3.39}$$

Similar as for the Maxwell element, the general solution is derived via integration of the differential equation (3.39) with respect to time. As described by Johlitz (2009), (3.39) is first multiplied by the term $\exp(t/\tau)$

$$\begin{aligned}
& \dot{\sigma} + \frac{1}{\tau}\,\sigma = \frac{E}{\tau}\varepsilon + (E+\mu)\,\dot{\varepsilon} \qquad \Big| \cdot \mathrm{e}^{\frac{1}{\tau}t} \\
\Leftrightarrow\ & \dot{\sigma}\,\mathrm{e}^{\frac{1}{\tau}t} + \frac{1}{\tau}\,\sigma\,\mathrm{e}^{\frac{1}{\tau}t} = \frac{E}{\tau}\varepsilon\,\mathrm{e}^{\frac{1}{\tau}t} + \mu\dot{\varepsilon}\,\mathrm{e}^{\frac{1}{\tau}t} + E\,\dot{\varepsilon}\,\mathrm{e}^{\frac{1}{\tau}t} \\
\Leftrightarrow\ & \left(\sigma\,\mathrm{e}^{\frac{1}{\tau}t}\right)^{\cdot} = \left(E\,\varepsilon\,\mathrm{e}^{\frac{1}{\tau}t}\right)^{\cdot} + \mu\,\dot{\varepsilon}\,\mathrm{e}^{\frac{1}{\tau}t} \,.
\end{aligned} \tag{3.40}$$

The subsequent integration with respect to time then results in the following constitutive equation

$$\begin{aligned}
\sigma(t) = {} & \sigma(0)\,\mathrm{e}^{-\frac{t}{\tau}} + E\,\varepsilon(t) - E\,\varepsilon(0)\,\mathrm{e}^{-\frac{t}{\tau}} \\
& + \int_0^t \mu\,\dot{\varepsilon}(s)\,\mathrm{e}^{-\frac{t-s}{\tau}}\,\mathrm{d}s \,.
\end{aligned} \tag{3.41}$$

If stress and strain at time $t = 0$ are equal to zero, the initial conditions $\varepsilon(0) = 0$ and $\sigma(0) = 0$ hold such that (3.41) can be written as

$$\begin{aligned} \sigma(t) &= E\,\varepsilon(t) + \int_0^t \mu\,\dot{\varepsilon}(s)\,\mathrm{e}^{-\frac{t-s}{\tau}}\,\mathrm{d}s \\ &= \int_0^t \left(E + \mu\,\mathrm{e}^{-\frac{t-s}{\tau}}\right)\dot{\varepsilon}(s)\,\mathrm{d}s \\ &= \int_0^t G(t-s)\,\dot{\varepsilon}(s)\,\mathrm{d}s\ . \end{aligned} \tag{3.42}$$

Therein, the relaxation function of the TPM is given by

$$G(t-s) = E + \mu\,\mathrm{e}^{-\frac{t-s}{\tau}}\ . \tag{3.43}$$

As presented in the manuscript by Johlitz (2009), the differential equation of the TPM can be evaluated with respect to specific loading conditions. First regarding very slow and fast deformation processes, the differential equation of the TPM can be reduced and two limiting cases of the stress response can be derived. In terms of very slow loadings, the temporal changes in stress and strain are comparatively small

$$\dot{\sigma} << \frac{1}{\tau}\,\sigma \quad , \quad \dot{\varepsilon} << \frac{1}{\tau}\,\varepsilon \tag{3.44}$$

such that the rates of stress and strain in (3.39) can be neglected. Considering this, the reduced form of the differential equation of the TPM is given by

$$\frac{1}{\tau}\,\sigma = \frac{E}{\tau}\,\varepsilon\ . \tag{3.45}$$

Multiplication with τ results in the corresponding stress response of the TPM

$$\sigma_{slow} = E\,\varepsilon \mathrel{\hat{=}} \sigma_{eq}\ . \tag{3.46}$$

Since this stress response corresponds to the stress σ_{eq} of the elastic spring, it is usually called equilibrium stress response (Johlitz 2009).

The second limiting case results from very fast loadings. In this case, the behaviour is opposite meaning that the rates of stress and strain are much larger than stress and strain itself

$$\dot{\sigma} >> \frac{1}{\tau}\,\sigma \quad , \quad \dot{\varepsilon} >> \frac{1}{\tau}\,\varepsilon\ . \tag{3.47}$$

On this basis, the non-differentiated terms in (3.39) can be omitted such that the reduced form of the differential equation is given by

$$\dot{\sigma} = (E + \mu)\,\dot{\varepsilon}\ . \tag{3.48}$$

With the initial conditions $\sigma(0) = 0$ and $\varepsilon(0) = 0$, the corresponding stress response of the TPM is obtained by integration with respect to time

$$\sigma_{fast} = (E + \mu)\,\varepsilon \,. \tag{3.49}$$

In contrast to (3.46), this stress response corresponds to that of two springs in parallel and denotes the spontaneous response of the TPM (Johlitz 2009). As illustrated in figure 3.6, the equilibrium and spontaneous stress responses of the TPM define lower and upper limits of stress meaning that stress responses at middle strain rates are located between both limit cases.

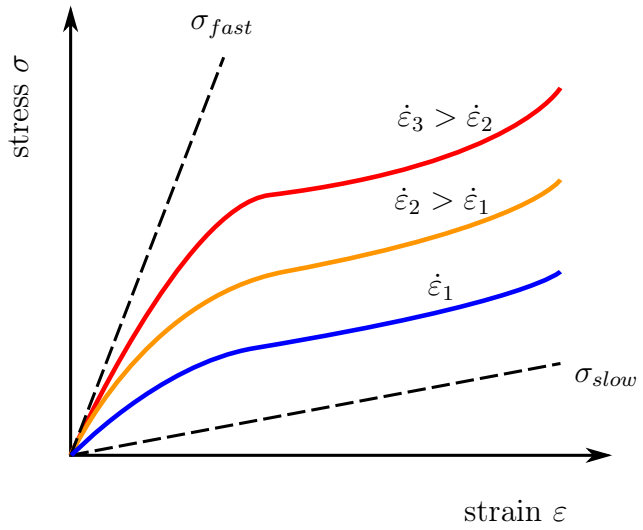

FIGURE 3.6: Stress response of the Three-parameter model at different rates of strain

Apart from slow and fast deformations, the stress response of the TPM can be derived with regard to several other loading conditions. Regarding experimental investigations, viscoelastic material behaviour of rubber is commonly studied via relaxation tests in the time domain. In this context, the quasi-static response of the TPM at constant strain is of importance. Taking into account simple relaxation tests, the material is usually loaded with a strain ε_0 which is held constant over time t. Mathematically, this loading procedure can be expressed by the following conditions

$$\varepsilon(t) = \begin{cases} 0 & \text{if} \quad t = 0 \\ \varepsilon_0 = \text{const.} & \text{if} \quad t > 0 \end{cases} \tag{3.50}$$

From this relation, the corresponding stress response of the TPM can be derived by inserting (3.50) into the differential equation (3.39). In so doing, the initial stress response at the time $t = 0$ reads as

$$\sigma(0) = (E + \mu)\,\varepsilon_0 \tag{3.51}$$

and the time-dependent stress response for times $t > 0$ follows to

$$\sigma(t) = \left(E + \mu\,\mathrm{e}^{-\frac{t}{\tau}}\right)\varepsilon_0 = G(t)\,\varepsilon_0 \,. \tag{3.52}$$

Therein, the relaxation function $G(t)$ is a decreasing exponential function which describes the time-dependent stress decrease at constant strain. For illustration, the applied strain and the relaxation function are displayed in figure 3.7 over time t. As described by Johlitz (2009), the relaxation function starts at the initial modulus $E+\mu$ and decreases for large times against the equilibrium modulus E.

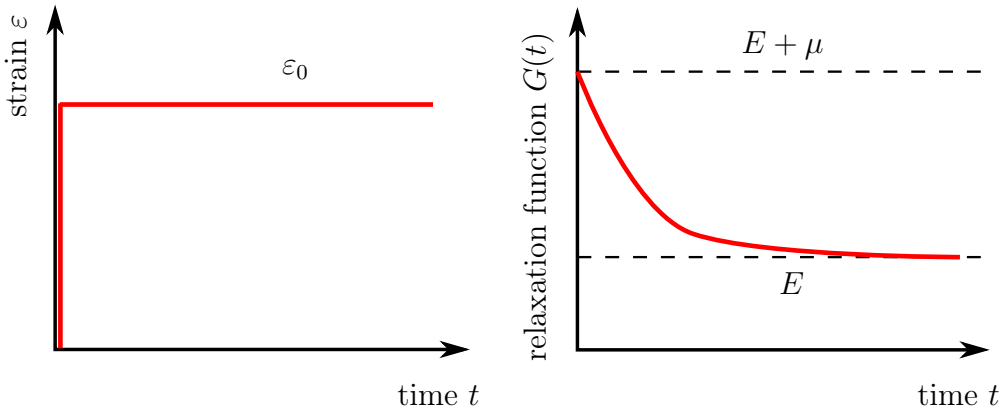

FIGURE 3.7: Applied strain (left) and corresponding relaxation function of the TPM (right)

Besides from the investigation of viscoelastic behaviour via relaxation tests in the time domain, it is straight forward to characterise viscoelastic material properties through dynamic mechanical analysis (DMA) in the frequency domain. There, the material is loaded with harmonic excitations of strain amplitude $\Delta\varepsilon$ and its material response is investigated in the frequency domain by means of the storage and loss modulus. A detailed description of dynamic mechanical analysis is given by Menard (1999). Considering this loading condition, the harmonic response of the TPM by means of the storage and loss modulus is of interest to represent the observed phenomena. In the case of strain-controlled excitations, the harmonic strain with amplitude $\Delta\varepsilon$ applied to the material is mathematically defined by

$$\varepsilon \;=\; \Delta\varepsilon(\omega)\,\mathrm{e}^{i\omega t} \tag{3.53}$$

with the angular frequency ω. The harmonic stress response given by the TPM reads as

$$\sigma \;=\; \Delta\sigma(\omega)\,\mathrm{e}^{i\omega t} \tag{3.54}$$

with the stress amplitude $\Delta\sigma$. If these relations (3.53) and (3.54) are inserted into the differential equation (3.39) and

$$\frac{\mathrm{d}}{\mathrm{d}t}\,\mathrm{e}^{i\omega t} \;=\; i\omega\,\mathrm{e}^{i\omega t} \tag{3.55}$$

is taken into account, the differential equation of the TPM leads to

$$\mathrm{i}\,\omega\,\Delta\sigma\,\mathrm{e}^{\mathrm{i}\omega t} \;+\; \frac{1}{\tau}\,\Delta\sigma\,\mathrm{e}^{\mathrm{i}\omega t} \;=\; \mathrm{i}\,\omega\,(E+\mu)\,\Delta\varepsilon\,\mathrm{e}^{\mathrm{i}\omega t} \;+\; \frac{1}{\tau}\,E\,\Delta\varepsilon\,\mathrm{e}^{\mathrm{i}\omega t}\;. \tag{3.56}$$

Since dynamic mechanical analysis is focused to the storage and the loss modulus, the quotient of harmonic stress and strain amplitudes is considered. To this end, the harmonic response of the TPM is given by means of the complex-valued dynamic modulus

$$G^*(\omega) = \frac{\Delta\sigma}{\Delta\varepsilon} = E + \frac{\mathrm{i}\,\omega\,\tau\,\mu}{1+\mathrm{i}\,\omega\,\tau}\,. \tag{3.57}$$

It is a frequency dependent function which characterises the dynamic mechanical transfer behaviour of the material under dynamic loadings. Apart from the relaxation function, the dynamic modulus is an essential quantity to describe viscoelastic material behaviour in the frequency domain. In order to obtain the storage and loss modulus, the complex-valued dynamic modulus (3.57) must be decomposed into its real and imaginary parts. For this purpose, (3.57) is extended by the complex conjugate $(1 - i\omega\tau)$, which then leads to the separation into real and imaginary parts

$$\begin{aligned} G^*(\omega) &= E + \frac{(\omega\,\tau\,)^2\,\mu}{1+(\omega\,\tau)^2} + \mathrm{i}\,\frac{\omega\,\tau\,\mu}{1+(\omega\,\tau)^2} \\ &= G'(\omega) + \mathrm{i}\,G''(\omega)\,. \end{aligned} \tag{3.58}$$

In this, the real part $G'(\omega)$ in (3.58) is the storage modulus and the imaginary part $G''(\omega)$ is the loss modulus. From a physical point of view, the storage modulus can be interpreted as the dynamic stiffness of the material or as a measure of the stored energy inside the material whereas the loss modulus can be described as a measure of energy dissipation or as a measure of damping effects. For illustration, the frequency dependence of storage and loss modulus is displayed in figure 3.8. At very low frequencies, the storage modulus is equal to the equilibrium modulus E and increases with larger frequency against the spontaneous modulus $E+\mu$. The loss modulus reaches its maximum value at the characteristic frequency $\omega = 1/\tau$ and decreases against zero for small and high frequencies (Johlitz 2009).

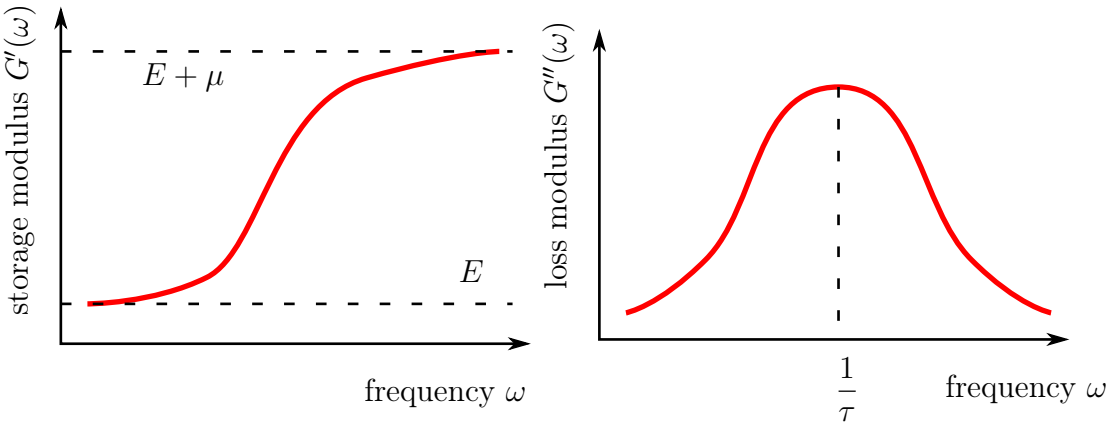

FIGURE 3.8: Frequency dependence of the storage and the loss modulus

Thermomechanical consistency of the TPM

Regarding isothermal processes at constant temperature, as it is the case in this work, the thermomechanical consistency of rheological elements can generally be proven on the basis of the of the Clausius-Planck inequality

$$\sigma\,\dot{\varepsilon} \;-\; \rho_0\,\dot{\Psi} \;\geq\; 0\;. \tag{3.59}$$

A detailed description of this approach is provided by Johlitz (2009). Referring to this concept, the derivative of the free energy of the TPM with respect to time must be calculated first. The free energy of the TPM is equal to the sum of the energy which is stored in the two elastic springs

$$\begin{aligned} \rho_0\,\Psi \;&=\; \frac{1}{2}\,E\,\varepsilon^2 \;+\; \frac{1}{2}\,\mu\,\varepsilon_e^2 \\ &=\; \frac{1}{2}\,E\,\varepsilon^2 \;+\; \frac{1}{2}\,\mu\,(\varepsilon-\varepsilon_{in})^2\;. \end{aligned} \tag{3.60}$$

Based on this, the derivative with respect to time is given by

$$\rho_0\,\dot{\Psi} \;=\; E\,\varepsilon\,\dot{\varepsilon} \;+\; \mu\,(\varepsilon-\varepsilon_{in})\,\dot{\varepsilon} \;-\; \mu\,(\varepsilon-\varepsilon_{in})\,\dot{\varepsilon}_{in}\;. \tag{3.61}$$

If this result is inserted into (3.59), the following inequality is obtained

$$(\sigma \;-\; [E\,\varepsilon \;+\; \mu\,(\varepsilon-\varepsilon_{in})]\,)\,\dot{\varepsilon} \;+\; \mu\,(\varepsilon-\varepsilon_{in})\,\dot{\varepsilon}_{in} \;\geq\; 0\;. \tag{3.62}$$

Referring to Coleman and Noll (1963), this inequality must hold for arbitrary deformation processes. Regarding this requirement, (3.62) must be satisfied for arbitrary strain rates $\dot{\varepsilon}$ which automatically implies that the first term in brackets must be equal to zero. On this basis, the stress in (3.62) is given by

$$\sigma \;=\; E\,\varepsilon \;+\; \mu\,(\varepsilon-\varepsilon_{in})\;. \tag{3.63}$$

Considering this relation, the last term of inequality (3.62) remains

$$\mu\,(\varepsilon-\varepsilon_{in})\,\dot{\varepsilon}_{in} \;\geq\; 0\;. \tag{3.64}$$

In this, a thermomechanically consistent relation for the inelastic strain rate is given by the linear differential equation

$$\dot{\varepsilon}_{in} \;=\; \frac{\mu}{\eta}\,(\varepsilon-\varepsilon_{in})\;. \tag{3.65}$$

If this relation is inserted into (3.64), the following formulation is obtained

$$\frac{\mu^2}{\eta}\,(\varepsilon-\varepsilon_{in})^2 \;\geq\; 0\;. \tag{3.66}$$

Since stiffness and viscosity are always positive ($\mu > 0$ and $\eta > 0$), this inequality is satisfied for arbitrary deformation processes, and the thermomechanical consistency of

the TPM is thus proven.

3.2.4 Maxwell chain

The previously introduced TPM can indeed describe viscoelastic material properties in a qualitative manner. However, a quantitative representation of real viscoelastic phenomena calls for more complex rheological models. Accordingly, it is straight forward to extend the TPM by adding a series of Maxwell elements in parallel. This extension is called the classical Maxwell chain. As illustrated in figure 3.9, the classical Maxwell chain is composed of a linear spring and n Maxwell elements in parallel. Based on this composition, the Maxwell chain is defined by the modulus E of the single spring and by $k = 1..n$ stiffness parameters μ_k and viscosities η_k of the parallel connected Maxwell elements. Hence, the Maxwell chain contains a number of $2n + 1$ material parameters.

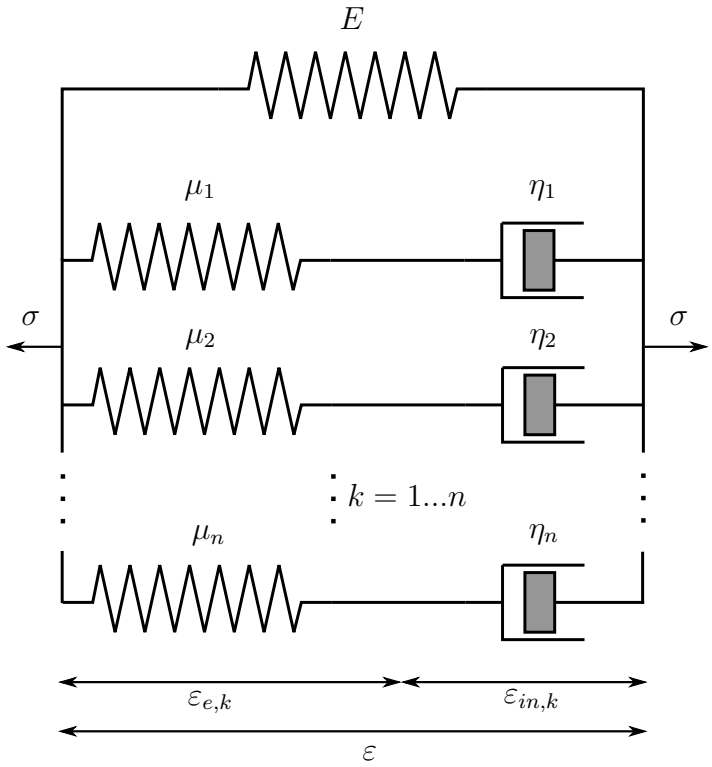

FIGURE 3.9: Maxwell chain

Since the general composition of the Maxwell chain is similar to that of the TPM, the total strain is given by the sum of elastic and inelastic strains $\varepsilon_{e,k}$ and $\varepsilon_{in,k}$

$$\varepsilon = \varepsilon_{e,k} + \varepsilon_{in,k} \quad , \quad k = 1...n \; . \tag{3.67}$$

Differentiation with respect to time leads to the corresponding strain rate

$$\dot{\varepsilon} = \dot{\varepsilon}_{e,k} + \dot{\varepsilon}_{in,k} \quad , \quad k = 1...n \; . \tag{3.68}$$

The total stress is additively decomposed into the equilibrium stress σ_{eq} of the individual spring and the sum of the inelastic overstresses $\sigma_{ov,k}$ of the $k = 1...n$ Maxwell elements

$$\sigma \;=\; \sigma_{eq} \;+\; \sigma_{ov} \;=\; \sigma_{eq} \;+\; \sum_{k=1}^{n} \sigma_{ov,k} \;. \tag{3.69}$$

Therein, the inelastic overstresses are defined by

$$\sigma_{ov,k} \;=\; \mu_k \, \varepsilon_{e,k} \;=\; \eta_k \, \dot{\varepsilon}_{in,k} \;. \tag{3.70}$$

From these definitions, the differential equations of the overstresses are obtained by differentiation of (3.70) with respect to time

$$\begin{aligned} \dot{\sigma}_{ov,k} \;=\; \mu_k \, \dot{\varepsilon}_{e,k} \quad &= \quad \mu_k \left(\dot{\varepsilon} \;-\; \frac{1}{\eta_k} \, \sigma_{ov,k} \right) \\ &= \quad \mu_k \, \dot{\varepsilon} \;-\; \frac{\mu_k}{\eta_k} \, \sigma_{ov,k} \;. \end{aligned} \tag{3.71}$$

Introducing relaxation times $\tau_k = \eta_k / \tau_k$ of each Maxwell element, (3.71) finally reads as

$$\dot{\sigma}_{ov,k} \;=\; \mu_k \, \dot{\varepsilon} \;-\; \frac{1}{\tau_k} \, \sigma_{ov,k} \;. \tag{3.72}$$

As described by Johlitz (2009), the stress response of the Maxwell chain is derived by multiplication of the differential equation (3.72) by the exponential term $\exp(1/\tau_k)$ and subsequent integration with respect to time in the limits $s = 0$ to $s = t$. These operations finally yield the following expression for the overstresses

$$\sigma_{ov,k}(t) \;=\; \int_0^t \mu_k \, \mathrm{e}^{-\frac{t-s}{\tau_k}} \, \dot{\varepsilon}(s) \, \mathrm{d}s \;. \tag{3.73}$$

If this result is then inserted into (3.69), the stress response of the Maxwell chain is given by

$$\begin{aligned} \sigma(t) \quad &= \quad E \, \varepsilon \;+\; \int_0^t \left(\sum_{k=1}^{n} \mu_k \, \mathrm{e}^{-\frac{t-s}{\tau_k}} \right) \dot{\varepsilon}(s) \, \mathrm{d}s \\ &= \quad \int_0^t \left(E \;+\; \sum_{k=1}^{n} \mu_k \, \mathrm{e}^{-\frac{t-s}{\tau_k}} \right) \dot{\varepsilon}(s) \, \mathrm{d}s \\ &= \quad \int_0^t G(t-s) \, \dot{\varepsilon}(s) \, \mathrm{d}s \;. \end{aligned} \tag{3.74}$$

In contrast to the TPM, the time-dependent relaxation function $G(t)$ of the Maxwell chain is not only defined by just one single exponential function, but by the sum of n exponentials which results from the combination of n Maxwell elements in parallel. On this basis, the Maxwell chain can be used to model more complex viscoelastic material properties. Considering dynamic mechanical analysis, the harmonic response of the Maxwell chain in the frequency domain can be derived in a similar manner as for the TPM. In order to describe its response with regard to harmonic strains or stresses, (3.53) and (3.54) are taken into account. Inserting these relations into (3.72) and separating the real and imaginary parts, the complex modulus G^*, the storage

modulus G' and the loss modulus G'' finally read as

$$\begin{aligned} G^*(\omega) &= G'(\omega) + \mathrm{i}\, G''(\omega) \\ &= E + \sum_{k=1}^{n} \mu_k \frac{(\omega\,\tau_k)^2}{1+(\omega\,\tau_k)^2} + \mathrm{i} \sum_{k=1}^{n} \mu_k \frac{\omega\,\tau_k}{1+(\omega\,\tau_k)^2} \,. \end{aligned} \tag{3.75}$$

Thermomechanical consistency of the Maxwell chain

The thermomechanical consistency of the Maxwell chain can be similarly proven as for the TPM. The free energy is first defined by

$$\rho_0\,\Psi \;=\; \frac{1}{2}\,E\,\varepsilon^2 \;+\; \frac{1}{2}\sum_{k=1}^{n} \mu_k\,(\varepsilon-\varepsilon_{in,k})^2 \,, \tag{3.76}$$

with the time derivative

$$\rho_0\,\dot{\Psi} \;=\; E\,\varepsilon\,\dot{\varepsilon} \;+\; \sum_{k=1}^{n} \mu_k\,(\varepsilon-\varepsilon_{in,k})\,\dot{\varepsilon} \;-\; \sum_{k=1}^{n} \mu_k\,(\varepsilon-\varepsilon_{in,k})\,\dot{\varepsilon}_{in,k} \,. \tag{3.77}$$

Inserting this relation into (3.59), the following inequality is obtained

$$\left(\sigma \;-\; \left[E\,\varepsilon \;+\; \sum_{k=1}^{n} \mu_k\,(\varepsilon-\varepsilon_{in,k})\right]\right)\dot{\varepsilon} \;+\; \sum_{k=1}^{n} \mu_k\,(\varepsilon-\varepsilon_{in,k})\,\dot{\varepsilon}_{in,k} \;\geq\; 0 \,. \tag{3.78}$$

Following the argumentation of Coleman and Noll (1963), inequality (3.78) is fulfilled if the stress is given by

$$\sigma \;=\; E\,\varepsilon \;+\; \sum_{k=1}^{n} \mu_k\,(\varepsilon-\varepsilon_{in,k}) \;=\; E\,\varepsilon \;+\; \sum_{k=1}^{n} \sigma_{ov,k} \,. \tag{3.79}$$

Considering this result, the remaining inequality reads as

$$\sum_{k=1}^{n} \mu_k\,(\varepsilon-\varepsilon_{in,k})\,\dot{\varepsilon}_{in} \;\geq\; 0 \,. \tag{3.80}$$

If the relation for the inelastic strain rates

$$\dot{\varepsilon}_{in,k} \;=\; \frac{\mu_k}{\eta_k}\,(\varepsilon-\varepsilon_{in,k}) \tag{3.81}$$

is taken into account and inserted into (3.80), the remaining inequality follows to

$$\sum_{k=1}^{n} \frac{\mu_k^2}{\eta_k}\,(\varepsilon-\varepsilon_{in,k})^2 \;\geq\; 0 \,. \tag{3.82}$$

In terms of positive stiffness parameters μ_k and positive viscosities η_k, this inequality holds for arbitrary deformation processes such that the thermomechanical consistence of the Maxwell chain is ensured.

3.3 Fractional viscoelasticity

The classical Maxwell chain introduced above is suitable to represent complex viscoelastic properties of rubber. However, the description of the material behaviour by this model is based on relaxation functions of the exponential type and is thus related to a discrete relaxation spectrum. For this reason, a fairly huge number of Maxwell elements and a huge number of material parameters is required to represent the dynamic properties of elastomers (Haupt and Lion 2002). In order to improve this situation, it has become well accepted to extend classical rheological models by the concept of fractional derivatives. In contrast to classical rheological elements, the fractional ones turned out to be very suitable to approximate complicated viscoelastic material behaviour with only a few material parameters. Caputo and Mainardi (1971) provide a comparison between classical constitutive approaches and constitutive models of fractional order which reveals the effective approximation of material behaviour by fractional models with less material parameters. Based on this advantage, the concept is commonly applied to represent long-term relaxations or the frequency dependence over a broad range of frequency.
Caputo (1967) and Slonimsky (1967) first introduced the concept of a fractional derivative to the theory of linear viscoelasticity, which is applied in a similar way in this work. A comprehensive overview of the mathematical theory of this concept and the application of fractional derivatives is provided in the textbooks by Oldham and Spanier (1974), Podlubny (1999) or Kilbas et al. (2006).
Referring to Haupt and Lion (2002) and regarding a function $f(t)$ with $f(t) = 0$ for $t \leq 0$, the concept of a fractional derivative is generally applied by replacing the standard time derivative of the function by a derivative of fractional order

$$\frac{\mathrm{d}}{\mathrm{d}t} f(t) \;\rightarrow\; \frac{\mathrm{d}^{\alpha}}{\mathrm{d}t^{\alpha}} f(t) \quad , \quad 0 < \alpha < 1 \; . \tag{3.83}$$

Thereby, the fractional derivative itself is defined by the linear functional

$$\frac{\mathrm{d}^{\alpha}}{\mathrm{d}t^{\alpha}} f(t) \;=\; \frac{1}{\Gamma(1-\alpha)} \int_0^t \frac{1}{(t-s)^{\alpha}} f'(s)\, \mathrm{d}s \quad \text{for} \quad 0 < \alpha < 1 \; , \tag{3.84}$$

with the Eulerian Gamma function

$$\Gamma(1-\alpha) \;=\; \int_0^{\infty} \xi^{-\alpha}\, \mathrm{e}^{-\xi}\, \mathrm{d}\xi \; . \tag{3.85}$$

If this concept is applied to the classical damping element by replacing the time derivative by a derivative of fractional order, the fractional damping element is obtained. Starting with this basic element, other rheological models can be motivated by combining it with other elements in series or parallel. One of these combinations is the

Maxwell element of fractional order which is defined by the series connection of an elastic spring and a fractional damping element. Among others, detailed discussions about the application of the concept of fractional derivatives to various viscoelastic models are provided by Bagley and Torvik (1983b), Koeller (1984), Nonnenbacher (1991) or Schiessel et al. (1995). Studies on the thermomechanical requirements of fractional models are given, for instance, by Gurtin and Herrera (1965) or Lion (2001).

As already stated, the concept of fractional derivatives is very effective in approximating viscoelastic phenomena with only a small number of material parameters and therefore frequently applied to represent long-term relaxation or frequency dependence over a broad range of frequencies. For instance, Adolfsson and Enelund (2003) introduce a fractional model in the time domain, which is based on the nonlinear viscoelastic approach by Simo (1987). A fractional modification of the viscoelastic model of Reese and Govindjee (1998) is proposed one year later by the same author (Adolfsson 2004). With respect to the focus of this work, fractional formulations in the frequency domain which are applied to describe complex rubber dynamics and damping phenomena are fairly common in the literature. In Kari (2001a) and Kari (2001b), the author introduces a viscoelastic waveguide model which is capable of describing the frequency dependent behaviour of the axial stiffness of cylindrical vibration isolators in a broad frequency range. Other frequency domain formulations based on rheological elements of fractional order are proposed by Bagley and Torvik (1979), Bagley and Torvik (1983a) and Bagley and Torvik (1985). Lewandowski and Pawlak (2011) recently presented an approach to describe the damping behaviour of VE dampers, which is based on a fractional Kelvin-Voigt model as well as on a fractional Maxwell model.
Several other constitutive models of fractional order are proposed, for instance, by Nonnenbacher (1991), Drozdov (1997), Haupt et al. (2000), Lion (1997b), Haupt et al. (2000) or Lion (2001).

With respect to finite element computations in the time domain, the numerical application of the fractional calculus is very time-consuming. Due to the non-local character of fractional derivatives, the entire history must be stored when solving the related equations by time integration (Schmidt and Gaul 2006). Schmidt (2003) provides a comprehensive overview of fractional viscoelastic material laws and their numerical implementation into a finite element code. For instance, the author proposes an efficient time domain implementation of a fractional model into a finite element code. Thereby, the author refers to the fading memory character of a fractional derivative whereupon parts in the history can be regarded with less temporal resolution, without losses of accurateness for the time integration. Among others, the works by Enelund and Josefson (1997), Enelund et al. (1999), Gaul and Schanz (1994) and Gaul and Schanz (1999) also deal with the finite element implementation of fractional viscoelastic models.
Apart from finite element implementation, Lewandowski and Chorazyczewski (2010) are concerned with the identification of the material parameters and provide an effective method with respect to fractional Kelvin-Voigt and Maxwell models. The constitutive approach presented in this work is also based on a fractional extension of a Maxwell chain, but transformed from the time in the frequency domain. Due to this, the mentioned numerical problems in the time domain do not arise.

In order to acquaint the reader with the fractional extension of the classical Maxwell chain, the fractional damping element and the fractional Maxwell element will be introduced in the following. Thereby, the presentation mainly refers to the argumentations by Haupt and Lion (2002).

3.3.1 Fractional damping element

The fractional damping element can be interpreted as a mix between spring and damper which is controlled by the fractional exponent α. As illustrated in figure 3.10, a fractional representation of the damper can be defined by the material parameters μ and α. Here, factor $\tau = 1s$ is not a parameter and only introduced for dimensional reasons.

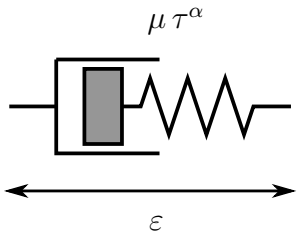

FIGURE 3.10: Fractional damping element

In order to derive the differential equation of the fractional damper, the time derivative of strain in the constitutive equation of the classical damping element (3.27) is first replaced by a derivative of fractional order

$$\sigma \;=\; \mu\,\tau^{\alpha}\,\frac{\mathrm{d}^{\alpha}}{\mathrm{d}t^{\alpha}}\,\varepsilon \quad , \quad 0 \;\leq\; \alpha \;<\; 1\;. \tag{3.86}$$

If the definition of the fractional derivative in (3.84) is taken into account, the stress response of the fractional damper is given by

$$\sigma(t) \;=\; \frac{\mu\,\tau^{\alpha}}{\Gamma(1-\alpha)}\,\int_0^t \frac{1}{(t-s)^{\alpha}}\,\dot{\varepsilon}(s)\,\mathrm{d}s\;. \tag{3.87}$$

In contrast to the Maxwell element, the relaxation function of the fractional damper is no exponential function, but it is a decreasing power law which reads as

$$G(t) \;=\; \frac{\mu}{\Gamma(1-\alpha)}\,\left(\frac{\tau}{t}\right)^{\alpha}\;. \tag{3.88}$$

In Lion (2000c), it is proven that this type of power-law can be written in terms of a continuous relaxation spectrum

$$G(t) \;=\; \int_0^{\infty} g(\zeta)\,\mathrm{e}^{-\frac{t}{\zeta}}\,\mathrm{d}\zeta \quad \text{with} \quad g(\zeta) \;=\; \frac{\mu\,\tau^{\alpha}}{\Gamma(1-\alpha)\,\Gamma(\alpha)\,\zeta^{\alpha+1}} \tag{3.89}$$

with the relaxation time ζ.

Moreover, the fractional damping element generally interpolates between Hookean elasticity and Newtonian viscosity (Lion 1997b). For the limit case $\alpha = 0$, the fractional damper results into the linear elastic spring

$$\sigma \;=\; \mu\,\varepsilon \;, \tag{3.90}$$

with modulus μ, whereas the limit case $\alpha = 1$ yields a constitutive equation similar to that of the viscous damper

$$\dot{\sigma} \;=\; \mu\,\tau\,\dot{\varepsilon} \;. \tag{3.91}$$

Considering the frequency dependent behaviour of rubber observed in DMA tests, the harmonic response of the fractional damper due to harmonic strain excitations is in focus. Taking a harmonic deformation of strain amplitude $\Delta\varepsilon$ and angular frequency ω into account

$$\varepsilon \;=\; \Delta\varepsilon(\omega)\,\mathrm{e}^{i\omega t} \;, \tag{3.92}$$

the harmonic stress response of the fractional damper is given by

$$\sigma \;=\; \Delta\sigma(\omega)\,\mathrm{e}^{i\omega t} \;. \tag{3.93}$$

Inserting both relations into (3.86) and taking into account the fractional derivative of the exponential function

$$\frac{\mathrm{d}^{\alpha}}{\mathrm{d}t^{\alpha}}\,\mathrm{e}^{i\omega t} \;=\; (i\omega)^{\alpha}\,\mathrm{e}^{i\omega t} \;, \tag{3.94}$$

the differential equation (3.86) changes to the following formulation

$$\Delta\sigma\,\mathrm{e}^{i\omega t} \;=\; (i\omega)^{\alpha}\,\mu\,\tau^{\alpha}\,\Delta\varepsilon\,\mathrm{e}^{i\omega t} \;. \tag{3.95}$$

On the basis of this relation, the harmonic response is obtained in terms of the complex modulus and reads as

$$G^{*}(\omega) \;=\; \frac{\Delta\sigma}{\Delta\varepsilon} \;=\; \mu\,(i\omega\tau)^{\alpha} \;. \tag{3.96}$$

In order to separate (3.96) into real and imaginary parts, the relation

$$i^{\alpha} \;=\; \cos\left(\alpha\,\frac{\pi}{2}\right) \;+\; i\,\sin\left(\alpha\,\frac{\pi}{2}\right) \tag{3.97}$$

must be taken into account. By applying this operation, the complex modulus is finally given by the sum of storage modulus $G'(\omega)$ and loss modulus $G''(\omega)$

$$G^{*}(\omega) \;=\; G'(\omega) \;+\; i\,G''(\omega) \;=\; \mu\,(\omega\tau)^{\alpha}\,\cos\left(\alpha\,\frac{\pi}{2}\right) \;+\; i\,\mu\,(\omega\tau)^{\alpha}\,\sin\left(\alpha\,\frac{\pi}{2}\right) \;. \tag{3.98}$$

Fractional Maxwell element

The fractional Maxwell element is defined by the connection of an elastic spring and a fractional damper in series. Since this element is quite similar to the classical Maxwell element, but extended by fractional derivatives, it can be interpreted as a generalisation of the latter one. As illustrated in figure 3.11, the fractional Maxwell element inherits

the material parameters μ and α. In contrast to the fractional damper, factor τ is also a material parameter using this type of representation.

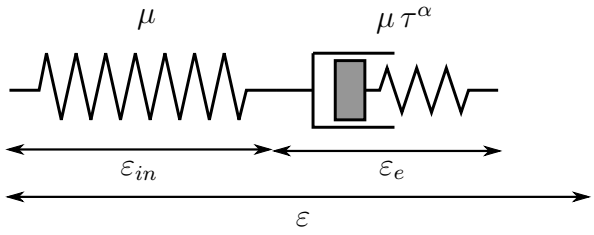

FIGURE 3.11: Fractional Maxwell element

The differential equation of the fractional Maxwell element is obtained by replacing the time derivatives in the differential equation of the classical Maxwell element (3.31) by derivatives of fractional order

$$\frac{\mathrm{d}^{\alpha}}{\mathrm{d}t^{\alpha}}\,\sigma \;+\; \frac{1}{\tau^{\alpha}}\sigma \;=\; \mu\,\frac{\mathrm{d}^{\alpha}}{\mathrm{d}t^{\alpha}}\,\varepsilon \;. \tag{3.99}$$

Inserting the definition of stress into (3.99)

$$\sigma \;=\; \mu\,\tau^{\alpha}\,\frac{\mathrm{d}^{\alpha}}{\mathrm{d}t^{\alpha}}\,\varepsilon_{in} \;, \tag{3.100}$$

the differential equation can alternatively be expressed by

$$\frac{\mathrm{d}^{\alpha}}{\mathrm{d}t^{\alpha}}\,\sigma \;=\; \mu\,\frac{\mathrm{d}^{\alpha}}{\mathrm{d}t^{\alpha}}\,\varepsilon \;-\; \mu\,\frac{\mathrm{d}^{\alpha}}{\mathrm{d}t^{\alpha}}\,\varepsilon_{in} \;. \tag{3.101}$$

For thermodynamical reasons, it is necessary to apply fractional derivatives of the same order to stress and strain (Lion 2001). Following the presentation by Haupt and Lion (2002), the stress response of the fractional Maxwell element can be derived by first transforming the differential equation into the complex domain via applying the Laplace transformation

$$f(t) \;\rightarrow\; \hat{f}(\omega) \;=\; \mathcal{L}\{f(t)\} \;=\; \int_0^{\infty} f(t)\,\mathrm{e}^{-\omega t}\,\mathrm{d}t \;. \tag{3.102}$$

On this basis, the stress response in the frequency domain reads as

$$\hat{\sigma}(\omega) \;=\; \mu\,\frac{(\tau\omega)^{\alpha}}{1+(\tau\omega)^{\alpha}}\,\hat{\varepsilon}(\omega) \;. \tag{3.103}$$

After that, (3.103) is transformed back such that the time domain formulation of the inelastic overstress is finally given by

$$\sigma_{ov} \;=\; \mu\int_0^t E_{\alpha}\left(-\left(\frac{t-s}{\tau}\right)^{\alpha}\right)\,\varepsilon'(s)\,\mathrm{d}s \;. \tag{3.104}$$

In this expression, the relaxation function of the fractional Maxwell element is given by

$$G(t-s) \;=\; \mu\, E_\alpha\left(-\left(\frac{t-s}{\tau}\right)^\alpha\right) \;. \tag{3.105}$$

Therein the kernel function

$$E_\alpha\left(-\left(\frac{t-s}{\tau}\right)^\alpha\right) \tag{3.106}$$

is related to the so-called Mittag-Leffler function

$$E_\alpha(x) \;=\; \sum_{k=0}^{\infty} \frac{x^k}{\Gamma(1+\alpha k)} \;. \tag{3.107}$$

In terms of the specification $\alpha = 1$, the kernel function E_α results in a classical exponential function such that the fractional Maxwell element turns into a classical Maxwell element. In contrast to the fractional damper, which is characterised by a singularity at time $t = 0$, the function converges for all $\alpha > 0$ and equals 1 at time $t = 0$ (Haupt and Lion 2002).

In order to derive the complex modulus of the fractional Maxwell element, harmonic deformation and stress responses are considered

$$\begin{aligned} \varepsilon &= \Delta\varepsilon(\omega)\, \mathrm{e}^{i\omega t} \;, \\ \sigma &= \Delta\sigma(\omega)\, \mathrm{e}^{i\omega t} \;. \end{aligned} \tag{3.108}$$

Inserting these relations into the differential equation of the fractional Maxwell element (3.99) and taking (3.94) into account, the complex modulus is finally given by

$$G^*(\omega) \;=\; \frac{\Delta\sigma}{\Delta\varepsilon} \;=\; \mu\, \frac{(i\omega\tau)^\alpha}{1+(i\omega\tau)^\alpha} \;. \tag{3.109}$$

In order to obtain the storage and the loss modulus on the basis of this definition, the complex modulus must be decomposed into real and imaginary parts

$$G^*(\omega) \;=\; G'(\omega) \;+\; i\, G''(\omega) \;. \tag{3.110}$$

After some mathematical calculations, the storage modulus reads as

$$\begin{aligned} G'(\omega) \;=\; \mu \Bigg(& \frac{\mathrm{e}^{\frac{1}{2}\,\alpha \log\left(\omega^2\tau^2\right)} \cos\left(\frac{1}{2}\,\alpha\pi\right) \left(1+\mathrm{e}^{\frac{1}{2}\,\alpha \log\left(\omega^2\tau^2\right)} \cos\left(\frac{1}{2}\,\alpha\pi\right)\right)}{\left(1+\mathrm{e}^{\frac{1}{2}\,\alpha \log(\omega^2\tau^2)} \cos\left(\frac{1}{2}\,\alpha\pi\right)\right)^2 + \left(\mathrm{e}^{\frac{1}{2}\,\alpha \log(\omega^2\tau^2)}\right)^2 \left(\sin\left(\frac{1}{2}\,\alpha\pi\right)\right)^2} \\ + \; & \frac{\left(\mathrm{e}^{\frac{1}{2}\,\alpha \log\left(\omega^2\tau^2\right)}\right)^2 \left(\sin\left(\frac{1}{2}\,\alpha\pi\right)\right)^2}{\left(1+\mathrm{e}^{\frac{1}{2}\,\alpha \log(\omega^2\tau^2)} \cos\left(\frac{1}{2}\,\alpha\pi\right)\right)^2 + \left(\mathrm{e}^{\frac{1}{2}\,\alpha \log(\omega^2\tau^2)}\right)^2 \left(\sin\left(\frac{1}{2}\,\alpha\pi\right)\right)^2} \Bigg) \end{aligned} \tag{3.111}$$

and the loss modulus is given by

$$G''(\omega) = \mu \left(\frac{\mathrm{e}^{\frac{1}{2}\alpha\log\left(\omega^2\tau^2\right)} \sin\left(\frac{1}{2}\alpha\pi\right) \left(1 + \mathrm{e}^{\frac{1}{2}\alpha\log\left(\omega^2\tau^2\right)} \cos\left(\frac{1}{2}\alpha\pi\right)\right)}{\left(1 + \mathrm{e}^{\frac{1}{2}\alpha\log(\omega^2\tau^2)} \cos\left(\frac{1}{2}\alpha\pi\right)\right)^2 + \left(\mathrm{e}^{\frac{1}{2}\alpha\log(\omega^2\tau^2)}\right)^2 \left(\sin\left(\frac{1}{2}\alpha\pi\right)\right)^2} - \frac{\left(\mathrm{e}^{\frac{1}{2}\alpha\log\left(\omega^2\tau^2\right)}\right)^2 \cos\left(\frac{1}{2}\alpha\pi\right) \sin\left(\frac{1}{2}\alpha\pi\right)}{\left(1 + \mathrm{e}^{\frac{1}{2}\alpha\log(\omega^2\tau^2)} \cos\left(\frac{1}{2}\alpha\pi\right)\right)^2 + \left(\mathrm{e}^{\frac{1}{2}\alpha\log(\omega^2\tau^2)}\right)^2 \left(\sin\left(\frac{1}{2}\alpha\pi\right)\right)^2} \right). \tag{3.112}$$

In order to illustrate the frequency dependent characteristics of the fractional Maxwell element, figure 3.12 provides a comparison between the storage and loss modulus of the classical and fractional Maxwell element for different values of α. In the case of $\alpha = 0$, the fractional Maxwell element represents linear elastic behaviour without any frequency dependence whereas the specification $\alpha = 1$ results in the representation of the classical Maxwell element. Hence, the frequency dependent characteristics and the viscous properties of the fractional Maxwell element are controllable by the material parameter α. If α is small, the fractional Maxwell element exhibits a frequency dependence which is spread over an extremely wide range.

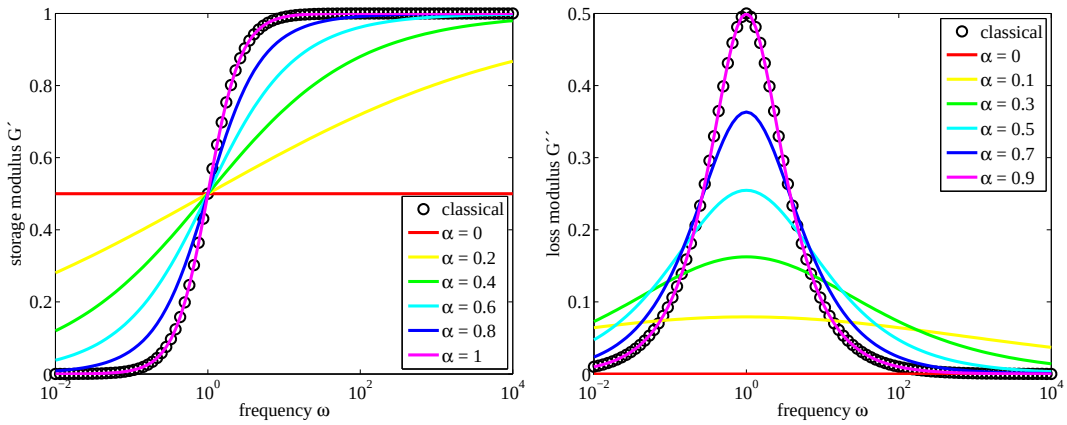

FIGURE 3.12: Approximation of the storage and loss modulus of the fractional Maxwell element compared to the approximation of the classical Maxwell element

3.4 Finite nonlinear viscoelasticity

The rheological elements introduced above are based on linear differential equations and are thus generally limited to describe linear viscoelastic material behaviour under small deformations. Since elastomer materials are often loaded with finite deformations, other concepts must be developed. A common concept to describe nonlinear viscoelastic properties on the basis of rheological elements refers to the introduction of additional internal variables to represent process dependent viscosities. Among others, this concept is applied by Hoefer (2009) to describe the amplitude dependent Payne

effect.
Coleman and Noll (1961) first extended the theory of linear viscoelasticity and provided a three-dimensional formulation of finite linear viscoelasticity which is based on convolution integrals. Nowadays, two concepts have become well accepted in the theory of finite nonlinear viscoelasticity to date. The first one is called multiplicative viscoelasticity and based on internal variable of strain. It is based on a multiplicative decomposition of the deformation gradient into elastic and inelastic parts which goes along with the introduction of an elastic-inelastic intermediate configuration. The elastic part of deformation is usually described via a specific Helmholtz free energy whereas the inelastic part of deformation is mostly represented by an evolution equation for the inelastic strain rate. The general concept of multiplicative decomposition was introduced early by Lee and Liu (1967) and Lee (1969) in the theory of finite plasticity. Among others, finite nonlinear viscoelastic formulations based on the multiplicative decomposition of the deformation gradient have been introduced by Lubliner (1985), Lion (1996), Reese and Govindjee (1998), Hartmann and Haupt (1999), Huber and Tsakmakis (1999), Lion (2000b), Middendorf (2002) or Johlitz (2008).
The second concept to describe nonlinear viscoelasticity under finite deformations is related to the early formulation by Coleman and Noll (1961) and based on the functional representation of viscoelasticity. In contrast to multiplicative viscoelasticity, this concept applies internal variables of stress and manages without an intermediate configuration. Instead of that, a specific Helmholtz free energy is defined for the overstress and the differential equations for the overstress are formulated directly. Viscoelastic models of this type are proposed, for instance, by Simo (1987), Govindjee and Simo (1992b), Holzapfel (1996), Kaliske and Rothert (1997a), Holzapfel (2000) or Haupt and Lion (2002). A comparison between selected models of both concepts of finite viscoelasticity is provided by Reese and Govindjee (1998). Since this work only deals with harmonic vibrations under small amplitudes of strain, the concept of finite nonlinear viscoelasticity will be introduced in a brief manner only.

3.4.1 Functional viscoelasticity with internal variables of the stress type

The functional viscoelasticity for finite deformations is commonly based on rate dependent functionals of strain history which are mostly expressed by means of convolution integrals. The stress is additively decomposed into an equilibrium part $\tilde{\mathbf{T}}_{eq}$ and an overstress part $\tilde{\mathbf{T}}_{ov}$

$$\tilde{\mathbf{T}} = \tilde{\mathbf{T}}_{eq} + \tilde{\mathbf{T}}_{ov} \ . \tag{3.113}$$

The equilibrium part can be related to the Green-Lagrange strain tensor $\mathbf{E}$ whereas the overstress part can be expressed via rate dependent functionals of the strain history $\mathbf{E}(s)$

$$\tilde{\mathbf{T}}_{eq} = \tilde{\mathbf{T}}_{eq}(\mathbf{E}) \ , \quad \tilde{\mathbf{T}}_{ov} = \underset{s \le t}{\mathcal{F}}[\mathbf{E}(s)] \ . \tag{3.114}$$

According to the principle of fading memory (Truesdell and Noll (1965)), the memory functional $\mathcal{F}$ must vanish for constant static histories $\mathbf{E}(s) = \mathbf{E}_0 = const.$

$$\underset{s \le t}{\mathcal{F}}[\mathbf{E}_0] \;=\; \mathbf{0} \;. \tag{3.115}$$

Instead of introducing an intermediate configuration, the differential equation is directly formulated for the inelastic overstress. In this context, a common formulation is given by

$$\dot{\tilde{\mathbf{T}}}_{ov} \;+\; \frac{1}{\tau}\,\tilde{\mathbf{T}}_{ov} \;=\; \frac{\mathrm{d}}{\mathrm{d}t}\left(2\,\frac{\partial \Psi_{ov}}{\partial \mathbf{C}}\right) \;. \tag{3.116}$$

Haupt and Lion (2002) introduce a general concept of finite nonlinear viscoelasticity which is based on functional viscoelasticity. This model can be interpreted as a generalisation of a classical Maxwell element and is shown to be compatible with the Clausius-Duhem inequality. The authors define two equivalent differential equations for the overstress which are closely related to the differential equation of a classical Maxwell element. The constitutive approach in this work is based on one of these formulations which is defined by the following differential equation for the overstress part of the 2nd Piola-Kirchhoff stress tensor

$$\dot{\tilde{\mathbf{T}}}_{ov} \;+\; \frac{1}{\tau}\,\tilde{\mathbf{T}}_{ov} \;=\; -\,2\,\mu\,\dot{\mathbf{e}} \;. \tag{3.117}$$

From this differential equation, the authors derive the constitutive equation of the 2nd Piola-Kirchhoff stress as follows

$$\tilde{\mathbf{T}}_{ov}(t) \;=\; -\,2\,\mu \int_{-\infty}^{t} \mathrm{e}^{-\frac{t-s}{\tau}}\,\mathbf{e}'(s)\,\mathrm{d}s \;. \tag{3.118}$$

It is a functional of the history of the Piola strain tensor $\mathbf{e}$ and thus a special case of the functional representation given in (3.114). In Haupt and Lion (2002), it is also shown, that a thermodynamically consistent formulation for the specific Helmholtz free energy is given by

$$\rho_0\,\Psi_{ov}(t) \;=\; -\,2\,\mu \int_{-\infty}^{t} \mathrm{e}^{-\frac{t-s}{\tau}}\,\mathbf{e}'(s) \cdot \mathbf{C}(t)\,\mathrm{d}s \;. \tag{3.119}$$

In order to represent more complicated nonlinear viscoelastic effects, such as temperature and amplitude dependent behaviour, the constitutive approach can be extended by process dependent relaxation times, which is very convenient in the theory of functional viscoelasticity. For instance, Hoefer and Lion (2009) represent the nonlinear viscoelastic effects of filler-reinforced rubber by applying relaxation times, which depend on the deformation history and the current deformation rate.

3.4.2 Multiplicative finite viscoelasticity

Multiplicative viscoelasticity is a well-known concept to describe nonlinear viscoelastic behaviour of polymers under finite deformations. A detailed description of multiplicative viscoelasticity, the following presentation refers to, is given by Johlitz (2009). The

concept is based on the multiplicative decomposition of the deformation gradient into an elastic part $\mathbf{F}_e$ and an inelastic part $\mathbf{F}_i$

$$\mathbf{F} = \mathbf{F}_e \mathbf{F}_i \ . \tag{3.120}$$

As illustrated in figure 3.13, the multiplicative split leads to an elastic-inelastic intermediate configuration $\mathcal{I}_e$.

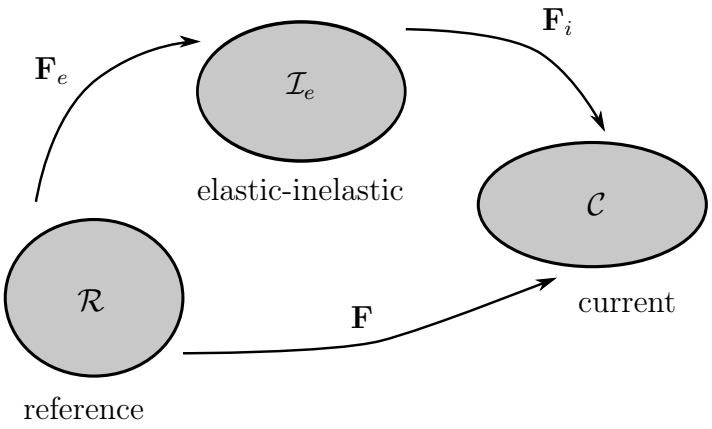

FIGURE 3.13: Elastic-inelastic decomposition with intermediate configuration

Via the elastic and inelastic parts of the deformation gradient, an inelastic right Cauchy-Green tensor $\mathbf{C}_i$ on the reference configuration and an elastic left Cauchy-Green tensor $\mathbf{B}_e$ on the current configuration can be defined by

$$\begin{aligned} \mathbf{C}_i &= \mathbf{F}_i^T \mathbf{F}_i \\ \mathbf{B}_e &= \mathbf{F}_e \mathbf{F}_e^T \ . \end{aligned} \tag{3.121}$$

Moreover, the intermediate configuration inherits its own measures of stress and strain. The strain tensor $\mathbf{\Gamma}$ operates on the intermediate configuration and can be obtained by the push forward of the Green-Lagrange strain tensor $\mathbf{E}$

$$\mathbf{\Gamma} = \mathbf{F}_i^{-T} \mathbf{E} \mathbf{F}_i^{-1} \tag{3.122}$$

or alternatively by the pull back of the Almansi strain tensor $\mathbf{A}$

$$\mathbf{\Gamma} = \mathbf{F}_e^T \mathbf{A} \mathbf{F}_e \ . \tag{3.123}$$

Based on these definitions and the relation between the Green-Lagrange strain tensor $\mathbf{E}$ and the right Cauchy-Green tensor $\mathbf{C}$ in equation (2.15), the strain tensor $\mathbf{\Gamma}$ can be additively decomposed into an elastic part $\mathbf{\Gamma}_e$ and an inelastic part $\mathbf{\Gamma}_i$ as well

$$\mathbf{\Gamma} = \mathbf{\Gamma}_e + \mathbf{\Gamma}_i \ . \tag{3.124}$$

Therein, the elastic component is given by

$$\mathbf{\Gamma}_e = \frac{1}{2} \left(\mathbf{F}_e^T \mathbf{F}_e - \mathbf{1} \right) \tag{3.125}$$

and the inelastic part reads as

$$\boldsymbol{\Gamma}_i \;=\; \frac{1}{2}\left(\mathbf{1} \;-\; \mathbf{F}_i^{-T}\,\mathbf{F}_i^{-1}\right) \;. \tag{3.126}$$

An objective rate of $\boldsymbol{\Gamma}$ can be defined via the derivative of the Green-Lagrange strain tensor $\mathbf{E}$ with respect to time

$$\overset{\triangle}{\boldsymbol{\Gamma}} = \; \mathbf{F}_i^{-T}\,\dot{\mathbf{E}}\,\mathbf{F}_i^{-1} \;=\; \dot{\boldsymbol{\Gamma}} \;+\; \mathbf{L}_i^{T}\,\boldsymbol{\Gamma} \;+\; \boldsymbol{\Gamma}\,\mathbf{L}_i \;. \tag{3.127}$$

Apart from the strain tensor $\boldsymbol{\Gamma}$, the inelastic stress tensor $\boldsymbol{\tau}_{neq}$ arises on the intermediate configuration

$$\boldsymbol{\tau}_{neq} \;=\; \mathbf{F}_i\,\tilde{\mathbf{T}}_{neq}\,\mathbf{F}_i^{T} \;=\; \mathbf{F}_e^{-1}\,\mathbf{T}_{neq}\,\mathbf{F}_e^{-T} \;. \tag{3.128}$$

In order to derive the constitutive equations from the elastic-inelastic decomposition, it is quite common to formulate the specific Helmholtz free energy and to define an evolution equation for the inelastic part of the deformation. Referring to Johlitz (2009) and regarding the current configuration, the specific Helmholtz free energy is usually decomposed into an elastic part Ψ_{eq} and an inelastic part Ψ_{neq} which are defined by deformation tensors $\mathbf{B}$ and $\mathbf{B}_e$

$$\Psi(\mathbf{B},\mathbf{B}_e) \;=\; \Psi_{eq}(\mathbf{B}) \;+\; \Psi_{neq}(\mathbf{B}_e) \;. \tag{3.129}$$

On the basis of this definition, the constitutive equation for the Cauchy stress tensor can be derived from the Clausius-Duhem inequality or from the isothermal Clausius-Planck inequality. This procedure finally results into an additive split of the Cauchy stress tensor in an elastic equilibrium stress and a non-equilibrium overstress

$$\mathbf{T} \;=\; \mathbf{T}_{eq} \;+\; \mathbf{T}_{neq} \;. \tag{3.130}$$

In Johlitz (2009), this concept is applied to the Three-parameter model. Considering this and assuming incompressible material behaviour, the Cauchy stress tensor can be defined by

$$\mathbf{T} \;=\; -\,p\,\mathbf{1} \;+\; 2\,\rho_0\,\mathbf{B}\,\frac{\partial \Psi_{eq}}{\partial \mathbf{B}} \;+\; 2\,\rho_0\,\mathbf{B}_e\,\frac{\partial \Psi_{neq}}{\partial \mathbf{B}_e} \;. \tag{3.131}$$

If a Neo-Hookean approach is applied for the equilibrium and the non-equilibrium part of the specific Helmholtz free energy

$$\Psi \;=\; \Psi_{eq}(\mathrm{I}_{\mathbf{B}}) \;+\; \Psi_{neq}(\mathrm{I}_{\mathbf{B}_e}) \;=\; \frac{1}{2}\,\mu\,(\mathrm{I}_{\mathbf{B}} - 3) \;+\; \frac{1}{2}\,\mu_e\,(\mathrm{I}_{\mathbf{B}_e} - 3) \;, \tag{3.132}$$

the Cauchy stress in (3.131) follows to

$$\mathbf{T} \;=\; -\,p\,\mathbf{1} \;+\; \mu\,\mathbf{B} \;+\; \mu_e\,\mathbf{B}_e \tag{3.133}$$

and the residual inequality is expressed by

$$\mu_e\,\mathbf{1}\cdot\left(\mathbf{F}_e\;\overset{\triangle}{\boldsymbol{\Gamma}}_i\;\mathbf{F}_e^{T}\right) \;=\; \mathbf{C}_e\,\mu_e\cdot\;\overset{\triangle}{\boldsymbol{\Gamma}}_i \geq\; 0 \;. \tag{3.134}$$

In order to satisfy (3.134), it is state of the art to introduce a relaxation time r as a proportional factor and to formulate an evolution equation for the inelastic strain rate. Taking incompressibility into account, a deviatoric formulation for the inelastic strain rate can be motivated

$$\overset{\triangle}{\boldsymbol{\Gamma}}_i = \frac{1}{r}\left[\mathbf{C}_e - \frac{1}{3}\,\mathrm{tr}(\mathbf{C}_e)\,\mathbf{1}\right] . \tag{3.135}$$

Using the pull-back of the inelastic strain rate

$$\dot{\mathbf{E}}_i = \frac{1}{2}\,\dot{\mathbf{C}}_i = \mathbf{F}_i^T\,\overset{\triangle}{\boldsymbol{\Gamma}}_i\,\mathbf{F}_i \tag{3.136}$$

and taking (3.135) into account, the evolution equation (3.135) can be reformulated in terms of the rate of the inelastic right Cauchy-Green tensor

$$\dot{\mathbf{C}}_i = 2\,\mathbf{F}_i^T\,\overset{\triangle}{\boldsymbol{\Gamma}}_i\,\mathbf{F}_i = \frac{2}{r}\,\mathbf{F}_i^T\left[\mathbf{C}_e - \frac{1}{3}\,\mathrm{tr}(\mathbf{C}_e)\,\mathbf{1}\right]\mathbf{F}_i . \tag{3.137}$$

Inserting the relations

$$\mathbf{C}_e = \mathbf{F}_e^T\,\mathbf{F}_e = \left(\mathbf{F}\,\mathbf{F}_i^{-1}\right)^T\,\mathbf{F}\,\mathbf{F}_i^{-1} = \mathbf{F}_i^{-T}\,\mathbf{F}^T\,\mathbf{F}\,\mathbf{F}_i^{-1} = \mathbf{F}_i^{-T}\,\mathbf{C}\,\mathbf{F}_i^{-1} \tag{3.138}$$

and

$$\mathrm{tr}(\mathbf{C}_e) = \mathrm{tr}\left(\mathbf{F}_i^{-T}\,\mathbf{C}\,\mathbf{F}^{-1}\right) = \mathrm{tr}\left(\mathbf{C}\,\mathbf{F}_i^{-1}\,\mathbf{F}_i^{-T}\right) = \mathrm{tr}\left(\mathbf{C}\,\mathbf{C}_i^{-1}\right) \tag{3.139}$$

into (3.137), the evolution equation finally reads as

$$\dot{\mathbf{C}}_i = \frac{2}{r}\left[\mathbf{C} - \frac{1}{3}\,\mathrm{tr}\left(\mathbf{C}\,\mathbf{C}_i^{-1}\right)\,\mathbf{C}_i\right] . \tag{3.140}$$

A very detailed description of the mentioned relations is given in the manuscript by Johlitz (2009).

3.5 Shifting principles

The viscoelastic properties of rubber-like materials are generally characterised by a pronounced dependence on temperature. For instance, stress relaxation and creep have been observed as proceeding more slowly at low temperatures and faster at high temperatures (Ferry 1980; Schwarzl 1990). Based on the connection between temperature and time as well as between temperature and frequency, the principles of time temperature and frequency temperature shifting are introduced by the theory of viscoelasticity. They are based on the assumption of thermorheological simple material behaviour meaning that the elastic parameters of the material are independent of the temperature and only the viscosities and relaxation times are influenced by temperature. Furthermore, each of the viscosities must depend on the temperature in the same manner.
Taking the assumption of thermorheological simple materials into account, the concepts of time temperature and frequency temperature shifting can be derived from

classical rheological elements. Referring to Lion (2007) and taking a Three-parameter model into account, the temperature-dependent viscosity is defined by the product of a temperature-dependent shift function $a_\theta(\theta, \theta_0)$ and the constant viscosity $\eta(\theta_0) = \eta_0$ at a constant reference temperature θ_0

$$\eta(\theta) \;=\; a_\theta(\theta, \theta_0)\, \eta_0 \;. \tag{3.141}$$

The temperature-dependent shift function is normalised and always positive

$$a_\theta(\theta_0, \theta_0) \;=\; 1 \quad , \quad a_\theta(\theta, \theta_0) \;>\; 0 \;. \tag{3.142}$$

The related relaxation time can be introduced as follows

$$\tau(\theta) \;=\; \frac{\eta(\theta)}{E} \;=\; a_\theta(\theta, \theta_0)\, \frac{\eta_0}{E} \;=\; a_\theta(\theta, \theta_0)\, \tau_0 \;. \tag{3.143}$$

By inserting (3.143) into (3.39), the differential equation of the Three-parameter model results in the temperature dependent differential equation

$$\dot\sigma \;+\; \frac{1}{a_\theta(\theta, \theta_0)\, \tau_0}\, \sigma \;=\; (E + \mu)\, \dot\varepsilon \;+\; \frac{E}{a_\theta(\theta, \theta_0)\, \tau_0}\, \varepsilon \;. \tag{3.144}$$

By assuming a constant temperature, the stress response is obtained as

$$\begin{aligned} \sigma(t) \;&=\; E\, \varepsilon(t) \;+\; \int_0^t \mu\, \dot\varepsilon(s)\, \mathrm{e}^{-\frac{t-s}{a_\theta\, \tau_0}}\, \mathrm{d}s \\ &=\; \int_0^t \left(E \;+\; \mu\, \mathrm{e}^{-\frac{t-s}{a_\theta\, \tau_0}} \right) \dot\varepsilon(s)\, \mathrm{d}s \\ &=\; \int_0^t G\left(\frac{t-s}{a_\theta} \right) \dot\varepsilon(s)\, \mathrm{d}s \;, \end{aligned} \tag{3.145}$$

wherein the temperature dependent relaxation function is expressed as

$$G(t, \theta) \;=\; G\left(\frac{t}{a_\theta(\theta, \theta_0)}, \, \theta_0 \right) \;. \tag{3.146}$$

If the relation

$$\frac{t}{a_\theta} \;=\; 10^{\log\left(\frac{t}{a_\theta}\right)} \;=\; 10^{\log t \,-\, \log a_\theta} \tag{3.147}$$

is taken into account, (3.146) can be rewritten as

$$G(t, \theta) \;=\; G\Big(10^{\log t \,-\, \log a_\theta}, \, \theta_0 \Big) \;. \tag{3.148}$$

Based on this expression, the relaxation function is shifted horizontally by the shift function $\log a_\theta$ in logarithmic time scale. Thereby, the function $a_\theta(\theta, \theta_0)$ determines the temporal scaling of the relaxation function between the reference temperature θ_0 and an arbitrary temperature θ. For $\theta > \theta_0$, the relaxation function is shifted to the left whereas temperatures below the reference temperature ($\theta < \theta_0$) result in a shift to the right. With respect to experimental investigations in a limited time or frequency

domain, this shifting technique is commonly applied to extend the domain or to reduce the experimental testing time by measuring at various temperatures.

The frequency temperature shifting principle can similarly be derived. If the temperature-dependent relaxation time (3.143) is inserted into the harmonic response of the Three-parameter model (3.58), the complex modulus follows to

$$G^*(\omega,\theta) \;=\; G^*\Big(\omega\, a_\theta(\theta,\theta_0),\, \theta_0\Big)\;. \tag{3.149}$$

Regarding the relation

$$\omega\, a_\theta \;=\; 10^{\log(\omega\, a_\theta)} \;=\; 10^{\log\omega\,+\,\log a_\theta} \tag{3.150}$$

and separating the complex modulus into its real and imaginary parts, the temperature dependent storage and loss modulus can finally be expressed by

$$\begin{aligned} G'(\omega,\theta) \;&=\; G'\Big(a_\theta(\theta,\theta_0)\,\omega,\theta_0\Big) \;=\; G'\Big(10^{\log\omega\,+\,\log a_\theta},\theta_0\Big)\;,\\ G''(\omega,\theta) \;&=\; G''\Big(a_\theta(\theta,\theta_0)\,\omega,\theta_0\Big) \;=\; G''\Big(10^{\log\omega\,+\,\log a_\theta},\theta_0\Big)\;. \end{aligned} \tag{3.151}$$

Similar to the time temperature shifting principle, both moduli can be shifted horizontally by the shift function $\log a_\theta$ in the logarithmic frequency scale. In terms of temperatures above the reference temperature ($\theta_1 > \theta_0$), both moduli are shifted to lower frequencies whereas lower temperatures ($\theta_2 < \theta_0$) result in a shift to higher frequencies. With respect to experimental investigations, the frequency temperature shifting technique is a powerful tool to extend the experimental limited frequency range to a broader one. The extended characteristics of the dynamic moduli are called master curves.

3.5.1 Master curves

As already mentioned in the previous section, the great benefit of the shifting principles consists in the possibility of accelerating time-consuming relaxation or creep tests or extending the experimentally limited frequency range to a broader one by measuring at different temperatures and generating a master curve. These master curves can be obtained by applying the shifting principles to the experimental data at different temperatures. In this work, the temperature frequency shifting principle is applied to extend the experimental frequency range to lower and higher frequencies. In order to obtain the master curves, the shift function $\log a_\theta$ is represented by the so-called WLF-function (Williams et al. 1955)

$$\log a_\theta \;=\; \frac{c_1\,(\theta\;-\;\theta_0)}{c_2\;+\;(\theta\;-\;\theta_0)}\;, \tag{3.152}$$

with the material parameters c_1 and c_2. In principle, the application of the WLF-function is limited to temperatures above the glass transition temperature, but there are various modifications to extend the applicable temperature range to lower temperatures

than the glass transition. For more details, the reader is referred to Schwarzl and Zahradnik (1980) or Klueppel (2008). If the shift function is determined, the frequency temperature shift can be applied to the experimental data to generate the master curve by horizontal shifting in the logarithmic frequency scale. An illustration of the shifting procedure with respect to the storage modulus at different temperatures $\theta_3 > \theta_2 > \theta_0 > \theta_1$ with reference temperature θ_0 is provided in figure 3.14.

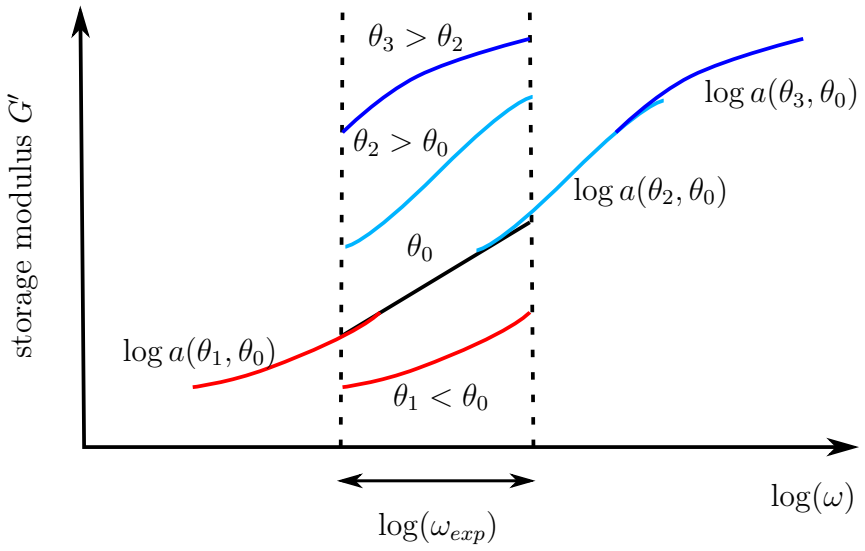

FIGURE 3.14: Master curve of storage modulus obtained by temperature frequency shifting

Chapter 4

Basics of elastomer materials

Introduction

The conventional term "rubber" generally denotes the material class of elastomers. In this, one can distinguish between natural rubber which is obtained by the natural product latex and synthesised rubbers which are artificially produced by polymerisation, polycondensation or polyaddition.
Due to their excellent mechanical properties, elastomer materials are frequently used in industrial applications. Thereby, the main focus is on their unique elastic properties which radically differ from those of other solid materials. Whilst the elastic deformation range of metals is generally limited to very small strains, elastomers are characterised by a huge capability to resist large deformations which can exceed much more than 100 % of strain. Apart from this behaviour, rubber materials exhibit the great benefit that their mechanical properties like stiffness or abrasion resistance can easily be controlled by the addition of different filler-types, such as silica or carbon-black, such that they can be designed for special technical applications. Thereby, one can distinguish between reinforcing active fillers which are commonly added to enhance the mechanical properties and inactive fillers which are mainly used to improve processability.
With respect to industrial applications, elastomer materials are especially applied in the tyre industry as well as in the automotive industry in which they are frequently applied as mounting systems for car engines. Whilst the tyre industry especially focuses on low abrasion resistance and high road adhesion, the automotive industry aims at isolating the vibrations produced by the running engine to prevent the vibrations from being transferred into the passenger cell.

Outline

This work is focused on the experimental investigation, constitutive modelling and finite element simulation of filler-reinforced rubber. Hence, it is essential to first characterise the material and its mechanical properties. On this basis, suitable experiments can be carried out and, subsequently, an adequate constitutive model can be derived to represent the observed material characteristics. For this reason, the aim of this chapter

is to provide an overview of the basics of elastomer materials and rubber compounds which form the basis of this work:

- natural rubber with 40 phr amount of carbon-black (NR40),
- styrene-butadiene rubber with 20 phr and 40 phr amount of carbon-black (SBR20 and SBR40),
- ethylene-propylen-diene rubber with 20 phr amount of carbon-black (EPDM20).

The focus of the following presentation is the classification and composition of elastomers, their mechanical properties, and the main areas of application. Thereby, the following presentation mostly refers to the detailed descriptions given in the textbooks by Michaeli (2006), Röthemeyer and Sommer (2006) and Schwarz and Ebeling (2007). For a comprehensive overview of the physics and mechanics of polymers, the reader is also referred to the textbooks by Tobolsky (1967), Schwarzl (1990), Ehrenstein (1999) or Sperling (2006).

4.1 Classification of elastomers

As presented in the textbooks by Röthemeyer and Sommer (2006) and Schwarz and Ebeling (2007), elastomer materials belong to the main class of polymers. These are organic compounds which mainly consist of carbon and hydrogen atoms which are connected to molecular chains. They are mostly obtained from the resource crude oil by polymerisation, polycondensation or polyaddition. The carbon and hydrogen atoms are combined to macro molecules which can be cross-linked by physical or chemical bonds. Due to the different degree of cross-linking, polymer materials are characterised by a huge diversity between their chemical and physical properties, such as mechanical stiffness, strain resistance, fusibility, solubility or swelling. Since these properties mostly depend on type and degree of cross-linking of the chain molecules, polymers are usually subclassified on the basis of this relation. Regarding this, polymer materials are usually divided into thermoplastics, elastomers and duromers. The general structure and properties of these types will shortly be introduced in this section. A detailed description is provided by Röthemeyer and Sommer (2006) and Hoefer (2009).

Thermoplastics

Thermoplastics are branched chain molecules which are merely cross-linked by weak physical bondings. Due to the absence of stronger covalent cross-links, thermoplastics are fusible and thus processable by injection moulding and extrusion. Furthermore, one can distinguish between amorphous and semi-crystalline thermoplastics. Amorphous thermoplastics are characterised by an orderless distribution of their macro molecules whereas the macro molecules of semi-crystalline thermoplastics exhibit a certain degree of arrangement. In contrast to amorphous thermoplastics which are easy fusible, the

fusibility of semi-crystalline thermoplastics decreases with increasing degree of crystallisation.

Elastomers

Elastomers are weakly cross-linked chain molecules which are neither fusible nor soluble, but strongly capable of swelling. Based on the weak cross-linking, the macro molecules of elastomers are very flexible which finally results in the unique elastic deformability of the material. In general, one can distinguish between natural rubber and synthesised rubbers which are mostly enhanced by active filler particles to guarantee suitable mechanical properties. The characteristic glass transition temperature T_g of elastomers is typically located below 0°C. Below this temperature, the macro molecules are in a frozen state and loose their flexibility. In Röthemeyer and Sommer (2006), the temperature dependent mechanical behaviour of elastomers is described by means of the shear modulus. Referring to this presentation, one can distinguish between four characteristic temperature regions in which the mechanical properties of elastomers significantly change. These are illustrated in figure 4.1 by means of the temperature dependent shear modulus.

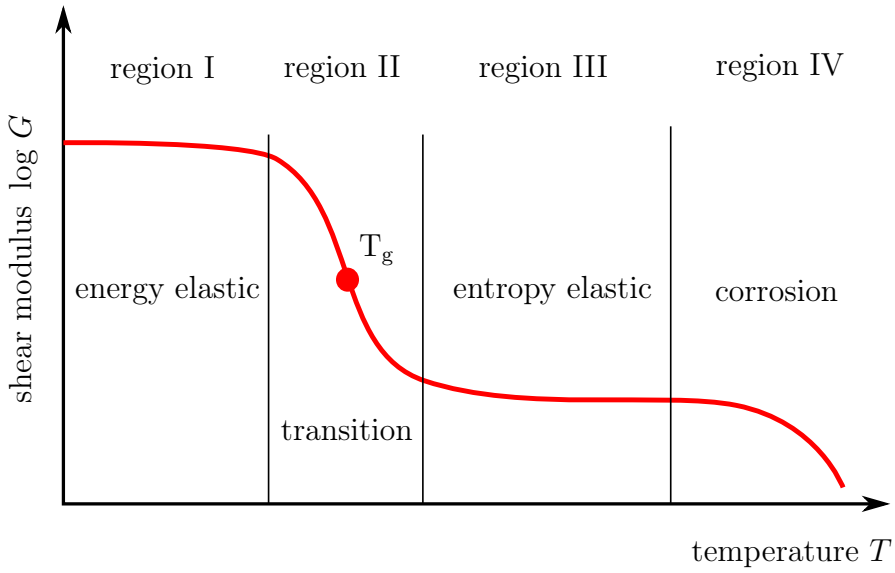

FIGURE 4.1: Temperature dependence of the shear modulus of elastomers (cf. Röthemeyer and Sommer (2006))

The first region is located at very low temperatures below the glass transition temperature and denotes the energy-elastic area. In this region, the molecular chains are in a frozen glassy state meaning that they are hindered from moving and thus not flexible. Consequently, the material looses its typical elastic properties and is characterised by huge stiffness below the glass transition temperature. If the temperature is raised, the flexibility of the molecular chains increases, which subsequently results in a softening of the material.
The second region is the glass transition area in which the material fades from the

energy-elastic state to the entropy-elastic state. In this area, the shear modulus is characterised by a pronounced decrease with increasing temperature. Thereby, the point of inflexion is usually defined as the characteristic glass transition temperature T_g.
The third region is the entropy-elastic area which characterises the commonly rated range of use. In this region, the molecular chains exhibit high flexibility such that elastomers adopt their typical elastic properties with increasing temperature. In contrast to the energy-elastic region at very low temperature, the dynamic mechanical behaviour is characterised by low storage and loss moduli at the entropy-elastic area.
The last region is located at very high temperatures and defines the area of corrosion. In this region, the heat resistance of elastomers is exceeded by temperature which results in a destruction of their molecular chains and thus in a loss of the material's stiffness. Based on these temperature dependent characteristics, the technically relevant operating area of rubber is usually located between the glass transition temperature and the decomposition temperature. More details about these temperature dependent characteristics are provided by Röthemeyer and Sommer (2006).

Duromers

In contrast to thermoplastics and elastomers, duromers are composed of strongly cross-linked chain molecules. They are linked via strong covalent bonding and thus reveal a lack of flexibility. Moreover, duromers are characterised by considerable stiffness at room temperature, non-fusibility, non-solubility and non-swellability. In comparison to elastomer materials, the glass transition temperature of duromers is usually located above room temperature and the technically relevant operating area is commonly below the glass transition temperature.

4.2 Mechanical properties

In contrast to other solid materials, such as thermoplastics or metals, elastomers are characterised by unique mechanical properties. As described by Röthemeyer and Sommer (2006) in detail, rubber-like materials are comparatively soft and exhibit a relatively small Young's modulus which is commonly located between 10^{-1} MPa and 10^2 MPa. Moreover, due to the high flexibility of the molecular chains, elastomers are characterised by excellent elastic properties and can resist huge deformations exceeding more than 100 %. For comparison, thermoplastics and metals possess a Young's modulus of 10^3 - 10^4 MPa respectively 10^5 MPa and are therefore much stiffer than rubber. Furthermore, the elastic deformability of thermoplastics and metals is limited to 10 % respectively 1 % of strain and is thus comparatively small.
Apart from their excellent elastic deformability, the material behaviour of elastomers is determined by numerous complex nonlinear effects, especially if the material is reinforced by filler particles. Apart from the nonlinear stress-strain relation, especially under finite deformation, rubber is characterised by several viscoelastic effects, such as rate and frequency dependence, stress relaxation or creep. Especially in terms of

filler-reinforced rubber, pronounced stress-softening phenomena, such as the Mullins effect (Mullins 1948) or the amplitude dependent Payne effect (Payne 1962a) can be observed.
In order to understand the nonlinear behaviour of elastomer materials, the general characteristics of elasticity and viscoelasticity as well as the Mullins and the Payne effect are described in the following. A detailed description of these phenomena and several other physical and mechanical properties of elastomers is provided in fundamental textbooks, e.g. Tobolsky (1967), Ehrenstein (1999). Michaeli (2006), Röthemeyer and Sommer (2006), Sperling (2006) or Schwarz and Ebeling (2007).

4.2.1 Elasticity & hyperelasticity

The elastic properties of elastomers are physically related to the high flexibility of the weakly cross-linked molecular chains and mainly result from changes in the entropy during loading and unloading of the material. In the undeformed state, the material is in its equilibrium meaning that the molecular chains are in a preferred state which is defined by maximum entropy. If external deformations are applied, the flexible molecular chains start moving and adopt a new spatial configuration which differs from the equilibrium. Due to this, the preferred state of maximum entropy is abandoned and the externally delivered work is stored as energy inside the material. A subsequent unloading of the material results in a release of the stored energy and thus in a return to the equilibrium state.
In general, the elastic material behaviour of rubber is linear in a limited range of deformations only which is typically located below 10 % of strain. Especially under finite deformations, elastomers exhibit a nonlinear relation between stress and strain which is mainly caused by material and geometrical nonlinearities. If the stress-strain relation can be calculated by differentiation of an energy function with respect to deformation, such as the specific Helmholtz free energy, this phenomenon is called hyperelasticity. An illustration of the nonlinear stress-strain relation is provided in figure 4.2.

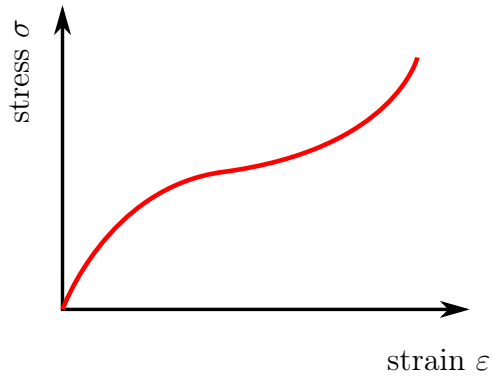

FIGURE 4.2: Nonlinear stress-strain relation of elastomers

4.2.2 Viscoelasticity

As presented in chapters 1 and 3, the mechanical properties of elastomers are characterised by pronounced time, rate and frequency dependences. These properties are classified as viscoelastic effects which mainly arise from simultaneous running of elastic and viscous processes. As explained by Röthemeyer and Sommer (2006), the elastic behaviour is based on the storage of energy during the loading process and a subsequent release of this energy during unloading whilst the viscous phenomena are physically related to the dissipation of energy. Characteristic viscous phenomena of elastomers are stress relaxation, retardation, rate or frequency dependence, hysteresis, damping effects or self heating.
From a physical point of view, the viscoelastic behaviour of elastomers can be explained by the fact that the molecular chains need a certain amount of time to change their position and are thus unable to instantly follow an applied deformation.
Regarding relaxation tests, the typical viscoelastic stress relaxation can be observed if the material is loaded with a certain amount of strain which is held constant over time. Since the molecular chains are unable to directly follow the deformation, the stress response temporally decreases until the material reaches its equilibrium state (figure 4.3).

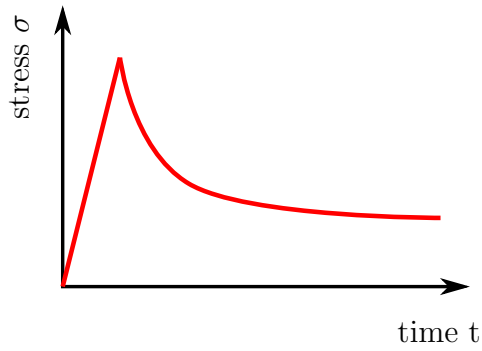

FIGURE 4.3: Viscoelasticity: stress relaxation of elastomers

In order to study the rate or frequency dependent properties of elastomers under dynamic loadings, it is common practice to use dynamic mechanical analysis (Menard 1999). This technique is also applied in the current work to study the influence of predeformation and frequency on storage and loss modulus. The material is deformed with a harmonic excitation and its response is evaluated by means of the dynamic moduli in the frequency domain. Thereby, the storage modulus can be interpreted as a measurement of the material's stiffness and the loss modulus can be described as a measurement of the dissipated energy. Based on this procedure, it is found that the storage modulus increases with increasing frequency (Sjoeberg and Kari 2003; Lion et al. 2009; Rendek and Lion 2010a; Suwannachit and Nackenhorst 2010), whereas the loss modulus reveals sigmoidal characteristics with a maximum at middle frequencies. Furthermore, the dynamic properties are observed to be more or less dependent on the static preload (Kim and Youn 2001; Kari 2003; Rendek and Lion 2010b), which seems to be related to the hyperelastic behaviour (Hoefer and Lion 2009). For illustration, the

frequency dependent characteristics of the storage and the loss modulus are displayed in figure 4.4.

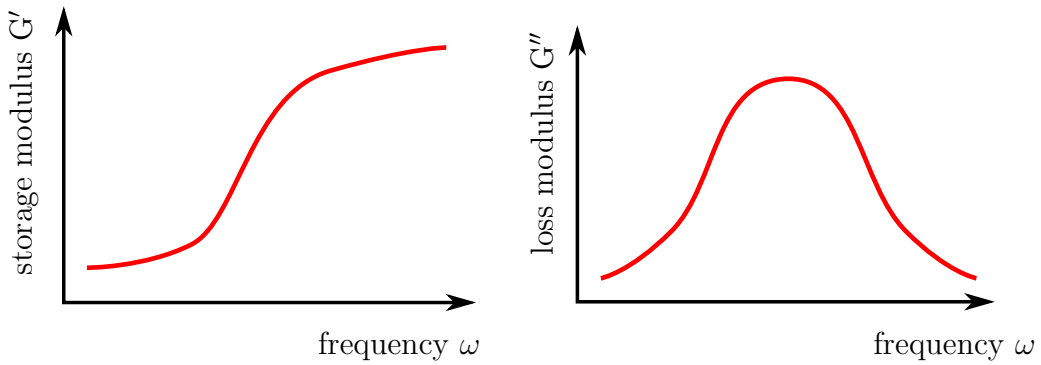

FIGURE 4.4: Viscoelasticity: frequency dependence of the dynamic moduli

4.2.3 Mullins effect

The Mullins effect is a strain-induced stress-softening phenomenon of virgin material which is mostly observed during the first loading cycle (Mullins 1948). It was found, that this softening effect depends on the maximum amount of strain in the loading history and is irreversible at moderate temperatures (Mullins 1950; Bueche 1961; Mullins 1969). Moreover, softening is observed in the case of unfilled and filler-reinforced rubber, but more pronounced for filler-loaded vulcanisates (Mullins 1950; Harwood et al. 1965; Harwood and Payne 1966). On the basis of these observations, stress-softening is mostly related to changes in the rubber matrix which mainly result from a breakdown of weak chemical bonds. The enhanced pronunciation of the Mullins effect in terms of filler-reinforced vulcanisates is due to the presence of the filler and can physically be related to an increase in the local deformation of the rubber matrix such that the material is in a state of higher deformation (Harwood et al. 1965; Mullins and Tobin 1965; Harwood and Payne 1966). Mathematically, this interpretation can be described by the strain-amplification factor which was proposed by Mullins and Tobin (1965).
For illustration, a schematic presentation of the Mullins effect is given in figure 4.5 as an example. The red coloured stress paths σ_{01}, σ_{02} and σ_{03} are virgin stress paths whereas the blue coloured stress paths σ_{D1}, σ_{D2} and σ_{D3} are damaged ones. If the virgin material is first loaded to strain ε_1 virgin stress response represented by path σ_{01} is obtained. Since the material has been damaged during this first loading, further loadings to strain ε_1 lead to a decreased stress response which is described by damage path σ_{D1}. If the strain is increased from ε_1 to ε_2, the material response is defined by virgin path σ_{02} because only strain ε_1 was reached in the history of the deformation. Due to further damage of the material in the previous loading, a second loading from zero strain to strain ε_2 then results in damaged stress path σ_{D2} and so on.

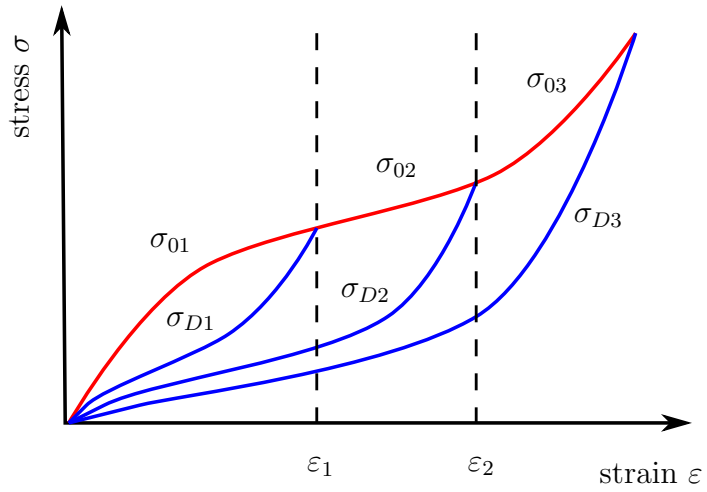

FIGURE 4.5: Exemplary illustration of the Mullins effect

4.2.4 Payne effect

The Payne effect is an amplitude dependent softening of filler-reinforced rubber which occurs under dynamic loadings. The effect was investigated early by Gehman et al. (1941) and Gehman (1942) and appears as a decrease of the material's dynamic stiffness with an increasing dynamic amplitude of strain. Whilst the storage modulus decreases with increasing dynamic strain, the loss modulus exhibits a pronounced maximum at middle strain amplitudes (Fletscher and Gent 1953; Payne 1961; Payne 1962a) and (Payne 1962b). It is observed that amplitude dependent softening is not present at arbitrary dynamic strains. At very small and high amplitudes of strain, the dynamic stiffness remains constant and amplitude dependent effects vanish (Payne 1960; Payne 1962a) and (Ulmer et al. 1974).
In contrast to the Mullins effect, the Payne effect is only present for filler-reinforced rubber vulcanisates. Moreover, the amplitude dependent softening was found to be strongly dependent on the amount, the size and the type of filler particles and to be more pronounced for high amounts and small sizes of filler particles (Gehman 1942; Payne 1974; Dannenberg 1975; Dutta and Tripathy 1992; Wang and Robertson 2005; Rendek and Lion 2010b). Furthermore, it is observed that the phenomenon is completely reversible (Gehman 1942; Fletscher and Gent 1953; Hoefer 2009; Rendek and Lion 2010b). For illustration, the amplitude dependent characteristics of the Payne effect are displayed in figure 4.6 for different amounts of filler particles.

A physical interpretation of the Payne effect is given by Lion and Kardelky (2004). The authors state, that the decrease of the storage modulus with increasing amplitude of strain is due to a decrease in the number of intact filler bonds at higher values of strain. The loss modulus is proportional to the breakage rate of the filler bonds which is on the other hand, proportional to the number of intact filler bonds. At small dynamic strains, the filler bonds are intact such that the loss modulus first increases with the dynamic amplitude of strain. After reaching its maximum value at middle strains, at which the breakdown and reformation of the filler network reaches its maximum, the loss modulus decreases again which is due to the breakdown of the filler network and the considerable reduction of filler bonds.

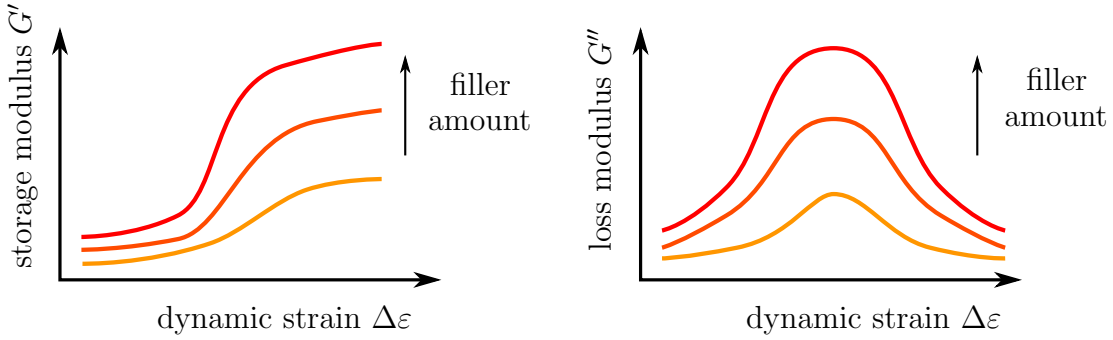

FIGURE 4.6: Exemplary illustration of the Payne effect

4.3 Natural rubber (NR)

The definition "natural rubber" includes a wide spectrum of different elastomer materials which are directly extracted from nature. As described in the detailed presentation by Schwarz and Ebeling (2007), the raw material of natural rubber is the juice of rubber trees which is usually called "latex". From this resource, natural rubber is mainly obtained by special flocculation and drying processes. Since latex is a natural product, the properties of processed natural rubber are strongly dependent on the production area and preparation process. Thus, natural rubber is divided into numerous different types, such as the popular and high quality "Standard Malaysian Rubber".
As illustrated in figure 4.7, natural rubber is based on polymeric bonds of isoprene molecules. This composition exhibits reactive double bonds which enable for a cross-linking of natural rubber with sulphur or peroxide, but they also make the material susceptible for an accumulation of ozone and oxygen. Therefore, natural rubber has to be stabilised by anti-ageing agents to avoid early ageing phenomena. For more details about natural rubber, its composition, mechanical properties and application, the reader is referred to the textbooks by Röthemeyer and Sommer (2006) and Schwarz and Ebeling (2007).

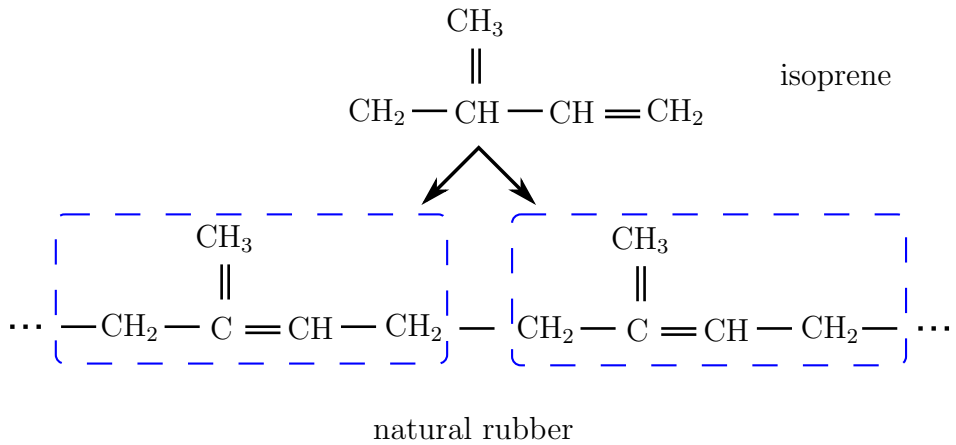

FIGURE 4.7: General composition of natural rubber

4.3.1 Properties

From a mechanical point of view, unfilled natural rubber is, compared to unfilled synthesised rubbers, characterised by high mechanical stiffness. As presented by Röthemeyer and Sommer (2006) and Schwarz and Ebeling (2007), the mechanical stiffness of the material is influenced by strain-induced crystallisation effects which take place under extremely large deformations in the progressive region of the stress-strain curve. Furthermore, the material features high elasticity and elongation at fracture, excellent tear growth and shock resistance as well as low permanent set after deformation. With respect to dynamic mechanical loadings, natural rubber exhibits low hysteresis effects, a low loss factor and a small amount of self-heating. Its thermal properties are characterised by low heat resistance, but excellent cold flexibility. On this basis, the application range of natural rubber typically reaches from about -50°C up to 70°C.
Due to its poor resistance against weather, ozone, oxygen and ultraviolet light, natural rubber is characterised by pronounced ageing phenomena and must therefore be stabilised by protecting agents.
Moreover, the material tends to low swelling effects in water and reveals good resistance against polar solvents, such as alcohol, ester or ketones whereas its resistance against unpolar solvents, such as oil and fuel, is to the contrary. A detailed description of the mentioned properties is provided by Röthemeyer and Sommer (2006) and Schwarz and Ebeling (2007).

4.3.2 Area of application

Due to the large number of attractive physical properties, natural rubber is used in many applications. With regard to its good dynamic mechanical properties, such as the relatively low loss factor and low self-heating effects, natural rubber is commonly used in dynamic mechanical applications. Based on this, the material is frequently used in the tyre industry as well as for decoupling applications in the form of rubber-metal elements, engine mounts or bridge mounts. In fact, natural rubber was often used as all-purpose rubber in the past, but nowadays it is more and more replaced by synthesised compounds which are mostly developed for special applications.

4.4 Styrene-butadiene-rubber (SBR)

In contrast to natural rubber, styrene-butadiene rubber is a synthetic rubber which is commonly used in various industrial applications. As illustrated in figure 4.8, the material is generally made up by the co-polimerisation of butadiene and styrene.

As described by Michaeli (2006), Röthemeyer and Sommer (2006) and Schwarz and Ebeling (2007), SBR is mostly manufactured by emulsion or solution polymerisation. SBR vulcanisates obtained from emulsion polymerisation are shortly called E-SBR and preferred by industry. Regarding this type, a distinction can be drawn between hot rubber which is polymerised at high temperatures of about 50°C and cold rubber

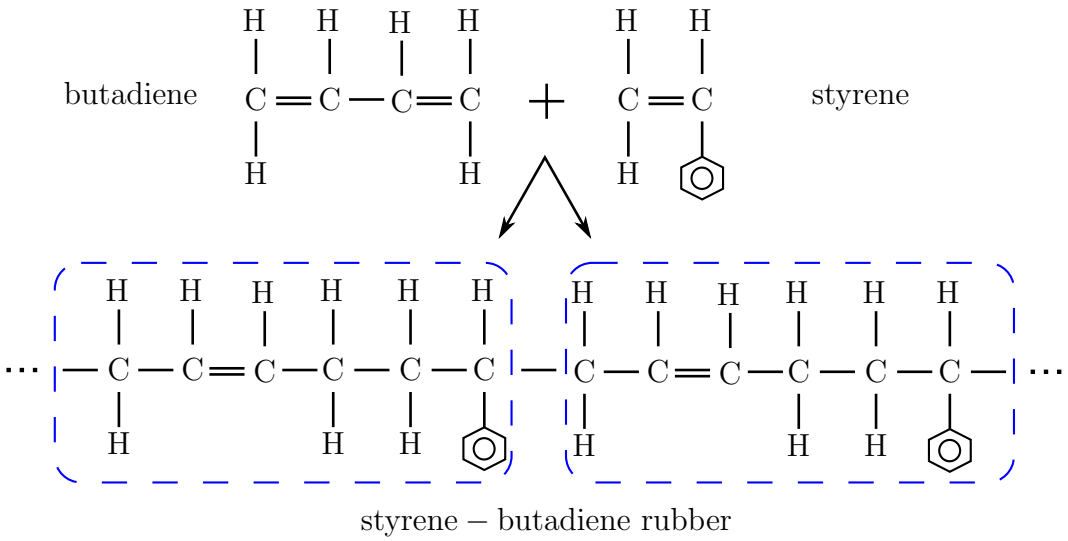

FIGURE 4.8: General composition of SBR

which is polymerised at low temperatures of about 5°C. In comparison to hot rubber, cold rubber offers the benefit of a low molecular weight which simplifies subsequent processing of the material. Due to its good processability, cold rubber is much more accepted in the industry today. Apart from emulsion polymerisation, only a little amount of SBR is produced by solution polymerisation. This type is called L-SBR, but not much preferred by the industry.

4.4.1 Properties

The mechanical properties of SBR are strongly dependent on the amount of styrene. Normally, SBR with 23.5 % amount of styrene is used in industrial applications. Types with a lower amount of styrene exhibit a lower glass transition temperature, lower self-heating, higher elasticity and higher abrasion resistance whereas the properties of compounds with a higher amount of styrene are opposite (cf. Röthemeyer and Sommer (2006)).
In contrast to natural rubber, SBR is characterised by low stiffness and tensile strength, especially in the unfilled state. Thus, the addition of filler particles is required to enhance its mechanical properties. Thereby, it is common practice to add high active fillers, such as carbon-blacks. Under dynamic mechanical loadings, SBR reveals a slightly greater amount of self-heating than natural rubber whereas its temperature resistance exists below 110°C and is therefore much better than that of NR. With a glass-transition temperature of -50°C, the operating area of SBR ranges from -50°C up to 110°C.
With respect to ageing phenomena, SBR is characterised by moderate resistance against weather phenomena, ageing and ozone, but its resistance can extensively be enhanced by the addition of protecting agents. Beyond this, the material is chemically resistant against unpolar solvents, weak acids and bases but tends to swell in oil and fuel. A comprehensive overview about the mentioned properties is given by Röthemeyer and Sommer (2006) and Schwarz and Ebeling (2007).

4.4.2 Area of application

Based on the cheapness of the raw material, SBR is frequently used in a broad range of applications. The major area of application is located in the tire industry. Besides this field, the material is also used for rubber tubes, conveyor bands and several other technical applications.

4.5 Ethylene-propylene-diene rubber (EPDM)

Similar to SBR, ethylene-propylene rubber is a synthetic type of rubber which is based on ethylene-propylene rubber (EPM). As described by Schwarz and Ebeling (2007), this type is mainly obtained by the co-polymerisation of ethylene and propylene and has no double bondings such that cross-linking with sulphur or peroxide is not possible without modification. For illustration, the chemical composition of EPM is displayed in figure 4.9.

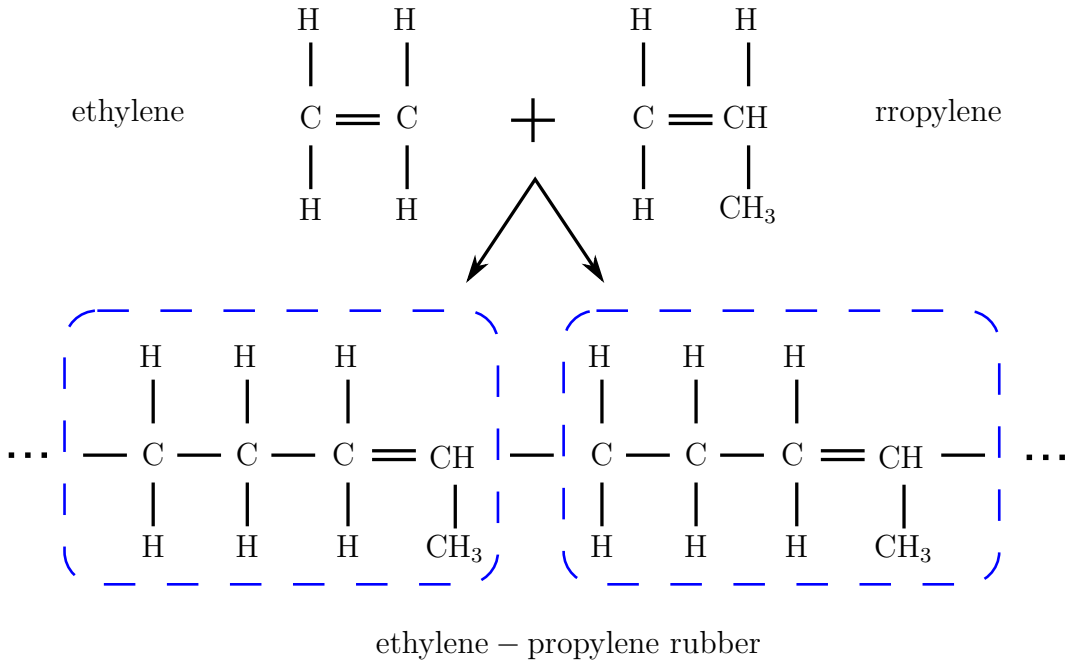

FIGURE 4.9: General composition of EPM

On the basis of EPM, EPDM is then obtained by the addition of another terpolymer, usually diene. This addition then results in the build up of reactive double bonds which allows for a cross-linking of EPDM with sulphur or peroxide.

4.5.1 Properties

The mechanical properties of EPDM vulcanisates are strongly dependent on the amount of ethylene. A detailed description of this relationship is provided by Röthemeyer and

Sommer (2006) and Schwarz and Ebeling (2007). Generally, higher amounts of ethylene cause an increase in crystallinity and thus result in an increase of the material's stiffness. On the other hand, the mechanical properties at low temperatures are degraded with increasing amount of ethylene. Based on the concentration of ethylene, the material can be classified into amorphous, semi-crystalline and crystalline types.
Lower ethylene concentrations between 45 % and 55 % result in amorphous polymers which exhibit low mechanical stiffness. These types must be reinforced by filler particles, such as carbon-black, to guarantee good mechanical properties.
In the case of middle concentrations of ethylene, which are typically located between 55 % and 65 %, semi-crystalline polymer types arise. These types reveal a partly crystalline structure and are characterised by higher stiffness in the unfilled state.
Crystalline EPDM types are characterised by very high concentrations of ethylene between 65 % and 75 % and thus exhibit much higher mechanical stiffness than the amorphous or semi-crystalline ones (cf. Röthemeyer and Sommer (2006)).
Apart from mechanical stiffness, the mechanical properties of EPDM are characterised by high elasticity, low permanent set and good tear growth resistance which is comparable to that of NR. But similar to SBR vulcanisates, amorphous and semi-crystalline EPDM types require the addition of filler particles to improve their mechanical properties.
With respect to temperature, the cold flexibility of EPDM also depends on the amount of ethylene. Amorphous EPDM types with a smaller amount of ethylene reveal a better behaviour at low temperatures and exhibit good flexibility down to -40°C. The material's resistance against high temperatures is quite good below 135°C in terms of sulphur cross-linked types, whereas peroxide cross-linked types are resistant against heat up to 150°C (cf. Röthemeyer and Sommer (2006)).
In contrast to NR or SBR, EPDM exhibits good resistance against weather, ozone and ultraviolet light such that ageing phenomena are not really pronounced. Beyond this, the material is characterised by good resistance against steam and hot water, weak acids and bases, acetones, alcohol, ketones and hydraulic liquids, but its resistance against oil and fuel is only weakly pronounced. A detailed description of the mentioned relations is provided by Röthemeyer and Sommer (2006) and Schwarz and Ebeling (2007).

4.5.2 Area of application

EPDM vulcanisates are used in a wide range of applications, mostly blended with other polymers. The major area of application are profiles, cable coatings, insulations and conveyor bands. Apart from these, the material is also applied in the car industry in the form of gaskets, tyre compounds or coolant hoses.

Chapter 5

Experimental investigations

Introduction

Although experimental investigations are more and more replaced by powerful simulation methods these days, they are indispensable to first characterise the physical and mechanical properties of the material. This is due to the fact that a comprehensive knowledge about the material behaviour under specified circumstances is an essential requirement to formulate suitable constitutive models from which powerful and efficient simulation methods can be developed. Regarding this point of view, experimental tests form the basis for a mathematical description of materials and will therefore be indispensable to perform efficient simulations. Moreover, experimental data is necessary to identify the unknown material parameters of the underlying constitutive model by suitable identification algorithms.

Outline

The focus of this chapter is on the experimental investigations carried out to characterise the predeformation and frequency dependent properties of the following four carbon-black filled rubber vulcanisates:

- styrene-butadiene rubber with 20 phr amount of filler (SBR20),
- styrene-butadiene rubber with 40 phr amount of filler (SBR40),
- ethylene-propylene-diene rubber with 20 phr amount of filler (EPDM20),
- and natural rubber with 40 phr amount of filler (NR40).

Due to the considered loading condition of constant static predeformation and superimposed harmonic vibration, the mechanical behaviour of these materials is investigated through quasi-static and dynamic tests.
The quasi-static investigations mainly focus on the equilibrium stress response of the

material which is characterised in stepwise relaxation tests at various values of deformation.
The dynamic experiments concentrate on the predeformation and frequency dependent characteristics of the storage and the loss modulus. These investigations are performed via dynamic mechanical analyses (Menard (1999)) and are closely related to the real loading situation of mounting systems. Hence, the material is loaded with various constant predeformations which are superimposed by harmonic vibrations of small amplitudes and varying frequency. Since the dynamic mechanical analyses are experimentally limited to a maximum frequency of 100 Hz, the frequency range is extended by applying the temperature frequency shifting technique (Williams et al. (1955), Ferry (1980), Schwarzl (1990)) to cover the broad frequency range of interest up to 10^5 Hz. To characterise the relation between temperature and frequency dependence of the dynamic moduli and to apply the temperature frequency shifting technique, the dynamic measurements are performed at different temperatures. Since the operating area of elastomer materials is determined by the entropy elastic range, the glass transition temperature is first determined by the differential scanning calorimetry. This step is necessary to ensure that the dynamic mechanical analyses are performed above the glass transition temperature.

With regard to the loading condition of engine mounts, stress-softening or amplitude dependent phenomena, such as the Mullins effect (Mullins (1948), Bueche (1961)) or the Payne effect (Payne (1962a), Fletscher and Gent (1953)), are not considered in this work. This is due to the assumption that typical mounting systems are already preloaded after assembly such that the material is preconditioned and no further Mullins softening appears. Moreover, the vibrations which occur during driving operations are of very small amplitudes such that the amplitude dependent Payne effect, known to be absent at very small dynamic strains (Payne (1960), Payne (1962a)), can be omitted.
In order to confirm these assumptions with respect to the underlying materials and the considered loading condition, the presence of both effects is studied through preliminary investigations.

Based on the experimental tests, this chapter is divided into three main sections. The first one deals with differential scanning calorimetry, the second section is concerned with the quasi-static experiments and the last one focuses on the dynamic mechanical analyses. The presentation of each section includes a description of the technical test equipment, the applied testing procedures, as well as the experimental findings.

It is pointed out, that some parts of the experimental investigations have been published in prior printed publications which were approved by the university (Wollscheid and Lion (2012), Wollscheid and Lion (2013a), Wollscheid and Lion (2013b) and Wollscheid and Lion (2014)).

5.1 Differential scanning calorimetry

Differential scanning calorimetry is a commonly used method to characterise chemical and physical phenomena which are influenced by temperature variations. These include melting, crystallisation, glass transition, heat capacity as well as other calorimetric data.
In this work, the differential scanning calorimetry is carried out to determine the glass transition temperature of the investigated carbon-black filled vulcanisates. This knowledge is essential to ensure that the subsequent dynamic mechanical analyses are performed above the glass transition temperature. Since the operating area of elastomers is located above the glass transition temperature, this temperature is adequate to define the lower temperature limit of the dynamic mechanical tests.

DSC testing device

The glass transition temperature is determined by the differential scanning calorimeter Maya of Netsch Gerätebau GmbH. As illustrated in figure 5.1, the system consists of a small chamber with two pans.

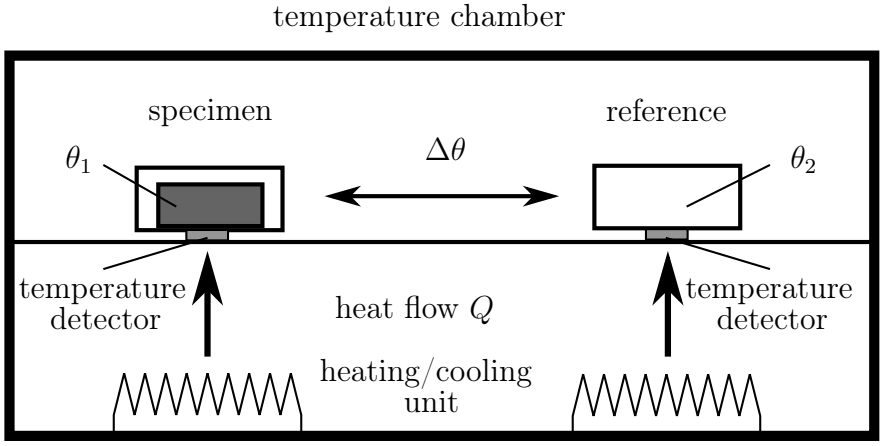

FIGURE 5.1: Illustration of the DSC measuring principle

One of the pans contains the specimen to be investigated whereas the other one is used as a reference which is usually calibrated by a sapphire specimen. Via a heating-/cooling unit, controlled temperature processes can be applied to the two pans. Since the pans are characterised by different heat capacities, a temperature difference arises between them. This difference is captured by super sensitive temperature detectors placed below the pans. Thereby, the temperature difference is measured as a function of the time and can be related to a differential heat flow rate on which basis the calorimetric behaviour of the specimen can be commented on. For a detailed overview of differential scanning calorimetry, the reader is referred to the textbook by Flammersheim et al. (2003).

5.1.1 Glass transition temperature

In order to determine the glass transition temperature, the specimen is first cooled from room temperature down to -100 °C and then heated up to 20 °C with a heating rate of 10°C/min. Through this procedure, the glass transition temperature can be determined by the specific heat flow rate which is captured during the heating process. For illustration, the specific heat flow rate over temperature is displayed in figure 5.2 in terms of the SBR40 vulcanisate.

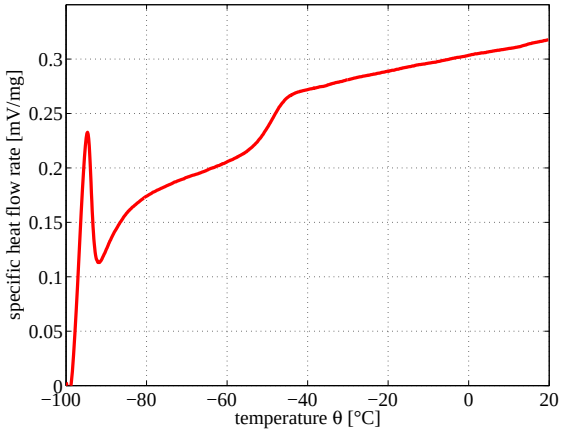

FIGURE 5.2: Specific heat flow rate of SBR40 over temperature

On the basis of this representation, a transition area between -60 °C and -40 °C can be observed in which the specific heat flow rate significantly increases. In this area, the mobility of the polymer chains starts to increase due to the rising temperature such that the material migrates from the glassy to the elastic state. Based on this characteristic, it is common to determine the glass transition temperature by the turning point of the curve. In so doing, the results of the glass transition temperature of each material finally obtained are listed in table 5.1.

SBR_{20}	-46,6 °C
SBR_{40}	-48,6 °C
$EPDM_{20}$	-49,9 °C
NR_{40}	-61,0 °C

TABLE 5.1: Glass transition temperatures of SBR20, SBR40, EPDM20 and NR40

5.2 Quasi-static experiments

The main focus of the quasi-static investigations is on determining the equilibrium response of the material. Since this work does not account for stress-softening phenomena, the Mullins effect is additionally studied through preliminary investigations to reveal the necessity of preconditioning.

The experimental tests concerned with the Mullins effect are carried out under uniaxial tension whereas the other experiments are performed under uniaxial tension, compression and pure shear to cover the range of different deformation types.
The geometries of the specimen for uniaxial tension, pure shear and compression are illustrated in figure 5.3. In order to prevent barrelling during the compression tests, some grease was applied on top and on bottom of the specimen such that the material is not hindered from moving at the clamps.

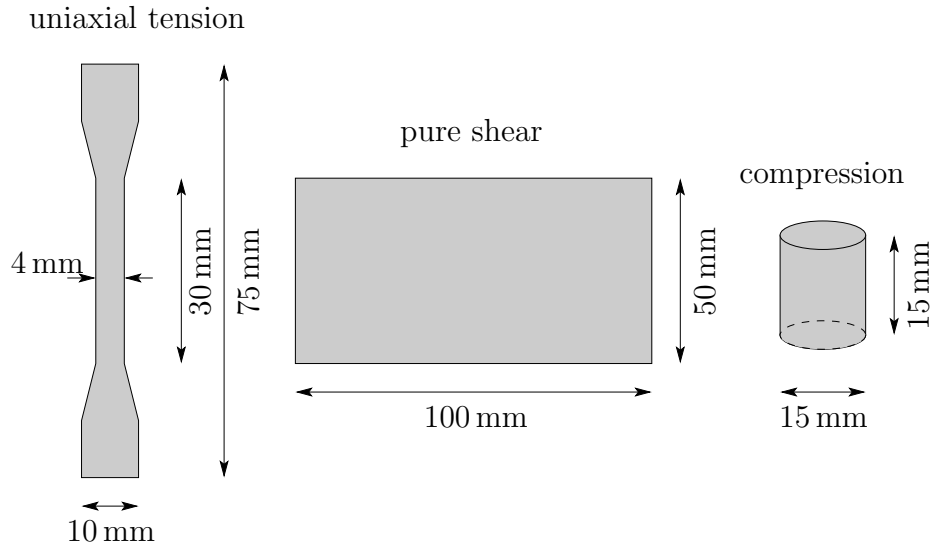

FIGURE 5.3: Geometries of the specimen for uniaxial tension, pure shear and compression

Quasi-static testing device

The following experiments are performed with the quasi-static testing device Zwick/Roell Z020.
The testing machine can generally be divided into three main components, a tension unit, a torsion unit and a temperature chamber. These components can be used separately or in combination such that complex types of deformation can be applied. Moreover, the temperature chamber allows for the possibility to perform isothermal measurements and to define more complicated temperature histories in a range from $-70\,°C$ up to $250\,°C$.
The force signal is measured by convertible force sensors of 150 N, 2.5 kN and 20 kN, whereas the momentum signal is captured by a sensor of 100 Nm. The displacement can be measured globally by the traverse sensor or locally with a camera. A brief overview of important technical specifications of the quasi-static testing device are listed in table 5.2.

The experimental investigations are performed by using the tension unit to study the material characteristics under uniaxial tension, compression and pure shear. Furthermore, the temperature chamber is utilised to set a constant reference temperature of $20\,°C$. Since the strain is mostly spread over the specimen inhomogeneously, it is measured locally by using the camera. The reaction force of the specimen is captured by

maximum force	150N / 2.5kN / 20kN
maximum momentum	100Nm
displacement sensor	traverse / camera
linear speed range	0.03 - 1000 mm/min
torsion speed range	0.001 - 10 rpm
temperature range	-70 - 250°C

TABLE 5.2: Technical specifications of Zwick/Roell Z020

the sensitive 150 N force transducer in uniaxial tension mode and by the 2.5 kN sensor in compression and pure shear mode which is due to higher values of force.

5.2.1 Mullins effect

The Mullins effect is an irreversible, strain-induced softening phenomenon which occurs during the first loading cycles of elastomers (Mullins (1948), Bueche (1961), Harwood et al. (1965)). Since this effect is not considered in this thesis, it is investigated in preliminary experiments by applying cyclic deformations under uniaxial tension. In a first loading process, the virgin specimen is loaded five times with a maximum strain of 100 %. After this procedure, the material is allowed to rest for three days and then loaded again through the same procedure. Due to the separated second loading process, superimposed viscoelastic effects, such as stress-relaxation, can be excluded such that the stress decrease is ensured to be solely caused by the Mullins effect. The experimentally obtained stress responses of the first and second loading processes are illustrated for each material in figure 5.4.

Comparing the first and second loading procedures, one can observe that the stress in the second loading process is decreasing again such that the stress-softening effect can not be neglected. Apart from this fact, the experimental data reveals the dependence of the Mullins effect on the amount of filler. Regarding the stress response of the SBR vulcanisates, the stress decrease of the higher filled SBR40 rubber is more pronounced than that of the lower filled SBR20. This observation corresponds to the early investigations made by Harwood et al. (1965) or Harwood and Payne (1966) and is physically related to the presence of the filler which results in an increase of the local strain in the rubber matrix.
In order to avoid stress-softening during the following investigations, the specimens are mechanically preconditioned. To this end, they are loaded up to a maximum strain which exceeds the maximum strain reached in the tests to determine the equilibrium stress-strain curves. Since the Mullins effect depends on the maximum strain in the loading history, this preconditioning guarantees that no stress-softening occurs in the following tests and that the Mullins effect can be omitted in the constitutive model.

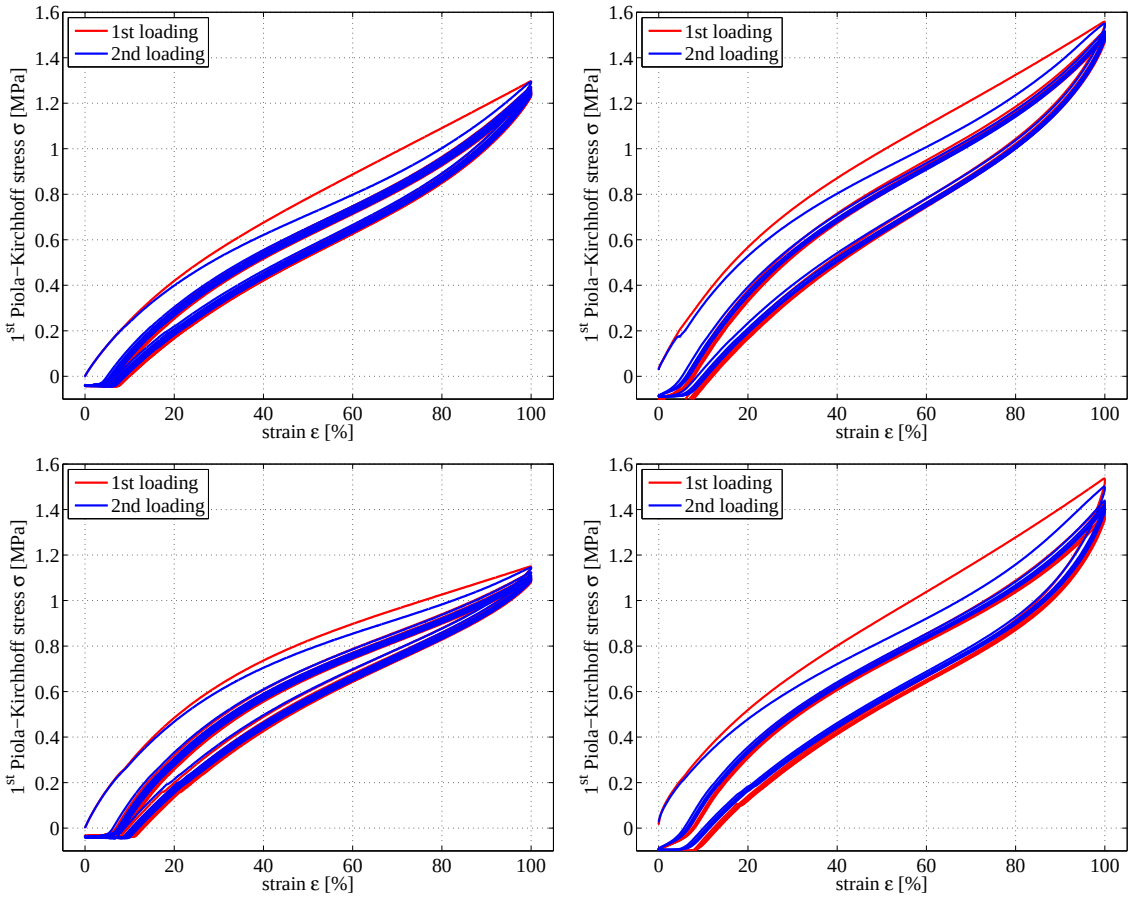

FIGURE 5.4: Stress-softening of SBR20 (upper left), SBR40 (upper right), EPDM20 (lower left) and NR40 (lower right)

5.2.2 Equilibrium stress

The equilibrium stress response of the material is determined under uniaxial tension, compression and pure shear. The maximum static strain is set to 85 % in tension mode, 40 % in compression mode and 70 % in pure shear.
Since filler-reinforced rubbers exhibit long-term relaxation (Simo and Huges (2000)), the equilibrium stress response is not investigated by using simple long-term relaxation tests. It is determined by stepwise loadings and unloadings with shortened holding times such that the duration of the experiment can be significantly reduced. For illustration, the stepwise loadcase is displayed as an example on the left-hand side of figure 5.5 in terms of the SBR40 under uniaxial tension. The specimen is loaded stepwise with specific strain amplitudes which are held constant for 1 hour in each step. Once the maximum strain is reached, the specimen is unloaded in a similar sense.

The corresponding stress response resulting from the stepwise loading procedure is illustrated on the right-hand side of figure 5.5. On the basis of this display, the equilibrium stress is located between the corresponding loading and unloading steps which belong to the same strain level. An easy method to determine the equilibrium stress would be to take the mean value of stress between the endpoints of the corresponding loading and unloading paths. However, the stress relaxation respectively the temporal

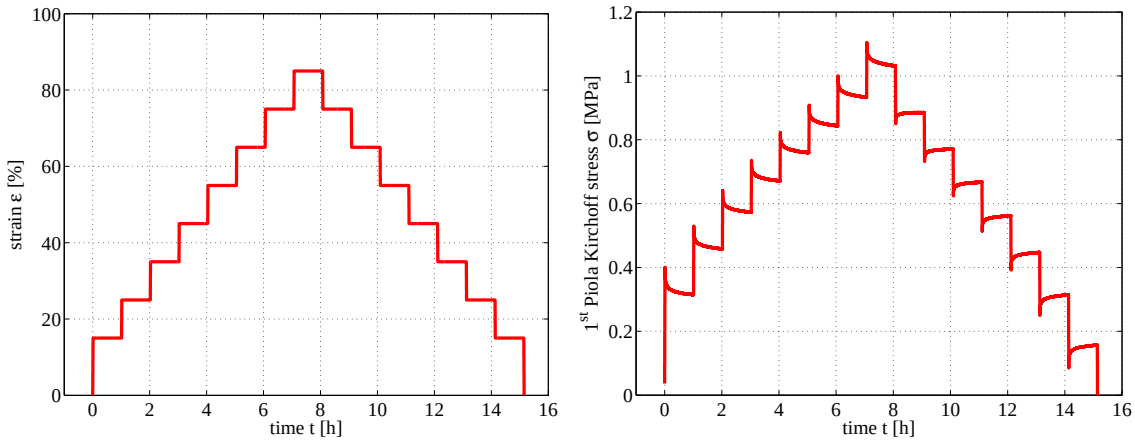

FIGURE 5.5: Stepwise loadcase (left) and resulting stress response of SBR40 (right) under uniaxial tension

decrease in the stress of the corresponding paths differ from each other. To illustrate the relaxation behaviour in more detail, the stress response of the loading and unloading paths at 75 % of strain is shown in figure 5.6. This figure reveals that the stress decrease on the loading path is considerably more pronounced than on the unloading path such that determining the equilibrium stress on the basis of the mean stress would be too inaccurate.

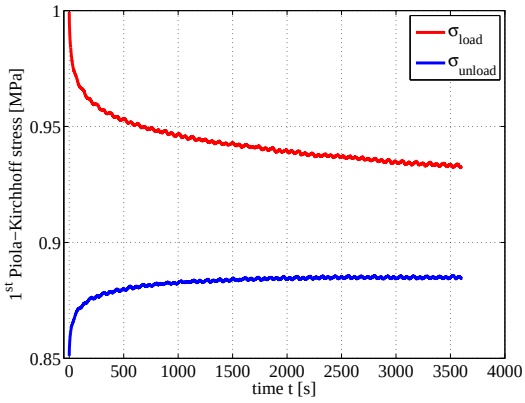

FIGURE 5.6: Detail of the stress responses at 75 % of strain (SBR40)

To make a more precise statement, the equilibrium stress is determined by the intersection of the tangents of the corresponding loading and unloading paths. As illustrated on the left-hand side of figure 5.7, the tangents of the relaxation paths are calculated with respect to the last 5 minutes of the holding time. On this basis, the intersection point of the extrapolated tangents is defined as the equilibrium stress. If this procedure is applied with respect to each level of strain, the equilibrium stress can be determined precisely for each strain level. The equilibrium stress determined through this procedure and corresponding to the experimental data in figure 5.5 is given on the right-hand side of figure 5.7.

Based on this procedure, the equilibrium stress is determined for each deformation mode and each material. The results obtained in terms of the 1st Piola-Kirchhoff stress are

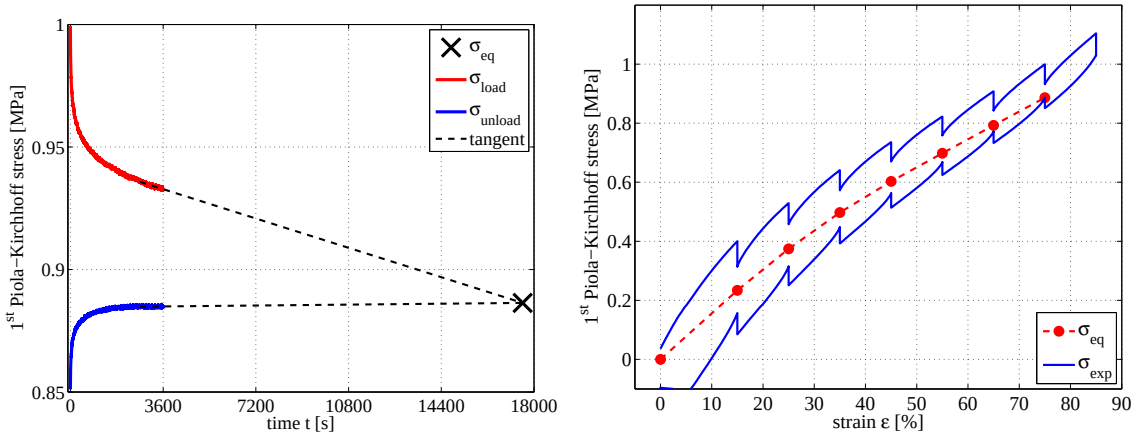

FIGURE 5.7: Calculation of the equilibrium stress at 75 % of strain (left) and resulting equilibrium stress under uniaxial tension (right) (SBR40)

plotted in figure 5.8 as a function of the stretch. Apart from the stress values, each material behaves approximately in the same manner and is characterised by the typical nonlinear stress-strain relation of elastomers. The effect of reinforcement due to the addition of carbon-black can be observed by a comparison between the slightly filled SBR20 vulcanisate and the higher filled SBR40 compound. Since the SBR40 rubber is reinforced with a higher amount of carbon-black, its stress responses are higher than those of the SBR20.

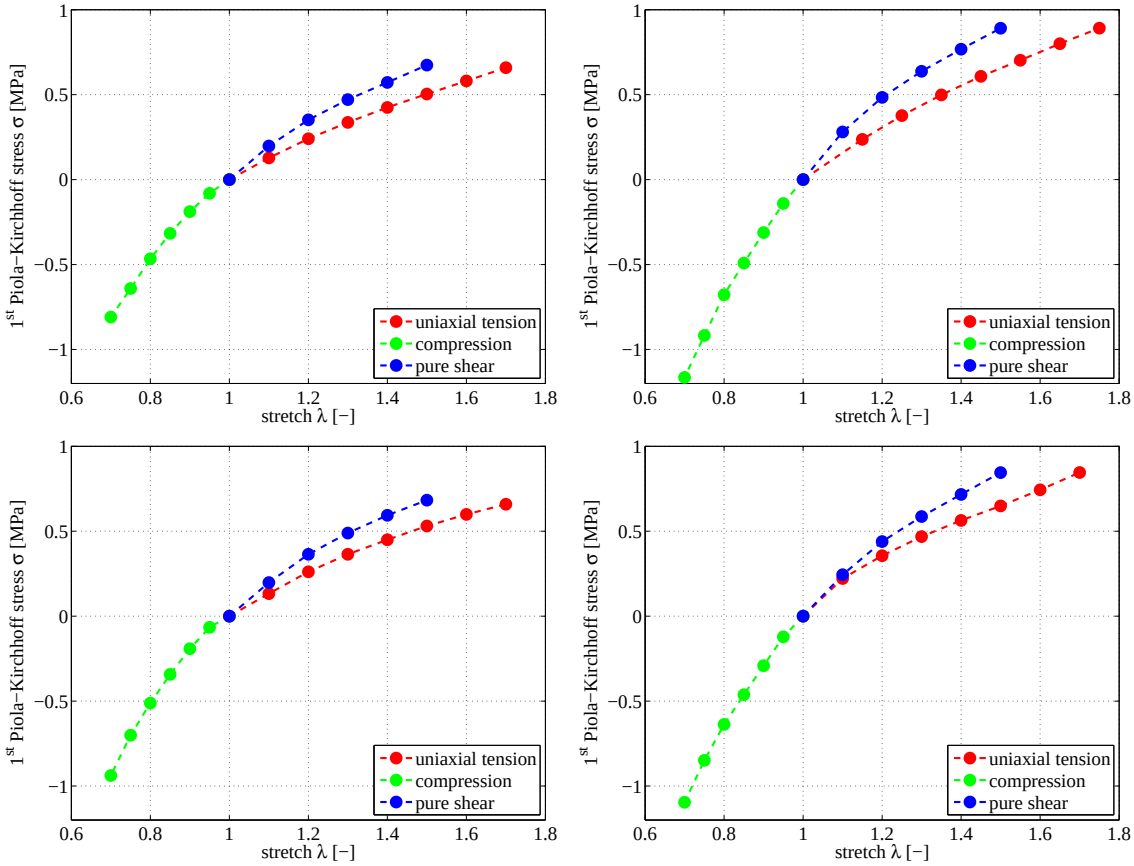

FIGURE 5.8: Equilibrium stress response under compression, pure shear and uniaxial tension (upper left: SBR20), (upper right: SBR40), (lower left: EPDM20), (lower right: NR40)

5.3 Dynamic investigations

The predeformation and frequency dependent characteristics of the storage and the loss modulus are studied via dynamic mechanical analyses in the frequency domain. A detailed overview about the dynamic mechanical analysis is provided by Menard (1999). In general, the material is loaded with harmonic oscillations and its dynamic mechanical material response is evaluated in the frequency domain in terms of the storage and the loss modulus. The variation of different measuring parameters offers the possibility to study frequency dependence, amplitude dependence, the influence of the static preload as well as various other dynamic material characteristics.
The dynamic mechanical tests are performed with the DMA testing device Gabo EPLEXOR 500N which allows for measurements up to 100 Hz. In order to extend the experimentally limited frequency range, the temperature-frequency shifting technique is applied.
Since this work does not consider amplitude dependent softening, the Payne effect is investigated in preliminary tests to prove its absence in the region of small amplitudes.

The basic loadcase of the dynamic experiments corresponds to that of engine mounts and is displayed in figure 5.9. The specimen is loaded by a constant static predeformation ε_0 which is then superimposed by a harmonic vibration of the amplitude $\Delta\varepsilon$ and the frequency ω.

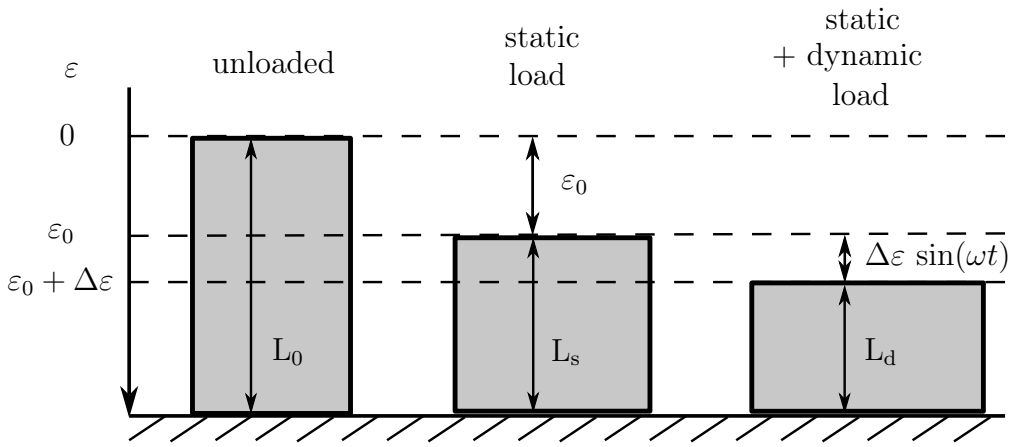

FIGURE 5.9: Loadcase of the dynamic investigations

Via a variation of the dynamic strain amplitude $\Delta\varepsilon$, the frequency ω or the static predeformation ε_0, the Payne effect as well as the frequency and predeformation dependence of the dynamic moduli are studied.

Dynamic mechanical analysis

In order to acquaint the reader with the technique of dynamic mechanical analysis, the measuring principle is first explained on the basis of figure 5.10.

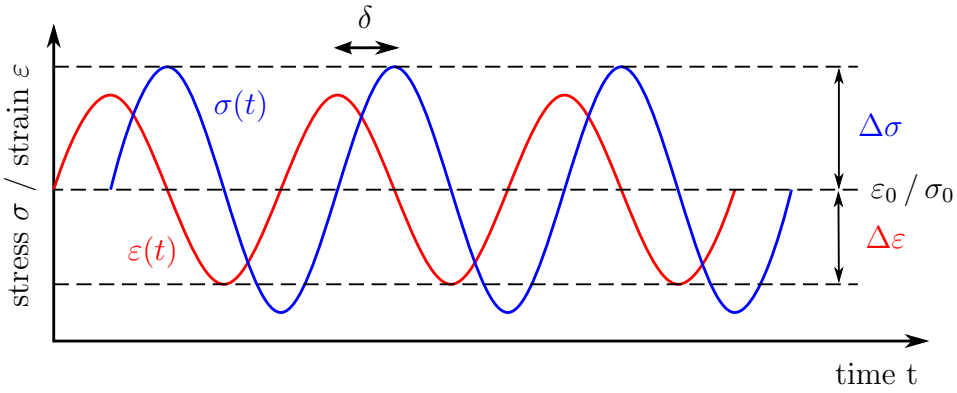

FIGURE 5.10: Sinusoidal excitation and phase shifted harmonic stress response

If the material is loaded with a sinusoidal excitation

$$u(t) = \Delta u \sin(\omega t) \tag{5.1}$$

with the frequency ω and the amplitude Δu, the material's dynamic response is given by the harmonic force response

$$F(t) = \Delta F \sin(\omega t + \delta) \tag{5.2}$$

with the amplitude ΔF. The harmonic force response oscillates with the same frequency ω as the excitation, but due to the viscoelastic material properties it is shifted by a loss angle δ. If the excitation and the force response are expressed in terms of the harmonic strain $\varepsilon(t)$ and stress $\sigma(t)$, the following relations hold

$$\begin{aligned} \varepsilon(t) &= \Delta\varepsilon \sin(\omega t) , \\ \sigma(t) &= \Delta\sigma \left(\cos(\delta) \sin(\omega t) + \sin(\delta) \cos(\omega t)\right) . \end{aligned} \tag{5.3}$$

On the basis of this description, the frequency dependent functions $G'(\omega)$ and $G''(\omega)$ are obtained by dividing the harmonic stress by the harmonic strain. The frequency dependent storage modulus $G'(\omega)$ is defined by the sine part of the stress

$$G'(\omega) = \frac{\Delta\sigma}{\Delta\varepsilon} \cos(\delta) , \tag{5.4}$$

whereas the loss modulus $G''(\omega)$ is identified by the cosine part of the stress

$$G''(\omega) = \frac{\Delta\sigma}{\Delta\varepsilon} \sin(\delta) . \tag{5.5}$$

Moreover, the complex modulus $G^*(\omega)$, its absolute value and the loss factor $\tan(\delta)$ can be expressed by the storage and the loss modulus

$$\begin{aligned} G^*(\omega) &= G'(\omega) + i\, G''(\omega) , \\ |G^*(\omega)| &= \sqrt{G'(\omega)^2 + G''(\omega)^2} , \\ \tan(\delta) &= \frac{G''(\omega)}{G'(\omega)} . \end{aligned} \tag{5.6}$$

Dynamic testing device

In contrast to the quasi-static testing machine, the DMA testing device Gabo EPLEXOR 500N offers the possibility to perform dynamic measurements at frequencies up to 100 Hz. For explanation, a schematic diagram of the machine setup is given in figure 5.11.

The mechanical unit of the system can be divided into a static loading unit (upper part) and a dynamic loading component (lower part). The static loading unit can be compared to a quasi-static testing device and is mainly used to apply constant static deformations. The dynamic loading component consists of an electro-dynamic shaker which operates on the principle of a speaker and thus allows for applying harmonic oscillations to the specimen.

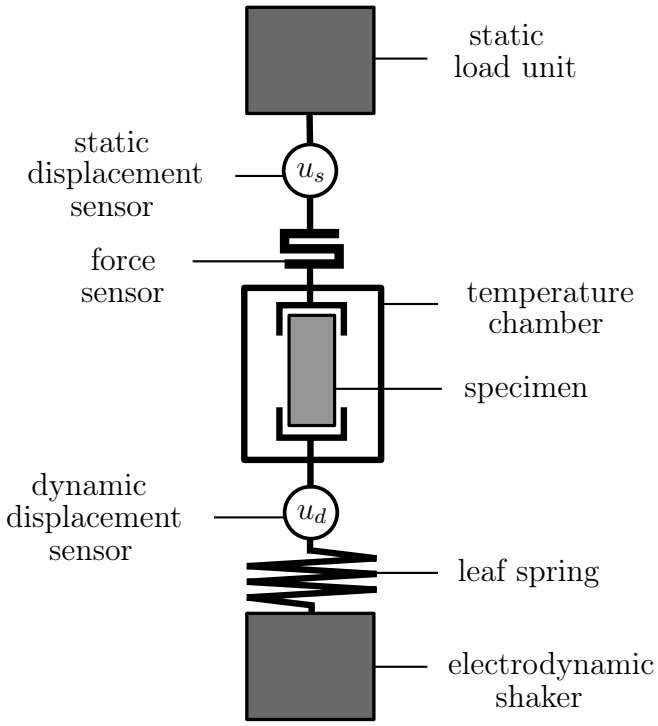

FIGURE 5.11: Schematic diagramm of DMA testing device Gabo EPLEXOR 500N

The force signal is measured by convertible sensors of 150 N, 500 N and 1500 N which are installed at the upper loading unit. On the basis of these force sensors, the maximum amount of applicable static and dynamic load is limited to 1500 N. However, the dynamic force is limited to a maximum of 500 N which is due to the limit of the electro-dynamic shaker system.
The spring system which is attached to the lower dynamic loading unit has the function of preventing the electro-dynamic shaker from reaching its mechanical end stop due to large static preloadings. For instance, at moderate preload, a soft carbon spring is used such that the force of the electro-dynamic shaker, which is necessary to apply harmonic oscillations, is reduced. At high preload, a stiffer steel spring must additionally be attached such that the shaker does not reach its end stop due to the static preload.
The static and dynamic displacements are captured by two sensors. The static displacement is measured by a dial gauge which is installed at the upper loading unit whereas the dynamic excitation is determined by exchangeable high sensitive range sensors of ± 1.5 mm and ± 7.5 mm.
Apart from the mechanical part, the DMA system inherits a temperature chamber which offers the possibility to control the temperature with liquid nitrogen in a range from $-150\,^{\circ}$C up to $500\,^{\circ}$C. For an overview, the important technical specifications of the DMA testing device are summarised in table 5.3.

The software of the Gabo EPLEXOR 500N provides several measuring procedures to apply dynamic loadings with changing frequency, varying static and/or dynamic amplitude, changing temperature and more. Thereby, the dynamic material response is analysed in terms of the storage and the loss modulus in the frequency domain. The most important measuring procedures provided by the software are static-sweep tests, amplitude-sweep tests, frequency-sweep-tests and temperature-frequency-sweep tests.

maximum static force	150 N / 500 N / 1500 kN
maximum dynamic force	±500 N
maximum static displacement	35 mm
maximum dynamic displacement	±1.5 mm
frequency range	0.01 - 100 Hz
temperature range	-150 - 500 °C

TABLE 5.3: Technical specifications of the Gabo EPLEXOR 500N

With respect to the dynamic loading, the difference between these sweeps consists in the specification, which of the testing parameters are held constant and which ones are varied during the measurement. For a better understanding, an overview of the sweeps is given below:

- **Static-sweep**
  The static-sweep test is defined by a harmonic loading with a stepwise variation of static prestrain. The other testing parameters, for instance, dynamic amplitude, frequency or temperature, are held constant. This procedure can be applied to investigate the predeformation dependence of the dynamic material properties at different states of static deformation.

- **Amplitude-sweep**
  The amplitude-sweep test is characterised by a harmonic loading with varying dynamic strain amplitudes at constant static preload, frequency and temperature. This testing procedure is commonly applied to investigate amplitude-dependent phenomena, such as the Payne effect.

- **Frequency-sweep**
  The frequency-sweep test is characterised by a harmonic loading with changing frequency. On the basis of this procedure, the frequency dependent properties of the material can be investigated at constant static preload, amplitude and temperature.

- **Temperature-frequency-sweep:**
  The temperature-frequency-sweep test is defined by a harmonic loading with a combined variation of frequency and temperature at constant static preload and dynamic amplitude. This procedure consists of a series of sequenced frequency-sweep tests which are performed at different temperatures. In terms of two frequency sweeps and two temperatures, the procedure is described by the following steps: At first, the first temperature is regulated and then held constant. After that, the first frequency-sweep is performed. Then, the second temperature is controlled and the frequency-sweep is applied again. Based on this procedure, the frequency and temperature dependence of the dynamic material properties can easily be investigated. Furthermore, the temperature frequency shifting technique can be applied to determine the master curve.

In this work, amplitude-sweep tests are carried out to investigate the Payne effect. The main investigations are based on temperature-frequency sweeps, which are performed at different states of static deformation. Due to this concept, the dependence of the storage and the loss modulus on predeformation, frequency and temperature is studied. Moreover, the experimental frequency range is extended on the basis of the relation between the frequency and temperature dependence by applying the temperature frequency shifting technique.

5.3.1 Payne effect

The Payne effect is an amplitude dependent softening phenomenon of filler-reinforced rubber which is generally related to a breakdown of the filler network (Payne 1962a; Payne 1962b; Payne 1972). It is characterised by a decrease in the storage modulus with increasing strain amplitude and a maximum of the loss modulus at middle strain amplitudes.
Since this work focuses on the dynamic material behaviour in the vibrational range at small strain amplitudes of 0.1 %, the Payne effect is not considered. The authority to neglect amplitude dependent effects is related to early investigations by Payne (1960) and Payne (1962a). The author observed a yield point at small strain amplitudes below which the dynamic stiffness of elastomers remains constant. Due to this fact, the amplitude dependence of the underlying materials is investigated in preliminary amplitude-sweep tests to prove the absence of the Payne effect at strains which are smaller than 0.1 %. The investigations are performed under uniaxial tension at a constant predeformation of 15 % which is then superimposed by harmonic oscillations of 10 Hz. During the harmonic loading, the strain amplitude is stepwise varied from 0.01 % up to 10 % such that the amplitude dependent characteristics of the materials come in sight. The experimental results of the storage and the loss modulus are illustrated in figure 5.12 for each material.

As one can observe from the experimental data, each material reveals the characteristic amplitude dependent decrease of the storage modulus with increasing strain amplitude. The amplitude dependence is more pronounced for the SBR40 and NR40 vulcanisates with higher amounts of filler. In comparison to the slightly filled SBR20 and EPDM20 compounds, the amplitude dependent decrease of the dynamic stiffness is larger for the SBR40 and NR40 vulcanisates. The same observation can be made in terms of the loss modulus. The typical sigmoidal behaviour is more pronounced for the vulcanisates with 40 phr of filler and nearly missing in terms of the slightly filled vulcanisates. These observations are in agreement with the studies by Payne (1962a) and Payne (1974) in which the dependence of the Payne effect on the amount of filler was investigated. From a physical point of view, the dependence of the Payne effect on the amount of filler can physically be related to the additional filler network (Lion and Kardelky 2004). The stronger decrease of the storage modulus in the case of the higher filled SBR40 and NR40 can thus be related to a breakage of more filler bonds.
On the other hand, the loss modulus as a measure of the energy dissipation is proportional to the breakage rate of the filler bonds. Due to the large amount of intact filler bonds at small strain amplitudes, the loss modulus first increases with increasing

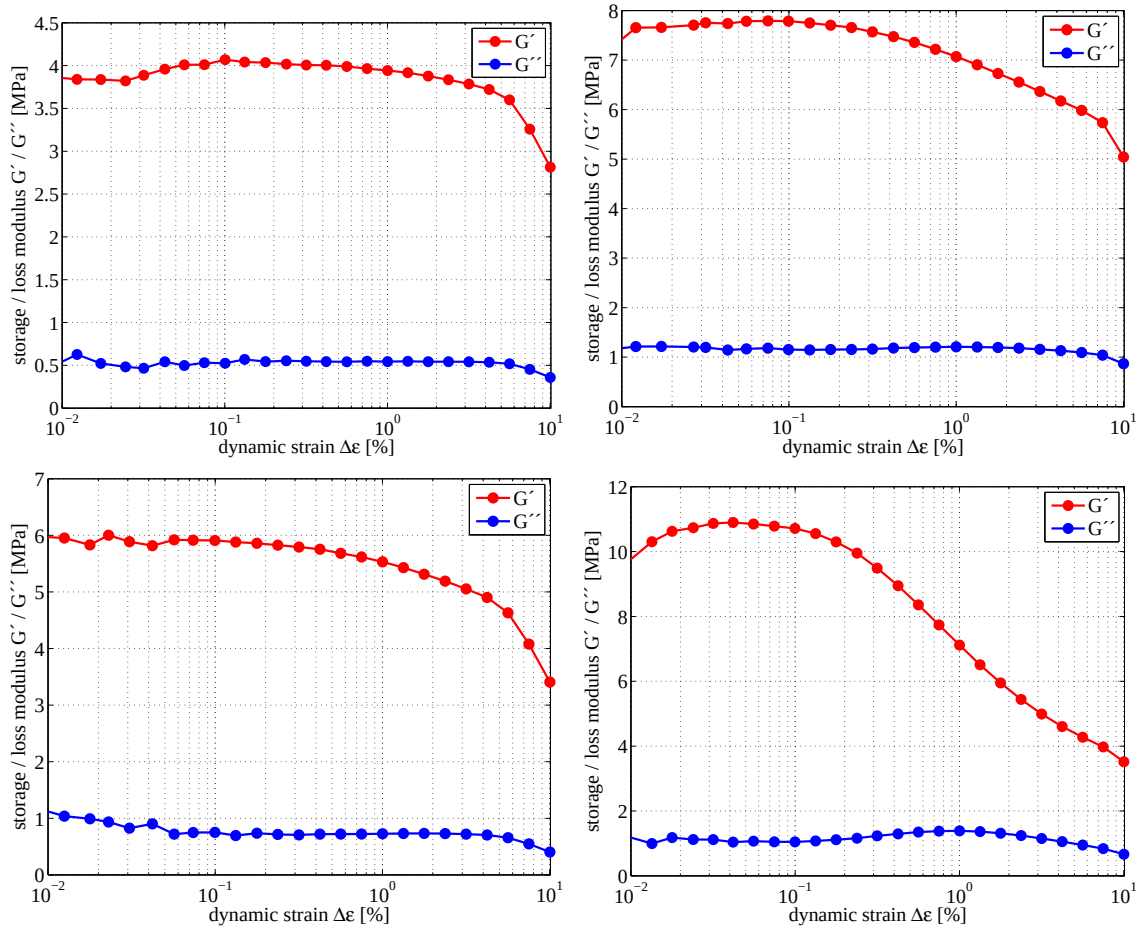

FIGURE 5.12: Amplitude dependence of the storage and the loss modulus (upper left: SBR20), (upper right: SBR40), (lower left: EPDM20), (lower right: NR40)

dynamic strain and subsequently declines after reaching its maximum value because the number of intact bonds has considerably decreased. Based on this assumption, the less pronounced sigmoidal behaviour of the loss modulus in the case of the slightly filled SBR20 and EPDM20 vulcanisates might be due to the low amount of filler bonds.

With respect to the focus of this work, the essential characteristics of the experimental observations are based on the fact that the storage modulus reveals a nearly constant plateau at sufficient small strain amplitudes. In order to make a precise statement about this domain, the normalised modulus G'/G'_{max} is plotted in figure 5.13.

If a decrease of 10 % from the maximum value of the storage modulus is defined as the limit case to neglect the Payne effect, the amplitude dependent softening can be omitted up to 1.4 % of dynamic strain in terms of the SBR20 compound, up to 1 % with respect to the SBR40 rubber and up to 1.05 % and 0.25 % with regard to the EPDM20 and NR40 vulcanistes. Since this work focuses on strain amplitudes of 0.1 %, the Payne effect is ensured to be omittable in this region.

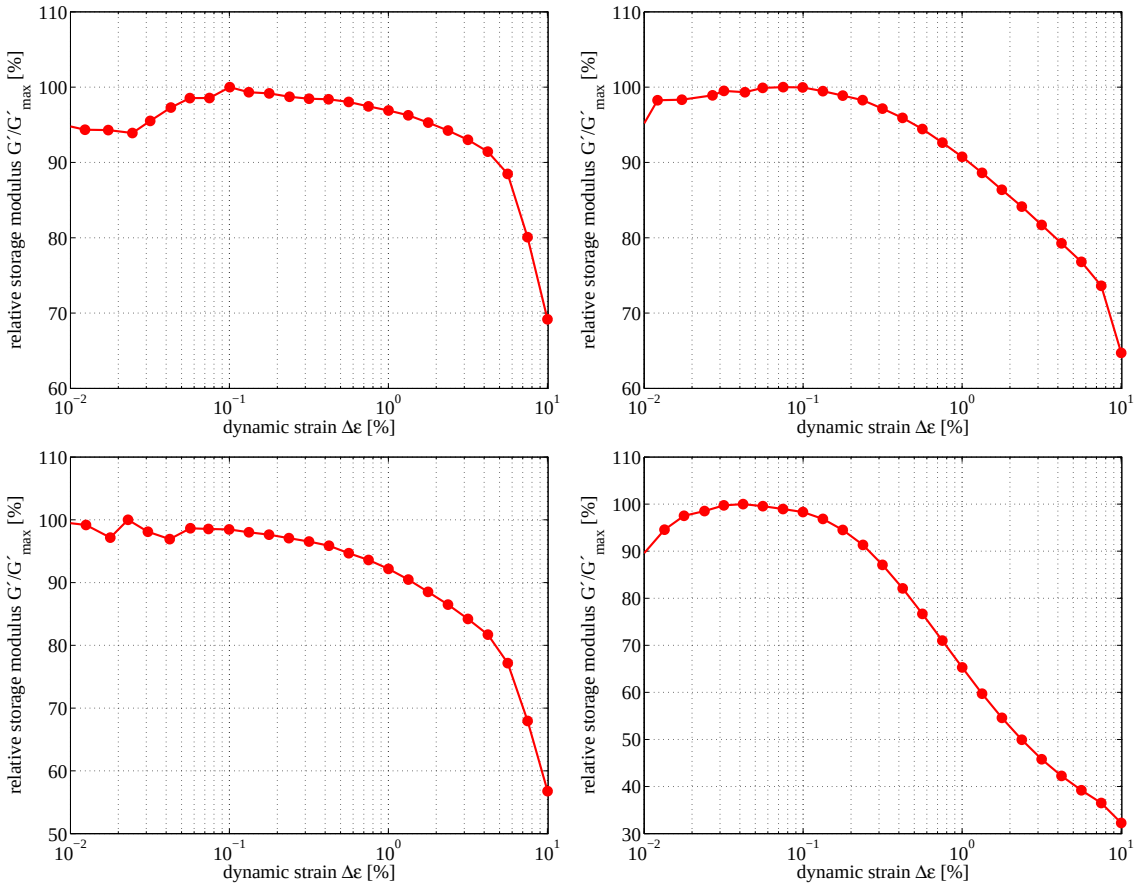

FIGURE 5.13: Amplitude dependence of the normalised storage modulus (upper left: SBR20), (upper right: SBR40), (lower left: EPDM20), (lower right: NR40)

5.3.2 Predeformation and frequency dependence

Motivated by engine mounts, the dynamic material properties are investigated under large static predeformations which are superimposed by harmonic oscillations of 0.1 % of strain in a frequency range up to 100 kHz.
The static predeformations are varied from -30 % of strain under compression up to 50 % of strain under tension such that a broad deformation range can be covered.
The experimental frequency domain is set from a minimum frequency of 0.2 Hz up to a maximum frequency of 60 Hz. The lower frequency limit is due to an optimisation of the testing period whereas the upper frequency limit is set to avoid resonance and inertia effects during measurement.
The temperature range investigated covers a domain from -30° C up to 60° C. Since engine mounts and elastomers are usually operating above the glassy state, the lower temperature limit is set to guarantee a measurement above the glass transition temperature. The upper temperature limit is set to prevent the material from thermal ageing during measurement.
In order to separately characterise the influence of predeformation on the dynamic moduli, the predeformation dependence is first investigated in static-sweep tests at constant temperature, constant frequency and constant dynamic amplitude. It should be mentioned that in terms of the slightly filled SBR20 and EPDM20 vulcanisates,

barrelling of the specimen was present during the dynamic mechanical analysis in compression. Due to the high frequencies, the application of some grease on top and on bottom of the specimen, as it was done in the quasi-static compression tests, was not possible. This fact implies that the measured stress responses of SBR20 and EPDM20 in compression are higher than those without barrelling. Therefore, correction factors were calculated by comparison of the equilibrium stress data with and without barrelling and finally applied to the experimental data in compression. These correction factors are listed in table 5.4 for each predeformation in compression. In contrast to that, the dynamic measurements of SBR40 and NR40 were performed later with the help of an advanced clamping system, such that barrelling of the specimen could be prevented during measurement and no corrections were applied.

EPDM20

-30 %	-20 %	-10 %
0.907	0.862	0.837

SBR20

-30 %	-20 %	-10 %
0.887	0.844	0.822

TABLE 5.4: Barrelling correction factors for EPDM20 and SBR20 in compression

Predeformation dependence

The dependence of the dynamic material properties on the static predeformation is first investigated in static-sweep tests. The preconditioned specimens are loaded with a constant static strain between -30 % and 50 % which is then superimposed by a harmonic sinusoidal oscillation of 0.1 % dynamic strain at a frequency of 10 Hz. The experimental results of the storage and the loss modulus are plotted in figure 5.14 as a function of the static stretch λ_0.

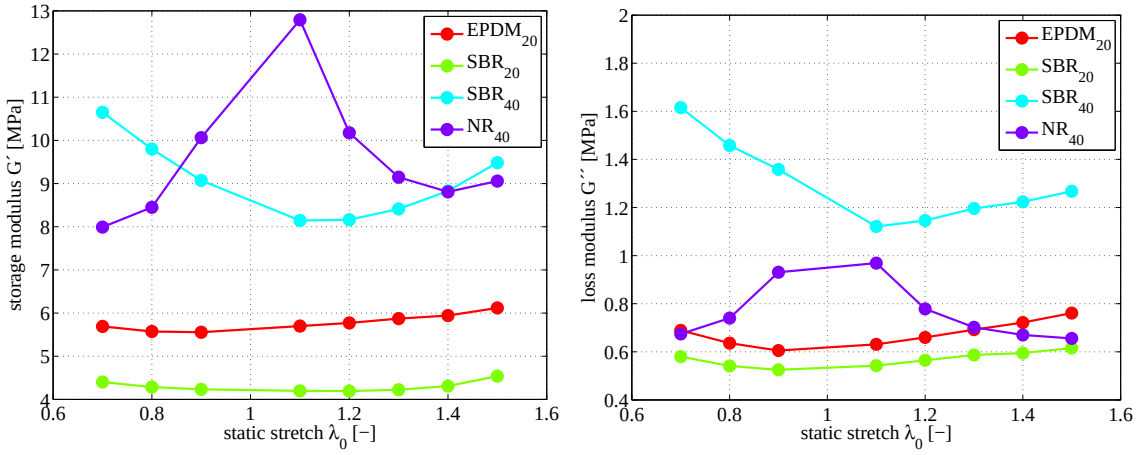

FIGURE 5.14: Predeformation dependence of the storage and the loss modulus at a dynamic strain amplitude of 0.1 % and a frequency of 10 Hz (left: storage modulus), (right: loss modulus)

It can first be observed that the static predeformation has an influence on both moduli, which is of a different character for each material. The slightly filled EPDM and SBR

rubbers with 20 phr of carbon-black behave quite similarly and reveal a smaller influence on the predeformation than the higher filled SBR40 and NR40 compounds. The predeformation dependence of the SBR20 and EPDM20 vulcanisates is characterised by an increase of the storage modulus with the static strain in the tension case, and an initial decrease of dynamic stiffness at small compressions which is followed by an increase of the storage modulus under higher compression. The loss modulus of both materials is less affected than that of the higher filled materials and reveals predeformation dependent characteristics quite similar as the storage modulus.
In contrast to the slightly filled compounds, the SBR vulcanisate with 40 phr of carbon-black is characterised by a pronounced increase of both moduli with the static predeformation in the tension and the compression mode. An initial decrease at small compression, as it is the case for the slightly filled SBR and EPDM vulcanisates, is not observed.
In the case of the NR with 40 phr of carbon-black, the predeformation dependence of the storage and the loss modulus is completely different from the other vulcanisates. Under tension, the storage modulus first decreases with the static strain up to 40 % and then slightly increases again, whereas a decrease with increasing compression is observed. On the other hand, the predeformation dependent characteristics of the loss modulus are determined by a decrease with increasing predeformation in tension and compression mode.

A physical interpretation of the predeformation dependent characteristics is given in various works in literature. For instance, Kim and Youn (2001) studied the influence of the dynamic modulus of filler-reinforced and unfilled natural rubber in compression tests. The authors observed an initial decrease of the storage modulus at small precompression and a subsequent increase at higher precompression. Furthermore, the effect of the static strain was observed to be proportional to the amount of filler. In the case of the vulcanisates with a small amount of carbon-black (NR / 0 phr and NR / 50 phr), it was found that the loss angle is not affected by the static compression whereas the loss angle of the rubber with a high amount of carbon-black (NR / 70 phr) was gradually reduced with the static compression. The authors explain the increase of the storage modulus by the limited extensibility of the elastomer chains, whereas the initial decrease is related to the disruption of the filler network.
Based on this interpretation, the predeformation dependent characteristics of the slightly filled SBR20 and EPDM20 can be interpreted in a similar manner. At small compression, the dynamic modulus is initially decreased due to a breakdown of the filler structure whereas the subsequent increase at higher compression can be related to the limited extensibility of the rubber chains. Since the behaviour of the EPDM20 and SBR20 vulcanisates is only characterised by an increase of the storage modulus in tension mode, the breakage of the filler network is less pronounced such that the limited extensibility of the rubber chains seems to be more pronounced and thus results in an increase in the dynamic modulus in the whole range of predeformations under tension. Since the higher filled SBR with 40 phr of carbon-black reveals an increase of the storage modulus in tension and compression mode, the breakdown of the filler bonds might be very small. On the contrary, the NR rubber with 40 phr is characterised by a decrease of the dynamic modulus under tension and compression which might be due

to a pronounced breakdown of filler bonds or due to a higher flexibility of the rubber chains.

Apart from the physical interpretation by Kim and Youn (2001), Hoefer (2009) provides a different proposal to interpret the predeformation dependent material characteristics. The author does not relate the effect to the microstructure of the material, but to its nonlinear equilibrium response, which seems to fit very well with the experimentally observed characteristics in this work. The connection between the nonlinear equilibrium curve and the predeformation dependence of the dynamic moduli becomes clear if the dependence of the dynamic moduli on the predeformation is plotted with respect to the undeformed reference configuration in terms of the 1st Piola-Kirchhoff stress (see figure 5.15).

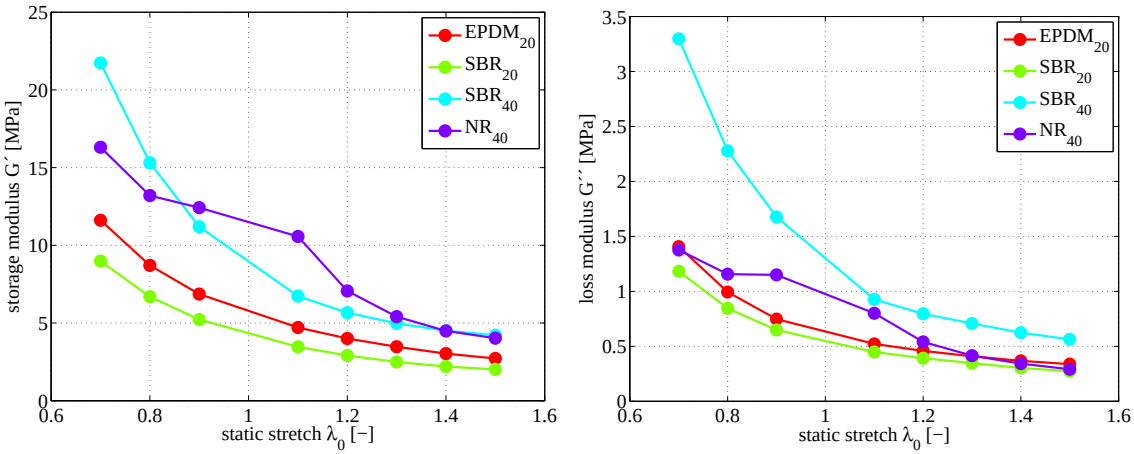

FIGURE 5.15: Predeformation dependence of the storage and the loss modulus at a dynamic strain amplitude of 0.1 % and a frequency of 10 Hz with regard to the 1st Piola-Kirchhoff stress (left: storage modulus), (right: loss modulus)

From this point of view, both dynamic moduli are increasing with decreasing predeformation in the whole range. If this behaviour is compared with the equilibrium stress data obtained from the quasi-static experiments in figure 5.8, the assumption of Hoefer (2009) fits excellently with the experimental results. Since the dynamic moduli are proportional to the dynamic stress response and the gradient of the equilibrium stress-strain curves increases with decreasing prestrain, the dynamic moduli increase as well. According to this fact, the current work follows the assumption made by Hoefer (2009) and relates the dependence of the dynamic moduli on the static predeformation to the nonlinear characteristics of the equilibrium stress-strain curves. Respecting this, the experimental data of the following presentation is expressed in terms of the 1st Piola-Kirchhoff stress tensor.

Temperature-frequency-sweep tests

In order to study the combined dependence of the dynamic moduli on static predeformation and frequency in a range up to 100 kHz, temperature-frequency-sweeps are

carried out. These consist of sequenced frequency-sweeps which are subsequently performed at different temperatures.
The range of predeformation is between −30 % of strain under compression and up to 50 % of strain under tension. The frequency-sweeps are performed from a minimum frequency of 0.2 Hz up to a maximum frequency of 60 Hz and the dynamic amplitude is set to 0.1 % of strain. The tests are performed at different temperatures between −30 °C and 60 °C such that the temperature frequency shifting technique (Ferry (1980), Schwarzl (1990)) can finally be applied to determine the master curves.

The experimental results of the temperature-frequency-sweeps at a prestrain of 10 % in uniaxial tension mode are illustrated in figure 5.16 - 5.19 for each material. These results reveal the dependence of the storage and the loss modulus on temperature and frequency. It is already well known that the storage and the loss modulus increase with the frequency, which is in agreement with other studies, e.g. Kari (2003) or Hoefer and Lion (2009).
The frequency dependence of the modulus of the carbon-black filled NR is less pronounced than for the other types of rubber.
The influence on temperature appears in a decrease of both moduli with increasing temperature which fits with other observations by Payne (1962a), Dutta and Tripathy (1992), Rendek and Lion (2008) or Hoefer (2009). Furthermore, the relative change in the dynamic moduli appears to be more pronounced in the case of low temperatures.

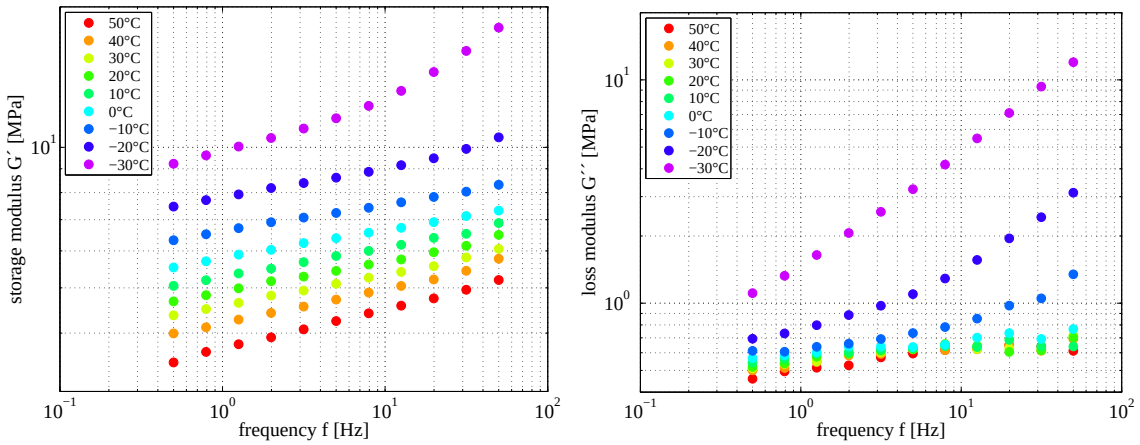

FIGURE 5.16: Temperature dependence of the dynamic moduli of EPDM20 at a prestrain of 10 % (left: storage modulus), (right: loss modulus)

In order to extend the experimental frequency range, the shifting function is first determined by the WLF equation (Williams et al. (1955))

$$\log a_\theta = \frac{c_1 \, (\theta - \theta_0)}{c_2 + \theta - \theta_0} \tag{5.7}$$

with the material parameters c_1 and c_2, the current temperature θ and the reference temperature θ_0. Similar to the quasi-static investigations, the reference temperature is set to 20 °C which is an average value for the application field of engine mounts. On this basis, the shifting function $\log a_\theta$ results in a horizontal shifting of the curves at higher temperatures ($\theta > \theta_0$) to lower frequencies whereas the curves at lower

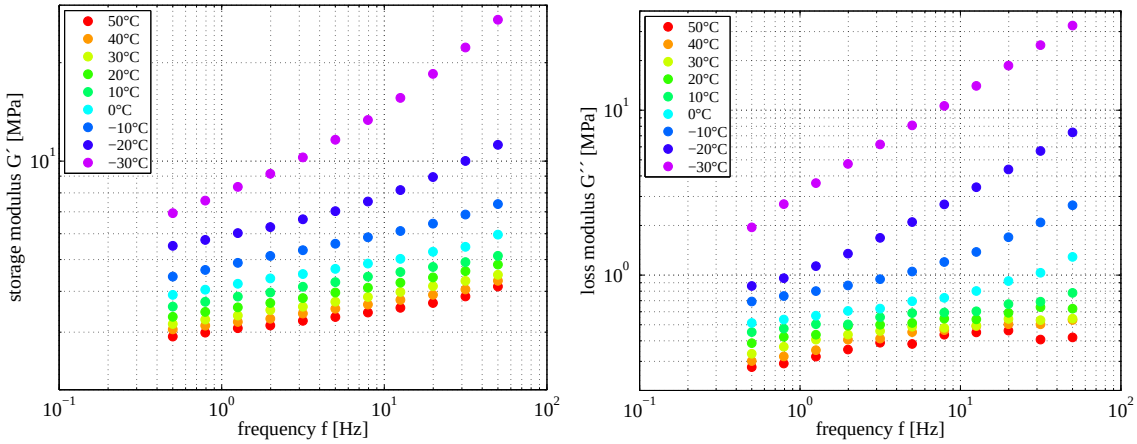

FIGURE 5.17: Temperature dependence of the dynamic moduli of SBR20 at a prestrain of 10 % (left: storage modulus), (right: loss modulus)

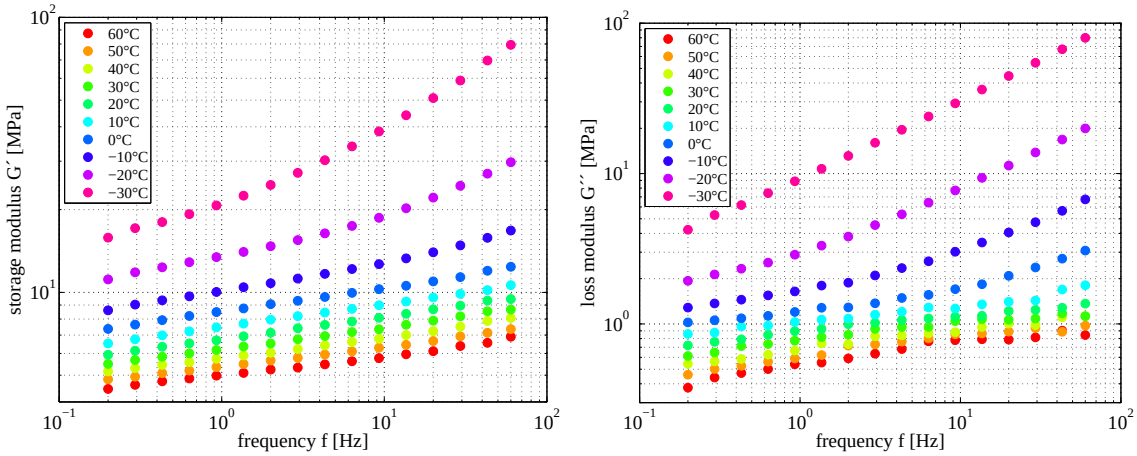

FIGURE 5.18: Temperature dependence of the dynamic moduli of SBR40 at a prestrain of 10 % (left: storage modulus), (right: loss modulus)

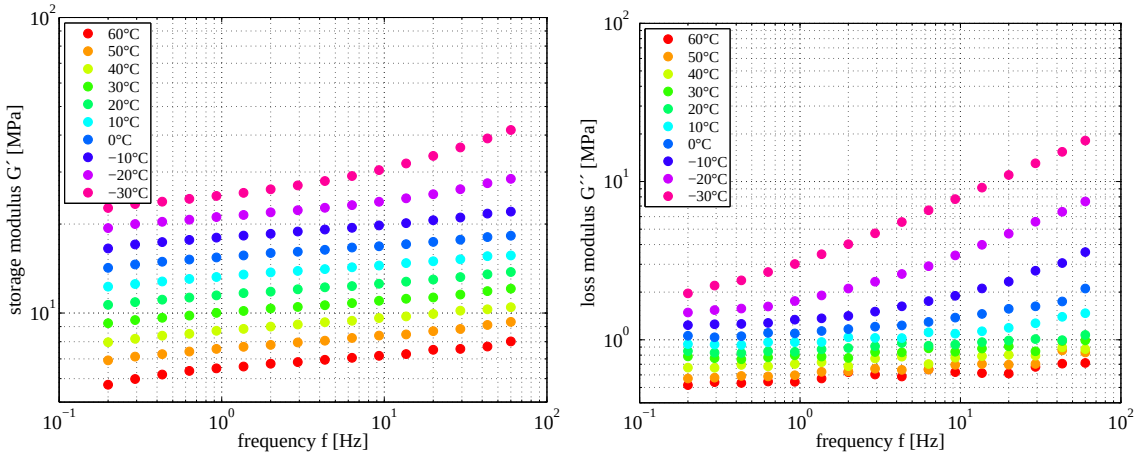

FIGURE 5.19: Temperature dependence of the dynamic moduli of NR40 at a prestrain of 10 % (left: storage modulus), (right: loss modulus)

temperatures ($\theta < \theta_0$) are shifted to higher frequencies in a logarithmic frequency scale. The unknown material parameters c_1 and c_2 are identified by an identification algorithm which is programmed in the mathematical software tool MATLAB. The identification is based on error minimisation to obtain a master curve which is as continuous as possible. Moreover, the identification of the parameters is performed with respect to the whole set of experimental data meaning the storage and the loss modulus at each predeformation are taken into account. This fact is due to the assumption that c_1 and c_2 are classified as material parameters. For physical reasons, these should be independent of the static predeformation.
The material parameters c_1 and c_2 obtained from this identification procedure are listed in table 5.5 for each material.

	c_1	c_2
SBR20	4.232	107.666
SBR40	7.317	134.554
EPDM20	5.571	107.925
NR40	53.371	459.784

TABLE 5.5: Identified material parameters c_1 and c_2 of the WLF-function

If these parameters are inserted into the WLF equation (5.7), the shifting function $\log a_\theta$ is obtained for each material. They are plotted in figure 5.20 for the different vulcanisates.

Using these results, the experimental frequency range can be extended by multiplying the shifting function with the experimental frequencies of the temperature-frequency-sweep tests. In so doing, the mastered frequency f_{master} is given by the product of $\log a_\theta(\theta_x)$ and the corresponding experimental frequency $f_{exp}(\theta_x)$ at temperature θ_x

$$f_{master} = \log a_\theta(\theta_x)\, f_{exp}(\theta_x) \; . \tag{5.8}$$

For illustration, the experimental temperature-frequency-sweep data of the storage modulus of SBR40 at a prestrain of 10 % and the corresponding master curve with respect to the reference temperature of 20 °C are displayed in figure 5.21.

Regarding the whole experimental data with respect to each material and each predeformation, the master curves of the storage and the loss modulus are obtained as per figures 5.22 - 5.25. According to the argumentation that the predeformation dependence is related to the nonlinear equilibrium stress curve, the moduli are displayed with respect to the reference configuration (1st Piola-Kirchhoff type).

As expected, the experimental observations exhibit an increase in both moduli with increasing frequency. Among others, this characteristic dynamic behaviour of rubber was also found in other investigations by Kari (2003), Hoefer and Lion (2009) or Rendek and Lion (2010b). As already observed in the static-sweep tests, both moduli increase with the predeformation which is due to the nonlinear hyperelastic material characteristics.

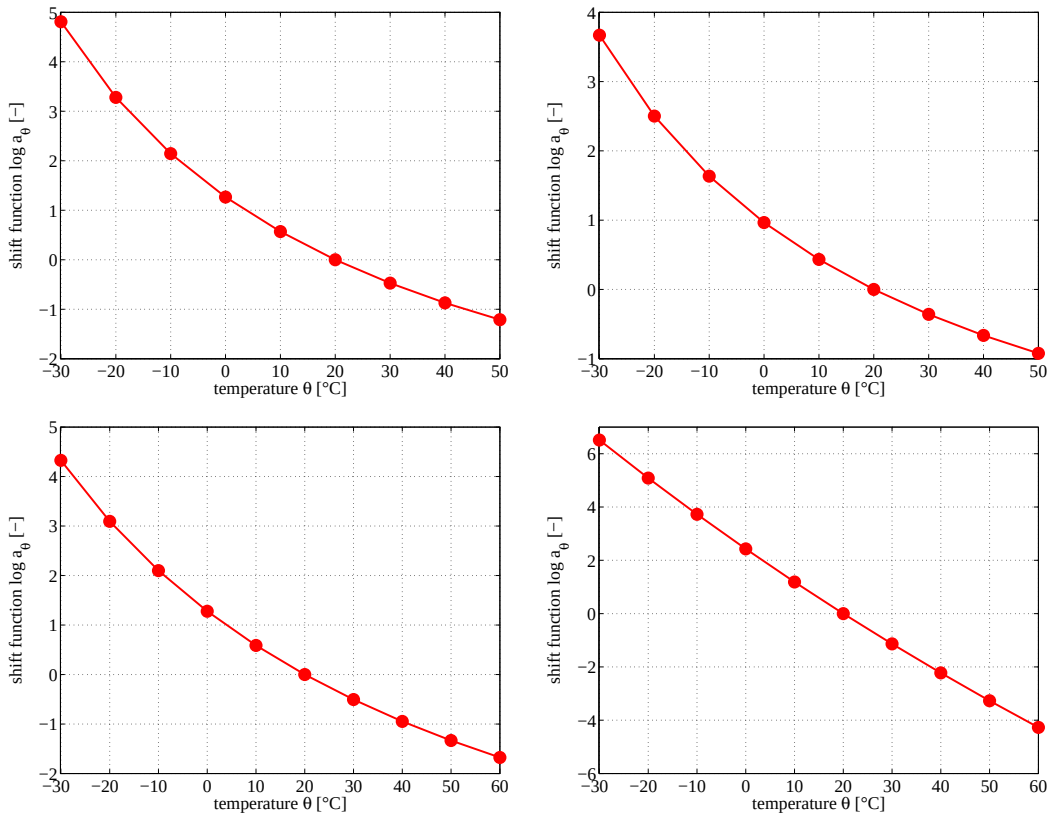

FIGURE 5.20: Shifting function for each material (upper left: EPDM20), (upper right: SBR20), (lower left: SBR40), (lower right: NR40)

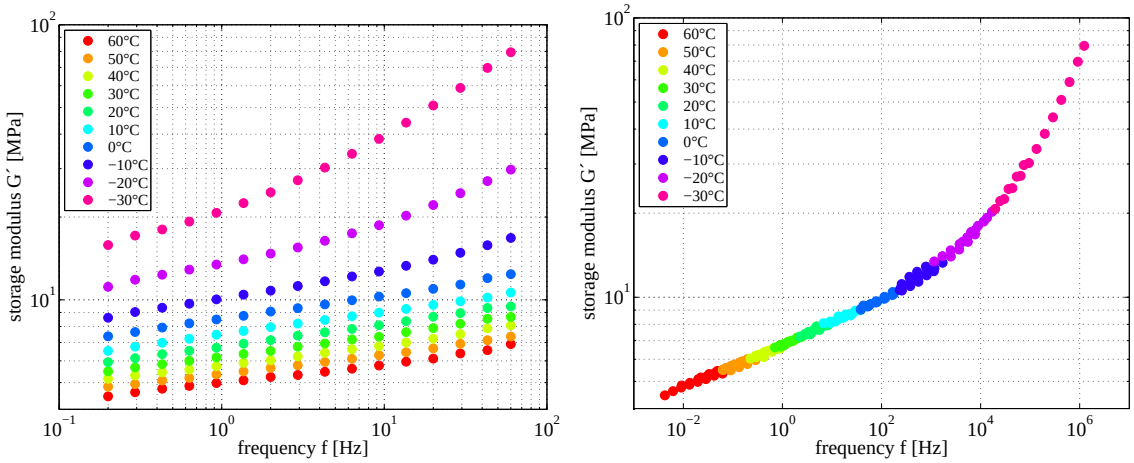

FIGURE 5.21: Temperature-frequency-sweep data of SBR40 (left) and calculated master curve (right)

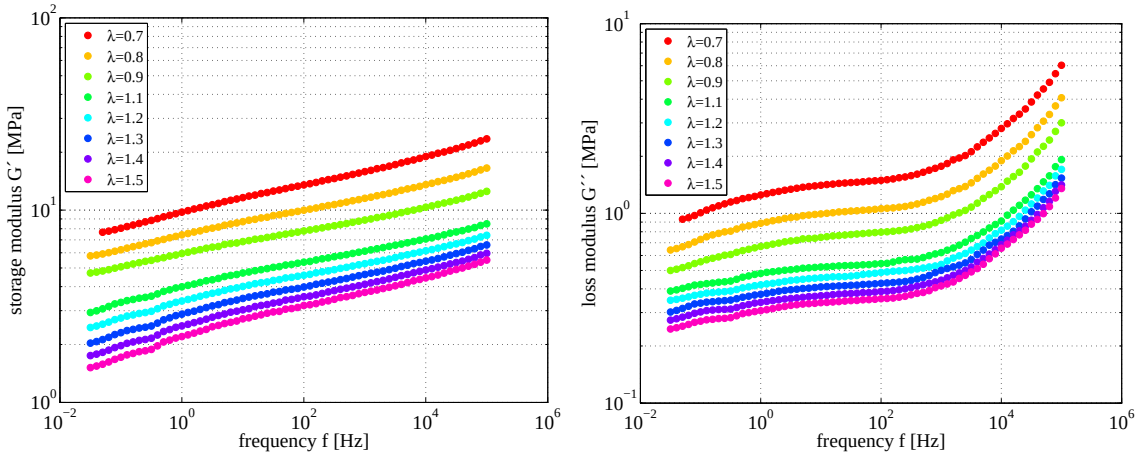

FIGURE 5.22: Master curves of EPDM20 (left: storage modulus), (right: loss modulus)

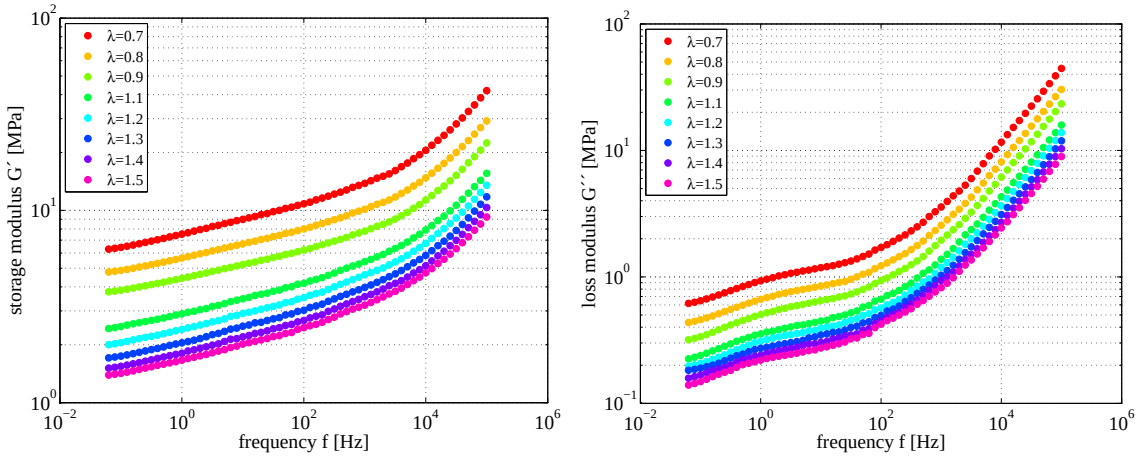

FIGURE 5.23: Master curves of SBR20 (left: storage modulus), (right: loss modulus)

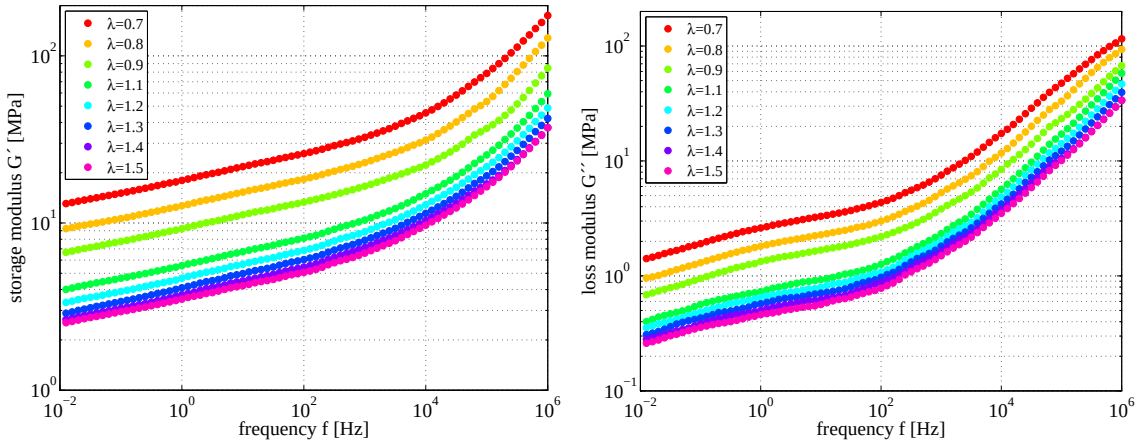

FIGURE 5.24: Master curves of SBR40 (left: storage modulus), (right: loss modulus)

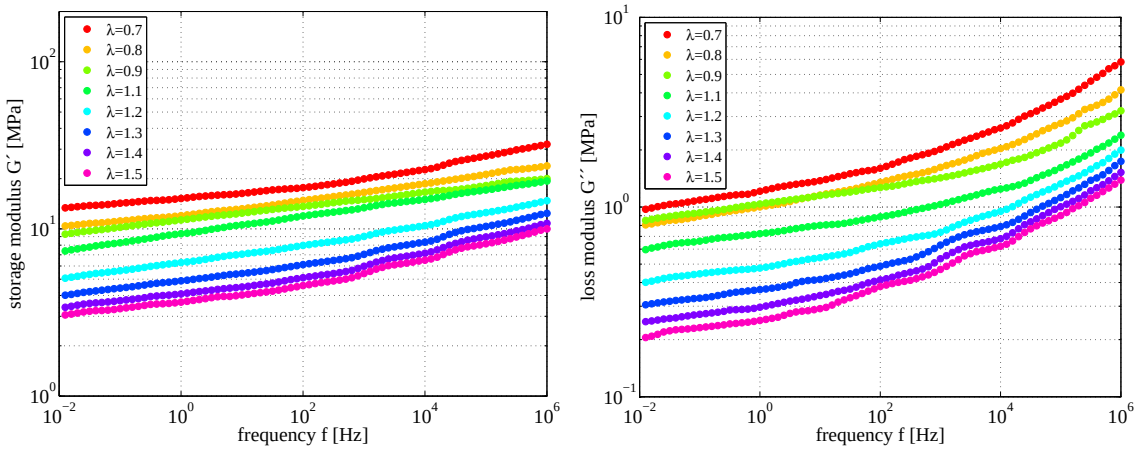

FIGURE 5.25: Master curves of NR40 (left: storage modulus), (right: loss modulus)

Moreover, the master curves reveal that the mutual influence of predeformation and frequency on each other is fairly small and thus negligible. As illustrated in figure 5.26 - 5.29, this fact becomes more clear if the predeformation dependence of the dynamic moduli is plotted in a logarithmic scale at different frequencies. Since the predeformation dependent characteristics of the storage and the loss modulus are identical for each frequency, they have no mutual influence on each other and thus can be considered separately.

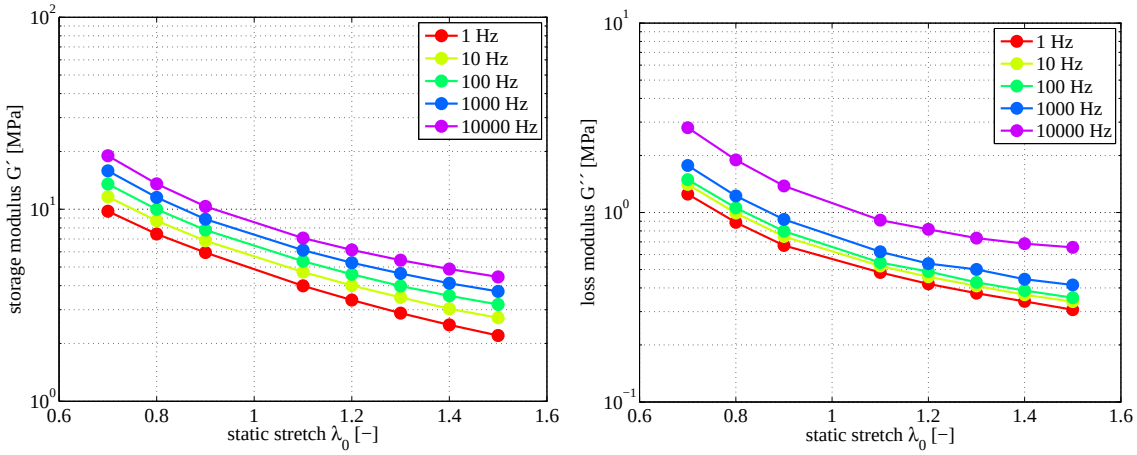

FIGURE 5.26: EPDM20: Independence of static predeformation and frequency from each other (left: storage modulus), (right: loss modulus)

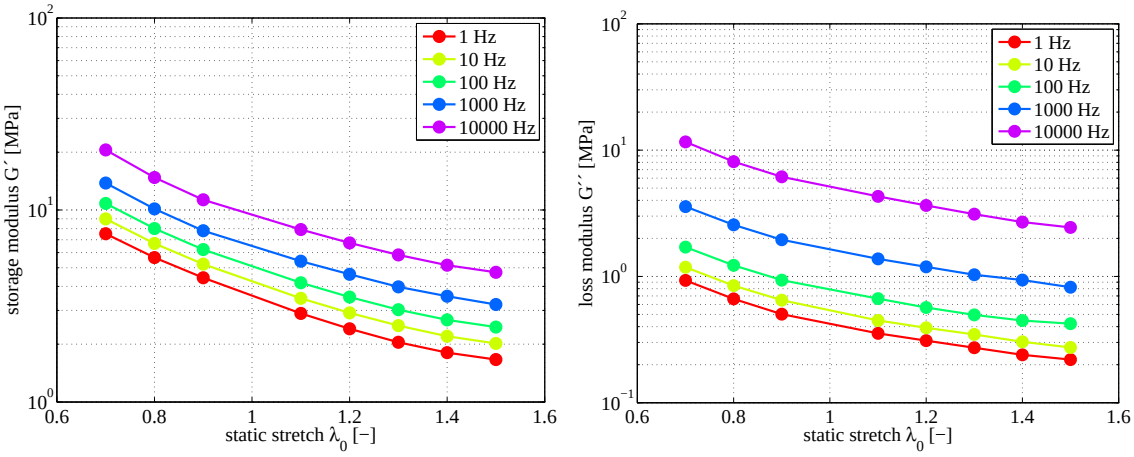

FIGURE 5.27: SBR20: Independence of static predeformation and frequency from each other (left: storage modulus), (right: loss modulus)

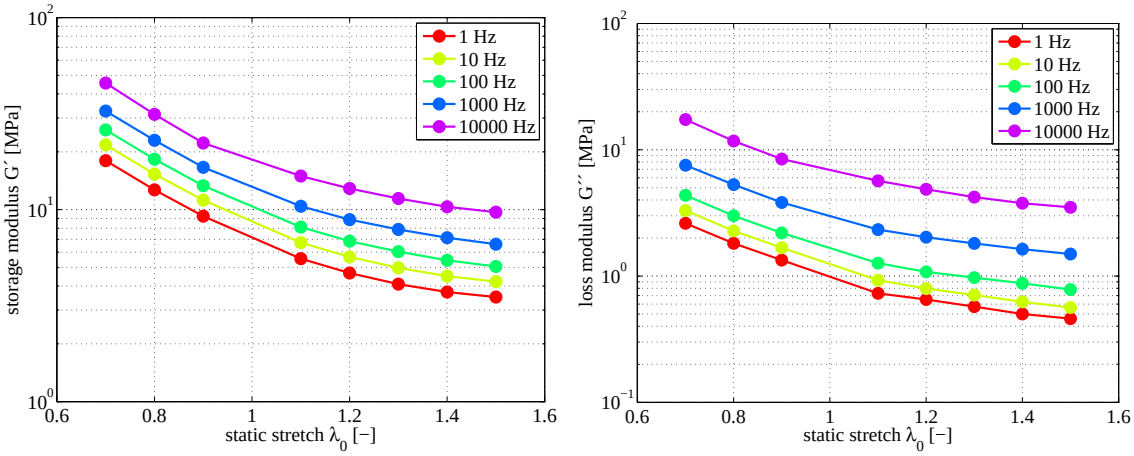

FIGURE 5.28: SBR40: Independence of static predeformation and frequency from each other (left: storage modulus), (right: loss modulus)

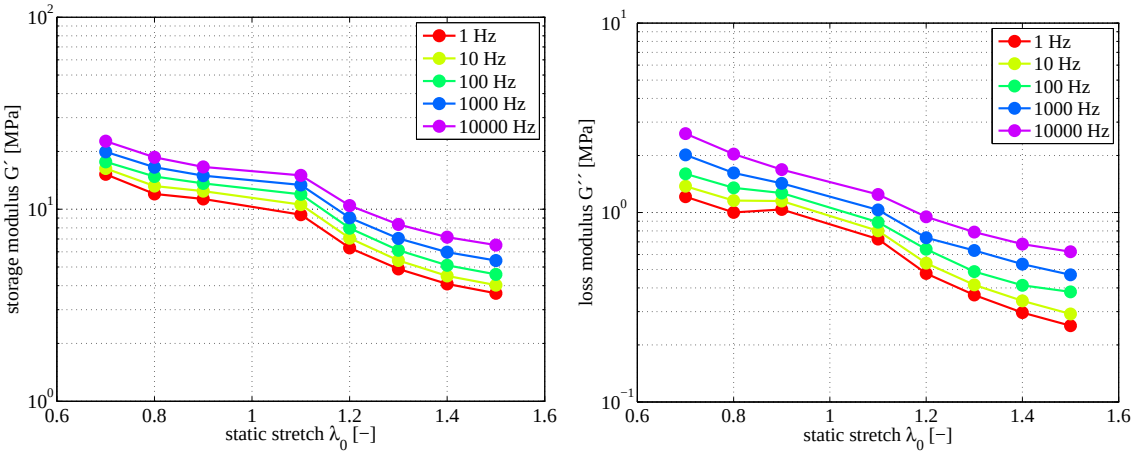

FIGURE 5.29: NR40: Independence of static predeformation and frequency from each other (left: storage modulus), (right: loss modulus)

5.4 Conclusion

Since the experimental observations are essential to formulate a suitable constitutive approach the results of the investigations are resumed in the following. Thereby, the most important conclusion is based on the fact that the storage and the loss modulus of the investigated carbon-black reinforced rubbers are strongly dependent on predeformation and frequency if large static predeformations are combined with superimposed harmonic excitations.

The quasi-static investigations revealed that each vulcanisate is characterised by the Mullins effect, whereas higher amounts of filler result in an increase of stress-softening. Moreover, the equilibrium stress response of the investigated materials depends on the static predeformation and is characterised by the typical nonlinear relation between stress and strain.

On the basis of the dynamic mechanical tests it was first observed that the amplitude dependent Payne effect is not pronounced for strain amplitudes of 0.1 % and is thus negligible.
The storage and the loss modulus exhibit a pronounced dependence on predeformation, in which the characteristics of both moduli can be related to the nonlinear equilibrium stress-strain curve. The influence on temperature appears in a decrease of the storage and the loss modulus with increasing temperature whereas the dependence of the both moduli on frequency is determined by an increase with increasing frequency in the entire frequency range.
Moreover, the dependence of the storage and the loss modulus on predeformation and frequency is independent of each other such that the influence of both parameters can be considered separately.

Chapter 6

Constitutive modelling

Introduction

Constitutive models focus on a mathematical description of materials and their specific material properties. Based on this, the main task of constitutive models is to represent the mechanical or thermomechanical material behaviour under specific environmental effects. In this context, the focus is mostly on a parallel description of various material properties, such as elasticity, rate or frequency dependence, softening effects or temperature dependence. But, in conjunction with the complex material behaviour of rubber and especially that of filler-reinforced vulcanisates, a mathematical description is generally limited to the representation of some of these effects.
The basic requirement to formulate suitable constitutive models consists in knowledge of specific material characteristics which are mostly obtained through experimental investigations.
In general, physically meaningful constitutive models must be thermomechanical consistent meaning that they have to be conform to the second law of thermodynamics. Moreover, the developed material laws constitute the basis for finite element simulations which are commonly applied by the industry to approximate the material behaviour of complex structures in simulations close to reality.

Outline

The aim of this chapter is to present two constitutive formulations of nonlinear finite viscoelasticity which are capable of describing the dynamic material characteristics of the investigated carbon-black filled rubber vulcanisates under large constant predeformation superimposed by harmonic vibrations of small amplitude. The first approach can be related to a classical Maxwell chain whereas the second one is based on an extension with fractional derivatives and can be interpreted as a fractional Maxwell chain. The focus of both constitutive models is on the representation of the experimentally observed dependence of the storage and the loss modulus on predeformation and frequency from $10^{-2}\,\mathrm{Hz}$ up to $10^{5}\,\mathrm{Hz}$. The constitutive formulations are based on the general approach by Haupt and Lion (2002) which is modified to describe the

predeformation and frequency dependent dynamic material properties in this work. Due to computational effort, both constitutive models are originally formulated in the time domain and then transferred into the frequency domain. A similar but less detailed approach to describe the frequency dependence of rubber structures without a full description of predeformation dependence is proposed by Retka (2011).

In order to introduce the basic concept of the fully three-dimensional constitutive models, the first section of this chapter starts with a one-dimensional formulation based on a classical Maxwell chain. This model is suitable to represent rate and frequency dependent material properties, but a description of the predeformation dependent material characteristics observed is not possible in its general form. In order to represent the predeformation dependence of the dynamic moduli as well, the classical Maxwell chain is extended by adding deformation dependence to the stiffness parameters of the Maxwell elements. On this basis, a representation of the frequency and predeformation dependent characteristics of the storage and the loss modulus becomes possible.

In the second section, a three-dimensional formulation of the classical and fractional constitutive models is derived. The section starts with a general time domain formulation of the constitutive approach with respect to an arbitrary deformation dependent relaxation function. After linearisation, the classical and fractional constitutive models are derived by specifying adequate relaxation functions and by transferring the linearised time domain formulation to the frequency domain.

The presentation of the three-dimensional concept starts with the introduction of the underlying kinematic relations which are required to derive the constitutive equations. To this end, the deformation gradient $\mathbf{F}$ is twice decomposed to formulate a specific Helmholtz free energy. The first decomposition is a multiplicative decomposition of the deformation gradient into an isochoric part $\hat{\mathbf{F}}$ and a volumetric part $\bar{\mathbf{F}}$ whereas the second decomposition is a time-relative decomposition of the isochoric part of the deformation gradient. On the basis of this decomposition, the specific Helmholtz free energy Ψ is formulated through an additive decomposition into an equilibrium part Ψ_{eq} and a non-equilibrium part Ψ_{ov}. The constitutive equation for the 2nd Piola-Kirchhoff stress tensor $\tilde{\mathbf{T}}$ is obtained from the isothermal Clausius-Planck inequality and results in an additive decomposition into an equilibrium part $\tilde{\mathbf{T}}_{eq}$ and an overstress part $\tilde{\mathbf{T}}_{ov}$ as well. In order to prepare the constitutive approach for a formulation in the frequency domain, the constitutive equations are linearised in the neighbourhood of the predeformation, as proposed by Haupt and Lion (2002). Following this procedure, the 2nd Piola-Kirchhoff stress tensor results in the additive composition of a temporally constant static stress $\tilde{\mathbf{T}}_0$ and a linearised dynamic overstress $\tilde{\mathbf{T}}_{ov,lin}$. Since the materials investigated are assumed to be incompressible, the constitutive equations are finally formulated for incompressible material behaviour.
After that, the linearised constitutive model is transferred to the frequency domain and the complex modulus tensors of fourth order are derived for the classical and the fractional constitutive models. In order to do that, adequate relaxation functions are defined and the harmonic stress response of both models is calculated. The classical model is based on a relaxation function of the exponential type which is related to that of a classical Maxwell chain whereas the relaxation function of the extended fractional

formulation is related to that of a fractional Maxwell chain. Therefore, both models can be interpreted as a generalisation of the classical and fractional Maxwell chain models.

Since the classical Maxwell chain approximates viscoelastic material properties by a discrete spectrum with relaxation functions of the exponential type, numerous Maxwell elements are required in parallel to quantitatively approximate the frequency dependent behaviour of the dynamic moduli in the broad frequency range this work is focused on. On the contrary, the fractional formulation of the constitutive approach is characterised by a continuous relaxation spectrum on the basis of which a better approximation of the dynamic material behaviour with less parameters can be achieved.

It is stated, that some parts of constitutive modelling have been published in prior printed publications which were approved by the university (Wollscheid and Lion (2012), Wollscheid and Lion (2013a), Wollscheid and Lion (2013b) and Wollscheid and Lion (2014)).

6.1 One-dimensional approach

In order to motivate the modelling concept, the classical Maxwell chain in figure 6.1 is discussed first. This model is composed of the parallel connection of an elastic spring with the stiffness E and $k = 1...n$ Maxwell elements with the stiffness parameters μ_k and the viscosities η_k.

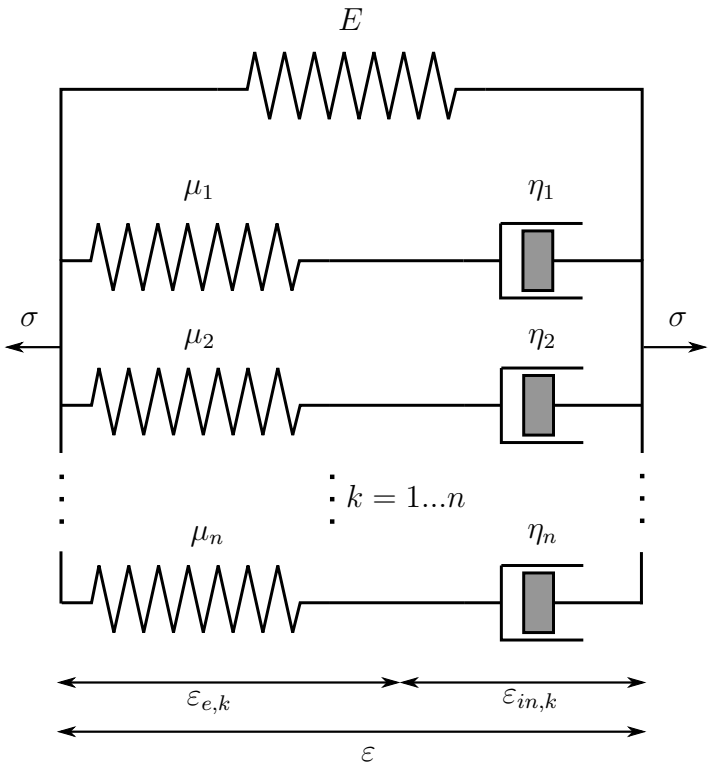

FIGURE 6.1: Classical Maxwell chain

If the corresponding differential equation

$$\dot{\sigma}_{ov,k} + \frac{\mu_k}{\eta_k}\,\sigma_{ov,k} = \mu_k\,\dot{\varepsilon} \tag{6.1}$$

is solved for a harmonic excitation

$$\varepsilon = \varepsilon_0 + \Delta\varepsilon\,\mathrm{e}^{i\omega t}\ , \tag{6.2}$$

the relations for the storage and the loss modulus of the k-th Maxwell element are obtained as

$$\begin{aligned} G'(\omega) &= \mu_k \frac{(\omega\,\tau_k)^2}{1+(\omega\,\tau_k)^2}\ , \\ G''(\omega) &= \mu_k \frac{\omega\,\tau_k}{1+(\omega\,\tau_k)^2}\ . \end{aligned} \tag{6.3}$$

The dynamic moduli of the complete Maxwell chain are calculated by summation and read as

$$\begin{aligned} G'(\omega) &= E + \sum_{k=1}^{n} \mu_k \frac{(\omega\,\tau_k)^2}{1+(\omega\,\tau_k)^2}\ , \\ G''(\omega) &= \sum_{k=1}^{n} \mu_k \frac{\omega\,\tau_k}{1+(\omega\,\tau_k)^2}\ . \end{aligned} \tag{6.4}$$

Both dynamic moduli are functions of the frequency ω. In order to add predeformation dependence through the back-door, the stiffness parameters μ_k of the Maxwell elements and the modulus E can be defined as functions of predeformation

$$\mu_k = \mu_k(\varepsilon_0) \quad , \quad E = E(\varepsilon_0)\ . \tag{6.5}$$

Regarding this extension, the storage and the loss modulus both depend on predeformation and frequency

$$\begin{aligned} G'(\omega,\varepsilon_0) &= E(\varepsilon_0) + \sum_{k=1}^{n} \mu_k(\varepsilon_0) \frac{(\omega\,\tau_k)^2}{1+(\omega\,\tau_k)^2}\ , \\ G''(\omega,\varepsilon_0) &= \sum_{k=1}^{n} \mu_k(\varepsilon_0) \frac{\omega\,\tau_k}{1+(\omega\,\tau_k)^2}\ . \end{aligned} \tag{6.6}$$

The functional correlation between the dynamic moduli and the predeformation can be obtained through experimental investigations. Apart from predeformation dependent stiffness parameters, it would also be possible to introduce predeformation dependent relaxation times or even both.

6.2 Three-dimensional approach

In this section, a three-dimensional formulation of the classical and of the fractional constitutive approaches will be introduced. The section starts with an introduction of

the kinematics and a general time domain formulation of the constitutive equations. After that, the frequency domain formulations are derived with respect to the classical and the fractional Maxwell chain.

6.2.1 Kinematics

In order to formulate the specific Helmholtz free energy, the deformation gradient $\mathbf{F}(t)$ is twice decomposed. The first separation is a volumetric-isochoric decomposition of the deformation gradient into a volumetric part $\bar{\mathbf{F}}(t)$ and an isochoric part $\hat{\mathbf{F}}(t)$

$$\mathbf{F}(t) \;=\; \bar{\mathbf{F}}(t)\,\hat{\mathbf{F}}(t) \quad \text{with} \quad \bar{\mathbf{F}}(t) \;=\; J^{\frac{1}{3}}(t)\,\mathbf{1}\;, \quad \hat{\mathbf{F}}(t) \;=\; J^{-\frac{1}{3}}\,\mathbf{F}(t) \tag{6.7}$$

and the Jacobian determinant $J = \det(\mathbf{F}(t))$. The volumetric part of the deformation gradient is related to the deformation induced by changes in the volume whereas the isochoric part is related to the deformation which is due to changes in the shape of the body. In terms of incompressible material behaviour, the Jacobian determinant is equal to 1 and the isochoric part $\hat{\mathbf{F}}(t)$ is equal to $\mathbf{F}(t)$. The second decomposition is a time-relative decomposition of the isochoric part of the deformation gradient, on the basis of which the relative isochoric deformation gradient arises

$$\hat{\mathbf{F}}_t(s) \;=\; \hat{\mathbf{F}}(s)\,\hat{\mathbf{F}}^{-1}(t) \quad , \quad 0 \;\leq\; s \;\leq\; t\;. \tag{6.8}$$

As illustrated in figure 6.2, the relative isochoric deformation gradient maps tangent vectors of the current isochoric configuration $\mathcal{I}_i$ at time t onto tangent vectors of a previous isochoric configuration $\mathcal{I}_{i,t}$ at time s. Thus, $\hat{\mathbf{F}}_t(s)$ represents a deformation state at time s.

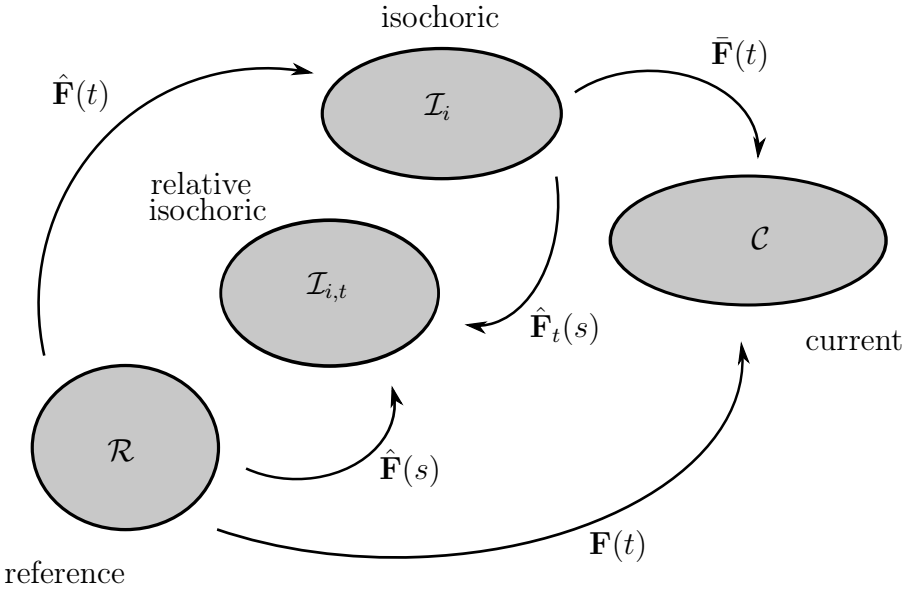

FIGURE 6.2: Relative-isochoric decomposition

Based on the double decomposition of the deformation gradient, the relative isochoric right Cauchy-Green deformation tensor and its inverse are defined by

$$\begin{aligned}
\hat{\mathbf{C}}_t(s) &= \hat{\mathbf{F}}_t^T(s)\,\hat{\mathbf{F}}_t(s) = \hat{\mathbf{F}}^{-T}(t)\,\hat{\mathbf{F}}^T(s)\,\hat{\mathbf{F}}(s)\,\hat{\mathbf{F}}^{-1}(t) = \hat{\mathbf{F}}^{-T}(t)\,\hat{\mathbf{C}}(s)\,\hat{\mathbf{F}}^{-1}(t)\ , \\
\hat{\mathbf{C}}_t^{-1}(s) &= \left(\hat{\mathbf{F}}_t^T(s)\,\hat{\mathbf{F}}_t(s)\right)^{-1} = \hat{\mathbf{F}}_t^{-1}(s)\,\hat{\mathbf{F}}_t(s)^{-T} \\
&= \hat{\mathbf{F}}(t)\,\hat{\mathbf{F}}^{-1}(s)\,\hat{\mathbf{F}}^{-T}(s)\,\hat{\mathbf{F}}^T(t) = \hat{\mathbf{F}}(t)\,\hat{\mathbf{C}}^{-1}(s)\,\hat{\mathbf{F}}^T(t)\ .
\end{aligned} \tag{6.9}$$

With the inverse of the relative isochoric right Cauchy-Green tensor in (6.9) and relation (2.17), the definition of the relative isochoric Piola strain tensor can be defined

$$\begin{aligned}
\hat{\mathbf{e}}_t(s) &= \frac{1}{2}\left[\hat{\mathbf{C}}_t^{-1}(s) - \mathbf{1}\right] \\
&= \frac{1}{2}\left[\hat{\mathbf{F}}(t)\,\hat{\mathbf{C}}^{-1}(s)\,\hat{\mathbf{F}}^T(t) - \mathbf{1}\right] \\
&= \frac{1}{2}\,\hat{\mathbf{F}}(t)\left[\hat{\mathbf{C}}^{-1}(s) - \hat{\mathbf{F}}^{-1}(t)\,\hat{\mathbf{F}}^{-T}(t)\right]\hat{\mathbf{F}}^T(t) \\
&= \frac{1}{2}\,\hat{\mathbf{F}}(t)\left[\hat{\mathbf{C}}^{-1}(s) - \hat{\mathbf{C}}^{-1}(t)\right]\hat{\mathbf{F}}^T(t) \\
&= \hat{\mathbf{F}}(t)\left[\hat{\mathbf{e}}(s) - \hat{\mathbf{e}}(t)\right]\hat{\mathbf{F}}^T(t)\ .
\end{aligned} \tag{6.10}$$

6.2.2 Specific Helmholtz free energy

The specific Helmholtz free energy is defined by the additive decomposition into an elastic part $\rho_0\,\Psi_{eq}(\mathbf{C}(t))$ and an overstress part $\rho_0\,\Psi_{ov}(t)$.

$$\rho_0\,\Psi(t) = \rho_0\,\Psi_{eq}(\mathbf{C}(t)) + \rho_0\,\Psi_{ov}(t)\ . \tag{6.11}$$

The elastic part is a function of the right Cauchy-Green tensor $\mathbf{C}(t)$ whereas the overstress part is a functional of the history of the relative isochoric Piola strain tensor $\hat{\mathbf{e}}_t$

$$\rho_0\,\Psi_{ov}(t) = -\int_{-\infty}^{t} G(t-s,\hat{\mathbf{C}}(t))\,\frac{\mathrm{d}}{\mathrm{d}s}\,\mathrm{tr}(\hat{\mathbf{e}}_t(s))\,\mathrm{d}s\ . \tag{6.12}$$

In order to describe the dependence of the dynamic moduli on predeformation, a deformation dependent relaxation function $G(t-s,\hat{\mathbf{C}}(t))$ depending on the current deformation is introduced. This formulation corresponds to a model of finite viscoelasticity in which the stress relaxation behaviour depends on the deformation at which the relaxation takes place. If this approach is linearised, it leads to dynamic moduli which depend on the static predeformation. Moreover, the linearised constitutive approach can be interpreted as a generalisation of the classical Maxwell chain in which the stiffness parameters and/or the viscosities of the Maxwell elements depend on the static predeformation.
On the basis of (6.11) and (6.12), the material time derivative of the specific Helmholtz

free energy is obtained by applying the product rule of differentiation

$$\begin{aligned}\rho_0\,\dot{\Psi}(t) \;=\; \rho_0\,\dot{\Psi}_{eq}(\mathbf{C}(t)) \;&\underbrace{-\,G(0,\hat{\mathbf{C}}(t))\,\frac{\mathrm{d}}{\mathrm{d}t}\,\mathrm{tr}(\hat{\mathbf{e}}_t(t))}_{\rho_0\,\dot{\Psi}_{ov,1}}\\ &\underbrace{-\int_{-\infty}^{t} G(t-s,\hat{\mathbf{C}}(t))\,\frac{\mathrm{d}}{\mathrm{d}t}\left[\frac{\mathrm{d}}{\mathrm{d}s}\,\mathrm{tr}(\hat{\mathbf{e}}_t(s))\right]\mathrm{d}s}_{\rho_0\,\dot{\Psi}_{ov,2}}\\ &\underbrace{-\left[\int_{-\infty}^{t}\frac{\partial G(t-s,\hat{\mathbf{C}}(t))}{\partial\hat{\mathbf{C}}(t)}\,\frac{\mathrm{d}}{\mathrm{d}s}\,\mathrm{tr}(\hat{\mathbf{e}}_t(s))\,\mathrm{d}s\right]\cdot\dot{\hat{\mathbf{C}}}(t)}_{\rho_0\,\dot{\Psi}_{ov,3}}\\ &\underbrace{-\int_{-\infty}^{t}\frac{\partial G(t-s,\hat{\mathbf{C}}(t))}{\partial t}\,\frac{\mathrm{d}}{\mathrm{d}s}\,\mathrm{tr}(\hat{\mathbf{e}}_t(s))\,\mathrm{d}s}_{\rho_0\,\dot{\Psi}_{ov,4}}\;.\end{aligned}\tag{6.13}$$

The rate of the overstress $\rho_0\,\dot{\Psi}_{ov}$ can be separated into four parts $\rho_0\,\dot{\Psi}_{ov,1}$, $\rho_0\,\dot{\Psi}_{ov,2}$, $\rho_0\,\dot{\Psi}_{ov,3}$ and $\rho_0\,\dot{\Psi}_{ov,4}$. These parts are first rearranged to derive a simplified formulation of the derivative of the specific Helmholtz free energy.
Since the relative intermediate configuration $\mathcal{I}_{i,t}$ and the reference configuration $\mathcal{C}$ match together at time $s = t$, the relative isochoric Piola strain tensor is equal to zero for $s = t$

$$\hat{\mathbf{e}}_t(t) \;=\; \mathbf{0}\;. \tag{6.14}$$

Taking this into account, the overstress part $\rho_0\,\dot{\Psi}_{ov,1}$ in equation (6.13) vanishes

$$\rho_0\,\dot{\Psi}_{ov,1}(t) \;=\; -\,G(0,\hat{\mathbf{C}}(t))\,\frac{\mathrm{d}}{\mathrm{d}t}\,\mathrm{tr}(\hat{\mathbf{e}}_t(t)) \;=\; 0\;. \tag{6.15}$$

In order to rearrange the other parts, the derivative of the trace of the relative isochoric Piola strain tensor with respect to s as well as its temporal derivative must first be calculated. Based on the derivative of the relative isochoric Piola strain tensor with respect to s

$$\frac{\mathrm{d}}{\mathrm{d}s}\,\hat{\mathbf{e}}_t(s) \;=\; \hat{\mathbf{F}}(t)\left(\frac{\mathrm{d}}{\mathrm{d}s}\,\hat{\mathbf{e}}(s)\right)\hat{\mathbf{F}}^T(t) \;=\; \hat{\mathbf{F}}(t)\,\hat{\mathbf{e}}'(s)\,\hat{\mathbf{F}}^T(t) \tag{6.16}$$

and the trace operation

$$\mathrm{tr}(\hat{\mathbf{e}}_t(s)) \;=\; [\hat{\mathbf{e}}(s) \;-\; \hat{\mathbf{e}}(t)]\;\cdot\;\hat{\mathbf{C}}(t)\;, \tag{6.17}$$

the derivative of the trace of $\hat{\mathbf{e}}_t(s)$ with respect to s reads as

$$\frac{\mathrm{d}}{\mathrm{d}s}\,\mathrm{tr}(\hat{\mathbf{e}}_t(s)) \;=\; \mathrm{tr}\left(\frac{\mathrm{d}}{\mathrm{d}s}\,\hat{\mathbf{e}}_t(s)\right) \;=\; \hat{\mathbf{e}}'(s)\;\cdot\;\hat{\mathbf{C}}(t)\;. \tag{6.18}$$

Evaluating this relation at time $s = t$ and taking the temporal derivative of the inverse isochoric right Cauchy-Green deformation tensor into account

$$\dot{\hat{\mathbf{C}}}^{-1}(t) = -\hat{\mathbf{C}}^{-1}(t)\,\dot{\hat{\mathbf{C}}}(t)\,\hat{\mathbf{C}}^{-1}(t)\;, \tag{6.19}$$

the following result is obtained

$$\begin{aligned}
\dot{\hat{\mathbf{e}}}(t)\cdot\hat{\mathbf{C}}(t) &= \frac{1}{2}\left[\hat{\mathbf{C}}^{-1}(t)-\mathbf{1}\right]^{\cdot}\cdot\hat{\mathbf{C}}(t) = \frac{1}{2}\left(\hat{\mathbf{C}}^{-1}(t)\right)^{\cdot}\cdot\hat{\mathbf{C}}(t)\\
&= -\frac{1}{2}\left[\hat{\mathbf{C}}^{-1}(t)\,\dot{\hat{\mathbf{C}}}(t)\,\hat{\mathbf{C}}^{-1}(t)\right]\cdot\hat{\mathbf{C}}(t)\\
&= -\frac{1}{2}\,\mathrm{tr}\left(\hat{\mathbf{C}}^{-1}(t)\,\dot{\hat{\mathbf{C}}}(t)\,\hat{\mathbf{C}}^{-1}(t)\,\hat{\mathbf{C}}(t)\right) = -\frac{1}{2}\,\mathrm{tr}\left(\hat{\mathbf{C}}^{-1}(t)\,\dot{\hat{\mathbf{C}}}(t)\right)\\
&= -\frac{1}{2}\,\mathrm{tr}\left(\hat{\mathbf{C}}^{-1}(t)\,\left[\dot{\hat{\mathbf{F}}}^{T}(t)\,\hat{\mathbf{F}}(t)+\hat{\mathbf{F}}^{T}(t)\,\dot{\hat{\mathbf{F}}}(t)\right]\right)\\
&= -\frac{1}{2}\,\mathrm{tr}\left(\dot{\hat{\mathbf{F}}}(t)\,\hat{\mathbf{F}}^{-1}(t)+\hat{\mathbf{F}}^{-T}(t)\,\dot{\hat{\mathbf{F}}}^{T}(t)\right)\\
&= -\frac{1}{2}\,\mathrm{tr}\left(\hat{\mathbf{L}}(t)+\hat{\mathbf{L}}^{T}(t)\right) = -\,\mathrm{tr}\left(\hat{\mathbf{D}}\right) = 0\;.
\end{aligned} \tag{6.20}$$

Using (6.20), the time derivative of (6.18) is obtained by applying the product rule of differentiation and finally reads as

$$\frac{\mathrm{d}}{\mathrm{d}t}\left(\frac{\mathrm{d}}{\mathrm{d}s}\,\mathrm{tr}(\hat{\mathbf{e}}_t(s))\right) = \frac{\mathrm{d}}{\mathrm{d}t}\left(\hat{\mathbf{e}}'(s)\cdot\hat{\mathbf{C}}(t)\right) = \dot{\hat{\mathbf{e}}}'(s)\cdot\hat{\mathbf{C}}(t)+\hat{\mathbf{e}}'(s)\cdot\dot{\hat{\mathbf{C}}}(t)\;. \tag{6.21}$$

Since $\dot{\hat{\mathbf{e}}}'(s)$ is a function of s, the first term in (6.21) equals zero. Taking the time derivative of the determinant of the right Cauchy-Green tensor into account

$$\frac{\mathrm{d}}{\mathrm{d}t}\left(\det\mathbf{C}(t)\right) = \frac{\partial\det\mathbf{C}(t)}{\partial\mathbf{C}(t)}\cdot\dot{\mathbf{C}}(t) = \left(\det\mathbf{C}(t)\right)\mathbf{C}^{-1}(t)\cdot\dot{\mathbf{C}}(t)\;, \tag{6.22}$$

the second term in (6.21) can be reformulated by applying the product rule of differentiation

$$\begin{aligned}
\hat{\mathbf{e}}'(s) \cdot \dot{\hat{\mathbf{C}}}(t) &= \hat{\mathbf{e}}'(s) \cdot \left[(\det \mathbf{C}(t))^{-\frac{1}{3}} \, \mathbf{C}(t) \right]^{\cdot} \\
&= \hat{\mathbf{e}}'(s) \cdot \left[-\frac{1}{3} (\det \mathbf{C}(t))^{-\frac{1}{3}} \left(\mathbf{C}^{-1}(t) \cdot \dot{\mathbf{C}}(t) \right) \mathbf{C}(t) + (\det \mathbf{C}(t))^{-\frac{1}{3}} \, \dot{\mathbf{C}}(t) \right] \\
&= \hat{\mathbf{e}}'(s) \cdot \left[(\det \mathbf{C}(t))^{-\frac{1}{3}} \left\{ \dot{\mathbf{C}}(t) - \frac{1}{3} \left(\dot{\mathbf{C}}(t) \cdot \mathbf{C}^{-1}(t) \right) \mathbf{C}(t) \right\} \right] \\
&= (\det \mathbf{C}(t))^{-\frac{1}{3}} \left\{ \hat{\mathbf{e}}'(s) \cdot \dot{\mathbf{C}}(t) - \frac{1}{3} (\hat{\mathbf{e}}'(s) \cdot \mathbf{C}(t)) \left(\dot{\mathbf{C}}(t) \cdot \mathbf{C}^{-1}(t) \right) \right\} \\
&= (\det \mathbf{C}(t))^{-\frac{1}{3}} \, \dot{\mathbf{C}}(t) \cdot \left\{ \hat{\mathbf{e}}'(s) - \frac{1}{3} (\hat{\mathbf{e}}'(s) \cdot \mathbf{C}(t)) \, \mathbf{C}^{-1}(t) \right\} \\
&= (\det \mathbf{C}(t))^{-\frac{1}{3}} \, \dot{\mathbf{C}}(t) \cdot \left\{ \overset{4}{\mathbf{1}} - \frac{1}{3} \mathbf{C}^{-1}(t) \otimes \mathbf{C}(t) \right\} \cdot \hat{\mathbf{e}}'(s) \\
&= \left[(\det \mathbf{C}(t))^{-\frac{1}{3}} \left\{ \overset{4}{\mathbf{1}} - \frac{1}{3} \mathbf{C}^{-1}(t) \otimes \mathbf{C}(t) \right\} \cdot \hat{\mathbf{e}}'(s) \right] \cdot \dot{\mathbf{C}}(t) \, .
\end{aligned} \tag{6.23}$$

In order to simplify this expression, the projection tensor of fourth order

$$\overset{4}{\mathbf{P}}(t) = (\det \mathbf{C}(t))^{-\frac{1}{3}} \left\{ \overset{4}{\mathbf{1}} - \frac{1}{3} \mathbf{C}^{-1}(t) \otimes \mathbf{C}(t) \right\} \tag{6.24}$$

is introduced and inserted into (6.23). In so doing, (6.21) changes to

$$\frac{\mathrm{d}}{\mathrm{d}t} \left(\frac{\mathrm{d}}{\mathrm{d}s} \operatorname{tr}(\hat{\mathbf{e}}_t(s)) \right) = \frac{\mathrm{d}}{\mathrm{d}t} \left(\hat{\mathbf{e}}'(s) \cdot \hat{\mathbf{C}}(t) \right) = \left[\overset{4}{\mathbf{P}}(t) \cdot \hat{\mathbf{e}}'(s) \right] \cdot \dot{\mathbf{C}}(t) \, , \tag{6.25}$$

such that the second part of the rate of the specific Helmholtz free energy in (6.13) can be rewritten as

$$\rho_0 \, \dot{\Psi}_{ov,2} = - \left[\int_{-\infty}^{t} G(t-s, \hat{\mathbf{C}}(t)) \, \overset{4}{\mathbf{P}}(t) \cdot \hat{\mathbf{e}}'(s) \, \mathrm{d}s \right] \cdot \dot{\mathbf{C}}(t) \, . \tag{6.26}$$

In order to reformulate the third part $\rho_0 \, \dot{\Psi}_{ov,3}$, the same procedure as in (6.23) can be applied. On this basis, the following relation is obtained

$$\frac{\partial G(t-s, \hat{\mathbf{C}}(t))}{\partial \hat{\mathbf{C}}(t)} \cdot \dot{\hat{\mathbf{C}}}(t) = \left[\overset{4}{\mathbf{P}}(t) \cdot \frac{\partial G(t-s, \hat{\mathbf{C}}(t))}{\partial \hat{\mathbf{C}}(t)} \right] \cdot \dot{\mathbf{C}}(t) \, , \tag{6.27}$$

such that the third part of the rate of the specific Helmholtz free energy is expressed by

$$\rho_0 \, \dot{\Psi}_{ov,3} = - \left[\int_{-\infty}^{t} \overset{4}{\mathbf{P}}(t) \cdot \frac{\partial G(t-s, \hat{\mathbf{C}}(t))}{\partial \hat{\mathbf{C}}(t)} \, \hat{\mathbf{e}}'(s) \cdot \hat{\mathbf{C}}(t) \, \mathrm{d}s \right] \cdot \dot{\mathbf{C}}(t) \, . \tag{6.28}$$

In order to redefine the last term $\rho_0 \dot{\Psi}_{ov,4}$ in (6.13), the mathematical relation

$$\frac{\partial G(t-s, \hat{\mathbf{C}}(t))}{\partial t} = -\frac{\partial G(t-s, \hat{\mathbf{C}}(t))}{\partial s} \tag{6.29}$$

is taken into account. Applying the partial integration, $\rho_0 \dot{\Psi}_{ov,4}$ first changes to

$$\begin{aligned} \rho_0 \dot{\Psi}_{ov,4} &= \int_{-\infty}^{t} \frac{\partial G(t-s, \hat{\mathbf{C}}(t))}{\partial s} \frac{\mathrm{d}}{\mathrm{d}s} \operatorname{tr}(\hat{\mathbf{e}}_t(s)) \, \mathrm{d}s \\ &= \left[\frac{\partial G(t-s, \hat{\mathbf{C}}(t))}{\partial t} \operatorname{tr}(\hat{\mathbf{e}}_t(s)) \right]_{-\infty}^{t} - \int_{-\infty}^{t} \frac{\partial^2 G(t-s, \hat{\mathbf{C}}(t))}{\partial t^2} \operatorname{tr}(\hat{\mathbf{e}}_t(s)) \, \mathrm{d}s \; . \end{aligned} \tag{6.30}$$

Based on the principle of fading memory, the relaxation function decays to zero for large times

$$\lim_{s \to -\infty} \frac{\partial G(t-s, \hat{\mathbf{C}}(t))}{\partial t} = 0 \; . \tag{6.31}$$

Considering this and $\hat{\mathbf{e}}_t(t) = \mathbf{0}$, the first term in (6.30) is equal zero

$$\left[\frac{\partial G(t-s, \hat{\mathbf{C}}(t))}{\partial t} \operatorname{tr}(\hat{\mathbf{e}}_t(s)) \right]_{-\infty}^{t} = 0 \; , \tag{6.32}$$

such that $\rho_0 \dot{\Psi}_{ov,4}$ can be reduced to

$$\rho_0 \dot{\Psi}_{ov,4} = -\int_{-\infty}^{t} \frac{\partial^2 G(t-s, \hat{\mathbf{C}}(t))}{\partial t^2} \operatorname{tr}(\hat{\mathbf{e}}_t(s)) \, \mathrm{d}s \; . \tag{6.33}$$

With the reformulation of the rate of the overstress parts in (6.15), (6.26), (6.28) and (6.33), the material time derivative of $\rho_0 \Psi$ can be written as

$$\begin{aligned} \rho_0 \dot{\Psi}(t) &= \rho_0 \frac{\partial \Psi_{eq}(\mathbf{C}(t))}{\partial \mathbf{C}(t)} \cdot \dot{\mathbf{C}}(t) \\ &\quad - \left[\int_{-\infty}^{t} G(t-s, \hat{\mathbf{C}}(t)) \overset{4}{\mathbf{P}}(t) \cdot \hat{\mathbf{e}}'(s) \, \mathrm{d}s \right] \cdot \dot{\mathbf{C}}(t) \\ &\quad - \left[\int_{-\infty}^{t} \overset{4}{\mathbf{P}}(t) \cdot \frac{\partial G(t-s, \hat{\mathbf{C}}(t))}{\partial \hat{\mathbf{C}}(t)} \hat{\mathbf{e}}'(s) \cdot \hat{\mathbf{C}}(t) \, \mathrm{d}s \right] \cdot \dot{\mathbf{C}}(t) \\ &\quad - \int_{-\infty}^{t} \frac{\partial^2 G(t-s, \hat{\mathbf{C}}(t))}{\partial t^2} \operatorname{tr}(\hat{\mathbf{e}}_t(s)) \, \mathrm{d}s \; . \end{aligned} \tag{6.34}$$

6.2.3 Clausius-Planck inequality

In order to derive a thermomechanically consistent constitutive relation between stress and strain, the Clausius-Planck inequality for isothermal processes is taken into account. With respect to the reference configuration, the Clausius-Planck inequality

reads as

$$\tilde{\mathbf{T}}(t) \cdot \dot{\mathbf{E}}(t) - \rho_0 \dot{\Psi}(t) \geq 0 \; . \tag{6.35}$$

Inserting (6.34) into the Clausius-Planck inequality and taking the relation

$$\dot{\mathbf{E}}(t) = \frac{1}{2} \left[\mathbf{C}(t) - \mathbf{1}\right]^{\cdot} = \frac{1}{2} \dot{\mathbf{C}}(t) \; , \tag{6.36}$$

into account, the following inequality is obtained:

$$\begin{aligned} & \left[\frac{1}{2} \tilde{\mathbf{T}}(t) - \rho_0 \frac{\partial \Psi_{eq}(\mathbf{C}(t))}{\partial \mathbf{C}(t)} \right. \\ & + \int_{-\infty}^{t} G(t-s, \hat{\mathbf{C}}(t)) \overset{4}{\mathbf{P}}(t) \cdot \hat{\mathbf{e}}'(s) \, \mathrm{d}s \\ & + \left. \int_{-\infty}^{t} \overset{4}{\mathbf{P}}(t) \cdot \frac{\partial G(t-s, \hat{\mathbf{C}}(t))}{\partial \hat{\mathbf{C}}(t)} \hat{\mathbf{e}}'(s) \cdot \hat{\mathbf{C}}(t) \, \mathrm{d}s \right] \cdot \dot{\mathbf{C}}(t) \\ & + \int_{-\infty}^{t} \frac{\partial^2 G(t-s, \hat{\mathbf{C}}(t))}{\partial t^2} \operatorname{tr}(\hat{\mathbf{e}}_t(s)) \, \mathrm{d}s \geq 0 \end{aligned} \tag{6.37}$$

This inequality is evaluated with respect to the standard argumentation of Coleman and Noll (1963). On this basis, the inequality is satisfied if the first term in brackets is equal to zero which automatically yields the constitutive equation of the 2nd Piola-Kirchhoff stress tensor

$$\begin{aligned} \tilde{\mathbf{T}}(t) &= \tilde{\mathbf{T}}_{eq}(t) + \tilde{\mathbf{T}}_{ov}(t) \\ &= 2\,\rho_0 \frac{\partial \Psi_{eq}(\mathbf{C}(t))}{\partial \mathbf{C}(t)} - 2 \int_{-\infty}^{t} G(t-s, \hat{\mathbf{C}}(t)) \overset{4}{\mathbf{P}}(t) \cdot \hat{\mathbf{e}}'(s) \, \mathrm{d}s \\ &\quad - 2 \int_{-\infty}^{t} \overset{4}{\mathbf{P}}(t) \cdot \frac{\partial G(t-s, \hat{\mathbf{C}}(t))}{\partial \hat{\mathbf{C}}(t)} \hat{\mathbf{e}}'(s) \cdot \hat{\mathbf{C}}(t) \, \mathrm{d}s \; . \end{aligned} \tag{6.38}$$

Since the projection tensor of fourth order $\overset{4}{\mathbf{P}}(t)$ is a function of time t, it is not influenced by the integration and can therefore be placed in front of the integral. In so doing, the overstress can alternatively be expressed by

$$\tilde{\mathbf{T}}_{ov}(t) = \overset{4}{\mathbf{P}} \cdot \left(\tilde{\mathbf{S}}_{ov,1}(t) + \tilde{\mathbf{S}}_{ov,2}(t) \right) \tag{6.39}$$

with the two overstresses

$$\begin{aligned} \tilde{\mathbf{S}}_{ov,1}(t) &= -2 \int_{-\infty}^{t} G(t-s, \hat{\mathbf{C}}(t)) \, \hat{\mathbf{e}}'(s) \, \mathrm{d}s \; , \\ \tilde{\mathbf{S}}_{ov,2}(t) &= -2 \int_{-\infty}^{t} \frac{\partial G(t-s, \hat{\mathbf{C}}(t))}{\partial \hat{\mathbf{C}}(t)} \hat{\mathbf{e}}'(s) \cdot \hat{\mathbf{C}}(t) \, \mathrm{d}s \; . \end{aligned} \tag{6.40}$$

This is the time domain formulation of a thermodynamically constitutive model of finite viscoelasticity which includes deformation dependent relaxation behaviour.

6.2.4 Geometric linearisation

In order to make the constitutive approach applicable for a formulation in the frequency domain, the constitutive equations are first linearised in the neighbourhood of a constant static predeformation $\mathbf{F}_0$. Referring to Haupt and Lion (2002), the deformation gradient $\mathbf{F}(t)$ is multiplicatively decomposed into a constant deformation $\mathbf{F}_0$ and a time depending deformation $\mathbf{f}(t)$

$$\mathbf{F}(t) \,=\, \mathbf{f}(t)\,\mathbf{F}_0 \quad \text{with} \quad \mathbf{f}(t) \,=\, \mathbf{1} + \mathbf{h}(t)\;, \quad ||\mathbf{h}|| \,\leq\, 1\;. \tag{6.41}$$

Thereby, the incremental displacement gradient $\mathbf{h}(t)$ represents the incremental displacement in the neighbourhood of the static predeformation $\mathbf{F}_0$. For the purpose of more clarity, the respective arguments will be neglected in the following presentation. All variables indexed with "0" are constant whereas the other ones are functions of time t if no other argument is explicitly mentioned.
Based on the assumptions in (6.41), the kinematic relations introduced above can be expressed in their linearised form. Since incremental terms of higher order are very small, they will be neglected during linearisation. Taking (6.41) into account, the linear approximation of the transposed, the inverse and the inverse transposed of the deformation gradient can first be expressed by

$$\begin{aligned} \mathbf{F}^T &= \mathbf{F}_0^T\,(\mathbf{1} + \mathbf{h}^T)\;, \\ \mathbf{F}^{-1} &= \mathbf{F}_0^{-1}\,(\mathbf{1} - \mathbf{h})\;, \\ \mathbf{F}^{-T} &= (\mathbf{1} - \mathbf{h}^T)\,\mathbf{F}_0^{-T}\;. \end{aligned} \tag{6.42}$$

With the incremental displacement gradient $\mathbf{h}$, the linearised strain tensor as well as its deviatoric part are introduced as

$$\begin{aligned} \mathbf{E}_{lin} &= \frac{1}{2}\left(\mathbf{h} + \mathbf{h}^T\right) \\ \mathbf{E}_{lin}^D &= \mathbf{E}_{lin} \,-\, \frac{1}{3}\,\mathrm{tr}(\mathbf{E}_{lin})\,\mathbf{1} \end{aligned} \tag{6.43}$$

On the basis of the definitions in (6.42), the linear approximation of the right Cauchy-Green tensor can be written as

$$\begin{aligned} \mathbf{C} &= \mathbf{F}^T\,\mathbf{F} \,=\, \mathbf{F}_0^T\,(\mathbf{1} + \mathbf{h}^T)\,(\mathbf{1} + \mathbf{h})\,\mathbf{F}_0 \\ &= \mathbf{F}_0^T\,(\mathbf{1} + \mathbf{h} + \mathbf{h}^T + \mathbf{h}\,\mathbf{h}^T)\,\mathbf{F}_0 \\ &= \mathbf{C}_0 \,+\, \mathbf{F}_0^T\,(\mathbf{h} + \mathbf{h}^T)\,\mathbf{F}_0 \\ &= \mathbf{C}_0 \,+\, 2\,\mathbf{F}_0^T\,\mathbf{E}_{lin}\,\mathbf{F}_0\;. \end{aligned} \tag{6.44}$$

The linearised version of the inverse reads as

$$\mathbf{C}^{-1} \,=\, \left(\mathbf{F}^T\,\mathbf{F}\right)^{-1} \,=\, \mathbf{F}^{-1}\,\mathbf{F}^{-T} \,=\, \mathbf{C}_0^{-1} \,-\, 2\,\mathbf{F}_0^{-1}\,\mathbf{E}_{lin}\,\mathbf{F}_0^{-T}\;. \tag{6.45}$$

In order to derive the linear approximation of the isochoric right Cauchy-Green tensor, the linear approximation of the determinant of $\mathbf{C}$ and the general definition with regards to its α^{th} power are first introduced

$$\begin{aligned}
\det \mathbf{C} &= \det(\mathbf{C}_0 + 2\,\mathbf{F}_0^T\,\mathbf{E}_{lin}\,\mathbf{F}_0) \\
&= \det(\mathbf{C}_0\,(\mathbf{1} + 2\,\mathbf{F}_0^{-1}\,\mathbf{E}_{lin}\,\mathbf{F}_0)) \\
&= (\det \mathbf{C}_0)\,\det(\mathbf{1} + 2\,\mathbf{F}_0^{-1}\,\mathbf{E}_{lin}\,\mathbf{F}_0) \\
&= (\det \mathbf{C}_0)\,(1 + 2\,\mathrm{tr}(\mathbf{F}_0^{-1}\,\mathbf{E}_{lin}\,\mathbf{F}_0)) \\
&= (\det \mathbf{C}_0)\,(1 + 2\,\mathrm{tr}(\mathbf{E}_{lin}))\ , \\
(\det \mathbf{C})^{\alpha} &= (\det \mathbf{C}_0)^{\alpha}\,(1 + 2\,\alpha\,\mathrm{tr}(\mathbf{E}_{lin}))\ .
\end{aligned} \tag{6.46}$$

On the basis of these relations, the linearisation of the isochoric right Cauchy-Green tensor is given by the expression

$$\begin{aligned}
\hat{\mathbf{C}} &= (\det \mathbf{C})^{-\frac{1}{3}}\,\mathbf{C} \\
&= (\det \mathbf{C}_0)^{-\frac{1}{3}}\,\left(1 - \frac{2}{3}\,\mathrm{tr}(\mathbf{E}_{lin})\right)\,\left(\mathbf{C}_0 + 2\,\mathbf{F}_0^T\,\mathbf{E}_{lin}\,\mathbf{F}_0\right) \\
&= (\det \mathbf{C}_0)^{-\frac{1}{3}}\,\left(\mathbf{C}_0 - \frac{2}{3}\,\mathrm{tr}(\mathbf{E}_{lin})\,\mathbf{C}_0 + 2\,\mathbf{F}_0^T\,\mathbf{E}_{lin}\,\mathbf{F}_0\right) \\
&= \hat{\mathbf{C}}_0 + 2\,(\det \mathbf{F}_0)^{-\frac{1}{3}}\,(\det \mathbf{F}_0)^{-\frac{1}{3}}\,\left(\mathbf{F}_0^T\,\mathbf{E}_{lin}\,\mathbf{F}_0 - \frac{1}{3}\,\mathbf{F}_0^T\,\mathrm{tr}(\mathbf{E}_{lin})\,\mathbf{1}\,\mathbf{F}_0\right) \\
&= \hat{\mathbf{C}}_0 + 2\,\hat{\mathbf{F}}_0^T\,\left(\mathbf{E}_{lin} - \frac{1}{3}\,\mathrm{tr}(\mathbf{E}_{lin})\,\mathbf{1}\right)\,\hat{\mathbf{F}}_0 \\
&= \hat{\mathbf{C}}_0 + 2\,\hat{\mathbf{F}}_0^T\,\mathbf{E}_{lin}^D\,\hat{\mathbf{F}}_0
\end{aligned} \tag{6.47}$$

and the corresponding derivative with respect to time reads as

$$\dot{\hat{\mathbf{C}}} = 2\,\hat{\mathbf{F}}_0^T\,\dot{\mathbf{E}}_{lin}^D\,\hat{\mathbf{F}}_0\ . \tag{6.48}$$

Moreover, the linearised version of the isochoric Piola strain tensor can be written as

$$\begin{aligned}
\hat{\mathbf{e}} &= \frac{1}{2}\,\left[\hat{\mathbf{C}}^{-1} - \mathbf{1}\right] = \frac{1}{2}\,\left[(\det \mathbf{C})^{\frac{1}{3}}\,\mathbf{C}^{-1} - \mathbf{1}\right] \\
&= \frac{1}{2}\,\left[(\det \mathbf{C}_0)^{\frac{1}{3}}\,\left(1 + \frac{2}{3}\,\mathrm{tr}(\mathbf{E}_{lin})\right)\,\left(\mathbf{C}_0^{-1} - 2\,\mathbf{F}_0^{-1}\,\mathbf{E}_{lin}\,\mathbf{F}_0^{-T}\right) - \mathbf{1}\right] \\
&= \frac{1}{2}\,\left[(\det \mathbf{C}_0)^{\frac{1}{3}}\,\left(\mathbf{C}_0^{-1} - 2\,\mathbf{F}_0^{-1}\,\mathbf{E}_{lin}\,\mathbf{F}_0^{-T} + \frac{2}{3}\,\mathrm{tr}(\mathbf{E}_{lin})\,\mathbf{C}_0^{-1}\right) - \mathbf{1}\right] \\
&= \frac{1}{2}\,\left[(\det \mathbf{C}_0)^{\frac{1}{3}}\,\mathbf{C}_0^{-1} - \mathbf{1}\right] - (\det \mathbf{C}_0)^{\frac{1}{3}}\,\mathbf{F}_0^{-1}\,\left[\mathbf{E}_{lin} - \frac{1}{3}\,\mathrm{tr}(\mathbf{E}_{lin})\,\mathbf{1}\right]\,\mathbf{F}_0^{-T} \\
&= \hat{\mathbf{e}}_0 - \hat{\mathbf{F}}_0^{-1}\,\mathbf{E}_{lin}^D\,\hat{\mathbf{F}}_0^{-T}\ .
\end{aligned} \tag{6.49}$$

The linear approximation of its material time derivative is given by

$$\dot{\hat{\mathbf{e}}} \;=\; -\,\hat{\mathbf{F}}_0^{-1}\,\dot{\mathbf{E}}_{lin}^{D}\,\hat{\mathbf{F}}_0^{-T}\;. \tag{6.50}$$

Based on the kinematic assumption in (6.41) and the corresponding linearisations in (6.42) – (6.50), the linearised version of the constitutive equations is derived in the following.

The linear approximation of the equilibrium part $\tilde{\mathbf{T}}_{eq}$ of the 2nd Piola-Kirchhoff stress tensor is obtained by inserting (6.44) into (6.38) and applying the Gateaux derivative. In so doing, the linearised formulation of the equilibrium stress tensor is given by

$$\begin{aligned}
\tilde{\mathbf{T}}_{eq,lin}(t) \;&=\; 2\,\rho_0\;\left.\frac{\partial\Psi_{eq}(\mathbf{C})}{\partial\mathbf{C}}\right|_{\mathbf{C}_0} \;+\; 2\,\rho_0\;\left.\frac{\partial^2\Psi_{eq}(\mathbf{C})}{\partial\mathbf{C}^2(t)}\right|_{\mathbf{C}_0} \cdot\,(\mathbf{C}\;-\;\mathbf{C}_0) \\
&=\; 2\,\rho_0\;\left.\frac{\partial\Psi_{eq}(\mathbf{C})}{\partial\mathbf{C}}\right|_{\mathbf{C}_0} \;+\; 2\,\rho_0\;\left.\frac{\partial^2\Psi_{eq}(\mathbf{C})}{\partial\mathbf{C}^2(t)}\right|_{\mathbf{C}_0} \cdot\,(2\,\mathbf{F}_0^T\,\mathbf{E}_{lin}\,\mathbf{F}_0)\;.
\end{aligned} \tag{6.51}$$

In order to obtain the linearisation of the overstress $\tilde{\mathbf{T}}_{ov}$, the linearised formulations of $\tilde{\mathbf{S}}_{ov,1}$ and $\tilde{\mathbf{S}}_{ov,2}$ in (6.40) as well as the linear approximation of the projection tensor $\overset{4}{\mathbf{P}}$ in (6.24) must first be derived. If the linearised formulation of the isochoric right Cauchy-Green tensor in (6.47) and the linear approximation (6.50) are inserted into (6.40), the linearisation of the first part of the overstress is obtained by applying the Gateaux derivative and by neglecting terms of higher order

$$\begin{aligned}
\tilde{\mathbf{S}}_{ov,lin,1}(t) \;&=\; -\,2\int_{-\infty}^{t} G\left(t-s,\hat{\mathbf{C}}_0\;+\;2\,\hat{\mathbf{F}}_0^T\,\mathbf{E}_{lin}^{D}\,\hat{\mathbf{F}}_0\right)\left(-\,\hat{\mathbf{F}}_0^{-1}\,\mathbf{E}_{lin}^{\prime D}(s)\,\hat{\mathbf{F}}_0^{-T}\right)\mathrm{d}s \\
&=\; 2\int_{-\infty}^{t}\left[G(t-s,\hat{\mathbf{C}}_0)\;+\;\left.\frac{\partial G(t-s,\,\hat{\mathbf{C}})}{\partial\hat{\mathbf{C}}}\right|_{\hat{\mathbf{C}}_0}\cdot\left(2\,\hat{\mathbf{F}}_0^T\,\mathbf{E}_{lin}^{D}\,\hat{\mathbf{F}}_0\right)\right] \\
&\qquad \hat{\mathbf{F}}_0^{-1}\,\mathbf{E}_{lin}^{\prime D}(s)\,\hat{\mathbf{F}}_0^{-T}\,\mathrm{d}s \\
&=\; 2\int_{-\infty}^{t} G(t-s,\hat{\mathbf{C}}_0)\,\hat{\mathbf{F}}_0^{-1}\,\mathbf{E}_{lin}^{\prime D}(s)\,\hat{\mathbf{F}}_0^{-T}\,\mathrm{d}s\;.
\end{aligned} \tag{6.52}$$

In order to obtain a linearised version of the second part of the overstress, the linearised form of the derivative of the relaxation function with respect to $\hat{\mathbf{C}}$ is first calculated. To this end, the linearised formulation in (6.47) is considered and the Gateaux derivative is applied

$$\begin{aligned}
\frac{\partial G(t-s,\hat{\mathbf{C}})}{\partial\hat{\mathbf{C}}} \;&=\; \frac{\partial G(t-s,\hat{\mathbf{C}}_0\;+\;2\,\hat{\mathbf{F}}_0^T\,\mathbf{E}_{lin}^{D}\,\hat{\mathbf{F}}_0)}{\partial\hat{\mathbf{C}}} \\
&=\; \left.\frac{\partial G(t-s,\hat{\mathbf{C}})}{\partial\hat{\mathbf{C}}}\right|_{\hat{\mathbf{C}}_0} \;+\; 2\left.\frac{\partial^2 G(t-s,\hat{\mathbf{C}})}{\partial\hat{\mathbf{C}}^2}\right|_{\hat{\mathbf{C}}_0}\cdot\left(\hat{\mathbf{F}}_0^T\,\mathbf{E}_{lin}^{D}\,\hat{\mathbf{F}}_0\right)\;.
\end{aligned} \tag{6.53}$$

By inserting (6.47), (6.50) and (6.53) into equation (6.40) and by neglecting terms of higher order, the linearised version of the second part of the overstress reads as

$$\begin{aligned}
\tilde{\mathbf{S}}_{ov,lin,2}(t) &= 2\int_{-\infty}^{t}\left[\left.\frac{\partial G(t-s,\hat{\mathbf{C}})}{\partial\hat{\mathbf{C}}}\right|_{\hat{\mathbf{C}}_0} + 2\left.\frac{\partial^2 G(t-s,\hat{\mathbf{C}})}{\partial\hat{\mathbf{C}}^2}\right|_{\hat{\mathbf{C}}_0}\cdot\left(\hat{\mathbf{F}}_0^T\,\mathbf{E}_{lin}^D\,\hat{\mathbf{F}}_0\right)\right] \\
&\qquad \left(\hat{\mathbf{F}}_0^{-1}\,\mathbf{E}_{lin}'^D(s)\,\hat{\mathbf{F}}_0^{-T}\right)\cdot\left(\hat{\mathbf{C}}_0 + \hat{\mathbf{F}}_0^T\,\mathbf{E}_{lin}^D\,\hat{\mathbf{F}}_0\right)\mathrm{d}s \\
&= 2\int_{-\infty}^{t}\left.\frac{\partial G(t-s,\hat{\mathbf{C}})}{\partial\hat{\mathbf{C}}}\right|_{\hat{\mathbf{C}}_0}\left(\hat{\mathbf{F}}_0^{-1}\,\mathbf{E}_{lin}'^D(s)\,\hat{\mathbf{F}}_0^{-T}\right)\cdot\hat{\mathbf{C}}_0\,\mathrm{d}s \\
&= 2\int_{-\infty}^{t}\left.\frac{\partial G(t-s,\hat{\mathbf{C}})}{\partial\hat{\mathbf{C}}}\right|_{\hat{\mathbf{C}}_0}\mathrm{tr}\left(\mathbf{E}_{lin}'^D(s)\right)\,\mathrm{d}s \;=\; \mathbf{0}\;.
\end{aligned} \tag{6.54}$$

Since $\mathrm{tr}(\mathbf{E}_{lin}^D) = 0$ holds, $\tilde{\mathbf{S}}_{ov,lin,2}(t)$ is equal to zero. From the definition of the fourth order projection tensor in equation (6.24), its linearised formulation is derived by inserting (6.44) and (6.47)

$$\begin{aligned}
\overset{4}{\mathbf{P}}(t) &= (\det\mathbf{C})^{-\frac{1}{3}}\left\{\overset{4}{\mathbf{1}} - \frac{1}{3}\,\mathbf{C}^{-1}\otimes\mathbf{C}\right\} \\
&= (\det\mathbf{C}_0)^{-\frac{1}{3}}\left(1 - \frac{2}{3}\,\mathrm{tr}(\mathbf{E}_{lin}(t))\right) \\
&\qquad \left\{\overset{4}{\mathbf{1}} - \frac{1}{3}\left[\mathbf{C}_0^{-1} - 2\,\mathbf{F}_0^{-1}\,\mathbf{E}_{lin}\,\mathbf{F}_0^{-T}\right]\otimes\left[\mathbf{C}_0 + 2\,\mathbf{F}_0^T\,\mathbf{E}_{lin}\,\mathbf{F}_0\right]\right\} \\
&= (\det\mathbf{C}_0)^{-\frac{1}{3}}\left\{\overset{4}{\mathbf{1}} - \frac{1}{3}\,\mathbf{C}_0^{-1}\otimes\mathbf{C}_0\right\} = \overset{4}{\mathbf{P}}_0\;.
\end{aligned} \tag{6.55}$$

Since (6.26) is already a linear function of the linearised strain tensor, it is sufficient to consider only the constant part in the linearisation of $\overset{4}{\mathbf{P}}(t)$ in (6.55). On the basis of the derived linearised fromulations of the overstresses and the fourth order projection tensor in equations (6.52), (6.54) and (6.55), the linearised version of the overstress in (6.38) can finally be written as

$$\tilde{\mathbf{T}}_{ov,lin}(t) = \overset{4}{\mathbf{P}}_0\cdot\left(2\int_{-\infty}^{t} G(t-s,\hat{\mathbf{C}}_0)\,\hat{\mathbf{F}}_0^{-1}\,\mathbf{E}_{lin}'^D(s)\,\hat{\mathbf{F}}_0^{-T}\,\mathrm{d}s\right)\;. \tag{6.56}$$

Since the constant part $\overset{4}{\mathbf{P}}_0$ of the projection tensor is independent of time s and thus not concerned with integration, the following term is obtained from (6.56)

$$\overset{4}{\mathbf{P}}_0\cdot\left(\hat{\mathbf{F}}_0^{-1}\,\mathbf{E}_{lin}'^D(s)\,\hat{\mathbf{F}}_0^{-T}\right)\;. \tag{6.57}$$

Rearrangement of this expression first leads to

$$\begin{aligned}
\overset{4}{\mathbf{P}}_0 \cdot \left(\hat{\mathbf{F}}_0^{-1}\,\mathbf{E}'^{D}_{lin}(s)\,\hat{\mathbf{F}}_0^{-T}\right) &= (\det \mathbf{C}_0)^{-\frac{1}{3}} \left\{\overset{4}{\mathbf{1}} - \frac{1}{3}\,\mathbf{C}_0^{-1}\otimes\mathbf{C}_0\right\} \\
&\quad \cdot \left(\mathbf{F}_0^{-1}\,\mathbf{E}'^{D}_{lin}(s)\,\mathbf{F}_0^{-T}\right)\,(\det \mathbf{C}_0)^{\frac{1}{3}} \\
&= \left\{\overset{4}{\mathbf{1}} - \frac{1}{3}\,\mathbf{C}_0^{-1}\otimes\mathbf{C}_0\right\} \cdot \left(\mathbf{C}_0^{-1}\mathbf{F}_0^{T}\,\mathbf{E}'^{D}_{lin}(s)\,\mathbf{F}_0\,\mathbf{C}_0^{-1}\right)\,.
\end{aligned} \tag{6.58}$$

Considering the following mathematical relations (Ehlers 2007)

$$\begin{aligned}
(\mathbf{A}\otimes\mathbf{B})\cdot\mathbf{C} &= (\mathbf{C}\cdot\mathbf{B})\,\mathbf{A}, \\
(\mathbf{A}\otimes\mathbf{B})^{T23}\cdot\mathbf{C} &= \mathbf{A}\,\mathbf{C}\,\mathbf{B}^{T}
\end{aligned} \tag{6.59}$$

and taking into account

$$\operatorname{tr}\left(\mathbf{E}'^{D}_{lin}(s)\right) = 0\,, \tag{6.60}$$

further calculations result in

$$\begin{aligned}
\overset{4}{\mathbf{P}}_0 \cdot \left(\hat{\mathbf{F}}_0^{-1}\,\mathbf{E}'^{D}_{lin}(s)\,\hat{\mathbf{F}}_0^{-T}\right) &= \mathbf{C}_0^{-1}\,\mathbf{F}_0^{T}\,\mathbf{E}'^{D}_{lin}(s)\,\mathbf{F}_0\,\mathbf{C}_0^{-1} - \frac{1}{3}\operatorname{tr}\left(\mathbf{E}'^{D}_{lin}(s)\right)\,\mathbf{C}_0^{-1} \\
&= \mathbf{C}_0^{-1}\,\mathbf{F}_0^{T}\,\mathbf{E}'_{lin}(s)\,\mathbf{F}_0\,\mathbf{C}_0^{-1} - \frac{1}{3}\operatorname{tr}\left(\mathbf{E}'_{lin}(s)\right)\,\mathbf{C}_0^{-1}\,\mathbf{F}_0^{T}\,\mathbf{F}_0\,\mathbf{C}_0^{-1} \\
&= \left[\mathbf{C}_0^{-1}\otimes\mathbf{C}_0^{-1}\right]^{T23}\cdot\left(\mathbf{F}_0^{T}\,\mathbf{E}'_{lin}(s)\,\mathbf{F}_0\right) - \frac{1}{3}\operatorname{tr}\left(\mathbf{E}'_{lin}(s)\right)\,\mathbf{C}_0^{-1}\,.
\end{aligned} \tag{6.61}$$

If the last term in (6.61) is reformulated as follows

$$\begin{aligned}
\frac{1}{3}\operatorname{tr}\left(\mathbf{E}'_{lin}(s)\right)\,\mathbf{C}_0^{-1} &= \frac{1}{3}\operatorname{tr}\left(\mathbf{F}_0^{-T}\,\mathbf{F}_0^{T}\,\mathbf{E}'_{lin}(s)\,\mathbf{F}_0\,\mathbf{F}_0^{-1}\right)\,\mathbf{C}_0^{-1} \\
&= \frac{1}{3}\operatorname{tr}\left(\mathbf{C}_0^{-1}\,\mathbf{F}_0^{T}\,\mathbf{E}'_{lin}(s)\,\mathbf{F}_0\right)\,\mathbf{C}_0^{-1} \\
&= \frac{1}{3}\left[\left(\mathbf{F}_0^{T}\,\mathbf{E}'_{lin}(s)\,\mathbf{F}_0\right)\cdot\mathbf{C}_0^{-1}\right]\,\mathbf{C}_0^{-1} \\
&= \frac{1}{3}\left[\mathbf{C}_0^{-1}\otimes\mathbf{C}_0^{-1}\right]\cdot\left(\mathbf{F}_0^{T}\,\mathbf{E}'_{lin}(s)\,\mathbf{F}_0\right)
\end{aligned} \tag{6.62}$$

and inserted into (6.61), formulation (6.57) can finally be expressed by

$$\begin{aligned}
\overset{4}{\mathbf{P}}_0 \cdot \left(\hat{\mathbf{F}}_0^{-1}\,\mathbf{E}'^{D}_{lin}(s)\,\hat{\mathbf{F}}_0^{-T}\right) &= \left\{\left[\mathbf{C}_0^{-1}\otimes\mathbf{C}_0^{-1}\right]^{T23} - \frac{1}{3}\left[\mathbf{C}_0^{-1}\otimes\mathbf{C}_0^{-1}\right]\right\} \\
&\quad \cdot \left(\mathbf{F}_0^{T}\,\mathbf{E}'_{lin}(s)\,\mathbf{F}_0\right) \\
&= \overset{4}{\mathbf{R}}_0 \cdot \left(\mathbf{F}_0^{T}\,\mathbf{E}'_{lin}(s)\,\mathbf{F}_0\right)\,.
\end{aligned} \tag{6.63}$$

Therein, the fourth order tensor $\overset{4}{\mathbf{R}}_0$ is another projection tensor

$$\overset{4}{\mathbf{R}}_0 = \left\{ \left[\mathbf{C}_0^{-1} \otimes \mathbf{C}_0^{-1}\right]^{T23} - \frac{1}{3} \left[\mathbf{C}_0^{-1} \otimes \mathbf{C}_0^{-1}\right] \right\} . \tag{6.64}$$

Considering (6.63), the linearised overstress of the 2nd Piola-Kirchhoff type in (6.56) reads as follows

$$\tilde{\mathbf{T}}_{ov,lin}(t) = \overset{4}{\mathbf{R}}_0 \cdot \tilde{\mathbf{S}}_{ov,lin,1} = \overset{4}{\mathbf{R}}_0 \cdot \left(2 \int_{-\infty}^{t} G(t-s, \hat{\mathbf{C}}_0)\, \mathbf{F}_0^T\, \mathbf{E}'_{lin}(s)\, \mathbf{F}_0 \, \mathrm{d}s \right) . \tag{6.65}$$

The linearised 2nd Piola-Kirchhoff stress tensor finally arises from the sum of its linearised equilibrium part (6.51) and its linearised overstress part (6.65)

$$\begin{aligned} \tilde{\mathbf{T}}_{lin}(t) &= \mathbf{T}_{eq,lin} + \tilde{\mathbf{T}}_{ov,lin}(t) \\ &= 2\,\rho_0 \left. \frac{\partial \Psi_{eq}(\mathbf{C})}{\partial \mathbf{C}} \right|_{\mathbf{C}_0} + 4\,\rho_0 \left. \frac{\partial^2 \Psi_{eq}(\mathbf{C})}{\partial \mathbf{C}^2} \right|_{\mathbf{C}_0} \cdot \left(\mathbf{F}_0^T\, \mathbf{E}_{lin}\, \mathbf{F}_0 \right) \\ &\quad + \overset{4}{\mathbf{R}}_0 \cdot \left(2 \int_{-\infty}^{t} G(t-s, \hat{\mathbf{C}}_0)\, \mathbf{F}_0^T\, \mathbf{E}'_{lin}(s)\, \mathbf{F}_0 \, \mathrm{d}s \right) . \end{aligned} \tag{6.66}$$

Taking a look at this result, the linearised 2nd Piola-Kirchhoff stress tensor can be additively separated into three different parts. The first one results from the linearisation of the equilibrium stress $\tilde{\mathbf{T}}_{eq}$. It is evaluated at the static predeformation $\mathbf{C}_0$, is constant in time and can be interpreted as the static stress response arising from the predeformation

$$\mathbf{T}_{eq,lin1} = \tilde{\mathbf{T}}_0 = 2\,\rho_0 \left. \frac{\partial \Psi_{eq}(\mathbf{C})}{\partial \mathbf{C}} \right|_{\mathbf{C}_0} . \tag{6.67}$$

The second term also arises from the linearisation of $\tilde{\mathbf{T}}_{eq}$ and is evaluated at the static predeformation $\mathbf{C}_0$. In contrast to the first part, the second one depends on time. It is a function of the actual incremental strain tensor $\mathbf{E}_{lin}$ at time t and thus represents the linear stress response resulting from the harmonic excitation in the neighbourhood of the static predeformation

$$\tilde{\mathbf{T}}_{eq,lin2}(t) = 4\,\rho_0 \left. \frac{\partial^2 \Psi_{eq}(\mathbf{C})}{\partial \mathbf{C}^2} \right|_{\mathbf{C}_0} \cdot \left(\mathbf{F}_0^T\, \mathbf{E}_{lin}\, \mathbf{F}_0 \right) . \tag{6.68}$$

The last part is a history functional which depends on the deformation dependent relaxation function $G(t-s, \hat{\mathbf{C}}_0)$ and on the history of the incremental strain tensor $\mathbf{E}_{lin}(s)$. It represents the viscoelastic effects arising from the harmonic excitation in the neighbourhood of the static predeformation

$$\tilde{\mathbf{T}}_{ov,lin}(t) = \tilde{\mathbf{T}}_{ov} = \overset{4}{\mathbf{R}}_0 \cdot \left(2 \int_{-\infty}^{t} G(t-s, \hat{\mathbf{C}}_0)\, \mathbf{F}_0^T\, \mathbf{E}'_{lin}(s)\, \mathbf{F}_0 \, \mathrm{d}s \right) . \tag{6.69}$$

6.2.5 Incompressible formulation

Since this work focuses on rubber, the constitutive equations are formulated for incompressible material behaviour in the following. For this purpose, an unknown pressure term p is firstly introduced. With regard to the additive decomposition of the 2nd Piola-Kirchhoff stress tensor, the pressure is additively decomposed into an equilibrium part p_0 and a dynamic overstress part $p_{ov}(t)$ as well

$$p(t) \;=\; p_0 \;+\; p_{ov}(t) \;. \tag{6.70}$$

In order to derive the constitutive equation for the 2nd Piola-Kirchhoff stress tensor for incompressible material behaviour, the Clausius-Planck inequality is extended by the unknown pressure term

$$\Big(-\left(p_0 \;+\; p_{ov}\right) \mathbf{C}^{-1} \;+\; \tilde{\mathbf{T}}(t) \Big) \cdot \dot{\mathbf{E}}(t) \;-\; \rho_0 \, \dot{\Psi}(t) \;\geq\; 0 \;. \tag{6.71}$$

The assumption that the constitutively undetermined reaction stress is given by the term $-p\,\mathbf{C}^{-1}$ is compatible with the statement, that it does not contribute to the stress power ($-p\,\mathbf{C}^{-1} \cdot \dot{\mathbf{E}} = 0$). As before, the inequality (6.71) is evaluated with respect to the argumentation by Coleman and Noll (1963), which finally yields the incompressible formulation of the 2nd Piola-Kirchhoff stress tensor

$$\begin{aligned} \tilde{\mathbf{T}}(t) \;\;=\;\; & -\left(p_0 \;+\; p_{ov}\right) \mathbf{C}^{-1} \;+ 2\,\rho_0 \; \left. \frac{\partial \Psi_{eq}(\mathbf{C})}{\partial \mathbf{C}} \right|_{\mathbf{C}_0} \\ & + 4\,\rho_0 \; \left. \frac{\partial^2 \Psi_{eq}(\mathbf{C})}{\partial \mathbf{C}^2} \right|_{\mathbf{C}_0} \cdot \left(\mathbf{F}_0^T \, \mathbf{E}_{lin} \, \mathbf{F}_0 \right) \\ & + \; \overset{4}{\mathbf{R}}_0 \cdot \left(2 \int_{-\infty}^{t} G(t-s, \hat{\mathbf{C}}_0) \, \mathbf{F}_0^T \, \mathbf{E}'_{lin}(s) \, \mathbf{F}_0 \, \mathrm{d}s \right) \;. \end{aligned} \tag{6.72}$$

In order to prepare the incompressible formulation for the transformation into the frequency domain, the first term in (6.72) must be linearised as well. By neglecting terms of higher order and by inserting (6.44), the linearisation of the first term in (6.72) follows to

$$\begin{aligned} -\left(p_0 \;+\; p_{ov}\right) \mathbf{C}^{-1} \;\;&=\;\; -\left(p_0 \;+\; p_{ov}\right) \left(\mathbf{C}_0^{-1} \;-\; 2\,\mathbf{F}_0^{-1} \, \mathbf{E}_{lin} \mathbf{F}_0^{-T} \right) \\ &=\;\; -\,p_0 \, \mathbf{C}_0^{-1} \;-\; p_{ov} \mathbf{C}_0^{-1} \;+\; 2\,p_0 \, \mathbf{F}_0^{-1} \, \mathbf{E}_{lin} \mathbf{F}_0^{-T} \\ &=\;\; -\,p_0 \, \mathbf{C}_0^{-1} \;-\; p_{ov} \, \mathbf{C}_0^{-1} \;+\; 2\,p_0 \, \mathbf{F}_0^{-1} \mathbf{F}_0^{-T} \, \mathbf{F}_0^T \, \mathbf{E}_{lin} \mathbf{F}_0 \, \mathbf{F}_0^{-1} \, \mathbf{F}_0^{-T} \\ &=\;\; -\,p_0 \, \mathbf{C}_0^{-1} \;-\; p_{ov} \, \mathbf{C}_0^{-1} \;+\; 2\,p_0 \, \mathbf{C}_0^{-1} \, \mathbf{F}_0^T \, \mathbf{E}_{lin} \, \mathbf{F}_0 \, \mathbf{C}_0^{-1} \\ &=\;\; -\,p_0 \, \mathbf{C}_0^{-1} \;-\; p_{ov} \, \mathbf{C}_0^{-1} \;+\; 2\,p_0 \, \left[\mathbf{C}_0^{-1} \otimes \mathbf{C}_0^{-1} \right]^{T23} \cdot \, \mathbf{F}_0^T \, \mathbf{E}_{lin} \, \mathbf{F}_0 \\ &=\;\; -\,p_0 \, \mathbf{C}_0^{-1} \;-\; p_{ov} \, \mathbf{C}_0^{-1} \;+\; 2\,p_0 \; \overset{4}{\mathbf{R}}_0 \cdot \mathbf{F}_0^T \, \mathbf{E}_{lin} \, \mathbf{F}_0 \;. \end{aligned} \tag{6.73}$$

The fourth order projection tensor in terms of incompressibility is given by

$$\overset{4}{\mathbf{R}}_0 = \left[\mathbf{C}_0^{-1} \otimes \mathbf{C}_0^{-1}\right]^{T23} \ , \tag{6.74}$$

because the second term in (6.64) leads to

$$\left[\mathbf{C}_0^{-1} \otimes \mathbf{C}_0^{-1}\right] \cdot \left(\mathbf{F}_0^T \, \mathbf{E}_{lin} \, \mathbf{F}_0\right) \ = \ \mathrm{tr}\left(\mathbf{C}_0^{-1} \, \mathbf{F}_0^T \, \mathbf{E}_{lin} \mathbf{F}_0\right) \ = \ \mathrm{tr}\left(\mathbf{E}_{lin}\right) \ = \ 0 \ . \tag{6.75}$$

The linearisation (6.73) is finally inserted into (6.72), such that the incompressible formulation of the linearised 2nd Piola-Kirchhoff stress reads as

$$\begin{aligned} \tilde{\mathbf{T}}_{lin}(t) \ = \ & -p_0 \, \mathbf{C}_0^{-1} \ + \ 2\,\rho_0 \ \left.\frac{\partial \Psi_{eq}(\mathbf{C})}{\partial \mathbf{C}}\right|_{\mathbf{C}_0} \ - \ p_{ov} \, \mathbf{C}_0^{-1} \\ & + \left(4\,\rho_0 \ \left.\frac{\partial^2 \Psi_{eq}(\mathbf{C})}{\partial \mathbf{C}^2}\right|_{\mathbf{C}_0} \ + \ 2\,p_0 \ \overset{4}{\mathbf{R}}_0 \right) \cdot \left(\mathbf{F}_0^T \, \mathbf{E}_{lin} \, \mathbf{F}_0\right) \\ & + \ \overset{4}{\mathbf{R}}_0 \cdot \left(2 \int_{-\infty}^{t} G(t-s, \hat{\mathbf{C}}_0) \, \mathbf{F}_0^T \, \mathbf{E}'_{lin}(s) \, \mathbf{F}_0 \, \mathrm{d}s \right) \ . \end{aligned} \tag{6.76}$$

Since the isochoric right Cauchy-Green tensor is equal to the right Cauchy-Green tensor in the case of incompressibility ($\hat{\mathbf{C}}_0 = \mathbf{C}_0$), the relaxation function in (6.76) can be expressed as a function of $\mathbf{C}_0$.

6.2.6 Dynamic modulus tensor

In order to derive the dynamic modulus tensor of fourth order, the linearised constitutive formulation (6.76) must be transferred to the frequency domain. Therefore, the corresponding relaxation function $G(t-s, \mathbf{C}_0)$ must first be defined such that the differential equation for the overstress $\tilde{\mathbf{S}}_{ov}$ and the resulting harmonic response, which arises from the harmonic excitations in the neighbourhood of the static predeformation, can be derived. Based on this procedure, the frequency domain formulations of the stress tensor and the corresponding dynamic modulus tensors are derived with respect to a classical Maxwell chain and finally deduced for the modified fractional formulation which is related to a fractional Maxwell chain.

6.2.6.1 Type A: Classical model

In terms of an interpretation of the linearised model as a classical Maxwell chain, the relaxation function is of the exponential type and reads as

$$G_A(t-s, \mathbf{C}_0) \ = \ \sum_{k=1}^{n} \mu_k(\mathbf{C}_0) \, \mathrm{e}^{-\frac{t-s}{\tau_k}} \ . \tag{6.77}$$

A dependence in the form of $\tau_k = \tau_k(\mathbf{C}_0)$ is possible but has been omitted for simplification. Based on this assumption, the 2nd Piola-Kirchhoff stress tensor in (6.76) reads

as

$$\begin{aligned}\tilde{\mathbf{T}}^A_{lin}(t) \;=\; & -\,p_0\,\mathbf{C}_0^{-1} \,+\, 2\,\rho_0\,\left.\frac{\partial \Psi_{eq}(\mathbf{C})}{\partial \mathbf{C}}\right|_{\mathbf{C}_0} \,-\, p_{ov}\,\mathbf{C}_0^{-1} \\ & +\left(4\,\rho_0\,\left.\frac{\partial^2 \Psi_{eq}(\mathbf{C})}{\partial \mathbf{C}^2}\right|_{\mathbf{C}_0} \,+\, 2\,p_0\,\overset{4}{\mathbf{R}}_0\right)\cdot\left(\mathbf{F}_0^T\,\mathbf{E}_{lin}\,\mathbf{F}_0\right) \\ & +\,\overset{4}{\mathbf{R}}_0\cdot\left(2\int_{-\infty}^{t}\sum_{k=1}^{n}\mu_k(\mathbf{C}_0)\,\mathrm{e}^{-\frac{t-s}{\tau_k}}\,\mathbf{F}_0^T\,\mathbf{E}'_{lin}(s)\,\mathbf{F}_0\,\mathrm{d}s\right)\,,\end{aligned} \tag{6.78}$$

wherein the viscoelastic overstress is given by

$$\tilde{\mathbf{S}}^A_{ov}(t) \;=\; 2\int_{-\infty}^{t}\sum_{k=1}^{n}\mu_k(\mathbf{C}_0)\,\mathrm{e}^{-\frac{t-s}{\tau_k}}\,\mathbf{F}_0^T\,\mathbf{E}'_{lin}(s)\,\mathbf{F}_0\,\mathrm{d}s\;. \tag{6.79}$$

The differential equation for the overstresses $\tilde{\mathbf{S}}^A_{ov,k}$ can be derived as presented in chapter 3 and reads as (cf. (3.71))

$$\dot{\tilde{\mathbf{S}}}^A_{ov,k}(t) \;=\; 2\,\mu_k(\mathbf{C}_0)\,\mathbf{F}_0^T\,\dot{\mathbf{E}}_{lin}\,\mathbf{F}_0 \,-\, \frac{1}{\tau_k}\,\tilde{\mathbf{S}}_{ov,k}\;. \tag{6.80}$$

In order to obtain the harmonic solution of this differential equation, the harmonic incremental strain tensor

$$\mathbf{E}_{lin}(\omega,t) \;=\; \Delta\mathbf{E}_{lin}\,\mathrm{e}^{i\omega t} \tag{6.81}$$

with the strain amplitude $\Delta\mathbf{E}_{lin}$ and the angular frequency ω is introduced. On this basis, the overstress response is given by

$$\tilde{\mathbf{S}}_{ov}(\omega,t) \;=\; \Delta\tilde{\mathbf{S}}_{ov}\,\mathrm{e}^{i\omega t}\;, \tag{6.82}$$

whereas the overstress part of the pressure reads as

$$p_{ov}(\omega,t) \;=\; \Delta p\,\mathrm{e}^{i\omega t}\;. \tag{6.83}$$

If the time derivatives of the incremental strain tensor and the overstress

$$\begin{aligned}\dot{\tilde{\mathbf{S}}}_{ov}(\omega,t) &= i\omega\,\Delta\tilde{\mathbf{S}}_{ov}\,\mathrm{e}^{i\omega t} \\ \dot{\mathbf{E}}_{lin}(\omega,t) &= i\omega\,\Delta\mathbf{E}_{lin}\,\mathrm{e}^{i\omega t}\;,\end{aligned} \tag{6.84}$$

are inserted into the differential equation (6.80), the following result is firstly obtained

$$i\omega\,\Delta\tilde{\mathbf{S}}^A_{ov,k}\,\mathrm{e}^{i\omega t} \;=\; 2\,i\omega\,\mu_k(\mathbf{C}_0)\,\mathbf{F}_0^T\,\Delta\mathbf{E}_{lin}\,\mathbf{F}_0\;\mathrm{e}^{i\omega t} \,-\, \frac{1}{\tau_k}\,\Delta\tilde{\mathbf{S}}^A_{ov,k}\;\mathrm{e}^{i\omega t}\;. \tag{6.85}$$

By rearranging this relation, the harmonic overstress response follows to

$$\Delta\tilde{\mathbf{S}}^A_{ov} \;=\; 2\sum_{k=1}^{n}\mu_k(\mathbf{C}_0)\,\frac{i\omega\tau_k}{1+i\omega\tau_k}\,\mathbf{F}_0^T\,\Delta\mathbf{E}_{lin}\,\mathbf{F}_0\;. \tag{6.86}$$

Based on this result and the definitions in (6.81), (6.82) and (6.83), the frequency domain formulation of the 2nd Piola-Kirchhoff stress in (6.78) is given by

$$\begin{aligned}
\tilde{\mathbf{T}}_A(\omega,t) &= \tilde{\mathbf{T}}_0 + \Delta\tilde{\mathbf{T}}_A\,\mathrm{e}^{i\omega t} \\
&= -p_0\,\mathbf{C}_0^{-1} + 2\,\rho_0\,\left.\frac{\partial\Psi_{eq}(\mathbf{C})}{\partial\mathbf{C}}\right|_{\mathbf{C}_0} - \Delta p\,\mathbf{C}_0^{-1}\,\mathrm{e}^{i\omega t} \\
&\quad + \left(4\,\rho_0\,\left.\frac{\partial^2\Psi_{eq}(\mathbf{C})}{\partial\mathbf{C}^2}\right|_{\mathbf{C}_0} + 2\,p_0\,\overset{4}{\mathbf{R}}_0\right. \\
&\quad \left. + 2\sum_{k=1}^{n}\mu_k(\mathbf{C}_0)\,\frac{i\omega\tau_k}{1+i\omega\tau_k}\,\overset{4}{\mathbf{R}}_0\right)\cdot\mathbf{F}_0^T\,\Delta\mathbf{E}_{lin}\,\mathbf{F}_0\,\mathrm{e}^{i\omega t}
\end{aligned} \tag{6.87}$$

and the dynamic modulus tensor of fourth order reads as

$$\overset{4}{\mathbf{G}}_A\,(\omega) = 4\,\rho_0\,\left.\frac{\partial^2\Psi_{eq}(\mathbf{C})}{\partial\mathbf{C}^2}\right|_{\mathbf{C}_0} + 2\,p_0\,\overset{4}{\mathbf{R}}_0 + 2\sum_{k=1}^{n}\mu_k(\mathbf{C}_0)\,\frac{i\omega\tau_k}{1+i\omega\tau_k}\,\overset{4}{\mathbf{R}}_0 \tag{6.88}$$

with the complex modulus

$$\overset{4\,*}{\mathbf{G}}_A\,(\omega) = 2\sum_{k=1}^{n}\mu_k(\mathbf{C}_0)\,\frac{i\omega\tau_k}{1+i\omega\tau_k}\,\overset{4}{\mathbf{R}}_0\ . \tag{6.89}$$

6.2.6.2 Type B: Fractional model

With regard to an interpretation of the linearised model as a fractional Maxwell chain, the frequency domain formulation of the 2nd Piola-Kirchhoff stress tensor and the definition of the dynamic modulus tensor are derived on the basis of the following relaxation function (Haupt and Lion (2002))

$$G_B(t-s,\mathbf{C}_0) = \sum_{k=1}^{n}\mu_k(\mathbf{C}_0)\,E_\alpha\left(-\left(\frac{t-s}{\tau_k}\right)^{\alpha_k}\right) \quad , \quad 0 \le \alpha \le 1\ . \tag{6.90}$$

Inserting this definition into (6.76), the 2nd Piola-Kirchhoff stress is given by

$$\begin{aligned}
\tilde{\mathbf{T}}^B_{lin}(t) &= -p_0\,\mathbf{C}_0^{-1} + 2\,\rho_0\,\left.\frac{\partial\Psi_{eq}(\mathbf{C})}{\partial\mathbf{C}}\right|_{\mathbf{C}_0} - p_{ov}\,\mathbf{C}_0^{-1} \\
&\quad + \left(4\,\rho_0\,\left.\frac{\partial^2\Psi_{eq}(\mathbf{C})}{\partial\mathbf{C}^2}\right|_{\mathbf{C}_0} + 2\,p_0\,\overset{4}{\mathbf{R}}_0\right)\cdot(\mathbf{F}_0^T\,\mathbf{E}_{lin}\,\mathbf{F}_0) \\
&\quad + \overset{4}{\mathbf{R}}_0\cdot\left(2\int_{-\infty}^{t}\sum_{k=1}^{n}\mu_k(\mathbf{C}_0)\,E_\alpha\left(-\left(\frac{t-s}{\tau_k}\right)^{\alpha_k}\right)\,\mathbf{F}_0^T\,\mathbf{E}'_{lin}(s)\,\mathbf{F}_0\,\mathrm{d}s\right)
\end{aligned} \tag{6.91}$$

wherein the viscoelastic overstress reads as

$$\tilde{\mathbf{S}}_{ov}^{B}(t) \;=\; 2\int_{-\infty}^{t}\sum_{k=1}^{n}\mu_k(\mathbf{C}_0)\,E_\alpha\left(-\left(\frac{t-s}{\tau_k}\right)^{\alpha_k}\right)\,\mathbf{F}_0^T\,\mathbf{E}'_{lin}(s)\,\mathbf{F}_0\,\mathrm{d}s\;. \tag{6.92}$$

On this basis, the related differential equation of fractional order of the overstresses $\tilde{\mathbf{S}}_{ov,k}^{B}$ is calculated as (cf. (3.99))

$$\frac{\mathrm{d}^{\alpha_k}}{\mathrm{d}t^{\alpha_k}}\tilde{\mathbf{S}}_{ov,k}^{B}(t) \;=\; 2\,\mu_k(\mathbf{C}_0)\,\mathbf{F}_0^T\,\frac{\mathrm{d}^{\alpha_k}}{\mathrm{d}t^{\alpha_k}}\mathbf{E}_{lin}(t)\,\mathbf{F}_0 - \;\frac{1}{\tau_k^{\alpha_k}}\,\tilde{\mathbf{S}}_{ov,k}^{B}\;. \tag{6.93}$$

If the fractional derivatives of (6.81) and (6.82) are defined

$$\begin{aligned}\frac{\mathrm{d}^{\alpha}}{\mathrm{d}t^{\alpha}}\tilde{\mathbf{S}}_{ov}(\omega,t) &= (i\omega)^{\alpha}\,\Delta\tilde{\mathbf{S}}_{ov}\,\mathrm{e}^{i\omega t}\\ \frac{\mathrm{d}^{\alpha}}{\mathrm{d}t^{\alpha}}\mathbf{E}_{lin}(\omega,t) &= (i\omega)^{\alpha}\,\Delta\mathbf{E}_{lin}\,\mathrm{e}^{i\omega t}\end{aligned} \tag{6.94}$$

and inserted into the differential equation (6.93), the following relation is first obtained

$$(i\omega)^{\alpha_k}\,\Delta\tilde{\mathbf{S}}_{ov,k}^{B}\,\mathrm{e}^{i\omega t} \;=\; 2\,(i\omega)^{\alpha_k}\,\mu_k(\mathbf{C}_0)\,\mathbf{F}_0^T\,\Delta\mathbf{E}_{lin}\,\mathbf{F}_0\;\mathrm{e}^{i\omega t} \;-\; \frac{1}{\tau_k^{\alpha_k}}\,\Delta\tilde{\mathbf{S}}_{ov,k}^{B}\;\mathrm{e}^{i\omega t}\;. \tag{6.95}$$

Based on the rearrangement of this relation, the harmonic overstress response can be obtained

$$\Delta\tilde{\mathbf{S}}_{ov}^{B} \;=\; 2\sum_{k=1}^{n}\mu_k(\mathbf{C}_0)\,\mathbf{F}_0^T\,\Delta\mathbf{E}_{lin}\,\mathbf{F}_0\,\frac{(i\omega\tau_k)^{\alpha_k}}{1+(i\omega\tau_k)^{\alpha_k}}\;. \tag{6.96}$$

Inserting this result and (6.81), (6.82) and (6.83) into equation (6.91), the frequency domain formulation of the 2nd Piola-Kirchhoff stress tensor is given by

$$\begin{aligned}\tilde{\mathbf{T}}_B(\omega,t) &= \tilde{\mathbf{T}}_0 \;+\; \Delta\tilde{\mathbf{T}}_B\,\mathrm{e}^{i\omega t}\\ &= -\,p_0\,\mathbf{C}_0^{-1} \;+\; 2\,\rho_0\;\left.\frac{\partial\Psi_{eq}(\mathbf{C})}{\partial\mathbf{C}}\right|_{\mathbf{C}_0} \;-\; \Delta p\,\mathbf{C}_0^{-1}\,\mathrm{e}^{i\omega t}\\ &\quad+\left(4\,\rho_0\;\left.\frac{\partial^2\Psi_{eq}(\mathbf{C})}{\partial\mathbf{C}^2}\right|_{\mathbf{C}_0} \;+\; 2\,p_0\;\overset{4}{\mathbf{R}}_0\right.\\ &\quad\left.+\,2\sum_{k=1}^{n}\mu_k(\mathbf{C}_0)\,\frac{(i\omega\tau_k)^{\alpha_k}}{1+(i\omega\tau_k)^{\alpha_k}}\;\overset{4}{\mathbf{R}}_0\right)\cdot\mathbf{F}_0^T\,\Delta\mathbf{E}_{lin}\,\mathbf{F}_0\,\mathrm{e}^{i\omega t}\end{aligned} \tag{6.97}$$

and the fourth order dynamic modulus tensor of the fractional model follows to

$$\overset{4}{\mathbf{G}}_B\;(\omega) \;=\; 4\,\rho_0\;\left.\frac{\partial^2\Psi_{eq}(\mathbf{C})}{\partial\mathbf{C}^2}\right|_{\mathbf{C}_0} \;+\; 2\,p_0\;\overset{4}{\mathbf{R}}_0 \;+2\sum_{k=1}^{n}\mu_k(\mathbf{C}_0)\,\frac{(i\omega\tau_k)^{\alpha_k}}{1+(i\omega\tau_k)^{\alpha_k}}\;\overset{4}{\mathbf{R}}_0 \tag{6.98}$$

with the complex modulus

$$\overset{4}{\mathbf{G}}{}^{*}_{B}(\omega) \;=\; 2\sum_{k=1}^{n}\mu_k(\mathbf{C}_0)\,\frac{(i\omega\tau_k)^{\alpha_k}}{1+(i\omega\tau_k)^{\alpha_k}}\;\overset{4}{\mathbf{R}}_0 \quad . \tag{6.99}$$

By comparing (6.88) with (6.98) or (6.89) with (6.99), one can observe that the frequency dependences of the classical and fractional constitutive models differ. In the case of $\alpha_k = 1$, both models are equal.

Chapter 7

Parameter identification

Introduction

Parameter identification is necessary to determine the unknown material constants of a constitutive model. The focus of the identification is the optimisation of these parameters such that the numerical approximation of the constitutive approach is able to represent the experimentally observed material characteristics. The general procedure can therefore be characterised as an optimisation process, which is commonly based on a minimisation of the error between the experimental data and the numerically simulated data provided by the constitutive model. Moreover, the identification process is usually performed on the basis of suitable optimisation algorithms, for instance, the local least squares method or the global genetic algorithm.
In order to perform an identification, the experimental testing procedures must be simulated by the constitutive model to provide the corresponding numerical results. To this end, the equations for the numerical simulation must first be derived on the basis of the constitutive equations.

Outline

The focus of this chapter is the identification of the material parameters of the classical and the fractional constitutive approaches. On account of this, the constitutive equations must be specialised with respect to the experimentally applied loading conditions and will be called identification equations.
On this basis, the first section of this chapter starts with an introduction to the general concept which is applied to derive the identification equations which belong to the quasi-static and dynamic investigations.
Moreover, the hyperelastic part of the specific Helmholtz free energy $\rho_0 \Psi$ is introduced and the deformation dependent parameters $\mu_k(\mathbf{C}_0)$ of the overstress part of the models are defined.
The second section is concerned with the static part of the model. Hence, the identification equations required to simulate the quasi-static experiments are derived for each deformation mode.

The parameter identification of the dynamic part of the classical and of the fractional models and their corresponding identification equations to represent the dynamic mechanical experiments are provided in the third section.
The fourth section is concerned with the numerical identification routine which is programmed in the form of a numerical software code in MATLAB.
In order to reveal the performance of the classical and the fractional constitutive model, the identification results of the quasi-static and dynamic experiments are presented in the last section of this chapter. Thereby, a comparison between both formulations is additionally drawn to reveal the benefits of the fractional constitutive model with respect to the number of material parameters required and the quality of the numerical approximation.

It is mentioned, that parts of the parameter identification have been published in prior printed publications which were approved by the university (Wollscheid and Lion (2013a), Wollscheid and Lion (2013b) and Wollscheid and Lion (2014)).

7.1 General procedure

The parameter identification in this work is generally divided into a static part and a dynamic part. The static one is concerned with the identification of the static part of the model whereas the dynamic part of identification focuses on the identification of the dynamic part of the classical and of the fractional models.

The static material parameters are identified by a minimisation of the error between the experimental equilibrium stress data and the corresponding numerical simulation. To this end, the following equation is used:

$$\tilde{\mathbf{T}}_0 \;=\; -\,p_0\,\mathbf{C}_0^{-1} \;+\; 2\,\rho_0\;\left.\frac{\partial \Psi_{eq}(\mathbf{C})}{\partial \mathbf{C}}\right|_{\mathbf{C}_0} \tag{7.1}$$

After that, the static material parameters are held constant and the dynamic ones are identified by a minimisation of the error between the mastered experimental data of the temperature-frequency-sweep tests and the corresponding numerical approximation of the model

$$\begin{aligned}\Delta\tilde{\mathbf{T}}\,\mathrm{e}^{i\omega t} \;=\; & -\,\Delta p\,\mathrm{e}^{i\omega t}\,\mathbf{C}_0^{-1} \;+\; \left(2\,p_0\;\overset{4}{\mathbf{R}}_0 \;+4\,\rho_0\;\left.\frac{\partial^2 \Psi_{eq}(\mathbf{C})}{\partial \mathbf{C}^2}\right|_{\mathbf{C}_0}\right.\\ & \left.+\,G^*_{A/B}\;\overset{4}{\mathbf{R}}_0\right)\cdot\mathbf{F}_0^T\,\Delta\mathbf{E}_{lin}\,\mathbf{F}_0\,\mathrm{e}^{i\omega t}\;.\end{aligned} \tag{7.2}$$

The complex part of the overstress is summarised in the variable $G^*_{A/B}$ and denotes the complex modulus. In terms of the classical model (type A), it reads as

$$G^*_A \;=\; 2\sum_{k=1}^{n}\mu_k(\mathbf{C}_0)\,\frac{i\omega\tau_k}{1+i\omega\,\tau_k}\;, \tag{7.3}$$

whereas its definition for the fractional approach (type B) is given by

$$G_B^* \;=\; 2 \sum_{k=1}^{n} \mu_k(\mathbf{C}_0)\, \frac{(i\omega\tau_k)^{\alpha_k}}{1+(i\omega\,\tau_k)^{\alpha_k}} \;. \tag{7.4}$$

In order to provide the identification equations, a suitable formulation of the specific Helmholtz free energy $\rho_0\,\Psi_{eq}(\mathbf{C})$ as well as of the deformation dependent dynamic parameters $\mu_k(\mathbf{C}_0)$ are chosen first. With respect to the subsequent finite element implementation of the constitutive models into the code MSC Marc, the specific Helmholtz free energy is defined by the Mooney approach (Mooney 1940)

$$\begin{aligned} \rho_0\,\Psi_{eq}(\mathbf{C}) \;&=\; C_{10}\,(\mathrm{I}_\mathbf{C}\,-\,3)\,+\,C_{20}\,(\mathrm{I}_\mathbf{C}\,-\,3)^2\,+\,C_{30}\,(\mathrm{I}_\mathbf{C}\,-\,3)^3 \\ &\quad +\,C_{11}\,(\mathrm{I}_\mathbf{C}\,-\,3)\,(\mathrm{II}_\mathbf{C}\,-\,3)\,+\,C_{01}\,(\mathrm{II}_\mathbf{C}\,-\,3)\;, \end{aligned} \tag{7.5}$$

with the first and second invariants $\mathrm{I}_\mathbf{C}$ and $\mathrm{II}_\mathbf{C}$ of the right Cauchy-Green tensor and the material parameters C_{10}, C_{20}, C_{30}, C_{11} and C_{01}. Since the experimentally obtained equilibrium stress response is determined by a single curvature, a mathematical representation on the basis of five material parameters is not necessary. Regarding this, the formulation applied in this work is reduced to the material constants C_{10} and C_{01}

$$\rho_0\,\Psi_{eq}(\mathbf{C}) \;=\; C_{10}\,(\mathrm{I}_\mathbf{C}\,-\,3)\,+\,C_{01}\,(\mathrm{II}_\mathbf{C}\,-\,3)\;. \tag{7.6}$$

In order to represent the predeformation dependent properties of the storage and the loss modulus, the dynamic parameters $\mu_k(\mathbf{C}_0)$ are defined by a function of the exponential type, which depends on the first and second invariants $\mathrm{I}_\mathbf{C}$ and $\mathrm{II}_\mathbf{C}$ of the right Cauchy-Green tensor. In terms of the SBR20, SBR40 and EPDM20 vulcanisates, the dynamic parameters are defined by

$$\mu_k(\mathbf{C}_0) \;=\; \mu_{0,k}\,\mathrm{e}^{\,a\,(\mathrm{I}_\mathbf{C}-3)\,+\,b\,(\mathrm{II}_\mathbf{C}-3)}\;. \tag{7.7}$$

The more complex deformation dependence of the NR40 vulcanisate is approximated by an additional term which depends on $\mathrm{I}_\mathbf{C}$ and $\mathrm{II}_\mathbf{C}$

$$\mu_k(\mathbf{C}_0) \;=\; \mu_{0,k}\,\mathrm{e}^{\,a\,(\mathrm{I}_\mathbf{C}-3)\,+\,b\,(\mathrm{II}_\mathbf{C}-3)\,+\,c\,(\mathrm{I}_\mathbf{C}-3)\,(\mathrm{II}_\mathbf{C}-3)}\;. \tag{7.8}$$

In this, the variables a, b and c are material parameters and the variables $\mu_{0,k}$ represent the reference value of the dynamic parameters $\mu_k(\mathbf{C}_0)$. With regard to the interpretation as a Maxwell chain, the parameters $\mu_{0,k}$ can be interpreted as a reference stiffness of the Maxwell elements.

7.2 Static part

In order to obtain the identification equation to identify C_{10} and C_{01}, the equilibrium stress in (7.1) must be specified with respect to each deformation mode. To this end, it is necessary to calculate the first derivative of the specific Helmholtz free energy with

respect to the right Cauchy-Green tensor first. If the chain rule of differentiation is applied, the first derivative of $\rho_0 \Psi_{eq}$ in (7.6) can be written as

$$\rho_0 \frac{\partial \Psi_{eq}}{\partial \mathbf{C}} = \rho_0 \frac{\partial \Psi_{eq}}{\partial \mathrm{I}_\mathbf{C}} \frac{\partial \mathrm{I}_\mathbf{C}}{\partial \mathbf{C}} + \rho_0 \frac{\partial \Psi_{eq}}{\partial \mathrm{II}_\mathbf{C}} \frac{\partial \mathrm{II}_\mathbf{C}}{\partial \mathbf{C}} . \tag{7.9}$$

By inserting the derivatives of the first and of the second invariant $\mathrm{I}_\mathbf{C}$ and $\mathrm{II}_\mathbf{C}$

$$\frac{\partial \mathrm{I}_\mathbf{C}}{\partial \mathbf{C}} = \mathbf{1} \tag{7.10}$$

$$\frac{\partial \mathrm{II}_\mathbf{C}}{\partial \mathbf{C}} = \mathrm{I}_\mathbf{C} \mathbf{1} - \mathbf{C} . \tag{7.11}$$

into (7.9), the first derivative of the equilibrium part of the specific Helmholtz free energy reads as

$$\rho_0 \frac{\partial \Psi_{eq}}{\partial \mathbf{C}} = C_{10} \mathbf{1} + C_{01} \Big(\mathrm{I}_\mathbf{C} \mathbf{1} - \mathbf{C} \Big) = \Big[C_{10} + C_{01} \mathrm{I}_\mathbf{C} \Big] \mathbf{1} - C_{01} \mathbf{C} . \tag{7.12}$$

If (7.12) is inserted into (7.1), the following result is obtained

$$\tilde{\mathbf{T}}_0 = - p_0 \mathbf{C}_0^{-1} + 2 \Big[C_{10} + C_{01} \mathrm{I}_\mathbf{C} \Big] \mathbf{1} - 2 C_{01} \mathbf{C}_0 . \tag{7.13}$$

In order to obtain the identification equation which belongs to (7.13), the equilibrium part of the 2nd Piola-Kirchhoff stress $\tilde{\mathbf{T}}_0$ must be specified with respect to the experimentally applied loadings. For this purpose, the kinematic relations with respect to uniaxial tension, compression and the pure shear are derived.

7.2.1 Uniaxial tension and compression

In order to derive the equilibrium stress response $\tilde{\mathbf{T}}_0$ with respect to uniaxial tension and compression, the corresponding kinematic relations must be defined. With regard to the experimental testing procedure, the loading condition displayed in figure 7.1 is taken into account.

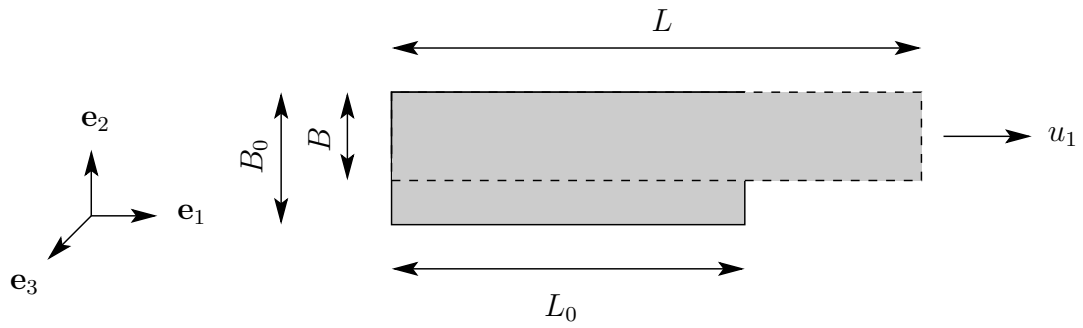

FIGURE 7.1: Loadcase of the quasi-static experiments in uniaxial tension and compression

The specimen is loaded by the uniaxial displacement u_1 in loading direction $\mathbf{e}_1$. Thus, the specimen is stretched from its initial length L_0 to the deformed length L, whereas its initial width B_0 and and its initial thickness D_0 are reduced to width B and thickness D in the deformed state. Based on this, the stretches in the $\mathbf{e}_1$, $\mathbf{e}_2$ and $\mathbf{e}_3$ directions are defined by the ratio of the deformed dimensions to the initial dimensions

$$\lambda_1 = \frac{L}{L_0} , \quad \lambda_2 = \frac{B}{B_0} , \quad \lambda_3 = \frac{D}{D_0} , \tag{7.14}$$

such that the deformation gradient reads as

$$\mathbf{F} = \begin{bmatrix} \lambda_1 & 0 & 0 \\ 0 & \lambda_2 & 0 \\ 0 & 0 & \lambda_3 \end{bmatrix} . \tag{7.15}$$

Regarding isotropic material behaviour, the stretches in directions $\mathbf{e}_2$ and $\mathbf{e}_3$ are identical such that $\lambda_2 = \lambda_3$ holds. Taking this relation and the incompressibility constraint

$$\det \mathbf{F} = \lambda_1 \, \lambda_2 \, \lambda_3 = 1 \tag{7.16}$$

into account, the deformation gradient (7.15) at stretch λ can be expressed by

$$\mathbf{F} = \begin{bmatrix} \lambda & 0 & 0 \\ 0 & \dfrac{1}{\sqrt{\lambda}} & 0 \\ 0 & 0 & \dfrac{1}{\sqrt{\lambda}} \end{bmatrix} . \tag{7.17}$$

Based on this definition and the relation $\mathbf{C} = \mathbf{F}^T \mathbf{F}$, the right Cauchy-Green tensor and its inverse read as

$$\mathbf{C} = \begin{bmatrix} \lambda^2 & 0 & 0 \\ 0 & \dfrac{1}{\lambda} & 0 \\ 0 & 0 & \dfrac{1}{\lambda} \end{bmatrix} , \quad \mathbf{C}_0^{-1} = \begin{bmatrix} \dfrac{1}{\lambda^2} & 0 & 0 \\ 0 & \lambda & 0 \\ 0 & 0 & \lambda \end{bmatrix} . \tag{7.18}$$

In order to obtain the identification equation with respect to uniaxial tension and compression, (7.18) is inserted into (7.13). Thereby, the unknown pressure p_0 must first be determined by one of the geometrical constraints

$$\tilde{T}_{0,22} = \tilde{T}_{0,33} = 0 . \tag{7.19}$$

With respect to the $\mathbf{e}_2$ direction, the corresponding one-dimensional equilibrium stress response at static prestretch λ_0 is given by

$$T_{0,22} = -p_0 \, \lambda_0 + 2 \left[C_{10} + C_{01} \, \mathrm{I}_{\mathbf{C}} \right] - 2 \, C_{01} \, \frac{1}{\lambda_0} = 0 . \tag{7.20}$$

This equation is solved with respect to the static pressure p_0

$$p_0 = 2\left[C_{10} + C_{01}\,\mathrm{I}_{\mathbf{C}}\right]\frac{1}{\lambda_0} - 2\,C_{01}\,\frac{1}{\lambda_0^2} \tag{7.21}$$

and inserted into the equilibrium stress of the loading direction

$$\tilde{T}_{0,11} = -\,p_0\,\frac{1}{\lambda_0^2} + 2\left[C_{10} + C_{01}\,\mathrm{I}_{\mathbf{C}}\right] - 2\,C_{01}\,\lambda_0^2\,. \tag{7.22}$$

On the basis of this procedure, the identification equation of the equilibrium stress $\tilde{T}_{0,11}$ with respect to uniaxial tension and compression reads as

$$\tilde{T}_{0,11} = 2\left[C_{10} + C_{01}\,\mathrm{I}_{\mathbf{C}}\right]\left(1 - \frac{1}{\lambda_0^3}\right) - 2\,C_{01}\left(\lambda_0^2 - \frac{1}{\lambda_0^4}\right)\,. \tag{7.23}$$

Since the experimental stress data provided by the quasi-static testing device is of the 1st Piola-Kirchhoff type, the identification equation for $\tilde{T}_{0,11}$ must be transformed into 1st Piola-Kirchhoff stresses. With the relation between the 1st and the 2nd Piola-Kirchhoff stress

$$\mathbf{P} = \tilde{\mathbf{T}}\,\mathbf{F} \quad \Rightarrow \quad P_{0,11} = T_{0,11}\,\lambda_0\,, \tag{7.24}$$

the identification equation to simulate the experimentally obtained equilibrium stress in uniaxial tension and compression reads as

$$P_{0,11} = 2\left[C_{10} + C_{01}\,\mathrm{I}_{\mathbf{C}}\right]\left(\lambda_0 - \frac{1}{\lambda_0^2}\right) - 2\,C_{01}\left(\lambda_0^3 - \frac{1}{\lambda_0^3}\right)\,. \tag{7.25}$$

7.2.2 Pure shear

The identification equation of the equilibrium stress with respect to pure shear can be derived in the same manner as for uniaxial tension and compression. With respect to this loadcase, figure 7.2 is taken into account.

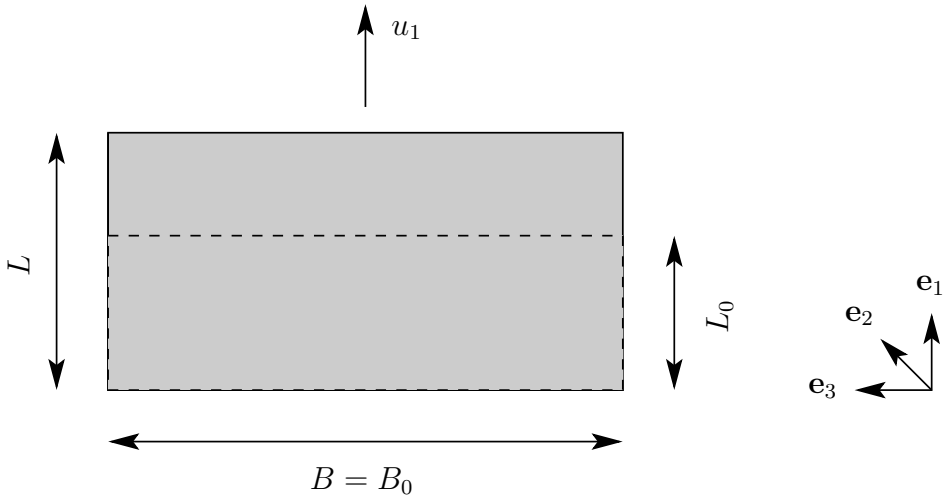

FIGURE 7.2: Loadcase of the quasi-static experiments in pure shear

The specimen is loaded by the displacement u_1 in direction $\mathbf{e}_1$ which results in an elongation of the specimen from its initial length L_0 to the deformed length L and a reduction of its initial thickness D_0 to the deformed thickness D. Since the width of the specimen is much larger than its thickness, the initial width remains constant during deformation such that $B = B_0$ holds. In view of this, the stretches in $\mathbf{e}_1$, $\mathbf{e}_2$ and $\mathbf{e}_3$ directions are defined by

$$\lambda_1 = \frac{L}{L_0} , \quad \lambda_2 = \frac{D}{D_0} , \quad \lambda_3 = \frac{B}{B_0} = 1 . \tag{7.26}$$

By taking isotropic material behaviour and incompressibility into account, the deformation gradient at stretch λ is given by

$$\mathbf{F} = \begin{bmatrix} \lambda & 0 & 0 \\ 0 & \frac{1}{\lambda} & 0 \\ 0 & 0 & 1 \end{bmatrix} \tag{7.27}$$

from which the right Cauchy-Green tensor and its inverse can be obtained

$$\mathbf{C} = \begin{bmatrix} \lambda^2 & 0 & 0 \\ 0 & \frac{1}{\lambda^2} & 0 \\ 0 & 0 & 1 \end{bmatrix} , \quad \mathbf{C}^{-1} = \begin{bmatrix} \frac{1}{\lambda^2} & 0 & 0 \\ 0 & \lambda^2 & 0 \\ 0 & 0 & 1 \end{bmatrix} . \tag{7.28}$$

Based on these relations, the equilibrium stress $T_{0,11}$ at static prestretch λ_0 can be derived. First, the static pressure p_0 is determined by the geometrical constraint $T_{0,22} = 0$

$$p_0 = 2 \left[C_{10} + C_{01} \, \mathrm{I}_{\mathbf{C}} \right] \frac{1}{\lambda_0^2} - 2 \, C_{01} \, \frac{1}{\lambda_0^4} . \tag{7.29}$$

By inserting this solution into (7.1), the equilibrium stress in loading direction reads as

$$\tilde{T}_{0,11} = 2 \left[C_{10} + C_{01} \, \mathrm{I}_{\mathbf{C}} \right] \left(1 - \frac{1}{\lambda_0^4} \right) - 2 \, C_{01} \left(\lambda_0^2 - \frac{1}{\lambda_0^6} \right) . \tag{7.30}$$

If the relation between the 1st and the 2nd Piola-Kirchhoff stresses in (7.24) is applied, the identification equation to simulate the experimentally obtained equilibrium stress with respect to pure shear is given by

$$P_{0,11} = 2 \left[C_{10} + C_{01} \, \mathrm{I}_{\mathbf{C}} \right] \left(\lambda_0 - \frac{1}{\lambda_0^3} \right) - 2 \, C_{01} \left(\lambda_0^3 - \frac{1}{\lambda_0^5} \right) . \tag{7.31}$$

7.3 Dynamic part

In order to derive the dynamic identification equations, the constitutive equation for the overstress $\Delta\tilde{\mathbf{T}}$ in (7.2) must be specified with respect to the harmonic loading in the dynamic-mechanical tests. In so doing, the second derivative of the equilibrium part of the specific Helmholtz free energy with respect to the right Cauchy-Green tensor must

be evaluated first. Starting from (7.12), the second derivative of $\rho_0\,\Psi_{eq}$ follows to

$$\rho_0\,\frac{\partial^2\Psi_{eq}}{\partial\mathbf{C}^2} \;=\; C_{01}\,\frac{\partial \mathrm{I}_{\mathbf{C}}}{\partial\mathbf{C}}\otimes\mathbf{1} \;-\; C_{01}\,\frac{\partial\mathbf{C}}{\partial\mathbf{C}}\;. \tag{7.32}$$

By inserting the derivatives of $\mathrm{I}_{\mathbf{C}}$ and $\mathrm{II}_{\mathbf{C}}$ in (7.10) in equation (7.32) and taking the relation

$$\frac{\partial\mathbf{C}}{\partial\mathbf{C}} \;=\; (\mathbf{1}\otimes\mathbf{1})^{T23} \tag{7.33}$$

into account, the second derivative of the specific Helmholtz free energy is written as

$$\rho_0\,\frac{\partial^2\Psi_{eq}}{\partial\mathbf{C}^2} \;=\; C_{01}\,(\mathbf{1}\otimes\mathbf{1}) \;-\; C_{01}\,(\mathbf{1}\otimes\mathbf{1})^{T23}\;. \tag{7.34}$$

If this result is inserted into (7.2), the equation for the 2nd Piola-Kirchhoff overstress reads as

$$\begin{aligned}\Delta\tilde{\mathbf{T}} \;=\;& -\Delta p\,\mathbf{C}_0^{-1} \;+\; 2\,p_0\;\overset{4}{\mathbf{R}}_0\cdot\left(\mathbf{F}_0^T\,\Delta\mathbf{E}_{lin}\,\mathbf{F}_0\right)\\ &+4\left[C_{01}\,(\mathbf{1}\otimes\mathbf{1}) \;-\; C_{01}\,(\mathbf{1}\otimes\mathbf{1})^{T23}\right]\cdot\left(\mathbf{F}_0^T\,\Delta\mathbf{E}_{lin}\,\mathbf{F}_0\right)\\ &+G^*_{A/B}\;\overset{4}{\mathbf{R}}_0\cdot\left(\mathbf{F}_0^T\,\Delta\mathbf{E}_{lin}\,\mathbf{F}_0\right)\;.\end{aligned} \tag{7.35}$$

Since the dynamic mechanical analyses are characterised by small harmonic excitations $\Delta\varepsilon$ in the neighbourhood of the predeformation $\mathbf{F}_0$, the same loadcase is considered as for the quasi-static experiments in tension and compression (figure 7.1). To this end, the $\mathbf{e}_1$ direction is the loading direction and the assumptions of incompressibility and isotropy are taken into account. Based on these assumptions, the deformation gradient of predeformation at static prestretch λ_0, its transpose and its inverse read as

$$\mathbf{F}_0 \;=\; \mathbf{F}_0^T \;=\; \begin{bmatrix}\lambda_0 & 0 & 0\\ 0 & \dfrac{1}{\sqrt{\lambda_0}} & 0\\ 0 & 0 & \dfrac{1}{\sqrt{\lambda_0}}\end{bmatrix}\;,\quad \mathbf{F}_0^{-1} \;=\; \begin{bmatrix}\dfrac{1}{\lambda_0} & 0 & 0\\ 0 & \sqrt{\lambda_0} & 0\\ 0 & 0 & \sqrt{\lambda_0}\end{bmatrix}\;, \tag{7.36}$$

On the basis of these relations, the right Cauchy-Green tensor at prestretch λ_0 and its inverse result in

$$\mathbf{C}_0 \;=\; \begin{bmatrix}\lambda_0^2 & 0 & 0\\ 0 & \dfrac{1}{\lambda_0} & 0\\ 0 & 0 & \dfrac{1}{\lambda_0}\end{bmatrix}\;,\quad \mathbf{C}_0^{-1} \;=\; \begin{bmatrix}\dfrac{1}{\lambda_0^2} & 0 & 0\\ 0 & \lambda_0 & 0\\ 0 & 0 & \lambda_0\end{bmatrix}\;. \tag{7.37}$$

With the dynamic strain amplitude $\Delta\varepsilon$, the incremental Green-Lagrange strain tensor can be expressed by

$$\mathbf{E}_{lin} = \frac{1}{2}(\mathbf{h} + \mathbf{h}^T) = \Delta\varepsilon \begin{bmatrix} 1 & 0 & 0 \\ 0 & -\frac{1}{2} & 0 \\ 0 & 0 & -\frac{1}{2} \end{bmatrix} \tag{7.38}$$

which results in the definition of the following term

$$(\mathbf{F}_0^T \, \Delta\mathbf{E}_{lin} \, \mathbf{F}_0) = \Delta\varepsilon \begin{bmatrix} \lambda_0^2 & 0 & 0 \\ 0 & -\frac{1}{2\,\lambda_0} & 0 \\ 0 & 0 & -\frac{1}{2\,\lambda_0} \end{bmatrix} . \tag{7.39}$$

By taking the projection tensor of fourth order

$$\overset{4}{\mathbf{R}}_0 = (\mathbf{C}_0^{-1} \otimes \mathbf{C}_0^{-1})^{T23} \tag{7.40}$$

and the relation (Ehlers 2007)

$$(\mathbf{A} \otimes \mathbf{B})^{T23} \cdot \mathbf{C} = \mathbf{A}\,\mathbf{C}\,\mathbf{B}^T , \tag{7.41}$$

into account, the following kinematic relation is obtained

$$\overset{4}{\mathbf{R}}_0 \cdot (\mathbf{F}_0^T \, \Delta\mathbf{E}_{lin} \, \mathbf{F}_0) = \Delta\varepsilon \begin{bmatrix} \frac{1}{\lambda_0^2} & 0 & 0 \\ 0 & -\frac{\lambda_0}{2} & 0 \\ 0 & 0 & -\frac{\lambda_0}{2} \end{bmatrix} . \tag{7.42}$$

Based on these expressions, the dynamic identification equation can be evaluated similarly as for the quasi-static loadcase in tension and compression. First, the pressure term Δp is calculated by one of the geometric constraints

$$\Delta\tilde{T}_{22} = \Delta\tilde{T}_{33} = 0 . \tag{7.43}$$

By taking the mathematical relations (Ehlers 2007)

$$\begin{aligned} (\mathbf{1} \otimes \mathbf{1})\,\mathbf{A} &= \mathrm{tr}(\mathbf{A})\,\mathbf{1} , \\ (\mathbf{1} \otimes \mathbf{1})^{T23}\,\mathbf{A} &= \mathbf{A} \end{aligned} \tag{7.44}$$

in combination with (7.36), (7.37), (7.39) and (7.42) into account, the pressure is evaluated by the geometric constraint for the $\mathbf{e}_2$ component of the dynamic part of the

2nd Piola-Kirchhoff stress tensor

$$\begin{aligned}\Delta\tilde{T}_{22} \;=\; & -\Delta p\,\lambda_0 \,+\, 2\,p_0\,\Delta\varepsilon\,\left(-\frac{\lambda_0}{2}\right) \\ & +4\,\left[C_{01}\,\Delta\varepsilon\,\left(\lambda_0^2 \,-\, \frac{1}{\lambda_0}\right) \,-\, C_{01}\,\Delta\varepsilon\,\left(-\frac{1}{2\,\lambda_0}\right)\right] \,+\, G^*_{A/B}\,\Delta\varepsilon\,\left(-\frac{\lambda_0}{2}\right) \,=\, 0\;.\end{aligned} \tag{7.45}$$

By rearranging this equation, the pressure finally reads as

$$\Delta p \,=\, \Delta\varepsilon\left\{ -\,p_0 \,+\, 4\,\left[C_{01}\,\left(\lambda_0 \,-\, \frac{1}{\lambda_0^2}\right) \,+\, C_{01}\,\frac{1}{2\,\lambda_0^2}\right] \,-\, \frac{1}{2}\,G^*_{A/B}\right\}\,. \tag{7.46}$$

By inserting this result into (7.2), the dynamic identification equation is derived and reads as

$$\Delta\tilde{T}_{11} \,=\, \Delta\varepsilon\left\{3\,p_0\,\frac{1}{\lambda_0^2} \,+\, 4\,C_{01}\,\left(\frac{1}{2\,\lambda_0^4} \,-\, \frac{2}{\lambda_0}\right) \,+\, \frac{3}{2}\,G^*_{A/B}\,\frac{1}{\lambda_0^2}\right\}\,. \tag{7.47}$$

In view of the dynamic-mechanical tests, the experimental results are provided in form of the storage and the loss modulus which are of the Cauchy stress type. Hence, equation (7.47) is firstly transformed into Cauchy stresses by applying the relation between the Cauchy stress $\mathbf{T}$ and the 2nd Piola-Kirchhoff stress $\tilde{\mathbf{T}}$

$$\mathbf{T} \,=\, \mathbf{F}\,\tilde{\mathbf{T}}\,\mathbf{F}^T \,=\, (\mathbf{1}+\mathbf{h})\,\mathbf{F}_0\,\tilde{\mathbf{T}}\,\mathbf{F}_0^T\,(\mathbf{1}+\mathbf{h}^T)\;. \tag{7.48}$$

If terms of higher order are neglected, the one-dimensional form of this relation can be expressed by

$$T_{11} \,=\, \tilde{T}_{11}\,\lambda_0^2\,(1\,+\,\Delta\varepsilon)^2 \,\approx\, \left(\tilde{T}_{0,11}(\lambda_0) \,+\, \Delta\tilde{T}_{11}(\lambda_0,\Delta\varepsilon)\right)\,\lambda_0^2\,(1\,+\,2\,\Delta\varepsilon)\;. \tag{7.49}$$

By inserting the static and dynamic identification equations $\tilde{T}_{0,11}$ and $\Delta\tilde{T}_{11}$ in (7.23) and (7.47) into the (7.49), the Cauchy stress reads as

$$\begin{aligned}T_{11} \;=\; & 2\left[C_{10} \,+\, C_{01}\,\mathrm{I}_{\mathbf{C}}\right]\,\left(\lambda_0^2 \,-\, \frac{1}{\lambda_0}\right) \,-\, 2\,C_{01}\,\left(\lambda_0^4 \,-\, \frac{1}{\lambda_0^2}\right) \\ & \Delta\varepsilon\left\{4\left[C_{10} \,+\, C_{01}\,\mathrm{I}_{\mathbf{C}}\right]\,\left(\lambda_0^2 \,-\, \frac{1}{\lambda_0}\right) \,-\, 4\,C_{01}\,\left(\lambda_0^4 \,-\, \frac{1}{\lambda_0^2}\right)\right. \\ & \left. +\,3\,p_0 \,+\, 4\,C_{01}\,\left(\frac{1}{2\,\lambda_0^2} \,-\, 2\,\lambda_0\right) \,+\, \frac{3}{2}\,G^*_{A/B}\right\} \\ & (\Delta\varepsilon)^2\left\{6\,p_0 \,+\, 8\,C_{01}\,\left(\frac{1}{2\,\lambda_0^2} \,-\, 2\,\lambda_0\right) \,+\, 3\,G^*_{A/B}\right\}\;.\end{aligned} \tag{7.50}$$

It consists of a static part and two dynamic parts whereby the first one is of first order in $\Delta\varepsilon$ and the second one is of second order in $\Delta\varepsilon$. Since the dynamic strain amplitude is very small, the dynamic term of second order can be neglected ($(\Delta\varepsilon)^2 \to 0$), such

that the final form of the dynamic identification equation follows to

$$\begin{aligned} \Delta T_{11} \;=\; \Delta\varepsilon \Bigg\{ & 4 \left[C_{10} \,+\, C_{01}\, \mathrm{I}_{\mathbf{C}} \right] \left(\lambda_0^2 \,-\, \frac{1}{\lambda_0} \right) \,-\, 4\, C_{01} \left(\lambda_0^4 \,-\, \frac{1}{\lambda_0^2} \right) \\ & +\, 3\, p_0 \,+\, 4\, C_{01} \left(\frac{1}{2\,\lambda_0^2} \,-\, 2\,\lambda_0 \right) \,+\, \frac{3}{2}\, G^*_{A/B} \Bigg\} \;. \end{aligned} \tag{7.51}$$

If the static pressure p_0 in (7.21) is inserted into (7.51), the dynamic identification equation finally reads as

$$\Delta T_{11} \;=\; \Delta\varepsilon \left\{ 4 \left[C_{10} \,+\, C_{01}\, \mathrm{I}_{\mathbf{C}} \right] \left(\lambda_0^2 \,+\, \frac{1}{2\,\lambda_0} \right) \,-\, 4\, C_{01} \left(\lambda_0^4 \,+\, 2\,\lambda_0 \right) \,+\, \frac{3}{2}\, G^*_{A/B} \right\} \;. \tag{7.52}$$

With the complex responses of the linearised overstress models $G^*_{A/B}$ in (7.3) and (7.4), the dynamic identification equation of the classical approach reads as

$$\begin{aligned} \Delta T^A_{11} \;=\; \Delta\varepsilon \Bigg\{ & 4 \left[C_{10} \,+\, C_{01}\, \mathrm{I}_{\mathbf{C}} \right] \left(\lambda_0^2 \,+\, \frac{1}{2\,\lambda_0} \right) \,-\, 4\, C_{01} \left(\lambda_0^4 \,+\, 2\,\lambda_0 \right) \\ & +\, 3 \sum_{k=1}^{n} \mu_k(\mathbf{C}_0)\, \frac{i\omega\tau_k}{1 + i\omega\,\tau_k} \Bigg\} \;, \end{aligned} \tag{7.53}$$

whereas the expression of the fractional formulation follows to

$$\begin{aligned} \Delta T^B_{11} \;=\; \Delta\varepsilon \Bigg\{ & 4 \left[C_{10} \,+\, C_{01}\, \mathrm{I}_{\mathbf{C}} \right] \left(\lambda_0^2 \,+\, \frac{1}{2\,\lambda_0} \right) \,-\, 4\, C_{01} \left(\lambda_0^4 \,+\, 2\,\lambda_0 \right) \\ & +\, 3 \sum_{k=1}^{n} \mu_k(\mathbf{C}_0)\, \frac{(i\omega\tau_k)^{\alpha_k}}{1 + (i\omega\,\tau_k)^{\alpha_k}} \Bigg\} \;. \end{aligned} \tag{7.54}$$

Since the identification of the material parameters is performed with respect to the storage and the loss modulus, the dynamic identification equations (7.53) and (7.54) must finally be transferred into the corresponding identification equations for the complex moduli G^*_A and G^*_B. For this purpose, ΔT^A_{11} and ΔT^B_{11} are divided by the strain amplitude $\Delta\varepsilon$ and then separated into real and imaginary parts. In so doing, the storage and the loss modulus of the classical approach are defined by

$$\begin{aligned} G'_A(\omega) \;=\; & 4 \left[C_{10} \,+\, C_{01}\, \mathrm{I}_{\mathbf{C}} \right] \left(\lambda_0^2 \,+\, \frac{1}{2\,\lambda_0} \right) \,-\, 4\, C_{01} \left(\lambda_0^4 \,+\, 2\,\lambda_0 \right) \\ & +\, 3 \sum_{k=1}^{n} \mu_k(\mathbf{C}_0)\, \frac{(\omega\,\tau_k)^2}{1 + (\omega\,\tau_k)^2} \end{aligned} \tag{7.55}$$

$$G''_A(\omega) \;=\; 3 \sum_{k=1}^{n} \mu_k(\mathbf{C}_0)\, \frac{\omega\,\tau_k}{1 + (\omega\,\tau_k)^2} \;.$$

In terms of the fractional model, the separation into real and imaginary parts is more

complicated, but the resulting formulations of the storage and the loss modulus are obtained the same way as for the fractional Maxwell element, which is given by equation (3.111) and (3.112). Since the identification routine is programmed in the numerical code MATLAB, the software provided functions *real()* and *imag()* can be applied to calculate the real and imaginary parts of a complex-valued function. Using these functions, the specified identification equations of the storage and the loss modulus read as

$$\begin{aligned} G'_B(\omega) &= 4\left[C_{10} + C_{01}\,\mathrm{I_C}\right]\left(\lambda_0^2 + \frac{1}{2\,\lambda_0}\right) - 4\,C_{01}\,\left(\lambda_0^4 + 2\,\lambda_0\right) \\ &\quad + real\left(3\sum_{k=1}^{n}\mu_k(\mathbf{C}_0)\,\frac{(i\,\omega\,\tau_k)^{\alpha_k}}{1+(i\,\omega\,\tau_k)^{\alpha_k}}\right), \\ G''_B(\omega) &= imag\left(3\sum_{k=1}^{n}\mu_k(\mathbf{C}_0)\,\frac{(i\,\omega\,\tau_k)^{\alpha_k}}{1+(i\,\omega\,\tau_k)^{\alpha_k}}\right). \end{aligned} \tag{7.56}$$

7.4 Numerical identification process

The identification procedure to determine the material parameters is programmed by a numerical code in the software MATLAB. The general concept of the implementation is based upon the minimisation of the error between the experimental data and the numerically simulated data

$$error = \left|\left|\frac{\sigma_{num} - \sigma_{exp}}{\sigma_{exp}}\right|\right| \rightarrow min\,. \tag{7.57}$$

From this, the identification equations (7.25), (7.31), (7.55) and (7.56) are implemented into a numerical code to simulate the quasi-static and dynamic-mechanical tests. The numerical results are then compared with the corresponding experimental ones and the error between both is calculated. The subsequent optimisation of the material parameters to minimise the error is performed by suitable optimisation routines provided by the software MATLAB.

The identification procedure is generally divided into the identification of the static material parameters C_{10} and C_{01} and the identification of the dynamic material parameters μ_{k0}, τ_k, a, b, c and α_k. Based on this division, the identification process is performed in two steps. The static material parameters are first identified with respect to the experimental and numerical equilibrium stress-strain data. After that, the identified static material parameters are held constant and the dynamic ones are identified by using the experimental and numerical data of the frequency and predeformation dependent storage and loss modulus in a subsequent second step.

The basis of the static parameter identification builds up the equilibrium stress data of the quasi-static investigations and the numerical equilibrium stress response $P_{0,11}$

provided by (7.25) and (7.31). The identification routine applied to optimise the static material parameters can be divided into four main steps which are initialisation, simulation, evaluation of the error and optimisation.

At the initialisation step, the experimental data σ_{exp} and ε_{exp} of the quasi-static tension, compression and pure shear tests are loaded from the experimental data files. Moreover, the initial values of the static material parameters C_{10} and C_{01} as well as their lower and upper bounds can be defined by the user (default values: 0 MPa up to 10 MPa).
After the initialisation is finished, the numerical simulation of the experimental equilibrium stress data is performed on the basis of (7.25) and (7.31) with respect to tension, compression and pure shear.
After that, the quality of the approximation is determined by the evaluation of the absolute error between the experimental equilibrium stress data σ_{exp} and the corresponding numerical one σ_{num}

$$error = \left|\left| \frac{\sigma_{num}(\varepsilon_{exp}) - \sigma_{exp}(\varepsilon_{exp})}{\sigma_{exp}(\varepsilon_{exp})} \right|\right| . \tag{7.58}$$

Thereby, the relative value of the error is chosen to assure that each data point is considered independently of its numerical value. Moreover, the individual errors of all data points from each deformation mode are summed up to get a total error such that each deformation mode is simultaneously taken into account during calculation of the error.
After evaluating the total error, the material parameters are optimised by a software-provided nonlinear least squares method which is given by the internal function *lsqnonlin*. Thereby, the focus is on the minimisation of the error such that the quality of the numerical approximation becomes as good as possible. Regarding this, the new set of optimised material parameters is automatically derived by the software MATLAB respectively by the function *lsqnonlin*. On the basis of the new set of material parameters, the whole identification process starts from the beginning again. This iteration takes place as long as the error is still higher than a user-defined minimum value. If the error is smaller than the defined minimum, the identification process automatically terminates and the identified static material parameters are saved in a file.

The procedure to identify the dynamic material parameters μ_{k0}, τ_k, a, b, c and α_k is similar to the identification process of the static ones. It is based on a minimisation of the error between the predeformation and frequency dependent storage and loss modulus which are obtained from the temperature-frequency-sweep tests and the corresponding responses G'_A and G''_A of the classical model in (7.55) respectively G'_B and G''_B of the fractional approach in (7.56). As before, the dynamic identification process is described by initialisation, numerical simulation, evaluation of the error and optimisation of the material parameters.
The initialisation step includes the import of the master curve data of the temperature-frequency-sweep tests at each predeformation. This data consists of the applied predeformation and frequency as well as of the corresponding storage and loss modulus at the given frequency and predeformation. Moreover, the initial values of the dynamic

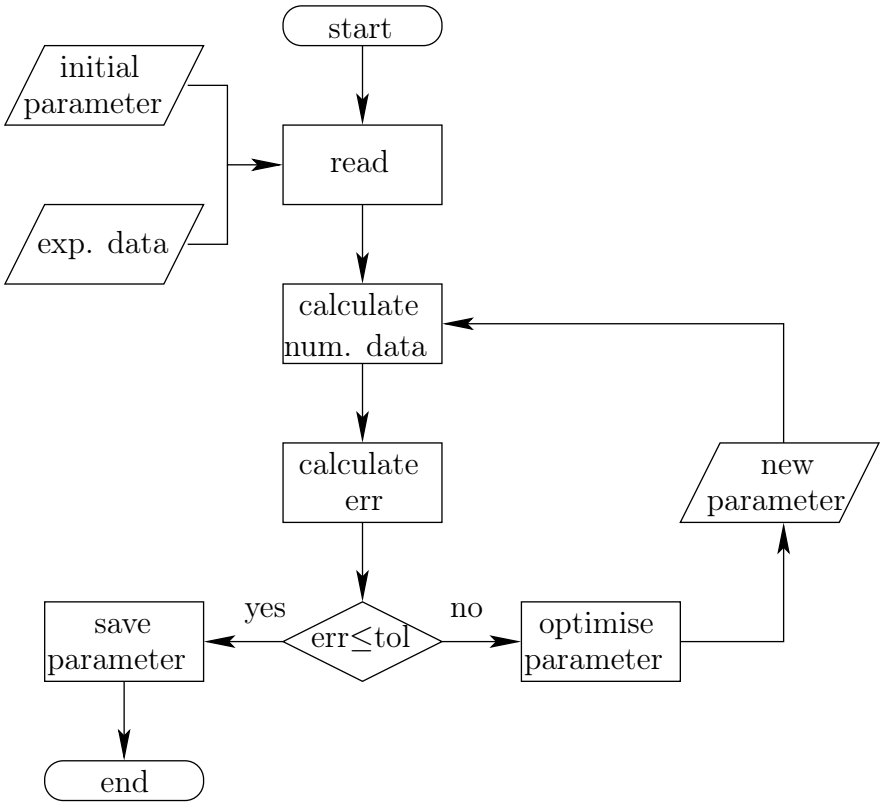

FIGURE 7.3: Numerical identification procedure

material parameters μ_{k0}, τ_k, a, b, c and α_k as well as their lower and upper bounds can be defined by the user. The previously identified static material parameters C_{10} and C_{01} are read from the saved file and are considered as constants during the dynamic part of the identification process.
The simulation of the experimental data is performed by an evaluation of the corresponding identification equations of the dynamic moduli in (7.55) and (7.56). Similar to the static identification process, the relative errors between the experimental storage and loss modulus G'_{exp} and G''_{exp} and the numerically computed moduli G'_{num} and G''_{num} are calculated in the next step

$$\begin{aligned} error_{G'} &= \left|\left| \frac{G'_{num} - G'_{exp}}{G'_{exp}} \right|\right| , \\ error_{G''} &= \left|\left| \frac{G''_{num} - G''_{exp}}{G''_{exp}} \right|\right| . \end{aligned} \tag{7.59}$$

After this, the individual errors of each data point and each predeformation are summed up to a total error which is minimised in the subsequent optimisation process.
In contrast to the static part of identification, the optimisation of the dynamic material parameters is performed by a genetic algorithm which is also provided by the software MATLAB as function *ga*. The genetic algorithm is a global optimisation algorithm and is applied to prevent the optimisation from sticking to a local minimum due to a great amount of material parameters. The new and optimised material parameters are again provided by the optimisation algorithm and are taken as new values for the next

iteration until the error between the experimental and numerical data reaches the user defined-minimum.

7.5 Identification results

The focus of this section is to present the identified static and dynamic material parameters as well as the corresponding results of the numerical approximation of the experimental data with regard to the equilibrium stress and the predeformation and frequency dependent storage and loss modulus.

7.5.1 Static identification results

The static part of the parameter identification was focused on the identification of C_{10} and C_{01} such that the simulated equilibrium stress fits as well as possible with the experimental equilibrium stress data. The identified values of the static material parameters with respect to each vulcanisate are listed in table 7.1. The simulation results of the experimental equilibrium stress data based on the identified values of C_{10} and C_{01} are plotted in figure 7.4 with regard to each vulcanisate and each deformation mode. On the basis of this figure, it can be observed that the numerical approximation is in very good agreement with the experimental equilibrium stress data. Based on this fact, the constitutive model is very suitable to quantitatively approximate the hyperelastic equilibrium response of each vulcanisate with only two material parameters.

7.5.2 Dynamic identification results

The dynamic part of the identification was focused on the determination of the parameters μ_k, τ_k, α_k, a, b and c. The identified material parameters of the classical and of the fractional approach are listed in tables 7.2 - 7.5 for each vulcanisate. The numerical results of both formulations are discussed in the following. Thereby, the numerical approximation of the classical model should be discussed first. After that, the numerical representation of the classical model is compared to that of the fractional approach to reveal the benefits of the fractional formulation. Initially, one can state that the numerical approximations of both constitutive approaches are in very good agreement with the experimental data of each vulcanisate.
As illustrated in figures 7.5, 7.7, 7.9 and 7.11, the classical model can already quantitatively approximate the predeformation and frequency dependent properties of the storage and the loss modulus of each material. In view of an interpretation of the classical model as a Maxwell chain, a relatively large number of 10 Maxwell elements in parallel is required to represent the dynamic properties of each vulcanisate over a broad frequency range of about seven decades. Hence, the classical model inherits 24 material parameters in terms of the SBR20, SBR40 and EPDM20 rubber and 25 parameters in the case of the NR40 vulcanisate. This fact implies a high complexity

of the identification process and a disadvantage with respect to computational effort. Apart from the large amount of material parameters, the numerical approximation of the loss modulus provided by the classical approach is characterised by pronounced oscillations, which are due to the discrete relaxation spectrum.

If the simulations of the fractional formulation given in figures 7.6, 7.8, 7.10 and 7.12 are taken into account, the numerical representation of the predeformation and frequency dependent dynamic properties seems to be nearly of the same quality at first sight. But, in contrast to the classical approach, the fractional model is characterised by two benefits. With respect to the quality of the approximation, the representation of the loss modulus by the fractional model reveals no oscillations and is thus much better than the approximation of the classical formulation. Regarding a Maxwell chain, the oscillations are natural and arise from the characteristic sigmoidal behaviour of the loss modulus of a single Maxwell element. This behaviour is also characteristic for discrete relaxation spectra. The absence of oscillations in terms of the fractional model is due to the continuous relaxation spectrum of the approach. Apart from this benefit, much less material parameters are required to quantitatively approximate the experimental data. If the interpretation as a fractional Maxwell chain is considered, the very suitable fit of the storage and the loss modulus is achieved by the application of only 4 fractional Maxwell elements which results in 16 instead of 24 material parameters in terms of the SBR20, SBR40 and EPDM20 rubber and 17 instead of 25 material parameters in terms of the NR40 vulcanisate. Based on this reduction, the identification of the material parameters is more simple in comparison with the classical constitutive model. Furthermore, the few amount of material parameters dramatically boosts the identification procedure, and moreover, the numerical simulation.

SBR20

C_{10} [MPa]	C_{01} [MPa]
0.17071	9.89934 e-2

SBR40

C_{10} [MPa]	C_{01} [MPa]
0.20338	0.17255

EPDM20

C_{10} [MPa]	C_{01} [MPa]
0.16993	0.10749

NR40

C_{10} [MPa]	C_{01} [MPa]
0.22473	0.13481

TABLE 7.1: Static material parameters of SBR20, SBR40, EPDM20 and NR40

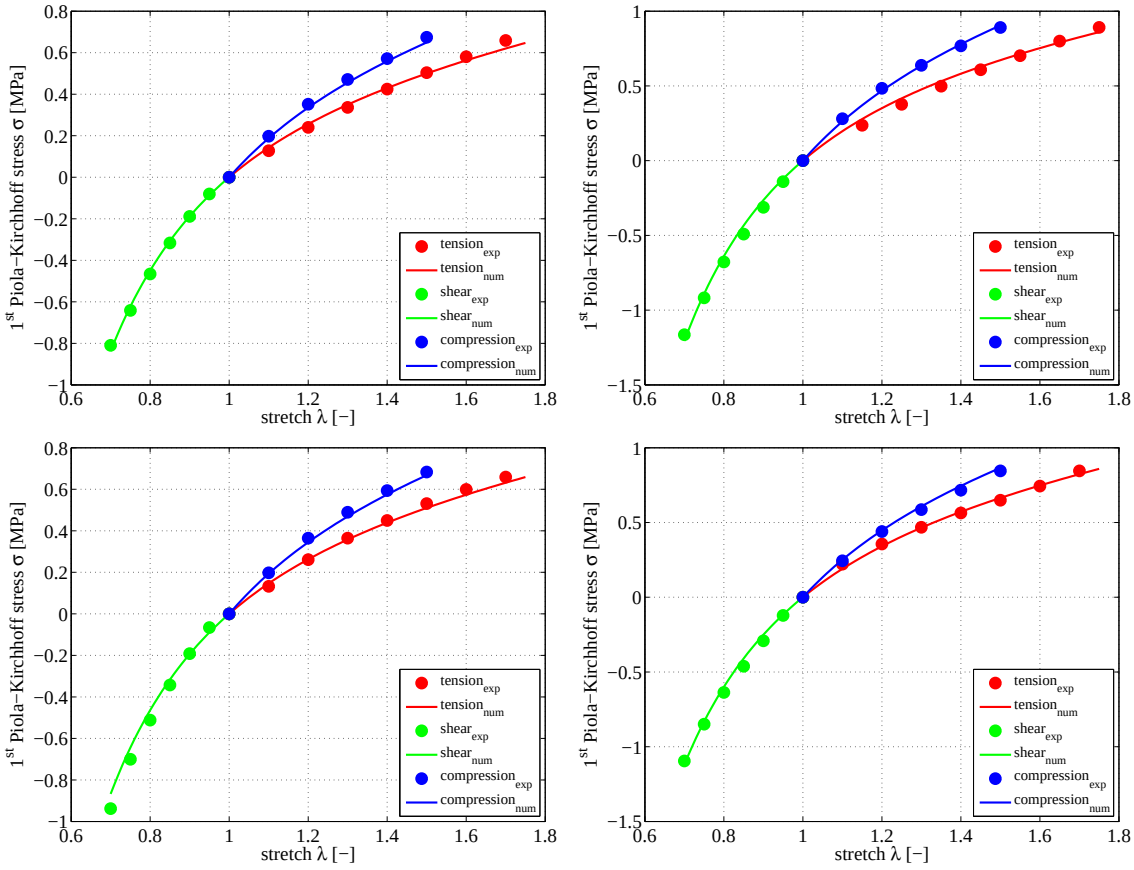

FIGURE 7.4: Identification results of the equilibrium stress in compression, pure shear and tension (upper left: SBR20), (upper right: SBR40), (lower left: EPDM20), (lower right: NR40)

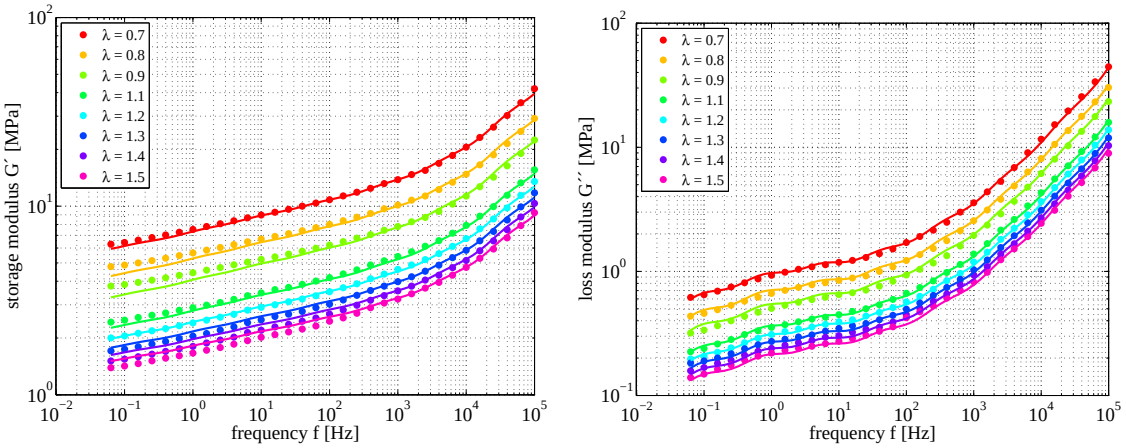

FIGURE 7.5: Identification result of the predeformation and frequency dependent dynamic moduli of SBR20 of the classical approach (left: storage modulus), (right: loss modulus)

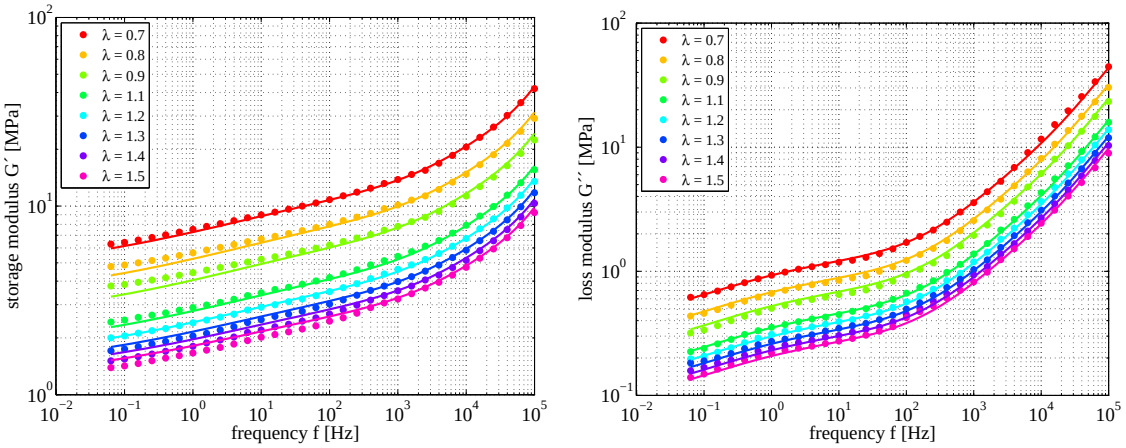

FIGURE 7.6: Identification result of the predeformation and frequency dependent dynamic moduli of SBR20 of the fractional approach (left: storage modulus), (right: loss modulus)

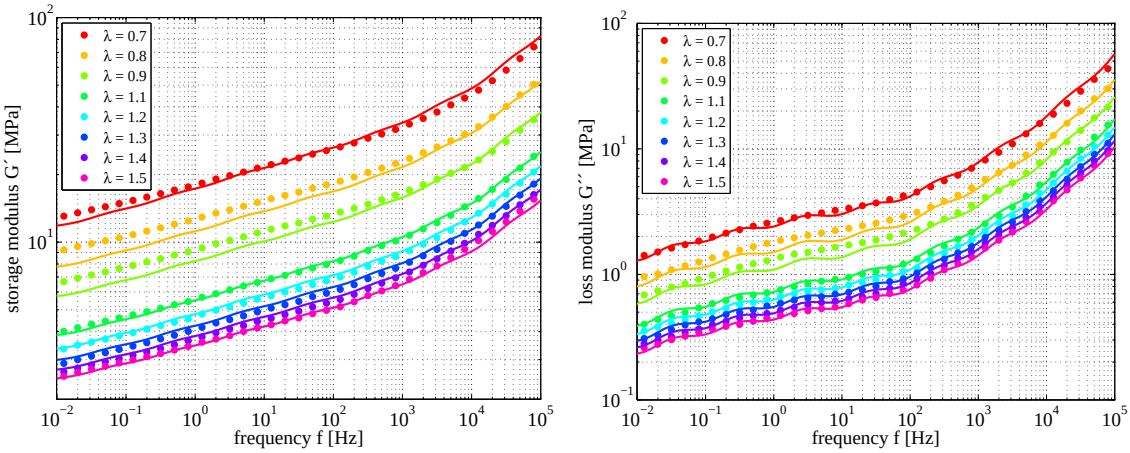

FIGURE 7.7: Identification result of the predeformation and frequency dependent dynamic moduli of SBR40 of the classical approach (left: storage modulus), (right: loss modulus)

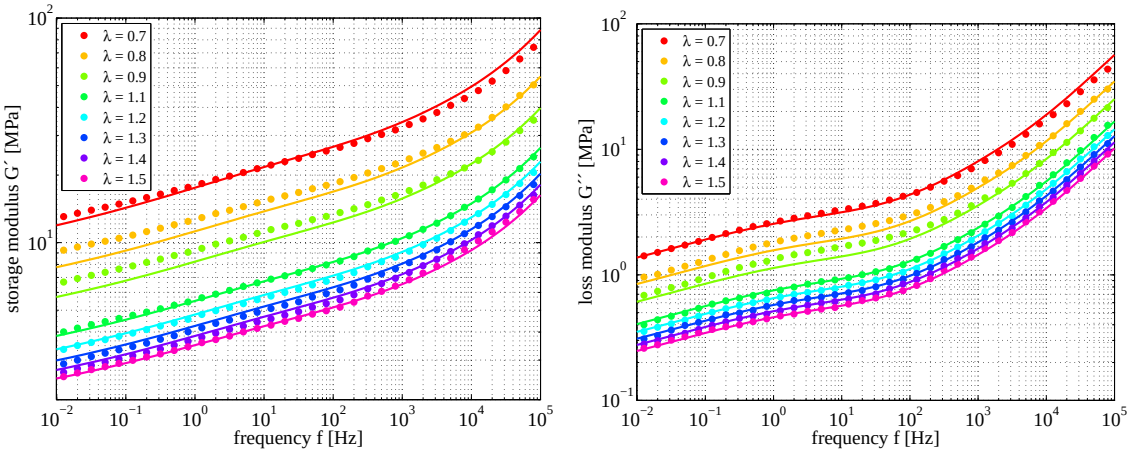

FIGURE 7.8: Identification result of the predeformation and frequency dependent dynamic moduli of SBR40 of the fractional approach (left: storage modulus), (right: loss modulus)

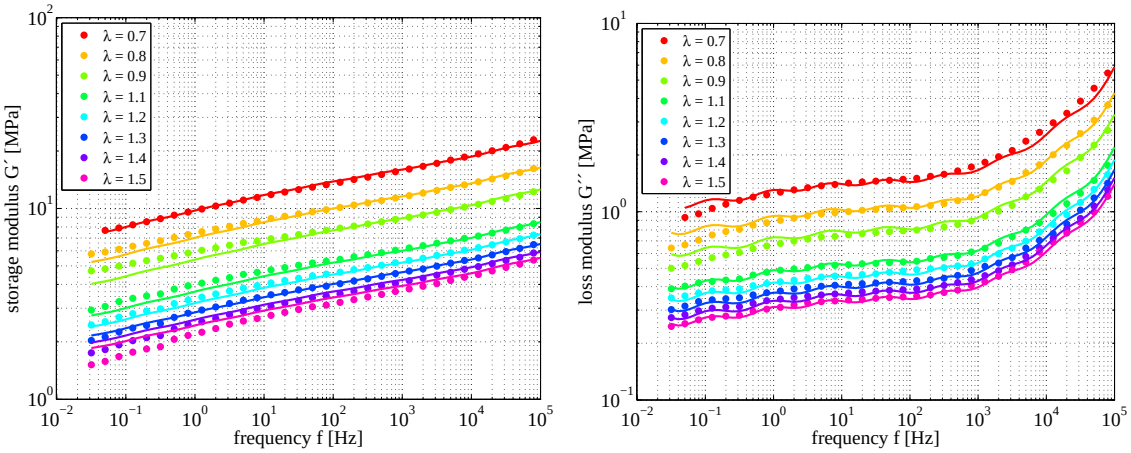

FIGURE 7.9: Identification result of the predeformation and frequency dependent dynamic moduli of EPDM20 of the classical approach (left: storage modulus), (right: loss modulus)

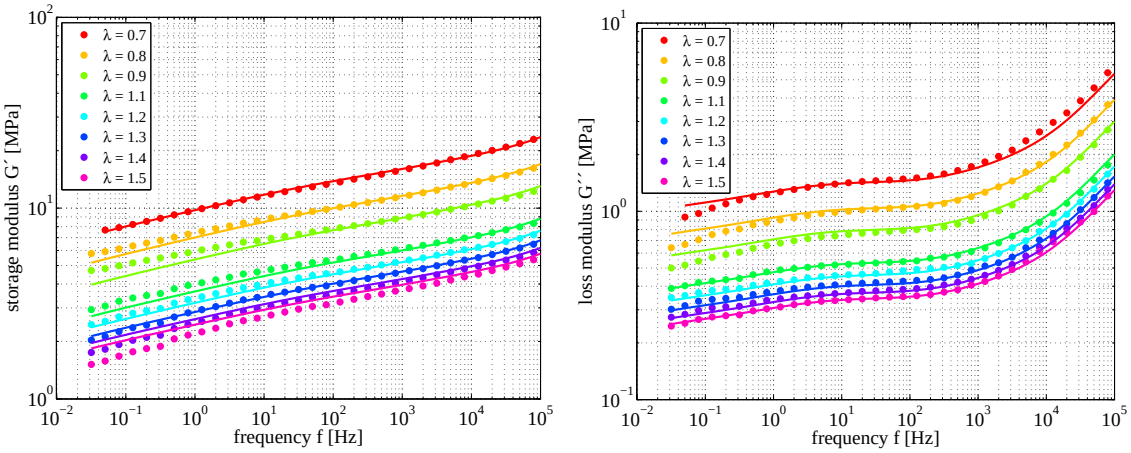

FIGURE 7.10: Identification result of the predeformation and frequency dependent dynamic moduli of EPDM20 of the fractional approach (left: storage modulus), (right: loss modulus)

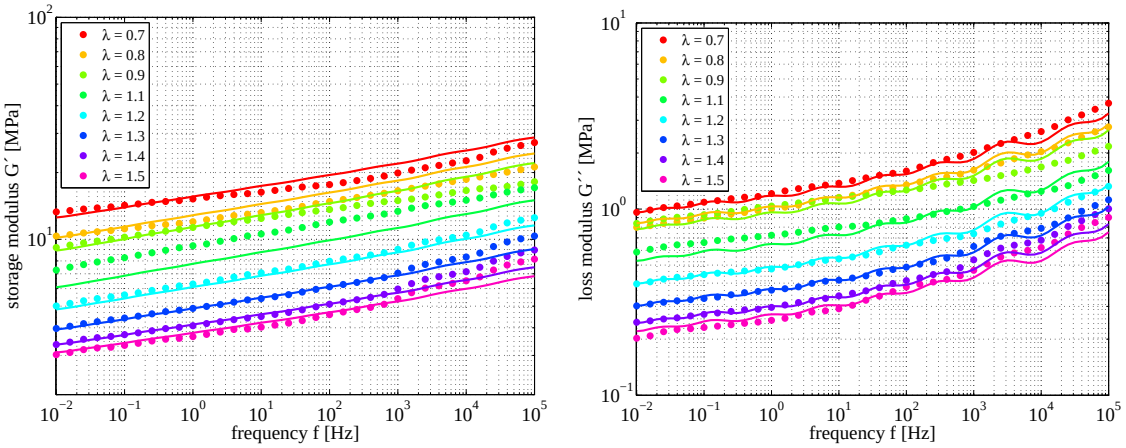

FIGURE 7.11: Identification result of the predeformation and frequency dependent dynamic moduli of NR40 of the classical approach (left: storage modulus), (right: loss modulus)

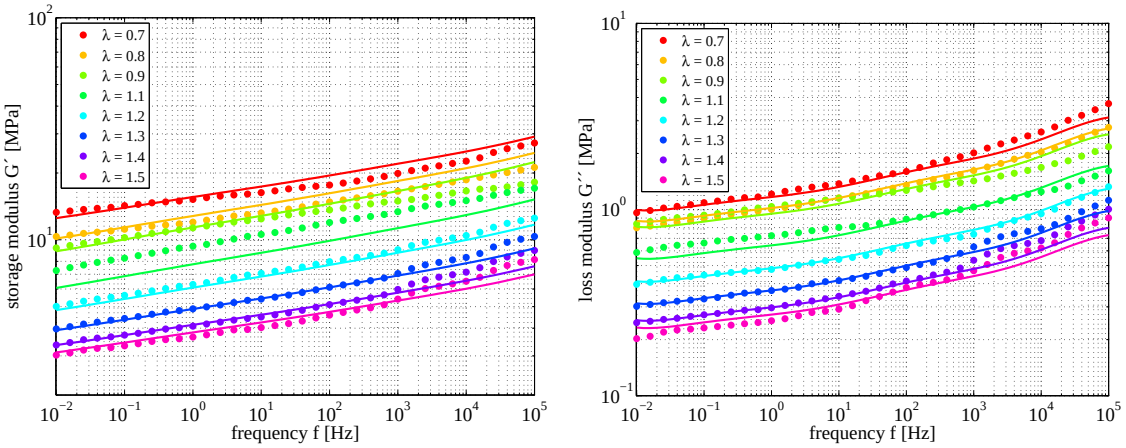

FIGURE 7.12: Identification result of the predeformation and frequency dependent dynamic moduli of NR40 of the fractional approach (left: storage modulus), (right: loss modulus)

Classical approach

a [-]	b [-]
6.89416 e-2	0.12571

k	μ_k [MPa]	τ_k [s]
1	48.3319	1.98097 e-7
2	2.49171	5.54839 e-6
3	0.83595	4.69067 e-5
4	0.41932	4.03828 e-4
5	0.26381	3.40498 e-3
6	0.21712	2.74666 e-2
7	0.18520	0.20242
8	0.13642	1.72733
9	0.19136	56.9035
10	0.11549	544.306

Fractional approach

a [-]	b [-]
0.11598	7.60850 e-2

k	μ_k [MPa]	τ_k [s]	α_k [-]
1	46.2521	1.62040 e-7	0.81581
2	2.28793	1.01101 e-5	0.56452
3	1.30408	1.20383 e-2	0.29352
4	0.14608	158.608	0.83250

TABLE 7.2: Dynamic material parameters of SBR20

Classical approach

a [-]	b [-]
-0.79307	1.32161

k	μ_k [MPa]	τ_k [s]
1	29.3852	3.39292 e-7
2	3.45354	6.27872 e-6
3	1.47962	6.34561 e-5
4	0.82855	5.76019 e-4
5	0.56381	5.83982 e-3
6	0.47559	5.38728 e-2
7	0.37131	0.49104
8	0.28175	4.42678
9	0.28293	81.2908
10	0.48645	507.516

Fractional approach

a [-]	b [-]
-0.82271	1.39609

k	μ_k [MPa]	τ_k [s]	α_k [-]
1	136.254	1.38155 e-8	0.57695
2	1.86687	4.70654 e-5	0.47569
3	1.33865	3.53095 e-2	0.36166
4	1.40752	6.68732	0.16599

TABLE 7.3: Dynamic material parameters of SBR40

Classical approach

a [-]	b [-]
0.39401	-0.11561

k	μ_k [MPa]	τ_k [s]
1	3.88191	3.27744 e-7
2	0.54257	8.05794 e-6
3	0.33374	6.59606 e-5
4	0.27757	4.90615 e-4
5	0.26738	3.51158 e-3
6	0.25947	2.43553 e-2
7	0.24219	0.17277
8	0.22276	1.34822
9	0.36251	18.4952
10	0.17808	542.940

Fractional approach

a [-]	b [-]
0.42808	-0.13149

k	μ_k [MPa]	τ_k [s]	α_k [-]
1	5.41962	1.18569 e-7	0.61082
2	0.62716	4.03573e -5	0.47682
3	1.18242	1.64750 e-2	0.34460
4	0.59755	19.7448	0.38693

TABLE 7.4: Dynamic material parameters of EPDM20

Classical approach

a [-]	b [-]	c [-]
-0.80646	-0.98208	2.35351

k	μ_k [MPa]	τ_k [s]
1	3.46551	2.33676 e-7
2	0.87572	5.40025 e-6
3	0.74353	5.56571 e-5
4	0.51671	5.16696 e-4
5	0.42521	3.78492 e-3
6	0.36573	2.73059 e-2
7	0.31533	0.18350
8	0.29750	1.20108
9	0.26786	7.31068
10	1.74780	293.531

Fractional approach

a [-]	b [-]	c [-]
-0.79693	-1.02881	2.46163

k	μ_k [MPa]	τ_k [s]	α_k [-]
1	3.14154	6.23204 e-7	0.49268
2	1.71258	3.08624 e-4	0.36819
3	1.86762	1.38236	0.27460
4	1.14150	570.341	1

TABLE 7.5: Dynamic material parameters of NR40

Chapter 8

Finite element implementation and simulation

Introduction

The finite element method, shortly FEM, has become a powerful tool to simulate the behaviour of complex geometrical structures under complex types of deformations. The procedure is based on mathematical material models and can be described as a numerical approximation used to solve complex initial and boundary value problems which are mathematically defined by partial differential equations. Basically, the complex geometry is simplified by separating the solution area into a finite number of elements, as for instance triangles or rectangles, which are spatially defined by nodes. The variables are calculated at these nodes and approximated in between by suitable shape functions which can be of linear, quadratic or even higher order.
In order to calculate an approximation of the solution, the underlying differential equations (strong form) are first transferred to their weak form by applying various principles, such as the minimum of the potential energy or the principle of virtual mechanical work. A benefit of the finite element method consists in the possibility of accounting for physical and geometrical nonlinearities. In this context, one can distinguish between three different types of nonlinearities. Physical or material nonlinearities define the first type and result from the material behaviour itself. As an example, the nonlinear stress-strain relation of elastomers can be mentioned in this context. The second type are geometrical nonlinearities which especially occur at finite deformations, such as finite displacements or twists. The last type of nonlinearities is found in nonlinear boundary conditions, as in case of contact problems.
In order to calculate a numerical solution of these nonlinear problems, it is quite common to apply stepwise, iterative algorithms, such as the Newton-Raphson method.

Outline

The focus of this chapter is the implementation of the derived classical and fractional constitutive models into the finite element code MSC Marc which offers the possibility to implement user-defined material laws in the frequency domain. The finite element simulation is only provided for the SBR40 vulcanisate, but can similarly be performed with respect to the other rubber materials. In the first section, the weak form of the equation of motion is derived on the basis of the principle of virtual work. The virtual mechanical work will be linearised in the second section and locally discretisised in the third section. Since this work assumes incompressibility, the derived linear system of differential equations will be extended by the method of Lagrangian multipliers to include incompressibility in the fourth section. The fifth section is about the implementation of the constitutive models into the finite element code MSC Marc. The implementation is based on the proposal of Morman and Nagtegaal (1983) and performed via the user subroutine UPHI. An implementation of another frequency domain formulation into the finite element code MSC Marc was done by Retka (2011) in a similar manner. In order to derive the equations for the implementation, the constitutive formulations defined by the finite element code MSC Marc will first be presented and subsequently be compared to those of the classical and the fractional constitutive models. In the last section, the finite element implementation is validated by a comparison between the numerical simulation and the finite element approximation of the frequency and predeformation dependent properties of the storage and loss modulus. For a detailed overview of the finite element method, the reader is referred to the textbooks by Zienkiewicz (1971), Schwarz (1988), Betten (1997), Betten (1998), or Zienkiewicz et al. (2005). Similar approaches for a finite element implementation of a viscoelastic and a thermoviscoelastic model into MSC Marc, the following presentation mostly refers to, are presented by J.Retka et al. (2007) and Retka (2011). With respect to the finite element code MSC Marc, information about the theory, element formulations, program input and user subroutines as well as some examples are provided by the documentation (MSC.Software 2010a; MSC.Software 2010b; MSC.Software 2010c; MSC.Software 2010d; MSC.Software 2010e).

Moreover, it is pointed out that parts of this chapter have been published in prior printed publications which were approved by the university (Wollscheid and Lion (2013a), Wollscheid and Lion (2014)).

8.1 Weak form

In order to calculate an approximation of the differential equations of a physical problem, it is necessary to transform these into their weak form. Considering the principle of virtual work, the local form of the underlying differential equations is first multiplied by a virtual test function and then integrated over the solution area. With respect to mechanical problems, as it is the case in this work, the test function is defined by the virtual displacement $\delta\mathbf{u}$. It can be interpreted as an imaginary, incremental displacement which must be compatible with the geometrical boundary conditions. Taking the

principle of virtual work into account, the local form of the equation of motion in the actual configuration

$$\operatorname{div}\mathbf{T} + \rho\,\mathbf{k} - \rho\,\frac{\mathrm{d}\mathbf{v}}{\mathrm{d}t} = 0 \tag{8.1}$$

is first multiplied by the virtual displacement $\delta\mathbf{u}$ by applying the simple scalar product[1] and then integrated over the volume of the structure. In so doing, the weak form of the equation of motion respectively the virtual mechanical work with respect to the actual configuration is obtained

$$\begin{aligned} \delta\mathcal{W} &= \int_v (\operatorname{div}\mathbf{T} + \rho\,\mathbf{k} - \rho\,\dot{\mathbf{v}})\;\delta\mathbf{u}\,\mathrm{d}v = 0 \\ &= \int_v \operatorname{div}(\mathbf{T})\,\delta\mathbf{u}\,\mathrm{d}v + \int_v \rho\,\mathbf{k}\,\delta\mathbf{u}\,\mathrm{d}v - \int_v \rho\,\dot{\mathbf{v}}\,\delta\mathbf{u}\,\mathrm{d}v = 0 \end{aligned} \tag{8.2}$$

.

Considering the product rule of differentiation as well as the symmetry of the Cauchy stress tensor ($\mathbf{T} = \mathbf{T}^T$), the first term in (8.2) can be reformulated by the following relation

$$\operatorname{div}(\mathbf{T})\,\delta\mathbf{u} = \operatorname{div}(\mathbf{T}^T\,\delta\mathbf{u}) - \mathbf{T}\cdot\operatorname{grad}(\delta\mathbf{u}) = \operatorname{div}(\mathbf{T}\,\delta\mathbf{u}) - \mathbf{T}\cdot\operatorname{grad}(\delta\mathbf{u})\;. \tag{8.3}$$

Taking the definition of the surface stress vector $\boldsymbol{\sigma}_a$ into account

$$\boldsymbol{\sigma}_a = \mathbf{T}\,\mathbf{n} \quad \Rightarrow \quad \int_a \boldsymbol{\sigma}_a\,\mathrm{d}a = \int_a \mathbf{T}\,\mathbf{n}\,\mathrm{d}a \tag{8.4}$$

and applying the Gaussian theorem of integration

$$\int_a \mathbf{T}\,\mathbf{n}\,\mathrm{d}a = \int_v \operatorname{div}\mathbf{T}\,\mathrm{d}v\;, \tag{8.5}$$

the first term in (8.2) can be rewritten as

$$\begin{aligned} \int_v (\operatorname{div}\mathbf{T})\,\delta\mathbf{u}\,\mathrm{d}v &= \int_v \Big(\operatorname{div}(\mathbf{T}\,\delta\mathbf{u}) - \mathbf{T}\cdot\operatorname{grad}(\delta\mathbf{u})\Big)\,\mathrm{d}v \\ &= \int_a (\mathbf{T}\,\mathbf{n})\,\delta\mathbf{u}\,\mathrm{d}a - \int_v \mathbf{T}\cdot\operatorname{grad}(\delta\mathbf{u})\,\mathrm{d}v \\ &= \int_a \boldsymbol{\sigma}_a\,\delta\mathbf{u}\,\mathrm{d}a - \int_v \mathbf{T}\cdot\operatorname{grad}(\delta\mathbf{u})\,\mathrm{d}v\;. \end{aligned} \tag{8.6}$$

The last term of this expression can be transformed again. If the definition of the deformation gradient (2.7) is considered, the relations

$$\delta\mathbf{F} = \operatorname{Grad}(\delta\mathbf{u}) \quad \text{and} \quad \operatorname{grad}(\mathbf{u}) = \operatorname{Grad}(\mathbf{u})\,\mathbf{F}^{-1} \tag{8.7}$$

[1] simple scalar product of vectors $\mathbf{a}$ and $\mathbf{b}$: $\mathbf{a}\,\mathbf{b} = a_i\,b_i$ (cf. Appendix A)

hold. On this basis, the virtual Almansi strain tensor $\delta\mathbf{A}$ is given by

$$\delta\mathbf{A} \;=\; \frac{1}{2}\left(\operatorname{grad}^T(\delta\mathbf{u}) \;+\; \operatorname{grad}(\delta\mathbf{u})\right) . \tag{8.8}$$

Regarding this relation and considering the symmetry of the Cauchy stress tensor again, the second term in (8.6) can be replaced by

$$\mathbf{T}\cdot\operatorname{grad}(\delta\mathbf{u}) \;=\; \mathbf{T}\cdot\delta\mathbf{A} \;, \tag{8.9}$$

such that (8.6) can finally be expressed by

$$\int_v (\operatorname{div}\mathbf{T})\,\delta\mathbf{u}\,\mathrm{d}v \;=\; \int_a \boldsymbol{\sigma}_a\,\delta\mathbf{u}\,\mathrm{d}a \;-\; \int_v \mathbf{T}\cdot\delta\mathbf{A}\,\mathrm{d}v \;. \tag{8.10}$$

By insertion of this outcome into (8.2), the virtual mechanical work with respect to the actual configuration is finally defined by

$$\delta\mathcal{W} \;=\; \underbrace{\int_v \mathbf{T}\cdot\delta\mathbf{A}\,\mathrm{d}v}_{\delta\mathcal{W}_{int}} \;-\; \underbrace{\int_a \boldsymbol{\sigma}_a\,\delta\mathbf{u}\,\mathrm{d}a \;-\; \int_v \rho\,\mathbf{k}\,\delta\mathbf{u}\,\mathrm{d}v}_{\delta\mathcal{W}_{ext}} \;+\; \underbrace{\int_v \rho\,\dot{\mathbf{v}}\,\delta\mathbf{u}\,\mathrm{d}v}_{\delta\mathcal{W}_{\rho}} \;=\; 0 \;. \tag{8.11}$$

Therein, the first term is the internal part of virtual work $\delta\mathcal{W}_{int}$ which is caused by internal stresses inside the material. The second and the third term define the external part of virtual work $\delta\mathcal{W}_{ext}$ which is a result of external surface and volume forces acting on the material. The last term denotes the inertia part of virtual work $\delta\mathcal{W}_{\rho}$ which is caused by the inertia forces.

In this work, the implementation into the finite element code MSC Marc is based on a formulation with respect to the reference configuration. Regarding this, the virtual mechanical work must be expressed by means of variables of the reference configuration. Considering (8.7) and (8.8), the virtual strain tensor $\delta\mathbf{A}$ can first be transferred to the reference configuration on the basis of (2.16)

$$\delta\mathbf{E} \;=\; \frac{1}{2}\left(\delta\mathbf{F}^T\,\mathbf{F} \;+\; \mathbf{F}^T\,\delta\mathbf{F}\right) \;=\; \mathbf{F}^T\,\delta\mathbf{A}\,\mathbf{F} \;. \tag{8.12}$$

Considering this expression and relations (2.11), (2.39) and (2.51), the virtual mechanical work with respect to the reference configuration is finally given by

$$\delta\mathcal{W} \;=\; \underbrace{\int_V \tilde{\mathbf{T}}\cdot\delta\mathbf{E}\,\mathrm{d}V}_{\delta\mathcal{W}_{int}} \;-\; \underbrace{\int_V \rho_0\,\mathbf{k}\,\delta\mathbf{u}\,\mathrm{d}V \;-\; \int_A \boldsymbol{\sigma}_A\,\delta\mathbf{u}\,\mathrm{d}A}_{\delta\mathcal{W}_{ext}} \;+\; \underbrace{\int_V \rho_0\,\ddot{\mathbf{u}}\,\delta\mathbf{u}\,\mathrm{d}V}_{\delta\mathcal{W}_{\rho_0}} \;=\; 0 \;. \tag{8.13}$$

In this expression, $\ddot{\mathbf{u}} = \dot{\mathbf{v}}$ and $\boldsymbol{\sigma}_A$ are the acceleration vector and the surface stress vector of the reference configuration. Similar to (8.11), the first term of this functional denotes the internal part of virtual work caused by internal stresses, the second and the third term represent the external part of virtual work which results from surface and volume forces and the last term specifies the inertia part of virtual work caused by inertia forces.

8.2 Linearisation of the virtual mechanical work

In this work, large static predeformations superimposed by small harmonic oscillations are considered. This loading condition is characterised by geometrical and physical nonlinearities which implies the necessity of linearisation of the mechanical functional. After linearisation, the mechanical problem can be iteratively solved by the Newton-Raphson algorithm. In this context, the boundary conditions, as for instance external displacements, are applied incrementally and the mechanical functional is iteratively solved for each increment. In order to calculate a linear approximation of the mechanical functional, its change in the direction of a small displacement increment $\Delta\mathbf{u}$ can mathematically be described by the Gateaux derivative. Considering this and regarding the current increment k and the iteration n, the linear approximation of the virtual mechanical functional at the next increment $k+1$ and iteration n can generally be expressed by the sum of its value at the current increment k and its corresponding Gateaux derivative at the current increment k

$$\delta\mathcal{W}\left(\mathbf{u}_n^{k+1},\,\delta\mathbf{u}\right) \;=\; \delta\mathcal{W}\left(\mathbf{u}_n^{k},\,\delta\mathbf{u}\right) \;+\; \mathrm{D}\left(\delta\mathcal{W}\left(\mathbf{u}_{\mathrm{n}}^{\mathrm{k}},\,\delta\mathbf{u}\right)\right)\,[\Delta\mathbf{u}]\;. \tag{8.14}$$

Linearisation of internal part of virtual mechanical work

In order to obtain a linear approximation of the internal part of the virtual mechanical work, the Gateaux derivative of the first term in (8.13) must be calculated. Doing this and considering the product rule of differentiation, the linearised formulation of the internal part of virtual work first reads as

$$\begin{aligned}
&\delta\mathcal{W}_{int}(\mathbf{u},\delta\mathbf{u}) \;+\; \mathrm{D}(\delta\mathcal{W}_{\mathrm{int}}(\mathbf{u},\delta\mathbf{u}))\,[\Delta\mathbf{u}] \;=\\
&= \int_V \tilde{\mathbf{T}}\cdot\delta\mathbf{E}\,\mathrm{d}V \;+\; \int_V \mathrm{D}(\tilde{\mathbf{T}}\cdot\delta\mathbf{E})\,[\Delta\mathbf{u}]\,\mathrm{dV}\\
&= \int_V \tilde{\mathbf{T}}\cdot\delta\mathbf{E}\,\mathrm{d}V \;+\; \int_V \delta\mathbf{E}\cdot\mathrm{D}(\tilde{\mathbf{T}})\,[\Delta\mathbf{u}]\,\mathrm{dV} \;+\; \int_{\mathrm{V}} \tilde{\mathbf{T}}\cdot\mathrm{D}(\delta\mathbf{E})\;[\Delta\mathbf{u}]\,\mathrm{dV}\;.
\end{aligned} \tag{8.15}$$

In order to reformulate this expression, the virtual deformation gradient $\delta\mathbf{F}$ and the Gateaux derivatives of the incremental and virtual displacement fields $\mathbf{u}$ and $\delta\mathbf{u}$ are first defined

$$\delta\mathbf{F} \;=\; \mathrm{D}(\mathbf{F})\,[\delta\mathbf{u}]\;,\quad \mathrm{D}(\mathbf{u})[\Delta\mathbf{u}] \;=\; \Delta\mathbf{u}\;,\quad \mathrm{D}(\delta\mathbf{u})[\Delta\mathbf{u}] \;=\; \mathbf{0}\;. \tag{8.16}$$

On the basis of these definitions, the virtual Green-Lagrange strain tensor $\delta\mathbf{E}$ and its Gateaux derivative can be expressed by

$$\begin{aligned}
\delta\mathbf{E} \qquad &= \;\frac{1}{2}\left(\delta\mathbf{F}^T\,\mathbf{F} \;+\; \mathbf{F}^T\,\delta\mathbf{F}\right) \;=\; \mathrm{D}(\mathbf{E})\,[\delta\mathbf{u}]\\
\mathrm{D}(\delta\mathbf{E})[\Delta\mathbf{u}] \;&= \;\frac{1}{2}\left(\,\mathrm{Grad}^T(\Delta\mathbf{u})\;\mathrm{Grad}(\mathbf{u}) \;+\; \mathrm{Grad}^T(\mathbf{u})\;\mathrm{Grad}(\Delta\mathbf{u})\right)\;.
\end{aligned} \tag{8.17}$$

Considering the Gateaux derivative of the 2nd Piola-Kirchhoff stress

$$\mathrm{D}(\tilde{\mathbf{T}})[\Delta\mathbf{u}] \;=\; \mathbb{C}\cdot\mathrm{D}(\mathbf{E})[\Delta\mathbf{u}]\;, \tag{8.18}$$

the linear approximation of the internal part of virtual mechanical work is finally given by

$$\begin{aligned}
&\delta\mathcal{W}_{int}(\mathbf{u},\delta\mathbf{u}) \;+\; \mathrm{D}(\delta\mathcal{W}_{\mathrm{int}}(\mathbf{u},\delta\mathbf{u}))\,[\Delta\mathbf{u}] \;=\\
&=\int_V \tilde{\mathbf{T}}\cdot\delta\mathbf{E}\,\mathrm{d}V \;+\; \int_V \mathrm{D}(\mathbf{E})\,[\delta\mathbf{u}]\cdot\mathbb{C}\cdot\mathrm{D}(\mathbf{E})\,[\Delta\mathbf{u}]\,\mathrm{dV} \;+\; \int_{\mathrm{V}} \tilde{\mathbf{T}}\cdot\mathrm{D}(\delta\mathbf{E})\;[\Delta\mathbf{u}]\,\mathrm{dV}\;.
\end{aligned} \tag{8.19}$$

Therein, variable $\mathbb{C}$ denotes the elasticity tensor

$$\mathbb{C} \;=\; 4\,\rho_0\,\frac{\partial^2\Psi_{eq}(\mathbf{C})}{\partial\mathbf{C}^2}\;. \tag{8.20}$$

Linearisation of external part of virtual mechanical work

The linear approximation of the external part of virtual mechanical work can similarly be derived by applying the Gateaux derivative. In so doing, the linearised version of the external part of the virtual mechanical work is first given by

$$\begin{aligned}
&\delta\mathcal{W}_{ext}(\mathbf{u},\delta\mathbf{u}) \;+\; \mathrm{D}(\delta\mathcal{W}_{\mathrm{ext}}(\mathbf{u},\delta\mathbf{u}))\,[\Delta\mathbf{u}] \;=\\
&=\int_A \boldsymbol{\sigma}_A\delta\mathbf{u}\,\mathrm{d}A \;+\; \int_A \mathrm{D}(\boldsymbol{\sigma}_{\mathrm{A}}\delta\mathbf{u})\,[\Delta\mathbf{u}]\,\mathrm{dA} \;+\; \int_{\mathrm{V}}\rho_0\,\mathbf{k}\,\delta\mathbf{u}\,\mathrm{dV} \;+\; \int_{\mathrm{V}}\mathrm{D}\big(\rho_0\,\mathbf{k}\,\delta\mathbf{u}\big)\,[\Delta\mathbf{u}]\,\mathrm{dV}\;.
\end{aligned} \tag{8.21}$$

Considering the product rule of differentiation and taking relations (8.16) into account, (8.21) finally reads as

$$\begin{aligned}
&\delta\mathcal{W}_{ext}(\mathbf{u},\delta\mathbf{u}) \;+\; \mathrm{D}(\delta\mathcal{W}_{\mathrm{ext}}(\mathbf{u},\delta\mathbf{u}))\,[\Delta\mathbf{u}] \;=\\
&=\int_A \boldsymbol{\sigma}_A\delta\mathbf{u}\,\mathrm{d}A \;+\; \int_A \mathrm{D}(\boldsymbol{\sigma}_{\mathrm{A}})\,[\Delta\mathbf{u}]\,\delta\mathbf{u}\,\mathrm{dA} \;+\; \int_{\mathrm{V}}\rho_0\,\mathbf{k}\,\delta\mathbf{u}\,\mathrm{dV}\int_{\mathrm{V}}\rho_0\,\mathrm{D}(\mathbf{k})\,[\Delta\mathbf{u}]\,\delta\mathbf{u}\,\mathrm{dV}\\
&=\int_A \big(\boldsymbol{\sigma}_A \;+\; \Delta\boldsymbol{\sigma}_A\big)\,\delta\mathbf{u}\,\mathrm{d}A \;+\; \int_V \rho_0\,(\mathbf{k} \;+\; \Delta\mathbf{k})\,\delta\mathbf{u}\,\mathrm{d}V\;.
\end{aligned} \tag{8.22}$$

Linearisation of inertia part of virtual mechanical work

The linearised formulation of the inertia part of the virtual mechanical work is similarly derived as for the external part. Considering the linearisation of the acceleration field

$$\mathrm{D}(\ddot{\mathbf{u}})[\Delta\mathbf{u}] \;=\; \Delta\ddot{\mathbf{u}} \tag{8.23}$$

and applying the Gateaux derivative, the linear approximation of the inertia part of the virtual mechanical work is given by

$$\begin{aligned}
&\delta\mathcal{W}_{\rho_0}(\mathbf{u},\,\delta\mathbf{u}) \,+\, \mathrm{D}\big(\delta\mathcal{W}_{\rho}(\mathbf{u},\,\delta\mathbf{u})\big)\,[\Delta\mathbf{u}] \,= \\
&= \int_V \rho_0\,\ddot{\mathbf{u}}\,\delta\mathbf{u}\,\mathrm{d}V \,+\, \int_V \mathrm{D}(\rho_0\,\ddot{\mathbf{u}}\,\delta\mathbf{u})\,[\Delta\mathbf{u}]\,\mathrm{dV} \\
&= \int_V \rho_0\,\ddot{\mathbf{u}}\,\delta\mathbf{u}\,\mathrm{d}V \,+\, \int_V \rho_0\,\mathrm{D}(\ddot{\mathbf{u}})\,[\Delta\mathbf{u}]\,\mathrm{dV} \\
&= \int_V \rho_0\,(\ddot{\mathbf{u}} \,+\, \Delta\ddot{\mathbf{u}})\,\delta\mathbf{u}\,\mathrm{d}V\ .
\end{aligned} \tag{8.24}$$

8.3 Local discretisation of the virtual work

The local discretisation of the virtual mechanical work is based on so-called shape functions $N_i(\xi)$. These can be of first, second or higher order and depend on isoparametric coordinates ξ which are given by the considered element type. On this basis, the local discretisation of displacement field $\mathbf{u}$, acceleration field $\ddot{\mathbf{u}}$, incremental displacement field $\Delta\mathbf{u}$ and virtual displacement field $\delta\mathbf{u}$ are given by

$$\mathbf{u} = \sum_i N_i\,\mathbf{u}_i\,, \quad \ddot{\mathbf{u}} = \sum_i N_i\,\ddot{\mathbf{u}}_i\,, \quad \Delta\mathbf{u} = \sum_i N_i\,\Delta\mathbf{u}_i\,, \quad \delta\mathbf{u} = \sum_i N_i\,\delta\mathbf{u}_i\ . \tag{8.25}$$

Therein, the index i is the nodal number and the variables $\mathbf{u}_i$ and $\ddot{\mathbf{u}}_i$ denote the nodal displacement and acceleration. Regarding these relations and taking into account (2.7), the local discretisation of deformation gradient and virtual deformation gradient can be expressed by

$$\begin{aligned}
\mathbf{F} &= \mathbf{1} + \sum_i \mathbf{u}_i \otimes \mathrm{Grad}(N_i)\ , \\
\delta\mathbf{F} &= \mathrm{Grad}(\delta\mathbf{u}) = \sum_i \delta\mathbf{u}_i \otimes \mathrm{Grad}(N_i)\ .
\end{aligned} \tag{8.26}$$

On this basis, the local discretisation of the virtual Green-Lagrange tensor can be defined

$$\begin{aligned}
\delta\mathbf{E} &= \frac{1}{2}\,(\delta\mathbf{F}^T\,\mathbf{F} \,+\, \mathbf{F}^T\,\delta\mathbf{F}) \\
&= \frac{1}{2}\left(\left[\sum_i \mathrm{Grad}(N_i)\otimes\delta\mathbf{u}_i\right]\,\mathbf{F} \,+\, \mathbf{F}^T\,\left[\sum_i \delta\mathbf{u}_i\otimes\mathrm{Grad}(N_i)\right]\right) \\
&= \frac{1}{2}\sum_i \delta\mathbf{u}_i\,\Big([\mathrm{Grad}(N_i)\otimes\mathbf{F}]^{T12} \,+\, [\mathbf{F}\otimes\mathrm{Grad}(N_i)]\Big)\ .
\end{aligned} \tag{8.27}$$

Taking into account the definition (8.17) and the local discretisation

$$\mathrm{Grad}(\Delta\mathbf{u}) = \sum_i \Delta\mathbf{u}_i \otimes \mathrm{Grad}(N_i)\ , \tag{8.28}$$

its related Gateaux derivative can be written as

$$\begin{aligned} \mathrm{D}(\delta\mathbf{E})\,[\Delta\mathbf{u}] &= \Big[\big(\,\mathrm{Grad}(N_j)\otimes\Delta\mathbf{u}_j\big)\,\big(\delta\mathbf{u}_i\otimes\mathrm{Grad}(N_i)\big)\Big] \\ &= \Big[\delta\mathbf{u}_i\,\Delta\mathbf{u}_j\,\big(\,\mathrm{Grad}(N_j)\otimes\mathrm{Grad}(N_i)\big)\Big]\,. \end{aligned} \tag{8.29}$$

Based on the introduced relations, the local discretisation of the virtual mechanical work can be derived. First regarding the internal part of virtual mechanical work in (8.19) and taking relation (8.27) into account, the local discretisation of its first term of the internal virtual mechanical work follows to

$$\begin{aligned} \int_V \tilde{\mathbf{T}}\cdot\delta\mathbf{E}\,\mathrm{d}V &= \delta\mathbf{u}_i\int_V \frac{1}{2}\,\tilde{\mathbf{T}}\cdot\Big[\big(\,\mathrm{Grad}(N_i)\otimes\mathbf{F}\big)^{T12}+\big(\mathbf{F}\otimes\mathrm{Grad}(N_i)\big)\Big]\,\mathrm{d}V \\ &= \delta\mathbf{u}_i\,\mathbf{R}_i^{int}\,. \end{aligned} \tag{8.30}$$

Therein, the introduced variable $\mathbf{R}_i^{int}$ denotes the nodal force resulting from the internal stresses inside the material. In order to derive the local discretisation of the remaining two terms of the internal part of virtual mechanical work, (8.29) is taken into account and inserted into (8.19). In so doing, the local discretisation of the remaining two terms is given by

$$\begin{aligned} &\int_V \mathrm{D}(\mathbf{E})\cdot\mathbb{C}\cdot\mathrm{D}(\mathbf{E})\,[\Delta\mathbf{u}]\,\mathrm{dV}+\int_{\mathrm{V}}\tilde{\mathbf{T}}\cdot\mathrm{D}(\delta\mathbf{E})\,[\Delta\mathbf{u}]\,\mathrm{dV} \\ =\;&\int_V \frac{1}{2}\,\delta\mathbf{u}_i\Big[\big(\,\mathrm{Grad}(N_i)\otimes\mathbf{F}\big)^{T12}+\big(\mathbf{F}\otimes\mathrm{Grad}(N_i)\big)\Big]\cdot\mathbb{C}\cdot \\ &\cdot\frac{1}{2}\Big[\big(\,\mathrm{Grad}(N_j)\otimes\mathbf{F}^T\big)+\big(\mathbf{F}^T\otimes\mathrm{Grad}(N_j)\big)^{T23}\Big]\,\Delta\mathbf{u}_j\,\mathrm{d}V \\ &+\int_V\tilde{\mathbf{T}}\cdot\Big[\delta\mathbf{u}_i\,\Delta\mathbf{u}_j\,\big(\,\mathrm{Grad}(N_j)\otimes\mathrm{Grad}(N_i)\big)\Big]\,\mathrm{d}V \\ =\;&\delta\mathbf{u}_i\Big(\mathbf{K}_{ij}^{\mathbb{C}}+\mathbf{K}_{ij}^{\tilde{\mathbf{T}}}\Big)\,\Delta\mathbf{u}_j\,. \end{aligned} \tag{8.31}$$

In this expression, the variables $\mathbf{K}_{ij}^{\mathbb{C}}$ and $\mathbf{K}_{ij}^{\tilde{\mathbf{T}}}$ are the components of the tangent stiffness matrix. Thereby, the part $\mathbf{K}_{ij}^{\mathbb{C}}$ is related to the material properties and $\mathbf{K}_{ij}^{\tilde{\mathbf{T}}}$ corresponds to the geometric properties. With the approximation of the virtual displacement field $\delta\mathbf{u}$ in (8.25), the discretisation of the external part of virtual mechanical work reads as

$$\int_A\big(\boldsymbol{\sigma}_A+\Delta\boldsymbol{\sigma}_A\big)\,N_i\,\delta\mathbf{u}_i\,\mathrm{d}A+\int_V\rho_0\,\big(\mathbf{k}+\Delta\mathbf{k}\big)\,N_i\,\delta\mathbf{u}_i\,\mathrm{d}V=\delta\mathbf{u}_i\,\mathbf{R}_i^{ext}\,. \tag{8.32}$$

Therein, the variable $\mathbf{R}_i^{ext}$ denotes the external nodal force which is caused by external forces acting on node i. In order to derive the local discretisation of the inertia part of the virtual mechanical work, the linearised definitions (8.25) are considered. Then, the

local discretisation of the inertia part of the virtual mechanical work is finally given by

$$\begin{aligned} \int_V \rho_0 \, N_j \, \ddot{\mathbf{u}}_j \, N_i \, \delta\mathbf{u}_i \, \mathrm{d}V \quad &+ \quad \int_V \rho_0 \, N_j \, \Delta\ddot{\mathbf{u}}_j \, N_i \, \delta\mathbf{u}_i \, \mathrm{d}V \\ = \qquad \delta\mathbf{u}_i \, \mathbf{R}_i^{\rho_0} \qquad &+ \qquad \delta\mathbf{u}_i \, \mathbf{M}_{ij} \, \Delta\ddot{\mathbf{u}}_j \; . \end{aligned} \tag{8.33}$$

The variable $\mathbf{R}_i^{\rho_0}$ defines the inertia nodal force which is present at node i whereas the variable $\mathbf{M}_{ij}$ is a component of the mass matrix. If the discretisised definitions (8.30), (8.31), (8.32) and (8.33) are taken into account, the local discretisation of the virtual mechanical work for a single node i can finally be expressed by

$$\delta\mathbf{u}_i \left[\mathbf{M}_{ij} \, \Delta\ddot{\mathbf{u}}_j \, + \, \left(\mathbf{K}_{ij}^{\mathbb{C}} \, + \, \mathbf{K}_{ij}^{\tilde{\mathbf{T}}} \right) \Delta\mathbf{u}_j \right] \, = \, \delta\mathbf{u}_i \left[- \, \mathbf{R}_i^{int} \, + \, \mathbf{R}_i^{ext} \, - \, \mathbf{R}_i^{\rho_0} \right] . \tag{8.34}$$

Since the virtual displacement $\delta\mathbf{u}_i$ can be arbitrary varied, this equation is automatically fulfilled if the terms in brackets on the left and right side of the equation are identical. Regarding the whole body instead of a single node i, the following linear system of equations is obtained

$$\left[\mathbf{M}\right] \left[\Delta\ddot{\mathbf{u}}\right] \, + \, \left[\mathbf{K}\right] \left[\Delta\mathbf{u}\right] \, = \, \left[\mathbf{R}\right] . \tag{8.35}$$

A detailed presentation of the introduced relations in sections 8.1, 8.2 and 8.3 with regard to the implementation of a thermoviscoelastic approach is provided by J.Retka et al. (2007).

8.4 Incompressibility

The developed classical and fractional constitutive models are defined for incompressible material behaviour meaning that the constraint

$$\det \mathbf{F} \, = \, 1 \tag{8.36}$$

has to be fulfilled. As described by J.Retka et al. (2007), a common possibility to account for this constraint is based on the method of Lagrange multipliers. In this context, the finite element code MSC Marc applies a special type of element formulation to account for incompressibility which is called "Hermann element". In order to realise incompressibility with regard to the finite element computation, the weak form of the balance equations can be derived via minimisation of potential energy. Considering this and referring to the argumentations by J.Retka et al. (2007), the whole potential energy is first defined by the sum of the internal and external energy

$$\Pi \, = \, \Pi_{int} \, + \, \Pi_{ext} \; . \tag{8.37}$$

If the Lagrange multiplier p is introduced, the method of Lagrange multipliers can be applied via extension of the specific Helmholtz free energy by the incompressibility

constraint. The result of this operation is given by

$$\Psi(\mathbf{C}, p) \;=\; \Psi(\mathbf{C}) \;+\; p\,(\det \mathbf{F} \;-\; 1)\;. \tag{8.38}$$

Taking this expression into account, the internal part of potential energy can be defined by

$$\Pi_{int} \;=\; \int_V \left(\rho_0 \Psi(\mathbf{C}) \;+\; p\,(\det \mathbf{F} \;-\; 1)\right) \mathrm{d}V\;. \tag{8.39}$$

Regarding this definition, the minimum of potential energy is present if the directional derivatives are stationary. The expression of this requirement is given by

$$\delta\Pi \;=\; \mathrm{D}(\Pi)\,\Delta\mathbf{u} \;+\; \mathrm{D}(\Pi)\,\Delta\mathrm{p} \;=\; 0\;. \tag{8.40}$$

Therein, the Lagrange multiplier p must be accounted for as an independent variable meaning that the first and second term in (8.40) must be considered separately. Based on this, the following two constraints must be fulfilled in terms of incompressibility

$$\delta\Pi \;=\; \mathrm{D}(\Pi)\,[\Delta\mathbf{u}] \;=\; 0 \quad \text{and} \quad \mathrm{D}(\Pi)\,[\Delta\mathrm{p}] \;=\; 0\;. \tag{8.41}$$

As a consequence, the consideration of incompressibility by the additional constraint $\mathrm{D}(\Pi)\,[\Delta\mathrm{p}] \;=\; 0$ leads to an extension of the linear system of equations given in (8.35) by a further equation. After local discretisation, the following extended system of equations is obtained

$$\begin{bmatrix} [\mathbf{M_{uu}}] & [\mathbf{0}] \\ [\mathbf{0}] & [0] \end{bmatrix} \begin{bmatrix} \Delta\ddot{\mathbf{u}} \\ \Delta p \end{bmatrix} \;+\; \begin{bmatrix} [K_{\mathbf{uu}}] & [K_{\mathbf{u}p}] \\ [K_{p\mathbf{u}}] & [0] \end{bmatrix} \begin{bmatrix} \Delta\mathbf{u} \\ \Delta p \end{bmatrix} \;=\; \begin{bmatrix} \mathbf{R_u} \\ \mathbf{R}_p \end{bmatrix}\;. \tag{8.42}$$

Comparing (8.35) and (8.42), one can observe, that the method of Lagrange multipliers leads to another unknown and thus raises the number of equations to solve (J.Retka et al. 2007; Retka 2011).

8.5 Implementation

In this section, the constitutive equations for the implementation of the classical and fractional constitutive models into the finite element code MSC Marc are derived. In this context, the constitutive formulations given by MSC Marc are presented and the implementation equations are derived by comparing them with the constitutive equations of the classical and fractional models. For clarification, the definitions in MSC Marc are identified by index "FE" whereas definitions of the material models are denoted by index "M" in the following.
The implementation of the constitutive models is based on the proposal by Morman and Nagtegaal (1983) and performed via the user-subroutine "UPHI". Based on this, the finite element computation is decomposed into a static and a dynamic loadcase. The static loadcase considers the static predeformation and is calculated in the time domain whereas the dynamic loadcase represents the superimposed harmonic vibration and is calculated in the frequency domain. On the basis of this separation, the displacement

field $\mathbf{u}$ is additively decomposed into a static displacement $\mathbf{u}_0$ which corresponds to the static loadcase and a dynamic displacement $\Delta\mathbf{u}\,\mathrm{e}^{i\omega t}$ which is related to the dynamic loadcase

$$\mathbf{u}(\omega, t) \;=\; \mathbf{u}_0 \;+\; \Delta\mathbf{u}\,\mathrm{e}^{i\omega t} \;. \tag{8.43}$$

As a consequence, the resulting 2nd Piola-Kirchhoff stress tensor is also additively decomposed into an equilibrium part $\tilde{\mathbf{T}}_{FE,0}$ and a harmonic part $\Delta\tilde{\mathbf{T}}_{FE}$

$$\tilde{\mathbf{T}}_{FE} \;=\; \tilde{\mathbf{T}}_{FE,0} \;+\; \Delta\tilde{\mathbf{T}}_{FE}\,\mathrm{e}^{i\omega t} \;. \tag{8.44}$$

In order to prepare the constitutive equations of the developed material models for an implementation into the finite element code MSC Marc, the definitions of the static and dynamic parts $\tilde{\mathbf{T}}_{M,0}$ and $\Delta\tilde{\mathbf{T}}_{M}$ of the constitutive approaches are compared with those of the finite element code $\tilde{\mathbf{T}}_{FE,0}$ and $\Delta\tilde{\mathbf{T}}_{FE}$ in the following.

Implementation of static part

In order to implement the static part $\tilde{\mathbf{T}}_{M,0}$ of the constitutive models into finite element code, its definition must be compared with the corresponding definition $\tilde{\mathbf{T}}_{FE,0}$ in MSC Marc. In so doing, one can observe, that both formulations are equal to each other

$$\tilde{\mathbf{T}}_{FE,0} \;=\; -\,p_0\,\mathbf{C}_0^{-1} \;+\; 2\,\rho_0\;\left.\frac{\partial\Psi_{eq}(\mathbf{C})}{\partial\mathbf{C}}\right|_{\mathbf{C}_0} \;=\; \tilde{\mathbf{T}}_{M,0} \;. \tag{8.45}$$

In MSC Marc, the specific Helmholtz free energy $\rho_0\,\Psi_{eq}(\mathbf{C})$ is defined by a Mooney approach (Mooney 1940)

$$\begin{aligned}\rho_0\,\Psi_{eq}(\mathbf{C}) \;&=\; C_{10}\,(\mathrm{I}_\mathbf{C} \,-\, 3) \,+\, C_{20}\,(\mathrm{I}_\mathbf{C} \,-\, 3)^2 \,+\, C_{30}\,(\mathrm{I}_\mathbf{C} \,-\, 3)^3 \\ &\quad +\, C_{11}\,(\mathrm{I}_\mathbf{C} \,-\, 3)\,(\mathrm{II}_\mathbf{C} \,-\, 3) \,+\, C_{01}\,(\mathrm{I}_\mathbf{C} \,-\, 3) \;,\end{aligned} \tag{8.46}$$

with five material parameters C_{10}, C_{20}, C_{30}, C_{11} and C_{01} and the first and second invariants $\mathrm{I}_\mathbf{C}$ and $\mathrm{II}_\mathbf{C}$ of the right Cauchy-Green tensor. Regarding the constitutive models applied in this work, the specific Helmholtz free energy is similarly defined by a Mooney approach, but only based on two material parameters C_{10} and C_{01}

$$\rho_0\,\Psi_{eq}(\mathbf{C}) \;=\; C_{10}\,(\mathrm{I}_\mathbf{C} \,-\, 3) \,+\, C_{01}\,(\mathrm{I}_\mathbf{C} \,-\, 3) \;. \tag{8.47}$$

Considering this, the static part can directly be implemented into finite element code MSC Marc by providing material parameters C_{10} and C_{01} as input variables via the user interface. Since parameters C_{20}, C_{30} and C_{11} are not considered by the constitutive models, they are simply set to "0".

Implementation of dynamic part

The finite element formulation overstress part $\Delta\tilde{\mathbf{T}}_{FE}$ in MSC Marc is given by

$$\Delta\tilde{\mathbf{T}}_{FE} \;=\; -\,\Delta p\,\mathbf{C}_0^{-1} \;+\; \left(\overset{4}{\mathbf{D}}_{FE} \;+2\,i\omega\;\overset{4}{\mathbf{G}}_{FE}\,(\omega,\mathbf{C}_0)\right)\;\cdot\;\left(\mathbf{F}_0^T\,\Delta\mathbf{E}_{lin}\,\mathbf{F}_0\right)\;. \tag{8.48}$$

Therein, variable $\overset{4}{\mathbf{D}}_{FE}$ is the fourth order elasticity tensor and variable $\overset{4}{\mathbf{G}}_{FE}$ is the complex modulus tensor of fourth order. Regarding the constitutive models, the overstress part $\Delta\tilde{\mathbf{T}}_M$ is defined by

$$\Delta\tilde{\mathbf{T}}_M(\omega,t) \;=\; -\,\Delta p\,\mathbf{C}_0^{-1} \;+\; \left(\overset{4}{\mathbf{D}}_{M} \;+\; \overset{4}{\mathbf{G}}_{A/B}\,(\omega,\mathbf{C}_0)\right)\;\cdot\;\left(\mathbf{F}_0^T\,\Delta\mathbf{E}_{lin}\,\mathbf{F}_0\right)\;. \tag{8.49}$$

The first term in (8.48) and (8.49) arises from the incompressibility constraint and is equal for the finite element code and the constitutive models

$$-\;\Delta p\,\mathbf{C}_0^{-1} \;=\; -\,\Delta p\,\mathbf{C}_0^{-1}\;. \tag{8.50}$$

On this basis, the finite element definition of this term can be applied for implementation without modification.

In order to compare the remaining terms of the dynamic parts $\Delta\tilde{\mathbf{T}}_{FE}$ and $\Delta\tilde{\mathbf{T}}_M$, the definition of the elasticity tensor $\overset{4}{\mathbf{D}}_{FE}$ in MSC Marc

$$\overset{4}{\mathbf{D}}_{FE} = \;p_0\;\left\{\left[\mathbf{C}_0^{-1}\;\otimes\;\mathbf{C}_0^{-1}\right]^{T23} \;+\; \left(\left[\mathbf{C}_0^{-1}\;\otimes\;\mathbf{C}_0^{-1}\right]^{T34}\right)^{T23}\right\} \;+\; 4\,\rho_0\;\left.\frac{\partial^2\Psi(\mathbf{C})}{\partial\mathbf{C}^2}\right|_{\mathbf{C}_0} \tag{8.51}$$

and the corresponding elasticity tensor $\overset{4}{\mathbf{D}}_M$ of the classical and fractional models

$$\overset{4}{\mathbf{D}}_M = \;2\,p_0\;\overset{4}{\mathbf{R}}_0\;+4\,\rho_0\;\left.\frac{\partial^2\Psi_{eq}(\mathbf{C})}{\partial\mathbf{C}^2}\right|_{\mathbf{C}_0} \tag{8.52}$$

are discussed at first. The last terms of both definitions are already equal to each other

$$4\,\rho_0\;\left.\frac{\partial^2\Psi(\mathbf{C})}{\partial\mathbf{C}^2}\right|_{\mathbf{C}_0} \;=\; 4\,\rho_0\;\left.\frac{\partial^2\Psi(\mathbf{C})}{\partial\mathbf{C}^2}\right|_{\mathbf{C}_0} \tag{8.53}$$

and can be implemented without any modification. In contrast to this, the first terms in (8.51) and (8.52) must satisfy the following equation for implementation

$$p_0\;\left\{\left[\mathbf{C}_0^{-1}\;\otimes\;\mathbf{C}_0^{-1}\right]^{T23} \;+\; \left(\left[\mathbf{C}_0^{-1}\;\otimes\;\mathbf{C}_0^{-1}\right]^{T34}\right)^{T23}\right\} \;\overset{!}{=}\; 2\,p_0\;\overset{4}{\mathbf{R}}_0 \tag{8.54}$$

For this purpose, the elasticity tensor $\overset{4}{\mathbf{D}}_{FE}$ of the finite element code can be reformulated. If the symmetry of the right Cauchy-Green tensor is taken into account, the

derivative of its inverse with respect to deformation can be expressed by

$$\begin{aligned} \left.\frac{\partial \mathbf{C}^{-1}}{\partial \mathbf{C}}\right|_{\mathbf{C}_0} &= -\frac{1}{2}\left\{\left[\mathbf{C}_0^{-1}\otimes\mathbf{C}_0^{-1}\right]^{T23}+\left(\left[\mathbf{C}_0^{-1}\otimes\mathbf{C}_0^{-1}\right]^{T34}\right)^{T23}\right\} \\ &= -\left[\mathbf{C}_0^{-1}\otimes\mathbf{C}_0^{-1}\right]^{T23} \mathrel{\widehat{=}} -\overset{4}{\mathbf{R}}_0 \ . \end{aligned} \tag{8.55}$$

By rearranging this expression, the following relation is obtained

$$\left\{\left[\mathbf{C}_0^{-1}\otimes\mathbf{C}_0^{-1}\right]^{T23}+\left(\left[\mathbf{C}_0^{-1}\otimes\mathbf{C}_0^{-1}\right]^{T34}\right)^{T23}\right\} = 2\ \overset{4}{\mathbf{R}}_0 \ . \tag{8.56}$$

Considering this, the elasticity tensors $\overset{4}{\mathbf{D}}_{FE}$ and $\overset{4}{\mathbf{D}}_{M}$ are proven to be equal to each other

$$\overset{4}{\mathbf{D}}_{FE} = 2\,p_0\ \overset{4}{\mathbf{R}}_0 + 4\,\rho_0\ \left.\frac{\partial^2\Psi(\mathbf{C})}{\partial\mathbf{C}^2}\right|_{\mathbf{C}_0} = \overset{4}{\mathbf{D}}_{M} \ , \tag{8.57}$$

such that the finite element definition of the elasticity tensor can be applied for implementation without modification.

At last, the definitions of the complex modulus tensors $\overset{4}{\mathbf{G}}_{FE}$ and $\overset{4}{\mathbf{G}}_{A/B}$ in (8.48) and (8.49) must be considered. In terms of the finite element code MSC Marc, the complex modulus tensors is defined by means of nine scalar material functions $G_k(\omega)$ and $G_{ij}(\omega)$ which depend on the angular frequency ω

$$\begin{aligned} \overset{4}{\mathbf{G}}_{FE}\,(\omega,\mathbf{C}_0) &= G_0(\omega)\left\{\left[\mathbf{C}_0^{-1}\otimes\mathbf{C}_0^{-1}\right]^{T23}+\left(\left[\mathbf{C}_0^{-1}\otimes\mathbf{C}_0^{-1}\right]^{T34}\right)^{T23}\right\} \\ &\quad + G_1(\omega)\left\{\left[\mathbf{1}\otimes\mathbf{C}_0^{-1}\right]^{T23}+\left(\left[\mathbf{C}_0^{-1}\otimes\mathbf{C}_0^{-1}\right]^{T34}\right)^{T23}\right\} \\ &\quad + G_2(\omega)\left\{\left[\mathbf{C}_0\otimes\mathbf{C}_0^{-1}\right]^{T23}+\left(\left[\mathbf{C}_0^{-1}\otimes\mathbf{C}_0^{-1}\right]^{T34}\right)^{T23}\right\} \\ &\quad + G_{10}(\omega)\left[\mathbf{1}\otimes\mathbf{C}_0^{-1}\right] + G_{20}(\omega)\left[\mathbf{C}_0\otimes\mathbf{C}_0^{-1}\right] \\ &\quad + G_{11}(\omega)\left[\mathbf{1}\otimes\mathbf{1}\right] + G_{22}(\omega)\left[\mathbf{C}_0\otimes\mathbf{C}_0\right] \\ &\quad + G_{12}(\omega)\left[\mathbf{1}\otimes\mathbf{C}_0\right] + G_{21}(\omega)\left[\mathbf{C}_0\otimes\mathbf{1}\right] \ . \end{aligned} \tag{8.58}$$

The definition of the complex modulus tensor $\overset{4}{\mathbf{G}}_{A/B}$ of the constitutive models is given by

$$\overset{4}{\mathbf{G}}_{A/B}\,(\omega,\mathbf{C}_0) = G^*_{A/B}(\omega,\mathbf{C}_0)\ \overset{4}{\mathbf{R}}_0 \ . \tag{8.59}$$

Therein, variable $G^*_{A/B}(\omega,\mathbf{C}_0)$ is the equivalent to the first material function $G^*_0(\omega)$. Thus, only the first term in (8.58) must be considered for implementation. Since the remaining terms are not part of the constitutive models, the other material functions can be set to "0". If definitions (8.55) and (8.56) are taken into account, the following relation between the finite element code and the proposed constitutive models must be

satisfied

$$2\,i\omega\ \overset{4}{\mathbf{G}}_{FE}\,(\omega,\mathbf{C}_0)\ =\ 4\,i\omega\,G_0(\omega)\ \overset{4}{\mathbf{R}}_0\quad\overset{!}{=}\quad\overset{4}{\mathbf{G}}_{A/B}\,(\omega,\mathbf{C}_0)\ =\ G^*_{A/B}(\omega,\mathbf{C}_0)\ \overset{4}{\mathbf{R}}_0\ . \tag{8.60}$$

Based on this, the definitions of the complex modulus of the classical approach G^*_A and of the fractional model G^*_B have to be discussed. In terms of the classical approach, the complex modulus in (8.60) is defined by

$$G^*_A(\omega,\mathbf{C}_0)\ =\ 2\sum_{k=1}^{n}\mu_k(\mathbf{C}_0)\,\frac{i\omega\,\tau_k}{1+i\omega\,\tau_k}\ . \tag{8.61}$$

If this relation is compared to the definition in MSC Marc (8.60), the scalar material function $G_{0,A}$ of the finite element code is given by

$$G_{0,A}(\omega,\mathbf{C}_0)\ =\ \frac{1}{4\,i\omega}\,G^*_A(\omega,\mathbf{C}_0)\ =\ \frac{1}{2\,i\omega}\sum_{k=1}^{n}\mu_k(\mathbf{C}_0)\,\frac{i\omega\,\tau_k}{1+i\omega\,\tau_k}\ . \tag{8.62}$$

Separating the real and imaginary parts in (8.62), the following equations of the real and imaginary parts must be implemented in the finite element code

$$\begin{aligned} G'_{0,A}(\omega,\mathbf{C}_0)\ &=\ \frac{1}{2}\sum_{k=1}^{n}\mu_k(\mathbf{C}_0)\,\frac{\omega\,\tau_k^2}{1+(\omega\,\tau_k)^2}\ ,\\ G''_{0,A}(\omega,\mathbf{C}_0)\ &=\ \frac{1}{2}\sum_{k=1}^{n}\mu_k(\mathbf{C}_0)\,\frac{\tau_k}{1+(\omega\,\tau_k)^2}\ . \end{aligned} \tag{8.63}$$

With respect to the fractional model, the complex modulus in (8.60) is given by

$$G^*_B(\omega,\mathbf{C}_0)\ =\ 2\sum_{k=1}^{n}\mu_k(\mathbf{C}_0)\,\frac{(i\omega\,\tau_k)^{\alpha_k}}{1+(i\omega\,\tau_k)^{\alpha_k}}\ . \tag{8.64}$$

If this relation is compared with the definition of the finite element code (8.60), the scalar material function $G_{0,B}$ is expressed by

$$G_{0,B}(\omega,\mathbf{C}_0)\ =\ \frac{1}{4\,i\omega}\,G^*_B(\omega,\mathbf{C}_0)\ =\ \frac{1}{2\,i\omega}\sum_{k=1}^{n}\mu_k(\mathbf{C}_0)\,\frac{(i\omega\,\tau_k)^{\alpha_k}}{1+(i\omega\,\tau_k)^{\alpha_k}}\ . \tag{8.65}$$

Regarding this relation and applying the software-provided functions $real()$ and $aimag()$, the implementation equations of the real and imaginary parts are defined by

$$\begin{aligned} G'_{0,B}(\omega,\mathbf{C}_0)\ &=\ real\left(\frac{1}{4\,i\omega}\,G^*_B(\omega,\mathbf{C}_0)\right)\\ G''_{0,B}(\omega,\mathbf{C}_0)\ &=\ aimag\left(\frac{1}{4\,i\omega}\,G^*_B(\omega,\mathbf{C}_0)\right)\ . \end{aligned} \tag{8.66}$$

8.6 Verification of the implementation

This section is about the verification of the finite element implementation to investigate the accurateness of the implemented code in MSC Marc. For this purpose, the numerical data of the parameter identification of the classical and of the fractional constitutive model is compared to the corresponding data of the finite element simulation. To this end, the predeformation and frequency dependent material characteristics of the storage and the loss modulus are simulated by means of a simple three-dimensional cube with respect to the SBR40 vulcanisate. The geometry is discretisised by a single hexahedral 8 node Hermann element which is, as well as the applied boundary conditions, illustrated in figure 8.1.

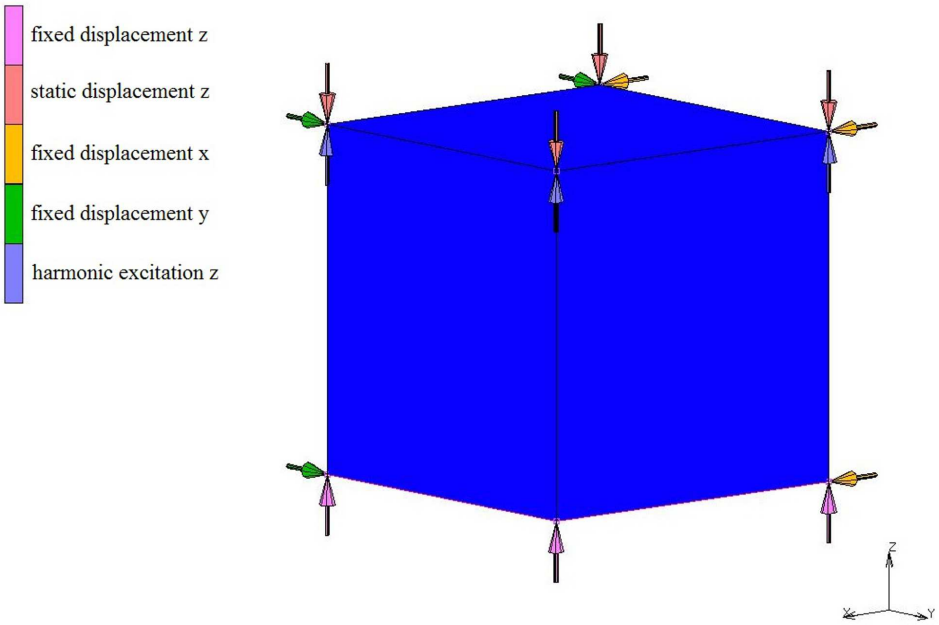

FIGURE 8.1: Three-dimensional cube and applied boundary conditions

The finite element calculation is divided into two *LOADCASES*, a static and a dynamic one. By first regarding the static loadcase, the cube is loaded on top with a constant predeformation in z-direction in a strain range from $-30\,\%$ up to $50\,\%$, which is incrementally applied in ten steps. At its lower side, the cube is fixed in z-direction whereas the faces which are normal to x- and y-directions are fixed in this direction. After the static predeformation is applied, the deformed structure is loaded by a harmonic oscillation of $0.1\,\%$ of strain which is applied on top of the cube in z-direction. The finite element simulation is performed in a frequency range from $10^{-2}\,\mathrm{Hz}$ up to $10^{5}\,\mathrm{Hz}$.
On the basis of the comparison in the previous section, the static material properties are directly defined in the user interface by choosing the material model *MOONEY* in the index card *MATERIAL PROPERTIES* and inserting the static material parameters C_{10} and C_{01}. The dynamic material laws are applied by choosing the property *PHI* by activating the option *RATE EFFECTS* and selecting the user subroutine *UPHI*. To start the finite element simulation, the option *TOTAL LAGRANGE* is

applied in the *SOLVER* menu meaning that the solution is calculated with respect to the reference configuration. This is due to the definition of a user subroutine which usually implies a calculation with respect to the reference configuration. Moreover, the nonlinear mechanical problem is computed on the basis of an iterative Newton-Raphson method.
The comparison between the finite element simulation and the corresponding numerical results of the parameter identification are displayed in figures 8.2 and 8.3 for each predeformation. As the figures reveal, the finite element simulations accurately fit to the numerical results in the whole range of predeformations and frequencies which ensures the correctness of the finite element implementation.

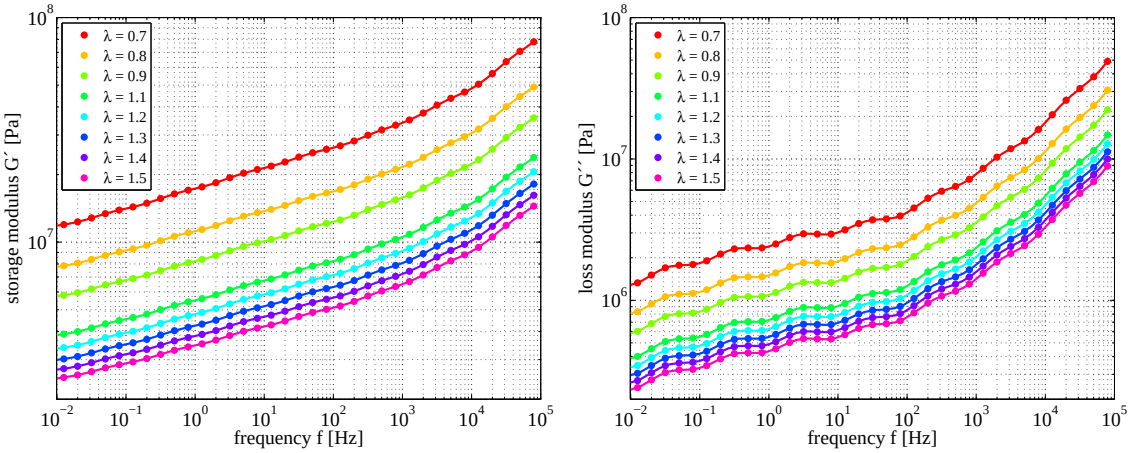

FIGURE 8.2: Comparison between the finite element simulation and the numerical results of the classical model: storage modulus (left), loss modulus (right)

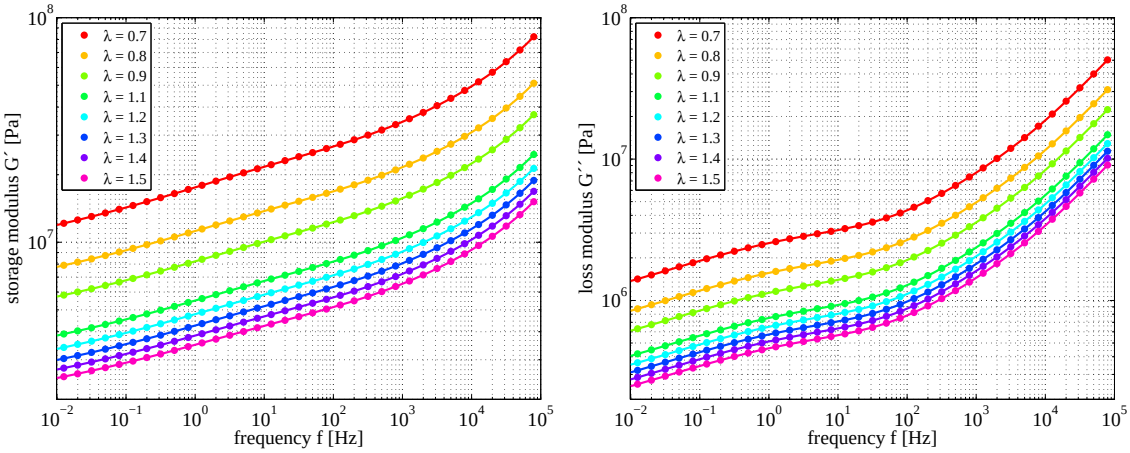

FIGURE 8.3: Comparison between the finite element simulation and the numerical results of the fractional model: storage modulus (left), loss modulus (right)

Chapter 9

Validation

Introduction

Validation of a constitutive model is essential to prove its ability to represent the behaviour of complex structures and loading conditions. Hence, validation of a material model is usually carried out by applying more complicated loadings to more complex structures than they were applied for the fitting of the model and by comparing the experimental results with the simulated one.

Outline

The focus of this chapter is the validation of the developed constitutive models. Since the classical and the fractional models for the overstress represent the material behaviour in a similar way, validation is only carried out for the fractional approach. To this end, measurements of a cylindrical SBR40 specimen with and without bonded steel plates are performed up to frequencies of 10 kHz and compared with the finite element simulations of the fractional model. Moreover, the last section provides the finite element simulation of a real engine mount and the computational results at three different predeformations.

9.1 Measuring setup and procedure

As illustrated in figure 9.1, validation measurements are performed on the basis of a cylindrical SBR40 specimen with and without bonded steel plates.

The measuring setup to validate the constitutive model is illustrated in figure 9.2. Via a dynamic shaker, a harmonic oscillation up to 10 kHz is applied to the top of the specimen. Due to the measuring equipment, a preloading of the specimen is not possible. The shaker is fixed at the upper side and the specimen is clamped at the bottom. Since the transfer behaviour of the specimen is of interest, the acceleration

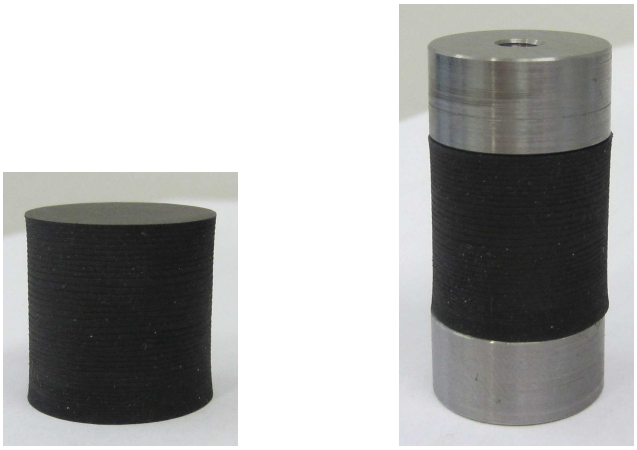

FIGURE 9.1: Cylindrical SBR40 specimen: pure rubber specimen (left) / with bonded steel plates (right)

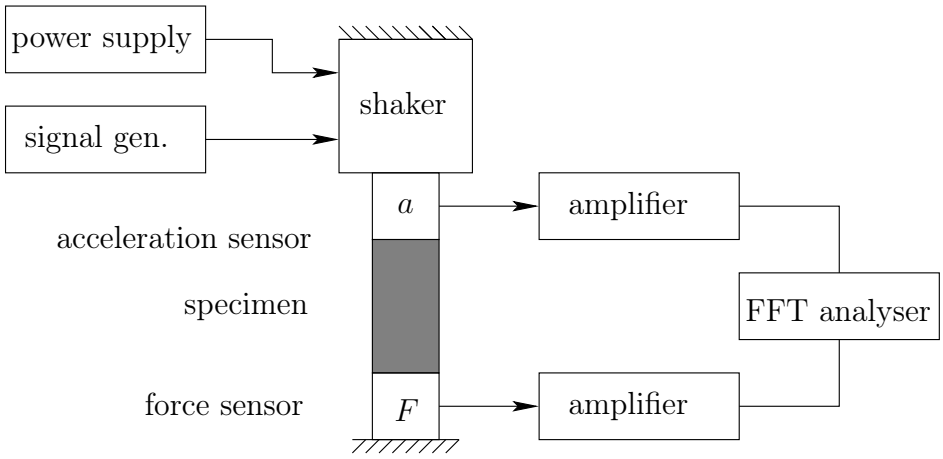

FIGURE 9.2: Measuring setup of validation experiments

caused by the harmonic oscillation is captured at the upper side of the specimen and its reaction force is measured with a force sensor at the lower side of the specimen. The shaker is actuated by a power supply by which the amplitude of the oscillation can be set, but not controlled. Due to the technical limits of the shaker, the amplitude of the oscillation decreases with increasing frequency. The type of the oscillation is a sinusoidal loading which is provided by a signal generator which is connected with the signal input of the shaker. In order to measure the force and acceleration signal of the sensors, they are connected with two amplifiers. These amplifiers pass a time-dependent voltage signal to a FFT analyser which is used to transfer the signals to the frequency domain. Since this work is focused on the storage and the loss modulus, force, displacement and the phase angle are of interest. Thus, the acceleration signal is twice integrated by the FFT analyser in the frequency domain

$$u = (i\omega)^2 a = -\omega^2 a \, . \tag{9.1}$$

On the basis of the displacement u and the reaction force F, the transfer function F/u is calculated by the FFT analyser and saved to a file for each frequency together with the phase angle δ between u and F.

In order to compare the measuring results with the finite element simulation, a representative dynamic transfer stiffness is calculated. Since the predeformation is zero and the harmonic oscillation is very small, the dynamic stress and strain can be expressed by

$$\Delta\sigma = \frac{F}{A} \quad , \quad \Delta\varepsilon = \frac{u}{l_0} \tag{9.2}$$

with the cross section A and the initial length l_0 of the specimen. Regarding these relations and taking (5.4) into account, the dynamic transfer stiffness can be calculated

$$G' = \frac{\Delta\sigma}{\Delta\varepsilon}\cos(\delta) = \frac{F}{u}\frac{l_0}{A}\cos(\delta) \ . \tag{9.3}$$

The experimental data for the dynamic transfer stiffness is provided in figure 9.3 for the SBR40 specimen with and without bonded steel plates.

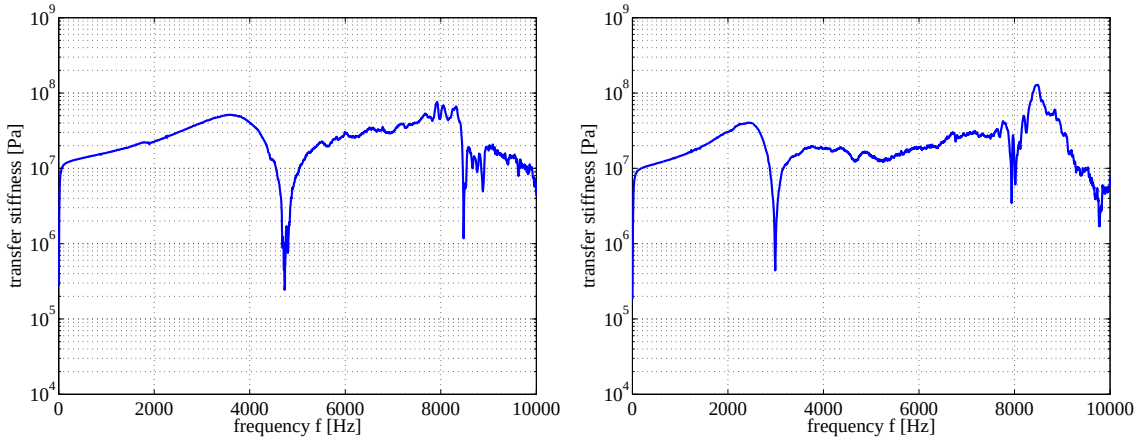

FIGURE 9.3: Measurement data of SBR40: pure rubber specimen (left) / with bonded steel plates (right)

The transfer stiffness of both specimens reveals similar characteristics, but the inertia frequencies differ from each other. The pure rubber specimen is characterised by two pronounced resonances located at 4500 Hz and 8200 Hz. The rubber with bonded steel plates also reveals two inertia frequencies which are located at lower frequencies of 3000 Hz and 8000 Hz. This behaviour was expected and can be related to the higher mass of the steel plates and their mass density, which results in a shift of the resonances to lower frequencies.

9.2 Finite element simulation

Finite element simulations are performed with the same geometries and boundary conditions as the measurements of the cylindrical SBR40 specimen with and without bonded steel plates. As illustrated in figure 9.4, both specimens are loaded on top with the harmonic displacement u in y-direction (vertical) and fixed on the bottom.

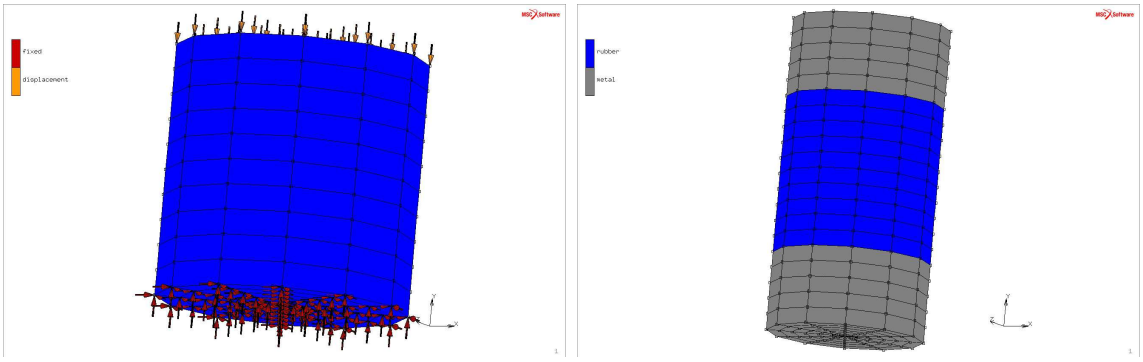

FIGURE 9.4: Finite element geometry of the specimen: pure rubber specimen (left) / with bonded steel plates (right)

In contrast to the simulations in chapter 8, the finite element computations to validate the constitutive model include the consideration of inertia effects. For this purpose, the mass density of the material must be provided as program input. In the case of the SBR40 vulcanisate and the steel plates, the mass density is $1120\,\mathrm{kg/m^3}$ and $7860\,\mathrm{kg/m^3}$.

In order to compare the results of the simulation with the experimental data, the dynamic transfer stiffness corresponding to (9.3) is calculated on the basis of the finite element results for the real part of the harmonic stress response $\Delta\sigma_{real}$ occurring at the bottom of the specimen, and the displacement u which is applied on the top of the specimen. With (5.4) and (9.2), the dynamic transfer stiffness reads as

$$G' = \frac{\Delta\sigma_{real}}{u}\, l_0 \ . \tag{9.4}$$

Similar to this relation, a dynamic transfer damping can be defined on the basis of the finite element results for the imaginary part of the harmonic stress response $\Delta\sigma_{imag}$

$$G'' = \frac{\Delta\sigma_{imag}}{u}\, l_0 \ . \tag{9.5}$$

The comparison between the measuring data and the finite element simulation in figure 9.5 reveals good agreement for both measurements, especially until the first inertia effects occur.

In the case of the pure rubber specimen, the first resonance frequency is captured exactly and the second one is in good agreement. With regard to the rubber with bonded steel plates, the first inertia frequency does not exactly match the measurement, but is still in good agreement with the experimental data. If one recognises, that the frequency of the dynamic analysis tests used to fit the model was only up to 60 Hz, parameter identification was performed without considering the bonded steel plates and the fact that the SBR40 used for the fitting of the model was from a different production process, one can state that the developed constitutive approach is suitable to represent the dynamic material properties of complex structures under complicated loading in a broad frequency range.

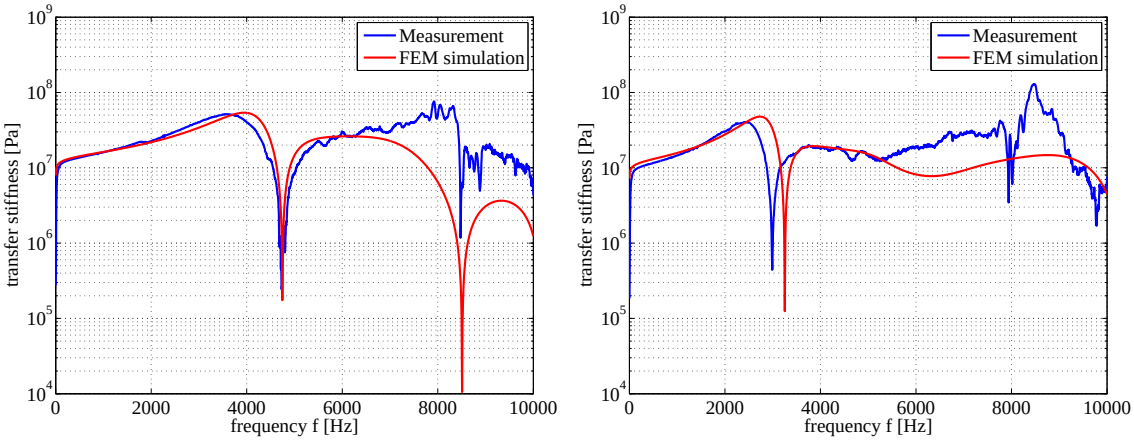

FIGURE 9.5: Comparison between the experimental data and the finite element simulation: pure rubber specimen (left) / with bonded steel plates (right)

For illustration, the deformed finite element structures of both specimens at their first eigenfrequency are displayed in figure 9.6, wherein factor 100 is applied for the display of the harmonic deformation.

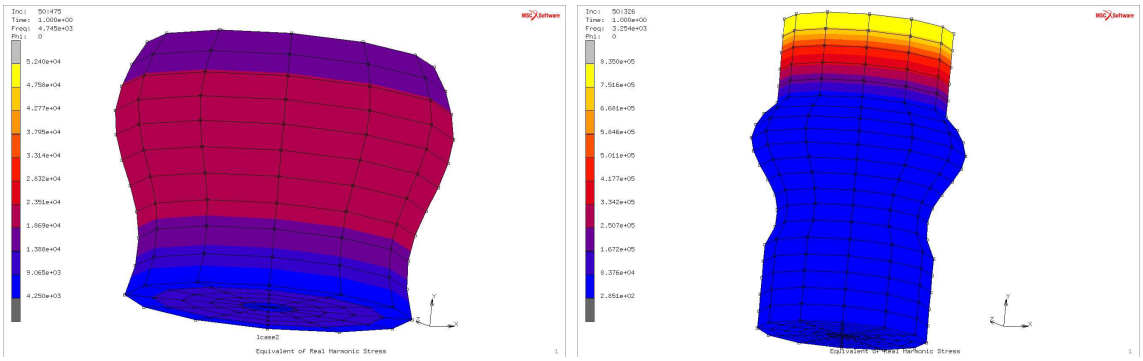

FIGURE 9.6: Deformed structures at the 1st resonance: pure rubber specimen (left) and specimen with bonded steel plates (right)

9.3 Simulation of a real engine mount

Finally, the dynamic behaviour of a real engine mount is simulated at predeformations of 10 %, 20 % and 30 % in compression which is superimposed by a harmonic oscillation of 0.1 % in a frequency range up to 10 kHz. The finite element simulations are performed on the basis of the material parameters of the SBR40 vulcanisate and include consideration of inertia effects to reveal the resonances of the engine mount. The engine mount and the undeformed finite element geometry of the pure rubber structure are displayed in figure 9.7.

The engine mount is fixed at the bottom and loaded on top in negative y-direction. With regard to the real structure of the engine mount, the rubber stays in direct contact with the metal parts and is thus hindered from moving at contact points. Hence,

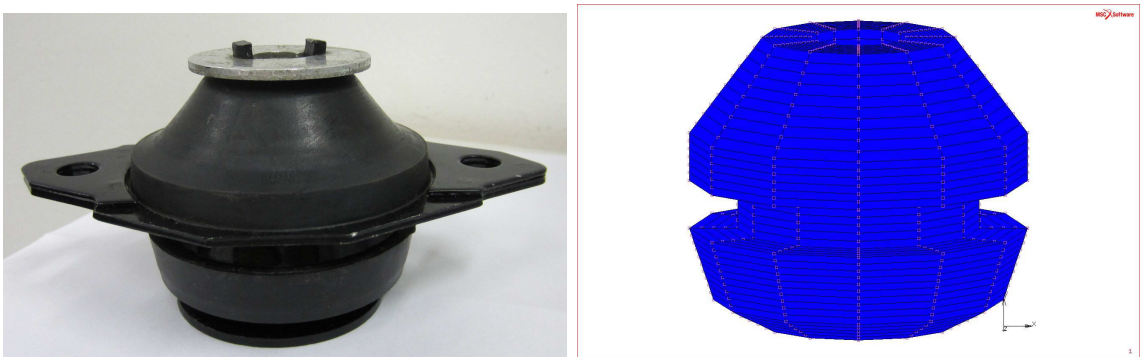

FIGURE 9.7: Engine mount (left) and finite element geometry (right)

finite element nodes located at the inner hole and at vertical faces of the outer notch of the structure are fixed in directions x and z whereas nodes located at horizontal faces of the outer notch are fixed in direction y.
Since the engine mount is rotationally symmetric, only a quarter of its structure is computed to shorten the simulation time. For this purpose, option $CYLIC\ SYMMETRY$ must be activated in MSC Marc. The results of the finite element simulations for the transfer stiffness and transfer damping are provided in figure 9.8 for each predeformation.

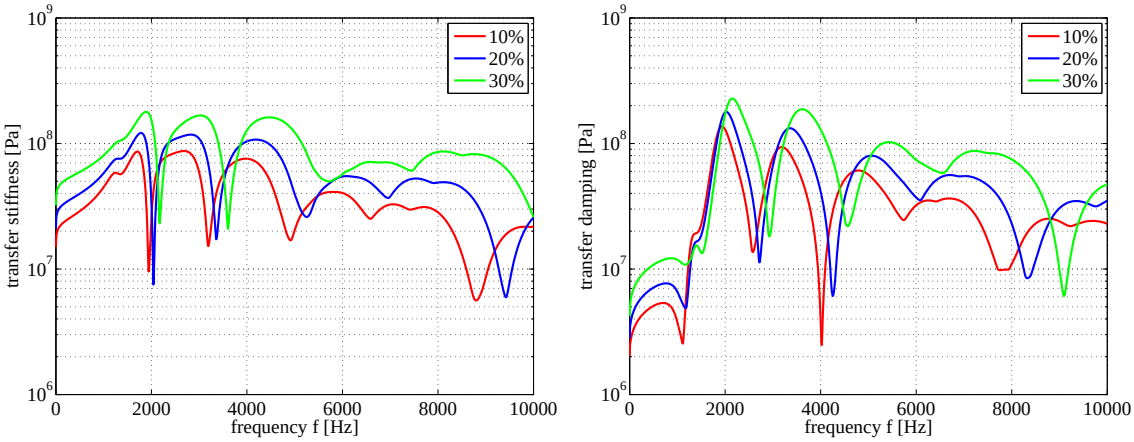

FIGURE 9.8: transfer stiffness and transfer damping of the engine mount at 10%, 20% and 30% predeformation

First, one can observe that the transfer stiffness and transfer damping are characterised by three significant eigenfrequencies. As expected, transfer stiffness and damping are increased for larger predeformations. Finally, the induced eigenfrequencies are shifted to higher values if predeformation is increased.

In order to illustrate the behaviour of the engine mount at the eigenfrequencies, the deformed finite element shapes and the corresponding real part of the harmonic stress response at the eigenfrequencies are displayed in figures 9.9, 9.10 and 9.11 for each predeformation and a scaling factor of 5 for the harmonic deformation.

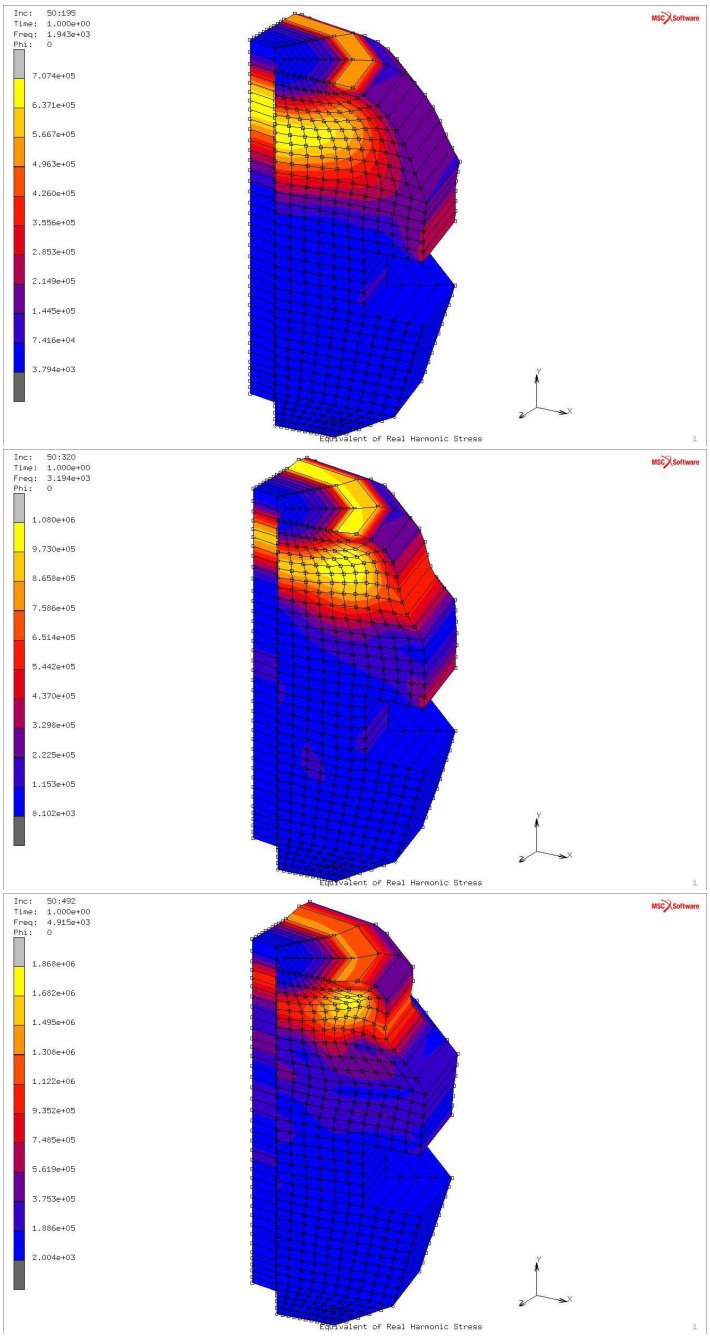

FIGURE 9.9: Deformed shapes of the engine mount at 10% predeformation: 1st eigenfrequency (top), 2nd eigenfrequency (middle) and 3rd eigenfrequency (bottom)

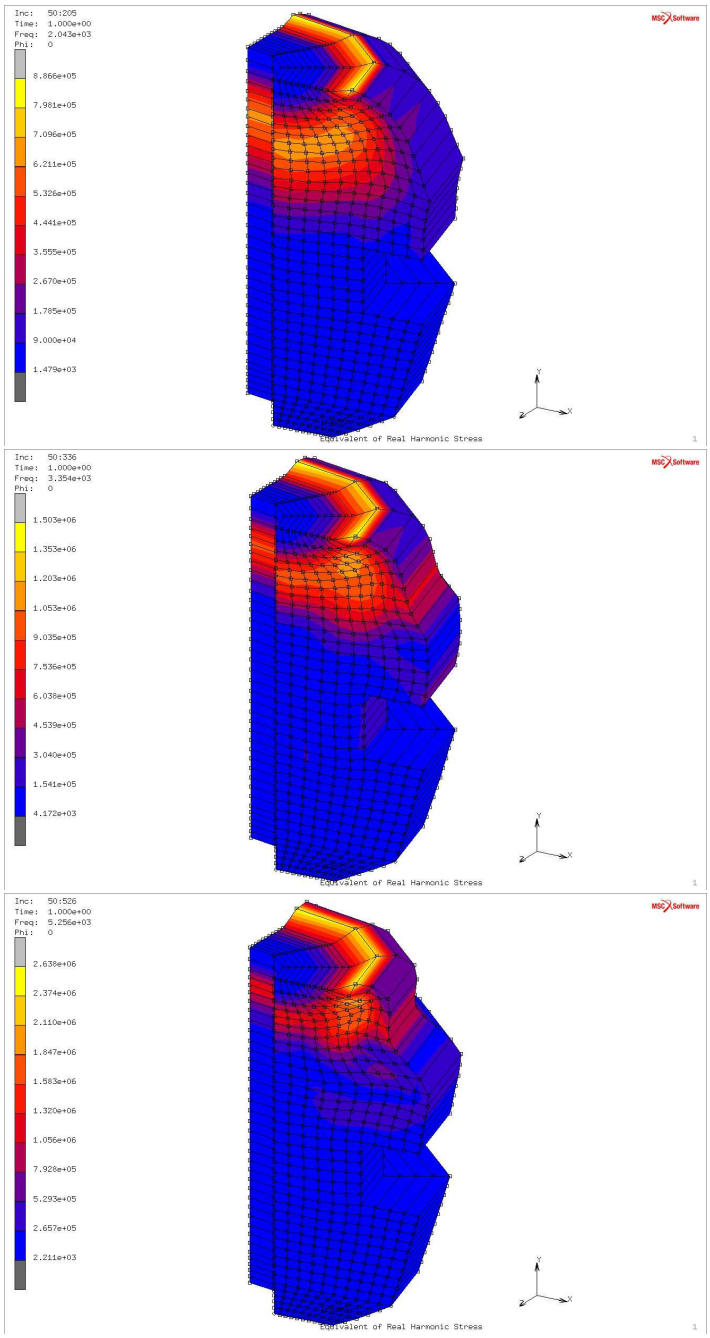

FIGURE 9.10: Deformed shapes of the engine mount at 20% predeformation: 1st eigenfrequency (top), 2nd eigenfrequency (middle) and 3rd eigenfrequency (bottom)

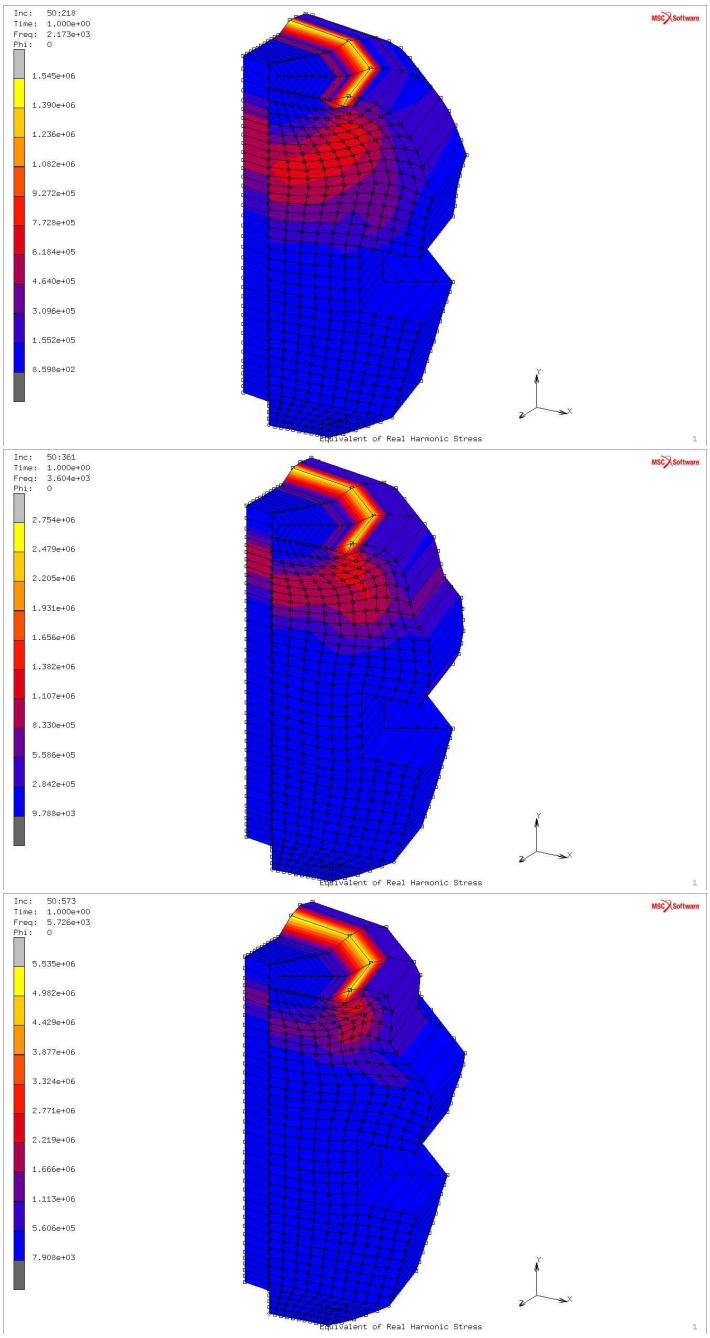

FIGURE 9.11: Deformed shapes of the engine mount at 30% predeformation: 1st eigenfrequency (top), 2nd eigenfrequency (middle) and 3rd eigenfrequency (bottom)

Chapter 10

Conclusion

This work focused on the investigation, mathematical description and finite element implementation of the predeformation and frequency dependent dynamics of filler-reinforced rubber structures loaded with a large static predeformation superimposed by small harmonic oscillations of 0.1 % of strain. Four different rubber vulcanisates were investigated in quasi-static and dynamic-mechanical analysis tests to characterise the material's equilibrium response and the dynamic characteristics of the storage and the loss modulus. The equilibrium stress-strain curves revealed the characteristic nonlinear behaviour of elastomers. The outcome of the dynamic mechanical analysis tests was a pronounced dependence of the storage and the loss modulus on both predeformation and frequency. The predeformation dependence was investigated in a range of prestrain from 30 % in compression up to 50 % in tension whereas the frequency dependent behaviour was characterised in a frequency range from 10^{-2} Hz up to 10^{5} Hz by applying the temperature frequency shifting technique.
Regarding the experimental results, the predeformation dependence was found to be mainly connected with the nonlinear equilibrium stress-strain behaviour of the material and thus implies an increase of the storage modulus with increasing predeformation. The loss modulus does not depend on the equilibrium stress but also depends on the predeformation. On the other hand, the frequency dependent characteristics of the storage and the loss modulus revealed an increase with the frequency in the whole frequency range.
Based on the experimental facts obtained, two constitutive formulations of nonlinear finite viscoelasticity have been formulated to describe the predeformation and frequency dependence of the investigated vulcanisates. Both formulations are based on the proposal by Haupt and Lion (2002), are defined as history functionals, and inherit a deformation dependent relaxation function to describe the predeformation dependent material characteristics. Moreover, the linearised version of the nonlinear model can be expressed in terms of differential equations of integer or of fractional order. The first constitutive approach is based on a differential equation of integer order and can be related to a classical Maxwell chain whereas the second model uses a fractional formulation and can be interpreted as a Maxwell chain of fractional order.
Based on error minimisation between experimental and numerical data of the constitutive models, the material parameters of both constitutive formulations were successfully

identified by a programmed identification routine in the software MATLAB.
By comparison, both models were found to be suitable to represent the dynamic material characteristics of the storage and the loss modulus with respect to the dependence on predeformation and frequency. Moreover, the fractional constitutive approach revealed the benefit of approximating the experimental data with much less material parameters but in the same quality as the classical model, which implies a significant increase in computational efficiency with respect to the identification process and the numerical simulation.
Last but not least, the classical and the fractional constitutive models were implemented into the finite element code MSC Marc to perform realistic simulations of more complex structures. The implementation is based on the proposal by Morman and Nagtegaal (1983) and performed via the user subroutine UPHI. The correctness of the implemented finite element code was ensured by a comparison between the numerically simulated data based on parameter identification, and the finite element computations. On this basis, the numerical and the finite element data was found to match exactly each other such that the implementation was proven to be correct.
The fractional constitutive model was validated by a comparison between dynamic measurements of SBR40 rubber cylinders with and without bonded metal plates loaded by harmonic oscillations up to 10 kHz, and the computational results of the finite element simulation. Since the validation revealed good agreement between the experimental and simulation data, the constitutive approach was found to be able to represent the dynamic characteristics of elastomers including inertia effects.
Finally, the finite element simulation of a real engine mount was performed at different predeformations to give a complex computation example. The simulation results revealed the expected predeformation and frequency dependent characteristics of the storage and the loss modulus as well as inertia frequencies which where found to be influenced by the predeformation.

In further investigations, it would be an improvement to develop a test setup to enable the experimental investigation of a real engine mount up to 10 kHz or even 100 kHz and compare the results with the finite element simulation. Moreover, the model may be extended by amplitude and temperature dependence, which are important in other dynamic applications, such as shock absorbers or tyres. Another benefit would be the investigation of the influence of ageing effects on the dynamics of the material and to develop an appropriate extension of the constitutive model.

Appendix A

Tensor algebra

The aim of this chapter is on the presentation of the mathematical notation of tensor algebra which is used in this work. On this, the simple scalar product, the double scalar product, the cross product, the dyadic product, the inverse and transposed, the trace operation and some mathematical relations are introduced. An overview about the mathematics and notation, this presentation mostly refers to, is also provided by Ehlers (2007).

A.1 Simple scalar product

The simple scalar product is characterised by no mathematical operator meaning that a mathematical operator is completely leaved out. The simple scalar product links two basis vectors standing directly to each other.

Simple scalar product of two vectors

Regarding two vectors $\mathbf{a}$ and $\mathbf{b}$, the simple scalar product is expressed by:

$$\boxed{\mathbf{a}\,\mathbf{b} \;=\; (a_i\,\mathbf{e}_i)\,(b_j\,\mathbf{e}_j) \;=\; a_i\,b_j\,\delta_{ij} \;=\; a_i\,b_i} \tag{A.1}$$

It links the basis vector $\mathbf{e}_i$ of vector $\mathbf{a}$ scalar with the basis vector $\mathbf{e}_j$ of vector $\mathbf{b}$ which results in a reduction of the order by factor 1. Regarding this, the outcome of the simple scalar product of two vectors $\mathbf{a}$ and $\mathbf{b}$ is a scalar value $a_i\,b_i$.

Simple scalar product of 2nd order tensor and vector

The simple scalar product of a 2nd order tensor $\mathbf{A}$ and a vector $\mathbf{b}$ is defined by:

$$\boxed{\mathbf{A}\,\mathbf{b} \;=\; (A_{ij}\,\mathbf{e}_i \otimes \mathbf{e}_j)\,(b_k\,\mathbf{e}_k) \;=\; A_{ij}\,b_k\,\delta_{jk}\,\mathbf{e}_i \;=\; A_{ij}\,b_j\,\mathbf{e}_i} \tag{A.2}$$

Based on this definition, the simple scalar product links the basis vector $\mathbf{e}_j$ of tensor $\mathbf{A}$ scalar with the basis vector $\mathbf{e}_k$ of vector $\mathbf{b}$ and thus leads to a reduction of the highest order by factor 1. The results is then a vector $A_{ij}\, b_j\, \mathbf{e}_i$, such that the 2nd order tensor $\mathbf{A}$ can be interpreted as a linear operator. In terms of the simple scalar product of a 2nd order tensor and a vector, the distributive and associative laws hold

$$\begin{aligned} \mathbf{A}(\mathbf{a} + \mathbf{b}) &= \mathbf{A}\,\mathbf{a} + \mathbf{A}\,\mathbf{b}\,, \\ \mathbf{a}(\mathbf{A} + \mathbf{B}) &= \mathbf{a}\,\mathbf{A} + \mathbf{a}\,\mathbf{B}\,, \\ \alpha\,(\mathbf{A}\,\mathbf{a}) &= (\alpha\,\mathbf{A})\,\mathbf{a} = \mathbf{A}\,(\alpha\,\mathbf{a})\,. \end{aligned} \tag{A.3}$$

Simple scalar product of two 2nd order tensors

Considering two 2nd order tensors $\mathbf{A}$ and $\mathbf{B}$, the simple scalar product reads as:

$$\boxed{\mathbf{A}\,\mathbf{B} = (A_{ij}\,\mathbf{e}_i \otimes \mathbf{e}_j)\,(B_{kl}\,\mathbf{e}_k \otimes \mathbf{e}_l) = A_{ij}\,B_{kl}\,\delta_{jk}\,\mathbf{e}_i \otimes \mathbf{e}_j = A_{ij}\,B_{ij}\,\mathbf{e}_i \otimes \mathbf{e}_j} \tag{A.4}$$

It links the basis vector $\mathbf{e}_j$ of tensor $\mathbf{A}$ scalar with the basis vector $\mathbf{e}_k$ of tensor $\mathbf{B}$ and thus results in a 2nd order tensor $A_{ij}\,B_{ij}\,\mathbf{e}_i \otimes \mathbf{e}_j$. Here, the order is not reduced by the simple scalar product. In terms of the simple scalar product of two 2nd order tensors, the distributive and associative laws hold, but the commutative law does not

$$\begin{aligned} \mathbf{A}\,(\mathbf{B} + \mathbf{C}) &= \mathbf{A}\,\mathbf{B} + \mathbf{A}\,\mathbf{C}\,, \\ \mathbf{A}\,(\mathbf{B}\,\mathbf{C}) &= (\mathbf{A}\,\mathbf{B})\,\mathbf{C}\,, \\ \mathbf{A}\,\mathbf{B} &\neq \mathbf{B}\,\mathbf{A}\,. \end{aligned} \tag{A.5}$$

A.2 Double scalar product

The double scalar product is characterised by a single dot "$\cdot$". In contrast to the simple scalar product, the double scalar product always links two basis vectors with two others. Therefore, the double scalar product can only be applied for tensors of 2nd or higher order. Regarding two 2nd order tensors $\mathbf{A}$ and $\mathbf{B}$, the double scalar product is expressed by:

$$\boxed{\mathbf{A} \cdot \mathbf{B} = (A_{ij}\,\mathbf{e}_i \otimes \mathbf{e}_j) \cdot (B_{kl}\,\mathbf{e}_k \otimes \mathbf{e}_l) = A_{ij}\,B_{kl}\,\delta_{ik}\,\delta_{jl} = A_{ij}\,B_{ij}} \tag{A.6}$$

It links the basis vector $\mathbf{e}_i$ of tensor $\mathbf{A}$ scalar with the basis vector $\mathbf{e}_k$ of tensor $\mathbf{B}$ and the basis vector $\mathbf{e}_j$ of tensor $\mathbf{A}$ scalar with the basis vector $\mathbf{e}_l$ of tensor $\mathbf{B}$. Thus, the order is twice reduced by applying the double scalar product such that a scalar value $A_{ij}\,B_{ij}$ is obtained. For the double scalar product of two 2nd order tensors, the

distributive, the associative and the commutative law hold

$$\begin{aligned} \mathbf{A}\cdot(\mathbf{B}+\mathbf{C}) &= \mathbf{A}\cdot\mathbf{B}+\mathbf{A}\cdot\mathbf{C}\,, \\ (\alpha\,\mathbf{A})\cdot\mathbf{B} &= \mathbf{A}\cdot(\alpha\,\mathbf{B}) = \alpha(\mathbf{A}\cdot\mathbf{B})\,\mathbf{C}\,, \\ \mathbf{A}\cdot\mathbf{B} &= \mathbf{B}\cdot\mathbf{A}\,. \end{aligned} \tag{A.7}$$

Moreover, the double scalar product between a 4th order tensor $\overset{4}{\mathbf{A}}$ and a 2nd order tensor $\mathbf{B}$ is defined by:

$$\boxed{\overset{4}{\mathbf{A}}\cdot\mathbf{B} = (A_{ijkl}\,\mathbf{e}_i\otimes\mathbf{e}_j\otimes\mathbf{e}_k\otimes\mathbf{e}_l)\cdot(B_{mn}\,\mathbf{e}_m\otimes\mathbf{e}_n) = A_{ijkl}\,B_{kl}\,\mathbf{e}_i\otimes\mathbf{e}_j} \tag{A.8}$$

A.3 Cross product

The cross product is characterised by the mathematical operator "$\times$". Considering two vectors $\mathbf{a}$ and $\mathbf{b}$, the cross product between both is defined by:

$$\boxed{\mathbf{a}\times\mathbf{b} = a_i\,b_j\,e_{ijk}\,\mathbf{e}_k = \begin{bmatrix} a_2\,b_3 & - & a_3\,b_2 \\ -a_1\,b_3 & + & a_3\,b_1 \\ a_1\,b_2 & - & a_2\,b_1 \end{bmatrix}} \tag{A.9}$$

A.4 Dyadic product

The dyadic product is characterised by the mathematical operator "$\otimes$". The dyadic product between two vectors $\mathbf{a}$ and $\mathbf{b}$ results in a 2nd order tensor $\mathbf{A}$ and is expressed by:

$$\boxed{\mathbf{A} = \mathbf{a}\otimes\mathbf{b} = (a_i\,\mathbf{e}_i)\otimes(b_j\,\mathbf{e}_j) = a_i\,b_j\,(\mathbf{e}_i\otimes\mathbf{e}_j) = A_{ij}\,(\mathbf{e}_i\otimes\mathbf{e}_j)} \tag{A.10}$$

Applying the dyadic product between two 2nd order tensors $\mathbf{A}$ and $\mathbf{B}$ results in a 4th order tensor $\overset{4}{\mathbf{A}}$:

$$\boxed{\begin{aligned} \overset{4}{\mathbf{A}} &= \mathbf{A}\otimes\mathbf{B} = (A_{ij}\,\mathbf{e}_i\otimes\mathbf{e}_j)\otimes(B_{kl}\,\mathbf{e}_k\otimes\mathbf{e}_l) \\ &= A_{ij}\,B_{kl}\,(\mathbf{e}_i\otimes\mathbf{e}_j\otimes\mathbf{e}_i\otimes\mathbf{e}_j) = \overset{4}{A}_{ijkl}\;(\mathbf{e}_i\otimes\mathbf{e}_j\otimes\mathbf{e}_i\otimes\mathbf{e}_j) \end{aligned}} \tag{A.11}$$

A.5 Transposed and inverse

The transposed of a tensor $\mathbf{A}$ with

$$\mathbf{A} = A_{ij} (\mathbf{e}_i \otimes \mathbf{e}_j) \tag{A.12}$$

is obtained by switching the basis vectors and can thus be defined by

$$\mathbf{A}^T = A_{ij} (\mathbf{e}_j \otimes \mathbf{e}_i) \ . \tag{A.13}$$

Moreover, the following relations hold

$$\begin{aligned} (\mathbf{A} + \mathbf{B})^T &= \mathbf{A}^T + \mathbf{B}^T \ , \\ (\alpha \, \mathbf{A})^T &= \alpha \, \mathbf{A}^T \ , \\ (\mathbf{A} \, \mathbf{B})^T &= \mathbf{B}^T \, \mathbf{A}^T \ . \end{aligned} \tag{A.14}$$

The inverse of tensor $\mathbf{A}$ is defined by the following relation

$$\mathbf{A} \, \mathbf{A}^{-1} = \mathbf{1} \ . \tag{A.15}$$

Furthermore, the following relations are defined

$$\begin{aligned} (\mathbf{A}^{-1})^T &= \mathbf{A}^{-T} \ , \\ (\mathbf{A} \, \mathbf{B})^{-1} &= \mathbf{B}^{-1} \, \mathbf{A}^{-1} \ . \end{aligned} \tag{A.16}$$

In terms of 4th order tensors, the special transposed T_{ij} is introduced. It indicates a switch of the indices i and j. Regarding this, the simple scalar product of three 2nd order tensors $\mathbf{A}$, $\mathbf{B}$ and $\mathbf{C}$ can be expressed by

$$\begin{aligned} \mathbf{A} \, \mathbf{B} \, \mathbf{C} &= [\mathbf{A} \otimes \mathbf{B}]^{T24} \cdot \mathbf{C}^T \\ &= \left[\mathbf{A} \otimes \mathbf{B}^T\right]^{T23} \cdot \mathbf{C} \\ &= [\mathbf{B} \otimes \mathbf{A}]^{T13} \cdot \mathbf{C}^T \\ &= \left[\mathbf{B} \otimes \mathbf{A}^T\right]^{T14} \cdot \mathbf{C} \ . \end{aligned} \tag{A.17}$$

A.6 Trace of a tensor

The trace operation of tensor $\mathbf{A}$ is defined by

$$\mathrm{tr}(\mathbf{A}) = \mathbf{A} \cdot \mathbf{1} \ . \tag{A.18}$$

Moreover, the following relations hold

$$\begin{aligned}
\mathrm{tr}(\alpha\,\mathbf{A}) &= \alpha\ \mathrm{tr}(\mathbf{A})\ , \\
\mathrm{tr}(\mathbf{a}\otimes\mathbf{b}) &= \mathbf{a}\cdot\mathbf{b}\ , \\
\mathrm{tr}(\mathbf{A}^T) &= \mathrm{tr}(\mathbf{A})\ , \\
\mathrm{tr}(\mathbf{A}\,\mathbf{B}) &= \mathrm{tr}(\mathbf{B}\,\mathbf{A})\ , \\
\mathrm{tr}(\mathbf{A}\,\mathbf{B}\,\mathbf{C}) &= \mathrm{tr}(\mathbf{B}\,\mathbf{C}\,\mathbf{A}) = \mathrm{tr}(\mathbf{C}\,\mathbf{A}\,\mathbf{B})\ ,\ .
\end{aligned} \tag{A.19}$$

A.7 Mathematical relations

Among others, some mathematical relations which are partly applied in this work can be defined from the relations introduced above:

$$\begin{aligned}
(\mathbf{1}\otimes\mathbf{1})\,\mathbf{A} &= \mathrm{tr}(\mathbf{A})\ , \\
(\mathbf{1}\otimes\mathbf{1})^{T23}\,\mathbf{A} &= \mathbf{A}\ , \\
(\mathbf{1}\otimes\mathbf{1})^{T24}\,\mathbf{A} &= \mathbf{A}^T\ .
\end{aligned} \tag{A.20}$$

$$\begin{aligned}
(\mathbf{A}\otimes\mathbf{B})^{T23}\,(\mathbf{C}\otimes\mathbf{D})^{T23} &= (\mathbf{A}\,\mathbf{C}\otimes\mathbf{B}\,\mathbf{D})^{T23}\ , \\
(\mathbf{A}\otimes\mathbf{B})^{T23}\,(\mathbf{C}\otimes\mathbf{D}) &= (\mathbf{A}\,\mathbf{C}\,\mathbf{B}^T\otimes\mathbf{D})\ , \\
(\mathbf{A}\otimes\mathbf{B})\,(\mathbf{C}\otimes\mathbf{D})^{T23} &= (\mathbf{A}\otimes\mathbf{C}^T\,\mathbf{B}\,\mathbf{D})\ , \\
(\mathbf{A}\otimes\mathbf{B})^{T23}\,\mathbf{C} &= \mathbf{A}\,\mathbf{C}\,\mathbf{B}^T\ .
\end{aligned} \tag{A.21}$$

Bibliography

Adolfsson, K. (2004). Nonlinear Fractional Order Viscoelasticity at Large Strains. *Nonlinear Dynamics 38*, 233–246.

Adolfsson, K. and M. Enelund (2003). Fractional Derivative Viscoelasticity at Large Deformations. *Nonlinear Dynamics 33*, 301–321.

Ahmadi, H. R., D. Besdo, J. Ihlemann, J. G. R. Kingston, and A. H. Muhr (2005). Transient response of inelastic materials to change of amplitude. *4th European Conference for Constitutive Models for Rubber (ECCMR 2005)*.

Ahmadi, H. R. and A. H. Muhr (1997). Modeling Dynamic Properties of Filled Rubber. *Rubber Comp. Proc. Appl.*, 451–461.

Arruda, E. M. and M. C. Boyce (1993). A three-dimensional constitutive model for the large stretch behavior of rubber elastic materials. *J. Mech. Phys. Solids 41*, 389–412.

Attard, M. M. and G. W. Hunt (2004). Hyperelastic constitutive modeling under finite strain. *Int. J. Solids Structures 41*, 5327–5350.

Bagley, R. L. and P. J. Torvik (1979). A generalized derivative model for an elastomer damper. *Shock and Vibration Bulletin 49*, 135–143.

Bagley, R. L. and P. J. Torvik (1983a). Fractional calculus – a different approach to the analysis of viscoelastically damped structures. *AIAA Journal 21*(5), 741–748.

Bagley, R. L. and P. J. Torvik (1983b). A theoretical basis for the application of fractional calculus to viscoelasticity. *J. Rheol. 27*(3), 201–210.

Bagley, R. L. and P. J. Torvik (1985). Fractional calculus in the transient analysis of viscoelastically damped structures. *AIAA Journal 23*(6), 918–925.

Besdo, D. and J. Ihlemann (1996). Zur Modellierung des Stoffverhaltens von Elastomeren. *Kautschuk Gummi Kunststoffe 49*, 495–503.

Besdo, D. and J. Ihlemann (2003). A phenomenological constitutive model for rubberlike materials and ist numerical applications. *Int. J. Plast. 19*(7), 1019–1036.

Betten, J. (1997). *Finite Elemente für Ingenieure 1: Grundlagen, Matrixmethoden, Elastisches Kontinuum*. Springer-Verlag, Berlin, Heidelberg, New York.

Betten, J. (1998). *Finite Elemente für Ingenieure 2: Variationsrechnung, Energiemethoden, Näherungsverfahren, Nichtlinearitäten*. Springer-Verlag, Berlin, Heidelberg, New York.

Blom, P. and L. Kari (2011). A nonlinear constitutive audio frequency magneto-sensitive rubber model including amplitude, frequency and magnetic field dependence. *Journal of Sound and Vibration 330*(5), 947–954.

Blom, P. and L. Kari (2012). The frequency, amplitude and magnetic field dependent torsional stiffness of a magneto-sensitive rubber bushing. *International Journal of Mechanical Sciences 60*(1), 54–58.

Boehm, J. (2001). *Der Payneffekt: Interpretation und Anwendung in einem neuen Materialgesetz für Elastomere*. Fakultät für Physik der Universität Regensburg, Dissertation.

Bueche, F. (1961). Mullins effect and rubber-filler interaction. *J. Appl. Polymer Sci. 5*, 271–281.

Caputo, M. (1967). Linear Models of Dissipation whose Q is almost Frequency Independent II. *Geographical Journal of the Royal Astronomical Society 13*(5), 529–539.

Caputo, M. and F. Mainardi (1971). Linear models of dissipation in anelastic solids. *La Rivista del Nuovo Cimento 1*, 161–198.

Chagnon, G., E. Verron, L. Gornet, G. Marckmann, and P. Charrier (2004). On the relevance of Continuum Damage Mechanics as applied to the Mullins effect in elastomers. *J. Mech. Phys. Solids 21*, 1627–1650.

Chazeau, L., J. Brown, L. Yano, and S. Sternstein (2000). Modulus Recovery Kinetics and other Insights into the Payne Effect for Filled Elastomers. *Polymer Composites 21*, 202–222.

Cho, J. H. and S. K. Youn (2006). A viscoelastic constitutive model of rubber under small oscillatory load superimposed on large static deformation considering the Payne effect. *Arch. Rat. Mech. Anal. 75*, 275–288.

Coleman, B. D. and W. Noll (1961). Foundations of Linear Viscoelasticity. *Reviews of Modern Physics 33*(2), 239–249.

Coleman, B. D. and W. Noll (1963). The thermodynamics of elastic materials with heat conduction and viscosity. *Arch. Rat. Mech. Anal. 13*, 167–178.

Dannenberg, E. (1975). The effects of surface chemical interactions on the properties of filler-reinforced rubbers. *Rubber Chem. Technol. 48*, 410–444.

Dorfmann, A. and R. W. Ogden (2003). A pseudo-elastic model for loading, partial unloading and reloading of particle reinforced rubber. *Int. J. Solids Structures 40*, 2699–2714.

Drozdov, A. D. (1997). Fractional differential models in finite viscoelasticity. *Acta Mater. 124*, 155–180.

Drozdov, A. D. (1998). A model for the nonlinear viscoelastic response in polymers at finite strains. *Int. J. Solids Structures 35*, 2315–2347.

Dutta, N. K. and D. K. Tripathy (1992). Effects of types of filler on the molecular relaxation characteristics, dynamic mechanical, and physical properties of rubber vulcanizates. *J. Appl. Polymer Sci. 44*, 1635–1648.

Ehlers, W. (2007). *Tensorrechnung: Eine Einführung*. Universität Stuttgart, Institut für Mechanik, WS 2007/08.

Ehrenstein, G. W. (1999). *Polymer-Werkstoffe, 2. vollständig überarbeitete Auflage*. Hanser Verlag.

Enelund, M. and L. Josefson (1997). Time-domain finite element analysis of viscoelastic structures with fractional derivatives constitutive relations. *AIAA Journal 35*(10), 1630–1637.

Enelund, M., L. Maehler, K. Runesson, and L. Josefson (1999). Formulation and integration of the standard linear viscoelastic solid with fractional order rate laws. *Int. J. Solids Structures 36*, 2417–2442.

Ferry, J. D. (1980). *Viscoelastic Properties of Polymers*. John Wiley, New York.

Flammersheim, H. J., W. F. Hemminger, and G. W. H. Höhne (2003). *Differential Scanning Calorimetry: An Introduction for Practitioners*. Springer Verlag, Berlin.

Fletscher, W. P. and A. N. Gent (1953). Non-linearity in the dynamic properties of vulcanized rubber compounds. *Transactions of the Institution of the Rubber Industry 29*, 266–280.

Freund, M. and J. Ihlemann (2010). Generalization of one-dimensional material methods for the finite element method. *Z. Angew. Math. Mech. 90*, 399–417.

Garcia, M. J. (2006). *Engineering rubber bushing stiffness formulas including dynamic amplitude dependence*. Royal Institute of Technology, Stockholm.

Garcia, M. J., L. Kari, J. Vinolas, and N. Gil-Negrete (2007). Frequency and amplitude dependence of the axial and radial stiffness of carbon-black filled rubber bushings. *Polymer Testing 26*(5), 629–638.

Gaul, L. and M. Schanz (1994). Dynamics of viscoelastic solids treated by boundary element approaches in time domain. *Eur. J. Mech., A/Solids 13*(4), 43–59.

Gaul, L. and M. Schanz (1999). A comparative study of three boundary element approaches to calculate the transient response of viscoelastic solids with unbounded domains. *Comp. Meth. Appl. Mech. Eng. 179*, 111–123.

Gehman, S. D. (1942). Rubber in Vibration. *J. Appl. Phys. 13*(6), 402–413.

Gehman, S. D., D. E. Woodford, and R. B. Stambaugh (1941). Dynamic properties of rubber. *Industrial and Engineering Chemistry 33*(8), 1032–1038.

Gent, A. N. (1996). A new constitutive relation for rubber. *Rubber Chem. Technol. 69*, 59–61.

Gil-Negrete, N., J. Vinolas, and L. Kari (2009). A Nonlinear Rubber Material Model Combining Fractional Order Viscoelasticity and Amplitude Dependent Effects. *J. Appl. Mech. 76*, 011009–1–011009–9.

Govindjee, S. and S. Reese (1997). A Presentation and Comparison of Two Large Deformation Viscoelasticity Models. *Journal of Engineering Materials and Technology 119*, 251–255.

Govindjee, S. and J. C. Simo (1991). A micro-mechanically based continuum damage model for carbon black-filled rubbers incorporating Mullins' effect. *J. Mech. Phys. Solids 39*(1), 87–112.

Govindjee, S. and J. C. Simo (1992a). Mullins' effect and the strain amplitude dependence of the storage modulus. *Int. J. Solids Structures 29*(14/15), 1737–1751.

Govindjee, S. and J. C. Simo (1992b). Transition from micro-mechanics to computationally efficient phenomenology: Carbon black filled rubbers incorporating Mullins effect. *J. Mech. Phys. Solids 40*, 213–233.

Greeve, R. (2003). *Kontinuumsmechanik: Ein Grundkurs für Ingenieure und Physiker*. Springer Verlag Berlin Heidelberg New York.

Gurtin, M. E. and I. Herrera (1965). On dissipation inequalities and linear viscoelasticity. *Quarterly Appl. Math. 23*(3), 235–245.

Hartmann, S. (2001). Parameter estimation of hyperelastic relations of generalized polynominal-type with constraint conditions. *Int. J. Solids Structures 38*, 7999–8018.

Hartmann, S. (2002). Computation in finite-strain viscoelasticity: Finite elements based on the interpretation as differential-algebraic equations. *Comp. Meth. Appl. Mech. Eng. 191*(13–14), 1439–1470.

Hartmann, S. (2003). *Finite-Elemente Berechnung inelastischer Kontinua (Interpretation als Algebro-Differentialgleichungssysteme)*. Institut für Mechanik, Universität Gesamthochschule Kassel, Habilitation.

Hartmann, S. and P. Haupt (1999). *Spannungsalgorithmus zur Berücksichtigung nichtlinearer Viskoelastizität*. Institut für Mechanik, Universität Gesamthochschule Kassel - Mitteilung 5/1999.

Harwood, J., L. Mullins, and A. Payne (1965). Stress Softening in Natural Rubber Vulcanisates. Part II. Stress Softening Effects in Pure Gum and Filler Loaded Rubbers. *J. Appl. Polymer Sci. 9*, 3011–3021.

Harwood, J. and A. Payne (1966). Stress Softening in Natural Rubber Vulcanisates. Part III. Carbon Black-Filled Vulcanisates. *J. Appl. Polymer Sci. 10*, 315–324.

Haupt, P. (2000). *Continuum Mechanics and Theory of Materials*. Springer-Verlag, Berlin & Heidelberg.

Haupt, P. and A. Lion (2002). On finite linear viscoelasticity of incompressible isotropic materials. *Acta Mater. 159*, 87–124.

Haupt, P., A. Lion, and E. Backhaus (2000). On the dynamic behavior of polymers under finite strains: constitutive modelling and identification of parameters. *Int. J. Solids Structures 37*, 3633–3646.

Haupt, P. and C. Tsakmakis (1989). On the application of dual variables in continuum mechanics. *Continuum Mech. Therm. 1*, 165–196.

Heimes, T. (2005). *Finite Thermoinelastizität*. Institut für Mechanik, Fakultät für Luft- und Raumfahrttechnik, Universität der Bundeswehr München, Dissertation.

Heinrich, G., G. Helmis, and T. A. Vilgis (1995). Polymere Netzwerke - Entwicklungsstand der molekular-statistischen Theorie. *Kautschuk Gummi Kunststoffe 48*, 689–702.

Heinrich, G. and M. Kaliske (1997). Theoretical and numerical formulation of a molecular based constitutive tube-model of rubber elasticity. *Computational and Theoretical Polymer Science 7*, 227–241.

Heinrich, G. and M. Klueppel (2002). Recent Advances in the Theory of Filler Networking in Elastomers. *Advances in Polymer Science 160*, 1–44.

Heinrich, G. and M. Klueppel (2004). The Role of Polymer-Filler-Interphase in Reinforcement of Elastomers. *Kautschuk Gummi Kunststoffe 57*, 452–454.

Heinrich, G., E. Straube, and G. Helmis (1988). Rubber elasticity of polymer networks: Theories. *Polymer Physics 85*, 33–87.

Heinrich, G., E. Straube, and G. Helmis (2002). *Recent Advances in the Theory of Filler Networking in Elastomers, Filled Elastomers Drug Delivery System*. Springer-Verlag, Berlin & Heidelberg.

Heinrich, G. and T. A. Vilgis (1993). Contribution of Entanglements of the Mechanical Properties of Carbon Black Filled Polymer Networks. *Macromolekules 26*, 1109–1119.

Hoefer, P. (2009). *Dynamische Eigenschaften technischer Gummiwerkstoffe*. Verlag Dr. Hut. ISBN 978-3-86853-204-3.

Hoefer, P. and A. Lion (2009). Modelling of frequency- and amplitude-dependent material properties of filler-reinforced rubber. *J. Mech. Phys. Solids 57*(5), 500–520.

Holzapfel, G. A. (1996). On Large Strain Viscoelasticity: Continuum Formulation and Finite Element Applications to Elastomeric Structures. *Int. J. Numer. Meth. Eng. 39*(22), 3903–3926.

Holzapfel, G. A. (2000). *Nonlinear Solid Mechanics - A Continuum Approach for Engineering*. John Wiley & Sons, LTD.

Huber, G., T. A. Vilgis, and G. Heinrich (1996). Universal properties in the dynamical deformation of filled rubbers. *Phys.: Condens. Matter 8*, 409–412.

Huber, N. and C. Tsakmakis (1999). *Finite Deformation Viscoelasticity Laws*. Forschungszentrum Karlsruhe, Institut für Materialforschung II (IMF II) - Forschungsbericht.

Ihlemann, J. (2005). Richtungsabhängigkeit beim Mullins-Effekt. *Kautschuk Gummi Kunststoffe 58*, 438–447.

James, H. M. and A. Green (1975). Strain Energy Functions of Rubber. II. The Characterization of Filled Vulcanizates. *J. Appl. Polymer Sci. 19*, 2319–2330.

James, H. M., A. Green, and G. Simpson (1975). Strain Energy Functions of Rubber. I. Characterization of Gum Vulcanizates. *J. Appl. Polymer Sci. 19*, 2033–2058.

Johlitz, M. (2008). *Experimentelle Untersuchung von Maßstabseffekten in Klebungen*. Dissertation, Universität des Saarlandes.

Johlitz, M. (2009). *Materialmodellierung*. Universität des Saarlandes, Lehrstuhl für Technische Mechanik.

Joshi, P. and A. I. Lenov (2001). Modelling of steady and time-dependent responses in filled, uncured and crosslinked rubbers. *Rheol. Acta 40*, 350–365.

J.Retka, P. Hoefer, and A. Lion (2007). Numerische Simulation aushärtender Klebstoffe. *Beiträge zur Materialtheorie (Heft 1/07). Editor: A. Lion. ISSN 1862-5703*.

Kaliske, M. and G. Heinrich (1999). An Extended Tube-Model for Rubber Elasticity: Statical-Mechanical Theorie and Finite Element Implementation. *Polymer Physics 72*, 602–632.

Kaliske, M. and H. Rothert (1997a). Formulation and implementation of three-dimensional viscoelasticity at small and finite strains. *Comp. Mech. 19*(3), 228–239.

Kaliske, M. and H. Rothert (1997b). On the finite element implementation of rubber-like materials at finite strains. *Eng. Comp. 14*, 216–232.

Kaliske, M. and H. Rothert (1998). Constitutive approach to rate-independent properties of filled elastomers. *Int. J. Solids Structures 35*(17), 2057–2071.

Kaliske, M., H. Rothert, and L. Nasdala (2001). On damage modelling for elastic and viscoelastic materials at finite strain. *Comput. Struct. 79*, 2133–2141.

Kari, L. (2001a). On the Waveguide Modelling of Dynamic Stiffness of Cylindrical Vibration Isolators, Part I: The Model, Solution and Experimental Comparison. *J. Sound Vib. 244*(2), 211–233.

Kari, L. (2001b). On the Waveguide Modelling of Dynamic Stiffness of Cylindrical Vibration Isolators, Part II: The Dispersion Relation Solution, Convergence Analysis and Comparison with Simple Models. *J. Sound Vib. 244*(2), 235–257.

Kari, L. (2003). On the dynamic stiffness of preloaded vibration isolators in the audible frequency range: Modeling and experiments. *J. Acoust. Soc. Am. 113*(4), 1909–1921.

Kilbas, A. A., H. M. Srivastava, and J. J. Trujillo (2006). *North-Holland Mathematics Studies – Theory and Applications of Fractional Differential Equations*, Volume 204. Elsevier B.V.

Kilian, H. G. and T. Viglis (1984). Fundamental aspects of rubber-elasticity in real networks. *Colloid and Polymer Science 262*, 15–21.

Kim, B. K. and S. K. Youn (2001). A viscoelastic constitutive model of rubber under small oscillatory load superimposed on large static deformation. *Arch. Appl. Mech. 71*, 748–763.

Klueppel, M. (2003). Hyperelasticity and Stress Softening of Filler Reinforced Polymer Networks. *Macromol. Symp. 200*, 31–43.

Klueppel, M. (2008). Evaluation of viscoelastic master curves of filled elastomers and applications to fracture mechanics. *J. Phys.: Condens. Matter 21*, 1–10.

Klueppel, M. and G. Heinrich (1995). Fractal Structures in Carbon Black Reinforced Rubbers. *Rubber Chem. Technol. 68*, 623–651.

Klueppel, M. and G. Heinrich (2002). Recent Advances in the Theory of Filler Networking in Elastomers. *Adv. Polym. Sci. 160*, 1–44.

Klueppel, M. and J. Schramm (2000). A generalized tube model of rubber elasticity and stress softening of filler reinforced elastomer systems. *Macromolecular Theory and Simulations 9*(9), 742–754.

Koeller, R. C. (1984). Applications of fractional calculus to the theory of viscoelasticity. *J. Appl. Mech. 51*, 299–307.

Kraus, G. (1984). Mechanical losses in carbon-black-filled rubbers. *J. Appl. Polymer Sci. 39*, 75–92.

Krawietz, A. (1986). Materialtheorie: Mathematische Beschreibung des phänomenologischen thermomechanischen Verhaltens. *J. Appl. Polymer Sci.*.

Lee, E. H. (1969). Elastic-Plastic Deformation at Finite Strains. *J. Appl. Mech. 36*, 1–6.

Lee, E. H. and D. T. Liu (1967). Finite-Strain Elastic-Plastic Theory with Application to Plane-Wave Analysis. *J. Appl. Phys. 38*, 19–27.

Lee, W. S., S. K. Youn, and B. K. Kim (2003). Finite element analysis and design optimization of rubber components for vibration isolation. *Arch. Mech. Warszawa 55*, 449–479.

Lewandowski, R. and B. Chorazyczewski (2010). Identification of the parameters of the Kelvin-Voigt and the Maxwell fractional models, used to modeling of viscoelastic dampers. *Comput. Struct. 88*(1-2), 1–17.

Lewandowski, R. and Z. Pawlak (2011). Dynamic analysis of frames with viscoelastic dampers modelled by rheological models with fractional derivatives. *J. Sound Vib. 330*(5), 923–936.

Lianis, G. (1963). Small deformations superposed on an initial large deformation in viscoelastic bodies. *Proceedings Fourth international congress on rheology, New York*, 104–119.

Lion, A. (1996). A Constitutive Model for Carbon Black Filled Rubber: Experimental Investigations and Mathematical Representation. *Continuum Mechanics and Thermodynamics 8*, 153–169.

Lion, A. (1997a). On the large deformation behaviour of reinforced rubber at different temperatures. *J. Mech. Phys. Solids 45*(11/12), 1805–1834.

Lion, A. (1997b). A Physically Based Method to Represent the Thermomechanical Behaviour of Elastomers. *Acta Mater. 123*, 1–26.

Lion, A. (1998). Thixotropic behaviour of rubber under dynamic loading histories: Experiments and theory. *J. Mech. Phys. Solids 46*(5), 895–930.

Lion, A. (2000a). Constitutive modelling in finite thermoviscoplasticity: a physical approach based on nonlinear rheological models. *Int. J. Plast. 16*, 469–494.

Lion, A. (2000b). Strain-Dependent Dynamic Properties of Filled Rubber: A Non-Linear Viscoelastic Approach Based on Structural Variables. *Rubber Chem. Technol. 72*, 410–429.

Lion, A. (2000c). Thermomechanik von Elastomeren. *Berichte des Instituts für Mechanik der Universität Kassel (Bericht 1/2000). ISBN 3-89792-023-9*.

Lion, A. (2001). Thermomechanically consistent formulations of the standard linear solid using fractional derivatives. *Arch. Mech. 53*, 253–273.

Lion, A. (2005). Phenomenological Modelling of Strain-Induced Structural Changes in Filler-Reinforced Elastomers. *Kautschuk Gummi Kunststoffe 58*(4), 157–162.

Lion, A. (2006). Dynamische Modellierung von elastomeren Bauteilen. *Universität der Bundeswehr München, Institut für Mechanik LRT 4*.

Lion, A. (2007). Einführung in die Lineare Viskoelastizität. *Beiträge zur Materialtheorie (Heft 4/07). ISSN 1862-5703*.

Lion, A. (2008). *Einführung in die Kontinuumsmechanik und Materialtheorie*. Universität dder Bundeswehr München, Fakultät für Luft- und Raumfahrttechnik, Institut für Mechanik.

Lion, A. and C. Kardelky (2004). The Payne effect in finite viscoelasticity: constitutive modelling based on fractional derivates and intrinsic time scales. *Int. J. Plast. 20*, 1313–1345.

Lion, A., J. Retka, and M. Rendek (2009). On the calculation of predeformation-dependent dynamic modulus tensors in finite nonlinear viscoelasticity. *Mech. Res. Commun. 36*, 623–658.

Lubarda, V. A. (2004). Constitutive theories based on the multiplicative decomposition of deformation gradient: Thermoelasticity, elastoplasticity and biomechanics. *Appl. Mech. Rev. 57*, 95–108.

Lubliner, J. (1985). A model of rubber viscoelasticity. *Mech. Res. Commun. 12*(2), 93–99.

Matsuda, A., O. Watanabe, and R. D. Borst (2004). The stress rate of hyperelasticity based on updated Lagrangian formulation. *JSME International Journal 47*, 164–172.

Meggyes, A. (2001). Multiple decomposition in finite deformation theory. *Acta Mater. 146*, 169–182.

Menard, K. (1999). *Dynamic Mechanical Analysis: A Practical Introduction*. CRC Press LLC.

Michaeli, W. (2006). *Einführung in die Kunststoffverarbeitung, 5. Auflage*. Carl Hanser Verlag München Wien.

Middendorf, P. (2001). Geometrisch nichtlineare Viskoelastiziät. *München*.

Middendorf, P. (2002). *Viskoelastisches Verhalten von Polymersystemen*. Institut für Mechanik, Fakultät für Luft- und Raumfahrttechnik, Universität der Bundeswehr München, Dissertation – Fortschritt-Berichte VDI, Reihe 5, Nr. 661.

Miehe, C. (1994). Aspects of the formulation and finite element implementation of large strain isotropic elasticity. *Int. J. Num. Meth. Eng. 37*, 1981–2004.

Miehe, C. (1995). Discontinuous and Continuous Damage Evolution in Ogden-Type Large Strain Elastic Materials. *Eur. J. Mech., A/Solids 14*(5), 697–720.

Miehe, C. and S. Goektepe (2005). A micro-macro approach to rubber-like materials. Part III: The micro-sphere model of anisotropic Mullins-type damage. *J. Mech. Phys. Solids 53*(10), 2259–2283.

Miehe, C. and J. Keck (2000). Superimposed finite elastic-viscoelastic-plastoelastic stress response with damage in filled rubber polymers. Experiments, modelling and algorithmic implementation. *J. Mech. Phys. Solids 48*, 323–365.

Mooney, M. (1940). A Theory of Large Elastic Deformation. *J. Appl. Phys. 11*, 582–592.

Morman, K. N. and J. C. Nagtegaal (1983). Finite element analysis of sinusoidal small-amplitude vibrations in deformed viscoelastic solids, Part I: Theoretical development. *Int. J. Numer. Meth. Eng. 19*(7), 1079–1103.

MSC.Software (2010a). *Marc 2010 Volume A: Theory and User Information*. MSC.Software Corporation.

MSC.Software (2010b). *Marc 2010 Volume B: Element Library*. MSC.Software Corporation.

MSC.Software (2010c). *Marc 2010 Volume C: Program Input*. MSC.Software Corporation.

MSC.Software (2010d). *Marc 2010 Volume D: User Subroutines and Special Routines*. MSC.Software Corporation.

MSC.Software (2010e). *Marc 2010 Volume E: Demonstration Problems*. MSC.Software Corporation.

Mullins, L. (1948). Effect of Stretching on the Properties of Rubber. *Rubber Chem. Technol. 21*(281), 281–300.

Mullins, L. (1950). The Thixotropic Behavior of Carbon Black in Rubber. *J. Phys. Chem. 54*(2), 239–251.

Mullins, L. (1969). Softening of rubber by deformation. *Rubber Chem. Technol. 42*, 339–362.

Mullins, L. and N. Tobin (1957). Theoretical model for the elastic behavior of filler-reinforced vulcanized rubber. *Rubber Chem. Technol. 30*, 551–571.

Mullins, L. and N. Tobin (1965). Stress Softening in Rubber Vulcanizates. Part I. Use of a Strain Amplification Factor to Describe the Elastic Behavior of Filler-Reinforced Vulcanized Rubber. *J. Appl. Polymer Sci. 9*, 2993–3009.

Nacar, A., A. Needleman, and M. Ortiz (1989). A finite element method for analyzing localization in rate dependent solids at finite strains. *Comp. Meth. Appl. Mech. Eng. 73*, 235–258.

Nackenhorst, U. (2004). The ALE-formulation of bodies in rolling contact: Theoretical foundations and finite element approach. *Comp. Meth. Appl. Mech. Eng. 193*, 4299–4322.

Nonnenbacher, T. F. (1991). Fractional relaxation equations for viscoelasticity and related phenomena. *Rheological Modelling: Thermodynamical and Statistical Approaches 381*, 309–320.

Ogden, R. W. (1972). Large Deformation Isotropic Elasticity - On the Correlation of Theory and Experiment for Incompressible Rubberlike Solids. *Proc. R. Soc. Lond. A 326*, 565–584.

Oldham, K. B. and J. Spanier (1974). *Mathematics in Science and Engineering – The fractional calculus: Theory and applications of differentiation and integration to arbitrary order*, Volume 111. London: Academic Press.

Payne, A. R. (1960). A note on the existance of a Yield Point in the dynamic Modulus of loaded Vulcanizates. *J. Appl. Polymer Sci. 3*, 127–127.

Payne, A. R. (1961). Dynamic mechanical properties of filler loaded vulcanizates. *Rubber and Plastics Age 42*, 963–967.

Payne, A. R. (1962a). The dynamic properties of carbon black-loaded natural rubber vulcanizates: Part I. *J. Appl. Polymer Sci. 6*(19), 57–63.

Payne, A. R. (1962b). The dynamic properties of carbon black-loaded natural rubber vulcanizates: Part II. *J. Appl. Polymer Sci. 6*(21), 368–372.

Payne, A. R. (1972). Effect of Vulcanization on the Low-Strain Dynamic Properties of Filled Rubbers. *J. Appl. Polymer Sci. 16*, 1191–1212.

Payne, A. R. (1974). Hysteresis in Rubber Vulcanizates. *Journal of Polymer Science: Symposium 48*, 169–196.

Podlubny, I. (1999). *Mathematics in Science and Engineering – Fractional Differential Equations: An Introduction to Fractional Derivatives, Fractional Differential Equations, to Methods of Their Solution and Some of Their Applications*, Volume 198. London: Academic Press.

Qi, H. J. and M. C. Boyce (2004). Constitutive model for stretch-induced softening of the stress-stretch behavior of elastic materials. *J. Mech. Phys. Solids 52*(10), 2187–2205.

Rabkin, M., T. Brueger, and P. Hinsch (2003). Material model and experimental testing of rubber components under cyclic deformation. *Busfield, J.J.C. (Hrsg.), Muhr, A.H. (Hrsg.): Constitutive Models for Rubber III*, 319–324.

Ramirez, L. and C. Coimbra (2007). A variable order constitutive relation for viscoelasticity. *Annalen der Physik 16*(7/8), 543–552.

Ranz, T. (2007). Elementare Materialmodelle der Linearen Viskoelastizität im Zeitbereich. Publisher A. Lion. *Beiträge zur Materialtheorie (Heft 5/07). ISSN 1862-5703*.

Reese, S. and S. Govindjee (1998). A theory of finite viscoelasticity and numerical aspects. *Int. J. Solids Structures 35*(26–27), 3455–3482.

Rendek, M. and A. Lion (2008). Amplitude- and temperature effects of filler-reinforced rubber: Experiments and Modelling. *Proc. Appl. Math. Mech. 8*, 10457–10458.

Rendek, M. and A. Lion (2010a). Amplitude dependence of filler-reinforced rubber: Experiments, constitutive modelling and FEM-Implementation. *Int. J. Solids Structures 47*(21), 2918–2936.

Rendek, M. and A. Lion (2010b). Strain induced transient effects of filler reinforced elastomers with respect to the Payne-Effect: experiments and constitutive modelling. *Z. Angew. Math. Mech. 90*(5), 436–458.

Retka, J. (2011). *Vibroakustisches Verhalten von viskoelastischen Strukturen unter finiter Vordeformation*. Dissertation, Universität der Bundeswehr München, Fakultät für Luft- und Raumfahrttechnik, Institut für Mechanik.

Richter, S., M. Saphiannikova, and G. Heinrich (2010). Fluctuation kinetics in the light of jamming physics: New insights into the payne-effects in filled rubbers. *6th European Conference for Constitutive Models for Rubber (ECCMR 2009)*.

Rivlin, R. S. (1948). Large Elastic Deformations of Isotropic Materials. I: Fundamental Concepts. *Phil. Trans. Roy. Soc. Lond A 240*, 459–490.

Robertson, C. G. and X. Wang (2006). Spectral hole burning to probe the nature of unjamming (Payne effect) in particle-filled elastomers. *Europhys. Lett. 76*, 278–284.

Röthemeyer, F. and F. Sommer (2006). *Kautschuk Technologie, 2. überarbeitete Auflage*. Carl Hanser Verlag München Wien.

Schiessel, H., R. Metzler, A. Blumen, and T. F. Nonnenbacher (1995). Generalized viscoelastic models: their fractional equations with solutions. *J. Physics A: Math. Gen. 28*, 6567–6584.

Schmidt, A. (2003). *Finite-Elemente-Formulierungen viskoelastischer Stoffgesetze mit fraktionalen Zeitableitungen*. Dissertation, Institut A für Mechanik der Universität Stuttgart.

Schmidt, A. and L. Gaul (2006). On a critique of a numerical scheme for the calculation of fractionally damped dynamical systems. *Mech. Res. Commun. 33*(1), 99–107.

Schwarz, H. R. (1988). *Finite Element Methods*. Academic Press Limited, London.

Schwarz, O. and F. W. Ebeling (2007). *Kunststoffkunde, 9. überarbeitete Auflage*. Vogel Buch Verlag Würzburg.

Schwarzl, F. R. (1990). *Polymermechanik - Struktur und mechanisches Verhalten von Polymeren*. Springer-Verlag.

Schwarzl, F. R. and F. Zahradnik (1980). The time temperature position of the glass-rubber transition of amorphous polymers and the free volume. *Rheol. Acta 19*, 137–152.

Simo, J. C. (1987). On a Fully Three-dimensional Finite-Strain Viscoelastic Damage Model: Formulation and Computational Aspects. *Comp. Meth. Appl. Mech. Eng. 60*, 153–173.

Simo, J. C. (1988). A framework for finite strain elastoplasticity based on maximum plastic dissipation and the multiplicative decomposition: Part I. Continuum formulation. *Computer Methods in Applied Mechanics and Engineering 66*(2), 199–219.

Simo, J. C. and T. J. R. Huges (2000). *Computational Inelasticity*. Springer, New York.

Simo, J. C. and W. Ju (1987). Strain- and stress-based continuum damage models - II. Computational Aspects. *Int. J. Solids Structures 23*(7), 840–869.

Sjoeberg, M. and L. Kari (2002). Non-Linear Behavior of a Rubber Isolator System Using Fractional Derivates. *Vehicle System Dynamics 37*, 217–236.

Sjoeberg, M. and L. Kari (2003). Nonlinear Isolator Dynamics at Finite Deformation: An Effective Hyperelastic, Fractional Derivate, Generalized Friction Model. *Nonlinear Dynamics 33*, 323–336.

Slonimsky, G. L. (1967). Laws of mechanical relaxation processes in polymers. *J. Polym. Sci., Part C 16*, 1667–1672.

Sperling, L. (2006). *Introduction to Physical Polymer Science*. Wiley & Sons.

Suwannachit, A. and U. Nackenhorst (2010). On the constitutive modeling of reinforced rubber in a broad frequency domain. *Z. Angew. Math. Mech. 90*(5), 418–435.

Tobolsky, A. V. (1967). *Mechanische Eigenschaften und Struktur von Polymeren*. Berliner Union, Stuttgart.

Treloar, L. R. G. (1975). *Physics of Rubber Elasticity*. Oxfort University Press.

Truesdell, C. and W. Noll (1965). *The Non-Linear Field Theories of Mechanics, 3rd edition*. Springer-Verlag, Berlin, Heidelberg, New York.

Tschoegl, N. W. (1989). *The phenomenological theory of linear viscoelastic behavior: An Introduction*. Springer-Verlag.

Ulmer, J. D. (1996). Strain Dependence of Dynamic Mechanical Properties of Carbon Black-Filled Rubber Compounds. *Rubber Chem. Technol. 69*(15), 15–47.

Ulmer, J. D., W. Hess, and V. Chirico (1974). The effects of carbon black on rubber hysteresis. *Rubber Chem. Technol. 47*, 729–757.

Vieweg, S., R. Unger, K. Schroeter, E. Donth, and G. Heinrich (1995). Frequency and temperature dependence of the small-strain behaviour of carbon-black filled vulcanizates. *Polym. Networks Blends 5*, 199–204.

Wang, X. and C. Robertson (2005). Strain-Induced nonlinearity of filled rubbers. *Physical Review E 72*.

Williams, M., R. Landel, and J. D. Ferry (1955). The Temperature Dependence of Relaxation Mechanisms in Amorphous Polymers and Other Glass-forming Liquids. *University of Wisconsin Department of Chemistry*, 3701–3707.

Wollscheid, D. and A. Lion (2012). Modelling of predeformation- and frequency-dependent material behaviour of filled rubber under large predeformations superimposed with harmonic deformations of small amplitudes. *Proc. Appl. Math. Mech. 12*(1), 291–292.

Wollscheid, D. and A. Lion (2013a). On the dynamic material behaviour of filled rubber with respect to preload and frequency. *Constitutive Models for Rubber VIII*, 87–93.

Wollscheid, D. and A. Lion (2013b). Predeformation- and frequency-dependent material behaviour of filler-reinforced rubber: Experiments, constitutive modelling and parameter identification. *Int. J. Solids Structures 50*(9), 1217–1225.

Wollscheid, D. and A. Lion (2014). The benefit of fractional derivatives in modelling the dynamics of filler-reinforced rubber under large strains: a comparison with the Maxwell-element approach. *Comp. Mech. 53*(5), 1015–1031.

Wrana, C., C. Fischer, and V. Haertel (2003). Dynamische Messungen an gefüllten Elastomersystemen bei mono- und bimodaler sinusförmiger Anregung. *Kautschuk Gummi Kunststoffe 56*, 437–443.

Wrana, C. and V. Haertel (2008). Dynamic Mechanical Analysis of Filled Elastomers: Amplitude Dependent Measurements under Mono- and Bimodal Sinusoidal Excitation. *Kautschuk Gummi Kunststoffe 56*, 647–655.

Yeoh, O. H. (1993). Some Forms of the Strain Energy Function for Rubber. *Rubber Chem. Technol. 66*(754), 754–771.

Zienkiewicz, O. C. (1971). *The Finite Element Method in Engineering Science*. McGraw-Hill, London.

Zienkiewicz, O. C., R. L. Taylor, and J. Z. Zhu (2005). *The Finite Element Method: Its Basis and Fundamentals (Sixth edition)*. Elsevier Butterworth-Heinemann.